Analysis of simulation and reconstruction methods used by the Pierre Auger Observatory

Steven J. Saffi

School of Physical Sciences
University of Adelaide

This dissertation is submitted for the degree of
Doctor of Philosophy

May 2020

Declaration

I certify that this work contains no material which has been accepted for the award of any other degree or diploma in my name, in any university or other tertiary institution and, to the best of my knowledge and belief, contains no material previously published or written by another person, except where due reference has been made in the text. In addition, I certify that no part of this work will, in the future, be used in a submission in my name, for any other degree or diploma in any university or other tertiary institution without the prior approval of the University of Adelaide and where applicable, any partner institution responsible for the joint-award of this degree.

I give permission for the digital version of my thesis to be made available on the web, via the University's digital research repository, the Library Search and also through web search engines, unless permission has been granted by the University to restrict access for a period of time.

I acknowledge the support I have received for my research through the provision of an Australian Government Research Training Program Scholarship.

March 2020

Abstract

Though a great deal of knowledge has been gained on the physics of ultra-high energy cosmic radiation, many questions remain unanswered. The largest experiment to date, the Pierre Auger Observatory, has been built by an international collaboration to detect and measure the properties of cosmic rays at the highest energies with unprecedented statistics. The Pierre Auger Observatory is a hybrid detector, containing both a surface detector array, and a fluorescence detector. The surface detector array covers an area of 3000 km^2, consisting of $\sim$1600 water Čerenkov detectors, operating with a nearly 100% duty cycle. The Fluorescence detector overlooks the surface detector array with 27 telescopes, each containing 440 PMT's, to measure the development of extensive air showers calorimetrically, operating on clear moonless nights. The two detectors each benefit each other, with the surface detector improving the geometric reconstruction of showers measured by the fluorescence detector, and the fluorescence detector providing an energy scale calibration for the surface detector. After over 15 years collecting data, the Pierre Auger Observatory is undergoing a number of upgrades, including upgrades to the surface detector to distinguish different particle types to better resolve the primary particles composition.

This thesis contains a number of studies related to the detection of cosmic rays. First is an examination of the pointing directions of the fluorescence telescopes, where misalignments in both the pointing directions and in camera positions are found. Second, a new method of dethinning is developed, reducing biases introduced into detector simulations when thinning is employed in extensive air shower simulations. Third, with the ability to distinguish the muon component of extensive air showers being introduced in the upgrades, the shape of the muon shower front has been examined in simulated showers, to determine the feasibility of using the shape of the muon front for composition determination.

Acknowledgements

My time as a PhD student has been long, and although I have had may great experiences, and gained so much knowledge and experience, it has also been filled with many adversities. It has only been with the support of so many of the people around me that I have been able to overcome these, and complete my research. It is here that I would like to express my gratitude to these people.

My supervisors, Bruce Dawson and José Bellido, have been an unwavering source of guidance and support throughout the years. They have provided a great amount wisdom and enthusiasm, without which completion of my PhD would not have been possible.

I would also like to extend my gratitude to the Adelaide High Energy Astrophysics Group. In addition to their advice and and input, they have also been great friends, particularly Max Malacari.

I am grateful for the opportunity provided by the Pierre Auger Observatory collaboration, allowing me to be a part of such an unprecedented experiment. I thank the researchers and staff not only for providing and maintaining the observatory, but also for their input and resources, particularly on our visit to the observatory.

The influence of my family has been crucial in allowing me to get to this point. The support provided by my family, particularly my parents, Paul and Tiz, have allowed me to pursue my passion for science from a very young age. I would also like to extend my gratitude to my sister Stephanie and brother-in-law Matthew, as well as my extended family, some of whom are no longer with us to see this. My family's constant belief in me, through both good and bad times, has given me the confidence and determination needed to overcome the hardships I have faced, that may have otherwise prevented me from achieving my goals. I will never be able to repay them for the opportunities they provided to me.

Lastly, I would like to thank my girlfriend, Emily. The love she has provided me over the last two years has given me the motivation required to complete my PhD. Our time together has given me a new outlook on life, and made me a better person. I would say that she helped keep me sane as I was writing my thesis, but I never was to start with!

Table of contents

Chapter 1

Introduction

1.1 Cosmic Radiation

1.1.1 Discovery of cosmic radiation

Prior to the discovery of cosmic radiation, it was thought that the only source of background radiation was from the decay of radioisotopes present in the environment. It was noticed that background radiation levels were higher at higher altitudes above sea level, but it was unclear whether or not this was due to higher concentrations of radioisotopes at locations with a higher altitude. In 1912, Victor Hess [55] carried out measurements of ionising radiation levels on a series of balloon flights to observe how radiation levels varied with increasing altitude (while also increasing distance from the ground) (see figure 1.1). It was expected that radiation levels would drop with increasing distance from the ground as the atmosphere would block radiation from radioisotopes in the ground. This drop was observed with a small increase in altitude up to about 1000 m, but at even higher altitudes, radiation levels increased. At 5000 m, radiation levels were approximately twice as high as at ground level. From this, it was concluded that there was a source of ionising radiation coming from space. Several ascents were made, at great risk to himself, during both day and night, as well as during a solar eclipse, finding no significant difference in the radiation increase at high altitude. This excluded the sun as the likely source of this radiation. The only suitable explanation was a cosmic origin.

1.1.2 Detection of extensive air showers

In 1939 Pierre Auger was experimenting with coincident detections in particle counters [12]. He was able to detect when two or three particle counters were triggered within less than 10^{-6}

Fig. 1.1. Victor Hess undertaking a balloon flight.

s of each other, for detector spacings up to 300 m. With this set-up, it is very unlikely that two unrelated particles would simultaneously trigger two detectors. Given the background rate of single detections, approximately 1 accidental trigger per hour was expected for two detectors. Three detectors being triggered simultaneously would be exceptionally rare so when this occurred, the only possible explanation for this is a particle shower originating from a single high energy particle. Experiments shielding one of the detectors with an increasing thickness of lead led to the conclusion that most of the ionising particles in these showers were electrons. Simultaneous triggers were detected at distances of up to 300 m. Longer distances were not tested as 300 m is the approximate distance light travels in 1 microsecond, so the geometry of the shower may not cause simultaneous triggers with a 1 microsecond resolution. It was concluded from this that showers of particles were being initiated by a primary particle with an energy of at least 10^{15} eV.

Over the decades following this discovery, a series of air shower detection experiments have led to the discovery and study of cosmic ray particles, primarily protons and atomic nuclei, with an energy range that extends past 10^{20} eV. This means that cosmic rays have now been studied over an energy range spanning an enormous 11 orders of magnitude.

1.1.3 Sources of cosmic rays

The high energy of cosmic ray particles is not attainable by any known mechanism other than acceleration in electro-magnetic fields. Particles cannot gain energy in a static magnetic field, but in the interstellar medium, magnetised plasma is constantly in motion. When charged particles move between regions of magnetised plasma with differing velocities, energy can be exchanged between the magnetic field region and cosmic rays. This process is stochastic, with it being possible for a particle to either gain or lose energy in an interaction, but the

overall effect over many interactions is an increase in energy. This is especially prevalent where there are strong shocks, such as supernova blast waves. This mode of acceleration is known as Fermi acceleration.

Consider a region of space with a strong shock. It is assumed that each interaction with an accelerating region leads to an increase in particle energy of $\Delta E = \xi E$. After n interactions, the energy will be:

$$E_n = E_0(1+\xi)^n \tag{1.1}$$

With each interaction, there is also a possibility that a given particle will leave the acceleration region, P_{esc}. This means that the probability of a particle remaining in the accelerating region after n interactions is $(1-P_{\text{esc}})^n$. From this, with N_0 particles injected with energy E_0, we get the number of particles with energy above E:

$$N(>E) = N_0\left(\frac{E}{E_0}\right)^{\gamma} \tag{1.2}$$

where

$$\gamma = \frac{\ln(1-P_{\text{esc}})}{\ln(1+\xi)} \approx \frac{P_{\text{esc}}}{\xi} \tag{1.3}$$

In Fermi's original theory, the source of acceleration is from gas clouds in the interstellar medium. These gas clouds have velocities of $\sim$15 kms^{-1} relative to the average motion orbiting the galaxy. Cosmic ray particles approaching the cloud are assumed to have an isotropic distribution in the galaxy frame. Upon entering the cloud, the particles are scattered and exit the cloud with an isotropic distribution in the cloud frame (see figure 1.2). In the cloud frame, a particle does not gain or lose energy, but in the galaxy frame, a particle can lose or gain energy depending on the angle that the particle has with respect to the cloud motion upon entering and exiting. A head on collision will result in an energy gain, whereas an overtaking collision will result in an energy loss. Due to relativistic transformations, head on collisions are more likely. The average energy gain in an interaction with the cloud is:

$$\frac{\langle \Delta E \rangle}{E} \simeq \frac{4}{3}\beta^2 \tag{1.4}$$

where $\beta = \frac{v_{cl}}{c}$, for a cloud velocity v_{cl}. This is known as second order Fermi acceleration, since the energy gained is second order with respect to cloud velocity. With typical cloud velocities of 15 kms^{-1}, $\beta \ll 1$, so the average energy gain in each interaction is negligible. The spectral index obtained with reasonable estimates of the escape time from the galaxy and the rate of interactions is far steeper than the observed index. Thus second order acceleration

from clouds in the interstellar medium is unlikely to be source that accelerates cosmic rays to ultra-high energies.

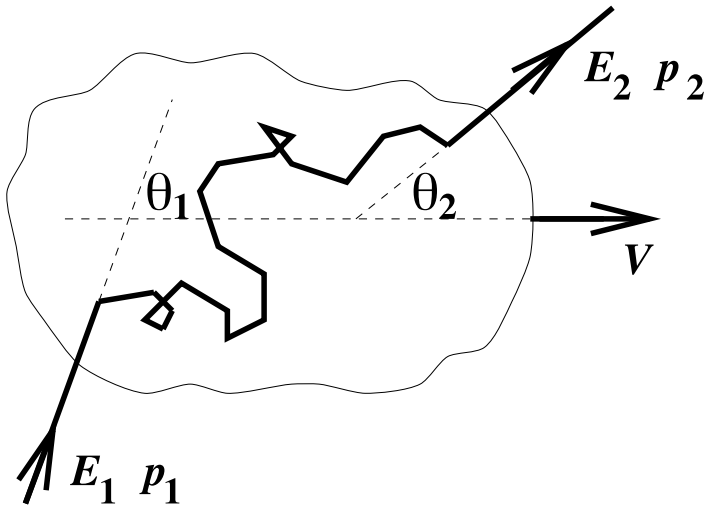

Fig. 1.2. Cosmic ray interaction with a moving cloud, showing the mechanism behind second order Fermi acceleration. From [84].

Another mechanism where cosmic rays can experience acceleration is at a strong shock, such as those produced by supernovae. In this case, the shock is approximated as a plane front, with fast moving supernova ejecta causing the interstellar medium to pile up at the shock front. Supernova ejecta have velocities in the order of 10^4 kms^{-1}. Calculation of the energy gain of the cosmic ray is similar to Fermi's original theory of magnetised clouds, by considering the supernova ejecta as one of the magnetised clouds. The difference is that to a particle on either side of the shock front, the plasma on the other side of the shock front appears to be approaching the shock front, so every crossing acts as a head on collision. This can be seen in figure 1.3. Because of this, the energy gain averaged over all possible interaction angles is:

$$\frac{\langle \Delta E \rangle}{E} \simeq \frac{4}{3}\beta \tag{1.5}$$

where $\beta = \frac{v_p}{c}$, for an ejecta velocity v_p. Cosmic rays may undergo repeated interactions, or escape into the interstellar medium by diffusion. Calculations of the rate of crossing and escape of particles, and the energy gain of a shock crossing, give an energy spectrum with a spectral index $\gamma = -2$. This spectral index is flatter than the index observed at Earth, though this can be explained. As Earth is (fortunately) not in the immediate vicinity of a supernova shock, cosmic rays produced by a supernova need to diffuse through the interstellar medium for a long time before arrival at Earth. Higher energy cosmic rays are more likely to escape the magnetic field of the galaxy before then, resulting in a steeper spectral index at Earth.

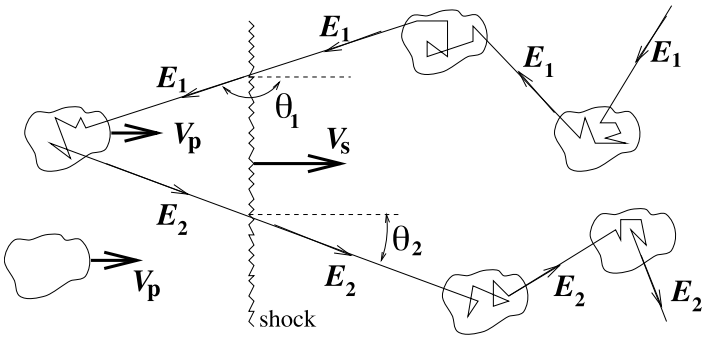

Fig. 1.3. Cosmic ray interaction with a strong shock, showing the mechanism behind first order Fermi acceleration. From [84].

Sources of cosmic ray acceleration have limits on the energy of particles they can produce. Though there are a number of factors that may limit the energy of a cosmic ray, the most relevant are the strength and extent of the magnetic fields. A requirement for cosmic ray acceleration is that, to an approximation, the accelerator must be larger than the magnetic gyroradius of the cosmic ray. The gyroradius of a particle of charge Z is $r_L = E/ZeB$, giving a maximum energy $E < ZeBL$ for an accelerator of size L. As a result of this, supernova remnants are not capable of accelerating cosmic rays to the highest energies. The velocity of shocks within the accelerating region also plays a significant role, with an energy limit $E < ZeBL\beta$, for scattering centres with velocity βc [57]. A plot of the strength and extent of magnetic fields for a number of possible accelerators is given in figure 1.4.

1.1.4 Propagation

Cosmic rays are subject to a number of effects when propagating from a source to Earth. Magnetic fields have an effect on charged cosmic rays of all energies, though the extent does vary. In a given magnetic field, the gyro-radius of a particle of charge Z is proportional to rigidity $R = pc/Ze$. For an ultra-relativistic particle of energy E, rigidity is proportional to E/Z, so for a given energy, heavier nuclei experience a greater deflection when compared to protons. At low energies, cosmic rays have a gyro-radius much shorter than their propagation distance to Earth, and as a result propagate diffusively through galactic magnetic fields. As rigidity increases, particles diffuse more rapidly and escape galactic magnetic fields in a shorter time. It is only at the very highest energies that magnetic deflections are expected to be small enough for cosmic ray arrival directions at Earth to be traceable to a source. For a rigidity of 10^{20} V, deflections of a few degrees are expected for cosmic rays propagating across intergalactic distances.

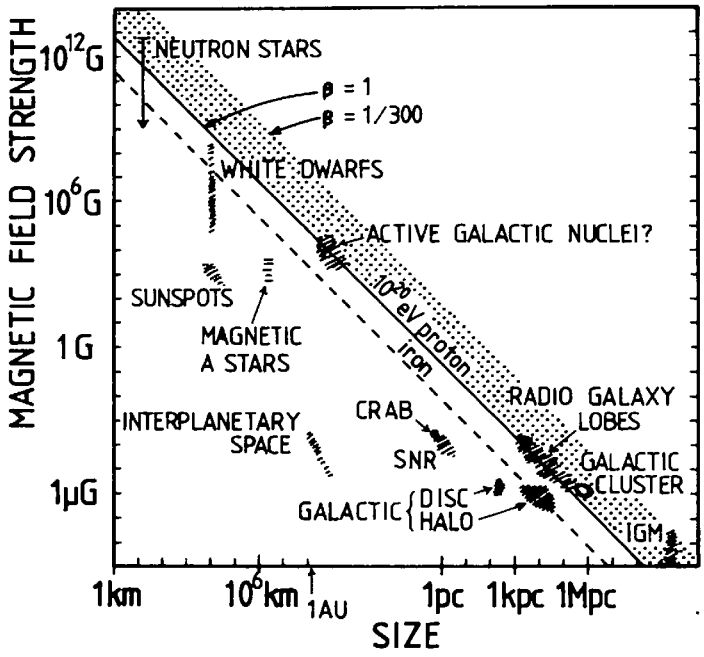

Fig. 1.4. The Hillas plot, showing the strength vs extent of magnetic fields for astrophysical objects. The lines show the requirements to accelerate cosmic rays to 10^{20} eV, with limits for protons at $\beta = 300$, and protons and iron at $\beta = 1$. Plausible regions need to be above the lines. From [57].

At the highest energies, cosmic rays propagating across intergalactic distances suffer from energy losses. Soon after the discovery of the cosmic microwave background (CMB), Greisen [47], and Zatsepin and Kuzmin [118] predicted that there would be a cutoff in the observed cosmic ray spectrum due to interactions with CMB photons. At the highest energies, the low energy CMB photons are blue-shifted to sufficient energy for particle production. Cosmic ray protons can undergo photo-pion production by the following interactions:

$$p + \gamma_{CMB} \rightarrow n + \pi^{+} \tag{1.6}$$

$$p + \gamma_{CMB} \rightarrow p + \pi^{0} \tag{1.7}$$

The threshold energy for this interaction is $\sim 5 \times 10^{19}$ eV [47, 118]. Protons above this energy have an interaction length of around 6 Mpc [14]. Protons will also undergo pair production at lower energies:

$$p + \gamma_{CMB} \rightarrow p + e^{+} + e^{-} \tag{1.8}$$

The proton threshold energy for pair production is $\sim 10^{18}$ eV [72]. Though both interactions will cause an energy loss, there is a crucial difference between the two. The energy loss

for a pair production interaction is $\sim 0.1\%$ of the proton energy, so pair production can be seen as a continuous, but slow energy loss, still allowing propagation over great distances. On average, photo-pion production interactions will cause a proton to lose $\sim 20\%$ of its energy. As a result of this, a proton with an initial energy above the photo-pion production threshold will rapidly lose energy to photo-pion production, until the energy is below the photo-pion production threshold. This occurs within a distance of ~ 100 Mpc, regardless of initial energy (see figure 1.5).

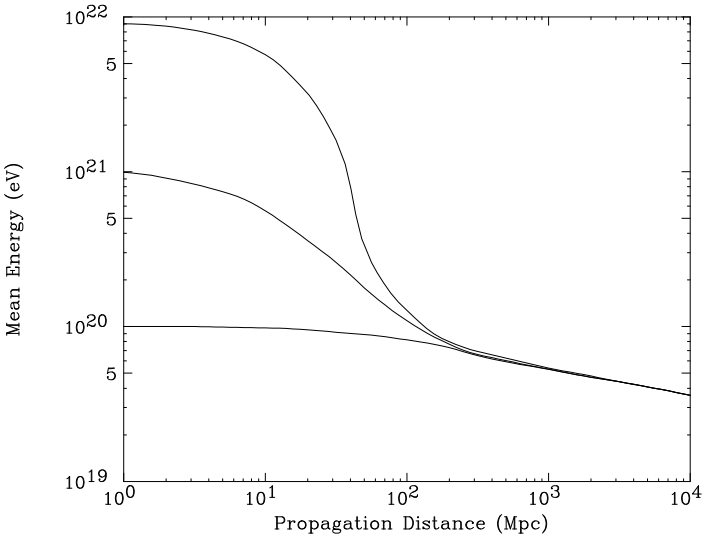

Fig. 1.5. The mean energy of protons propagating through the CMB, with starting energies of 10^{20} eV, 10^{21} eV, and 10^{22} eV. From [32].

Heavier nuclei will also interact with the CMB, with the dominant process being pair production and photo-disintegration. The energy threshold for pair production increases in proportion to the mass, A. The photo-disintegration energy threshold also increases with increasing A, with energies being similar to the proton photo-pion threshold. The energy loss length due to CMB interactions for protons and heavier nuclei are shown in figure 1.6.

The energy loss of cosmic ray particles at energies above $\sim 10^{20}$ eV, regardless of composition, means that any cosmic rays observed above this energy must have been produced within ~ 100 Mpc. Since particles above this energy have been observed, this implies that an accelerator is nearby.

1.1.5 Spectrum

The range of energy of cosmic rays observed is very broad, from the very numerous particles with $\sim$GeV energy up to exceptionally rare particles with an energy above 10^{20} eV. The

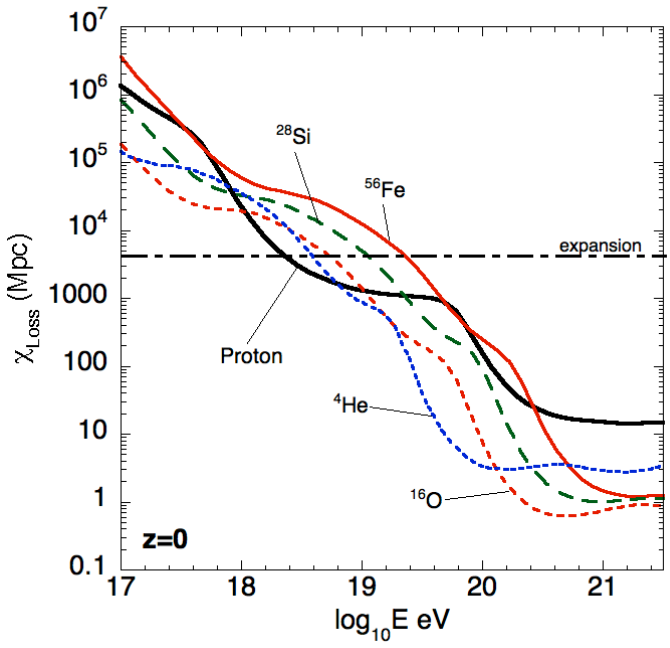

Fig. 1.6. Energy loss length χ of nuclei vs energy. Also shown is the effective energy loss length from the expansion of the universe. From [4].

energy spectrum of cosmic rays approximately follows a power law:

$$\frac{dN}{dE} \propto E^{-\gamma} \tag{1.9}$$

where N is the number flux of particles arriving at the top of the Earth's atmosphere. At the lowest energies, the flux is suppressed, due to the outward moving solar winds. The flux at the lowest energies also varies depending on solar activity, with high solar activity corresponding to lower cosmic ray flux, as stronger solar winds reduce the inward diffusion of low energy cosmic rays. The value of γ is approximately 2.7, but varies with energy, with notable changes in the hardness of the spectrum. This can be seen in Figure 1.7, and a closer view of the highest energy part of the spectrum in figure 1.8. Notable features in the energy spectrum include a steepening of the energy spectrum at $\sim 10^{15.5}$ eV, known as the knee, a further steepening at $\sim 10^{17}$ eV, known as the second knee, a flattening of the spectrum at $\sim 10^{18.5}$ eV, known as the ankle, and a cutoff in the spectrum beyond $\sim 10^{19.5}$ eV. There is also a recently discovered steepening of the energy spectrum between the ankle and the cutoff [110].

At the energy where the knees in the spectrum are observed, cosmic rays are likely due to galactic sources, such as supernova remnants. The first knee has been found to be a steepening of the spectrum for light nuclei [6], while the second knee is due to a steepening

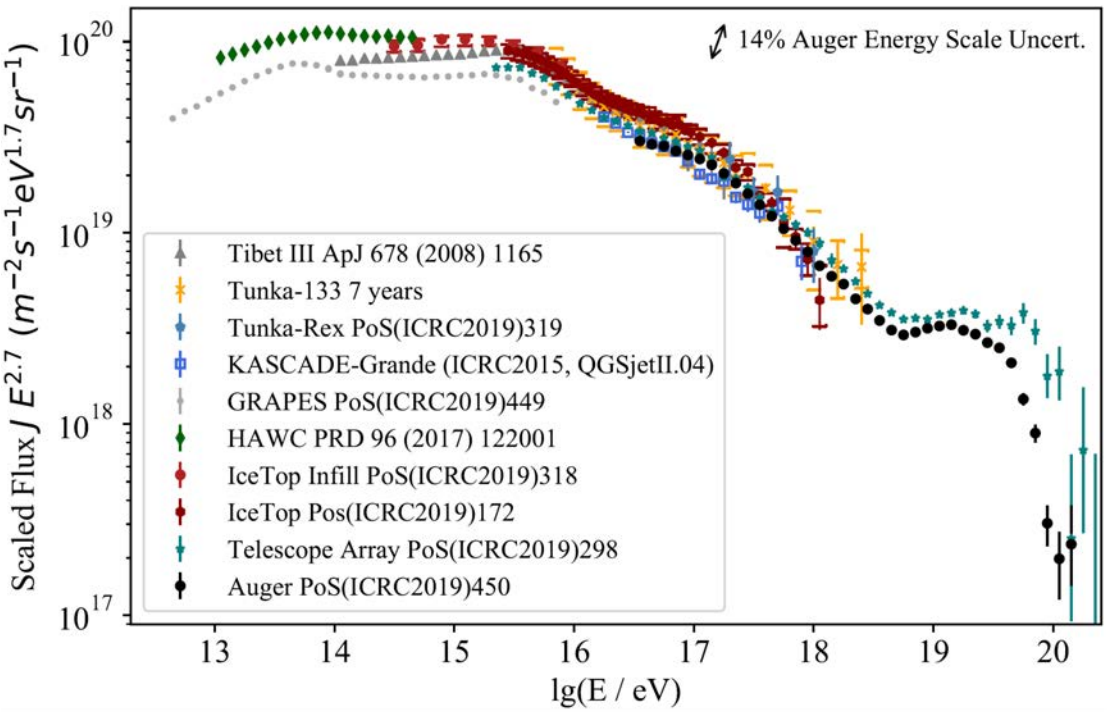

Fig. 1.7. The cosmic ray energy spectrum, with measurements from a number of observatories combined. From [88].

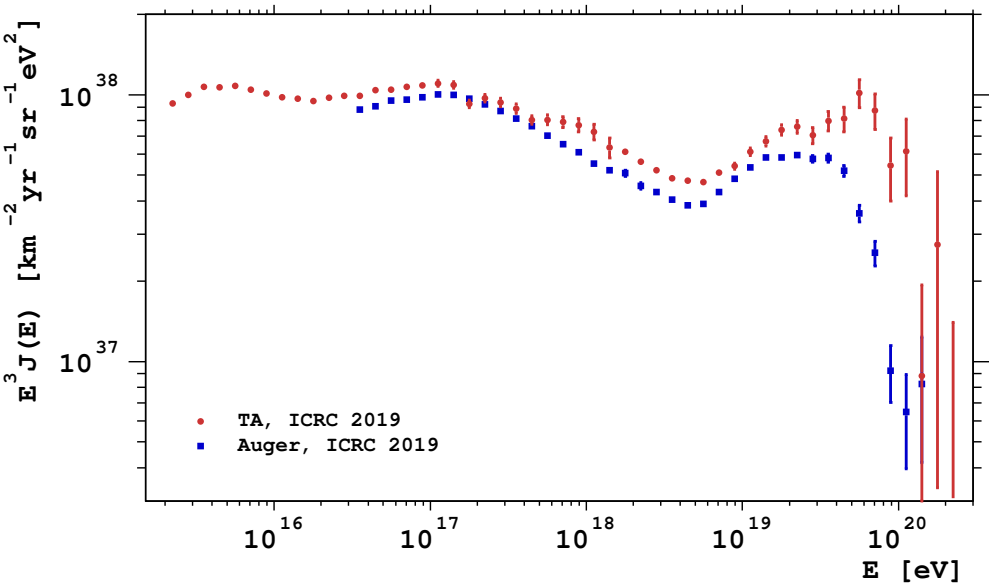

Fig. 1.8. The cosmic ray energy spectrum at the highest energies, measured with the two largest experiments, the Pierre Auger Observatory, and the Telescope Array. From [35].

in the spectrum of heavier nuclei [7]. The reason for the knees is not entirely clear. The prominent theory is that the knees represent an upper limit to the energy of the sources of

cosmic rays within the galaxy. For ultra relativistic particles, the deflection due to magnetic fields is proportional to the charge. As a result of this, for acceleration due to magnetic fields, the maximum energy attainable will be proportional to Z. The first knee would therefore be an acceleration limit of the light nuclei, H and He. As H and He are the most abundant cosmic ray nuclei below the knee, this is seen in the overall spectrum. As iron nuclei are the heaviest with a significant contribution to the cosmic ray flux, a second knee is expected at a higher energy. The energy ratio of the two knees is consistent with an acceleration limit for H and He for the first, and iron for the second. The steepening of the energy spectrum between the knees may be expected due to elements of intermediate mass, but nuclei of intermediate mass are likely to be less abundant than iron. Another theory is that the knees are due to cosmic rays escaping the galaxy. Cosmic rays of lower energy are likely to remain trapped within galactic magnetic fields. At higher energies, cosmic rays have a larger gyro-radius and thus diffuse out of the galaxy more rapidly. This would similarly occur at higher energies for heavier compositions, explaining the knee and second knee.

The next prominent feature in the energy spectrum is the ankle, occurring at an energy around $10^{18.6}$ eV, where the spectrum flattens out to a spectral index of $\sim$2.2. There are a number of theories explaining the ankle in the spectrum. Anisotropy studies suggest that around this energy, cosmic rays are transitioning from galactic to extra-galactic in origin. Composition studies suggest a light composition near the energy of the ankle, with composition becoming heavier with increasing energy above the ankle energy. There are a numerous theories to explain the ankle. These include:

- The ankle represents a transition from galactic to extra-galactic cosmic rays. In this case, the galactic spectrum is steeper than the extra-galactic spectrum, and dominates at low energies, with the extra-galactic component dominant above the ankle [5]. If this were true, a strong anisotropy would be expected at ankle energies in the direction of the galactic centre due to galactic cosmic rays. Only a very small anisotropy is observed near the ankle energy. A transition from galactic to extra-galactic cosmic rays at the ankle also has difficulties explaining the light composition observed around the ankle, as galactic cosmic rays at this energy are expected to be heavy due to accelerator limits. Additional galactic sources with higher rigidity limits would be required to explain the light composition at the ankle energy.

- Since the composition is light near the ankle, it has been suggested that the flux at ankle energies is suppressed by pair production interactions with the cosmic microwave background. In this model [5], the extragalactic component is mostly protons, becoming the dominant component of cosmic rays above the second knee. This explains the light

composition around the ankle, as well as the lack of a strong anisotropy towards the galactic centre below the ankle energy.

- A recent model has shown that the ankle can be explained by photo-disintegration near the accelerator [109]. In this model, the accelerators exist in a region of high photon density and strong magnetic fields. The accelerators have a rigidity limit, so heavier nuclei can accelerate to higher energy. Heavier nuclei are subject to photo-disintegration at both lower and higher energies. Cosmic rays are trapped in this region of strong magnetic fields, and escape this region by diffusion. Because the mean escape time is energy dependent, nuclei at lower energies are likely to suffer photo-disintegration, while higher energy nuclei are more likely to escape, creating an abundance of protons around the ankle energy, while also predicting a transition to a heavier composition at higher energy due to the rigidity limit of the accelerators and the escape of high energy nuclei.

The final feature in the energy spectrum is the cutoff, where the spectrum drops off with a very high spectral index (~ 5), above 5×10^{19} eV. This has previously been considered as a gradual steepening in the spectrum above the ankle energy, but recent results [110] suggest two steepenings in the spectrum: one from $\gamma = 2.2$ to $\gamma = 3.2$ at 1.2×10^{19} eV, and another to $\gamma = 5.4$ at 5×10^{19} eV. There are two possible explanations for the observed cutoff in the spectrum. One is that it is a suppression of higher energy cosmic rays due to GZK interactions. In this case, most of the cosmic rays at energies below the cutoff come from distant sources (> 100 Mpc), with cosmic rays of higher energy attenuated due to interactions with CMB photons. This could be photo-pion production for light nuclei, or photo-disintegration for heavier nuclei. The other possibility is that the sources of the highest energy cosmic rays have a rigidity limit, so the cutoff would represent the maximum rigidity of the accelerator. For a given rigidity, heavier nuclei have a higher energy, so composition would be expected to transition from light to heavy approaching the cutoff, consistent with the observed mass composition results.

1.1.6 Composition

The composition of cosmic rays is crucial to gain an understanding of possible sources of cosmic rays and of their propagation to Earth, as well as explaining features in the cosmic ray spectrum. Cosmic rays at low energies have a sufficiently high arrival rate that direct detection experiments are possible, allowing a determination of the composition of each individual cosmic ray particle. A plot of the relative abundance of cosmic ray nuclei is shown in figure 1.9, compared to the abundance of elements in the solar system. Overall

the relative abundance of cosmic ray nuclei are similar to those in the solar system, with the exception of elements with a very low solar system abundance, such as lithium, beryllium, and boron. The abundance of these nuclei can be attributed to spallation of heavier nuclei as they collide with matter in the interstellar medium. These observed abundances of these otherwise rare elements, and abundances of unstable radionuclides in cosmic rays, allow for the determination of the time taken to propagate to Earth, and the amount of matter traversed from the source. This has shown that cosmic rays diffuse not only through the galactic disk, but also in the less dense galactic halo [43].

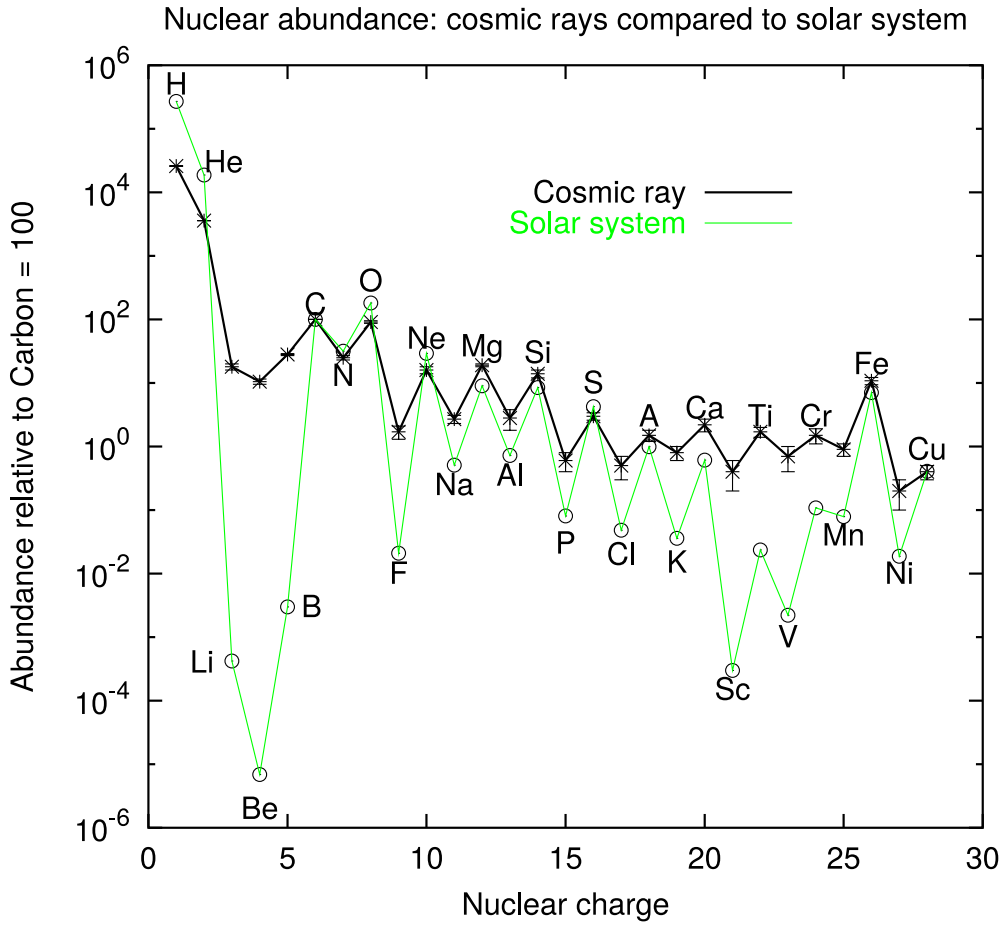

Fig. 1.9. Relative abundance of cosmic ray nuclei, compared to the abundance of elements in the solar system. From [43].

At higher energies, the low arrival rate makes direct detection unfeasible, so observations of extensive air showers must be used to deduce mass composition. Due to inherent fluctuations in shower properties, it is not possible to deduce the exact composition of each individual cosmic ray, though average composition can be deduced over a large number of events. At the highest energies, an additional complication arises due to uncertainties in the

physics of hadronic interactions at the highest energies. The most robust measure comes from the depth of shower maximum, $X_{\max}$, the details of which will be discussed later. $X_{\max}$ results from the Pierre Auger Observatory and Telescope Array are shown in figures 1.10 and 1.11.

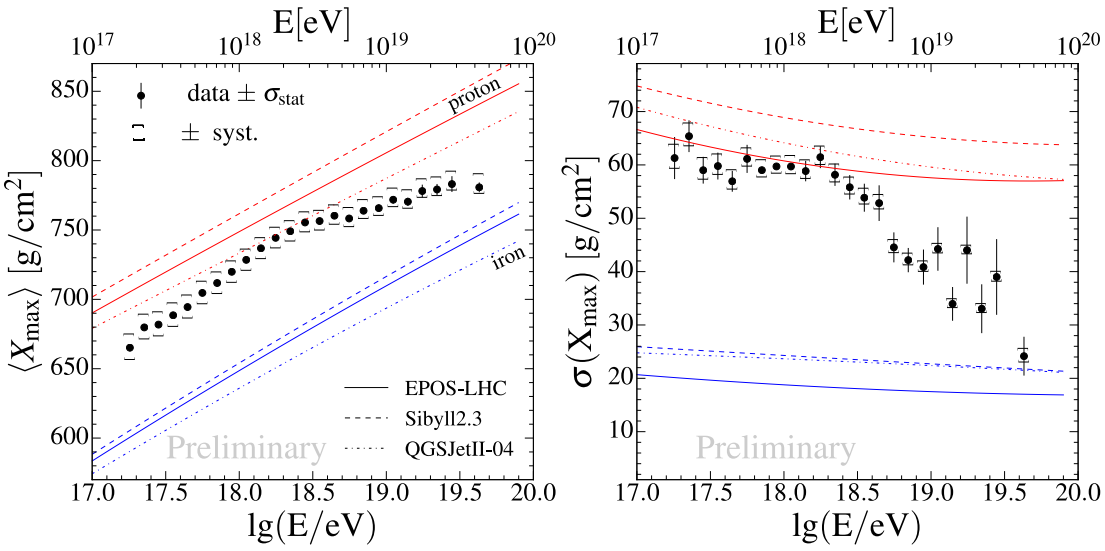

Fig. 1.10. (left) $\langle X_{\max} \rangle$ vs energy measured by the Auger FD. (right) $\sigma(X_{\max})$ vs energy measured by the Auger FD. The lines shown are the predictions for proton and iron primaries. From [117].

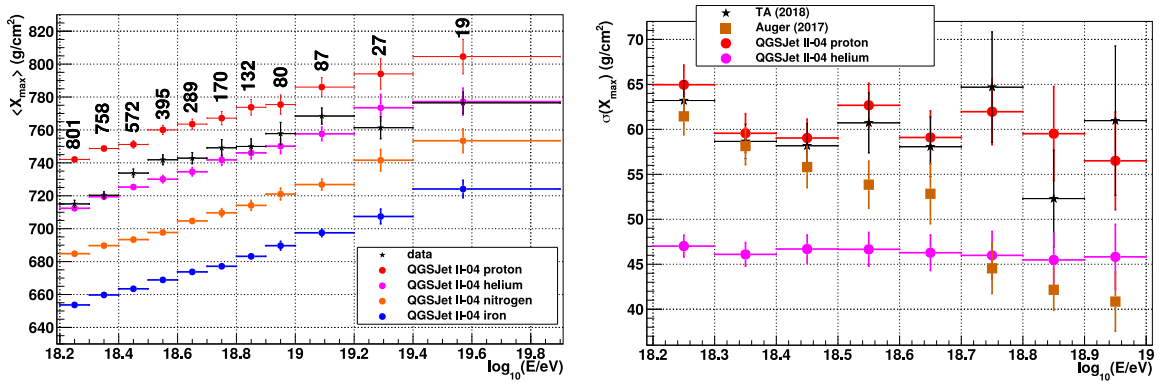

Fig. 1.11. (left) $\langle X_{\max} \rangle$ results from Telescope Array, with Monte Carlo predictions using QGSJetII-04. (right) $\sigma(X_{\max})$ vs energy measured with Telescope Array, with Pierre Auger measurements and Monte Carlo predictions using QGSJetII-04. From [48].

The Pierre Auger FD (fluorescence detector) results indicate a light composition at $10^{18.32}$ eV, with composition becoming heavier at both higher and lower energies. The results from Telescope Array seem to show a lighter composition at the highest energies, though it should

be noted that values of $\langle X_{\max} \rangle$ obtained by Telescope Array are not directly comparable to the Pierre Auger results due to the analysis methods used. In the Pierre Auger analysis, events with a limited field of view are removed from the analysis as they may cause a bias in the $X_{\max}$ distribution, so the values of $\langle X_{\max} \rangle$ and $\sigma(X_{\max})$ are estimates of the true $\langle X_{\max} \rangle$ and $\sigma(X_{\max})$. The Telescope Array analysis does not exclude these events, as the smaller exposure does not allow for data to be rejected. Instead, the data is compared to detector simulations of pure primary compositions, which are expected to include an identical bias. To obtain a comparison between the two datasets, the $X_{\max}$ distributions obtained by the Pierre Auger are injected into the detector simulations of Telescope Array [48]. A graph of this comparison is shown in figure 1.12, showing that the observed Telescope Array $\langle X_{\max} \rangle$ is reasonably consistent with the Pierre Auger $X_{\max}$ distribution when simulated through Telescope Array.

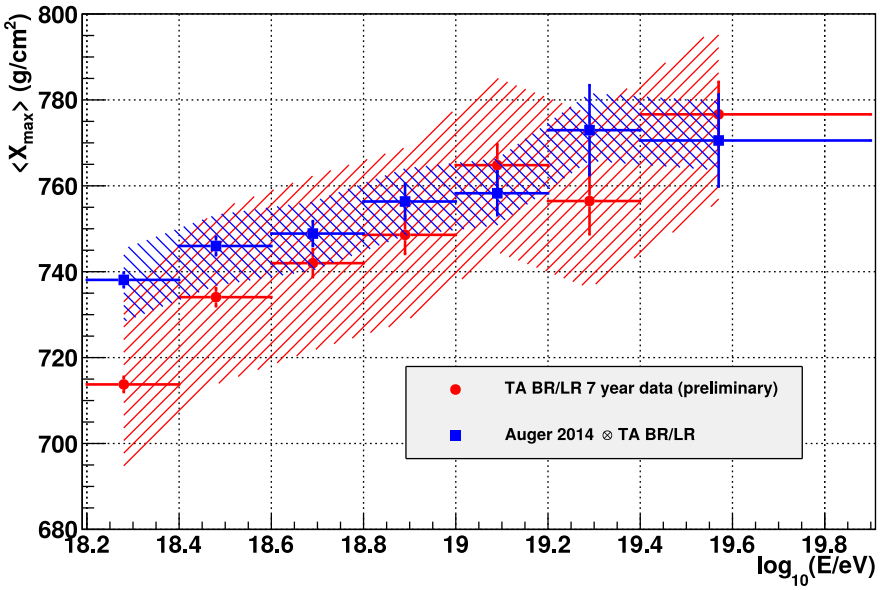

Fig. 1.12. Comparison of Pierre Auger and Telescope Array $\langle X_{\max} \rangle$ measurements. The red points are $\langle X_{\max} \rangle$ obtained from Telescope Array, while the blue points are the $\langle X_{\max} \rangle$ obtained from simulating the Pierre Auger $X_{\max}$ distributions in Telescope Array. From [48]

Composition and spectrum data from a number of cosmic ray observatories has been combined to give a spectrum separated into different mass components, covering a wide energy range [36]. This is shown in figure 1.13.

1.1.7 Anisotropy

Due to deflections by magnetic fields, anisotropies at small angular scales are only expected at the highest energies. The two largest observatories, the Pierre Auger Observatory and the

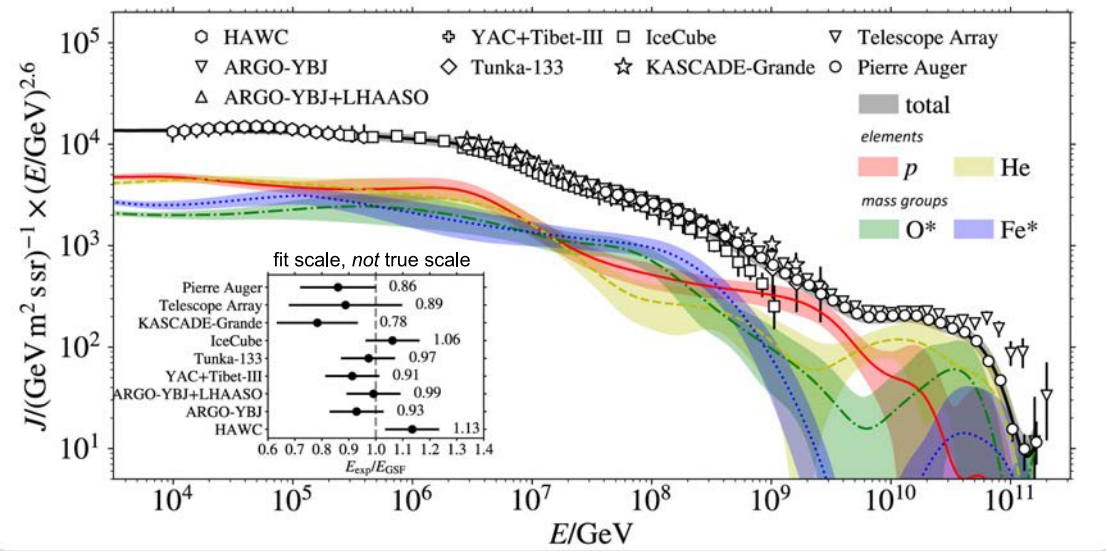

Fig. 1.13. Combined cosmic ray spectrum with spectra separated for different mass components. From [88], updated from [36].

Telescope Array have both detected significant anisotropies at high energies. The Telescope Array has detected a hotspot [60] with a local significance of 5.1σ, within a 25° circle for energies above 57 EeV, which equates to a 2.9σ significance when accounting for scans in position, angular scale, and energy. The TA hotspot does not coincide with any known candidates for production of ultra-high energy cosmic rays. The Pierre Auger Observatory has observed a hotspot [28] for energies above 38 EeV within a 27° radius, with a local significance of 5.6σ. This hotspot is very close to Centaurus A, the nearest AGN (active galactic nucleus) to Earth. The significance for an excess at Centaurus A, accounting for scans in energy and angular scale, is 3.9σ. A combined anisotropy map, using data from both observatories, is shown in figure 1.14. Anisotropy results will be discussed further in section 2.7.2.

1.2 Extensive air showers

For energies up to about 10^{14} eV, the cosmic ray flux is high enough that a detector with a collecting area in the order of $\sim$1 m^2 will detect a sufficient number of particles to be studied. This allows for direct detection experiments which are done at high altitude, in balloon or satellite based detectors. Direct detection experiments are capable of accurately determining particle energy and composition and so are preferred when possible. Above this energy, a much larger collecting area is required. The only feasible way this has been done is to utilise the atmosphere as a detector by observing the cascade of particles produced in an extensive

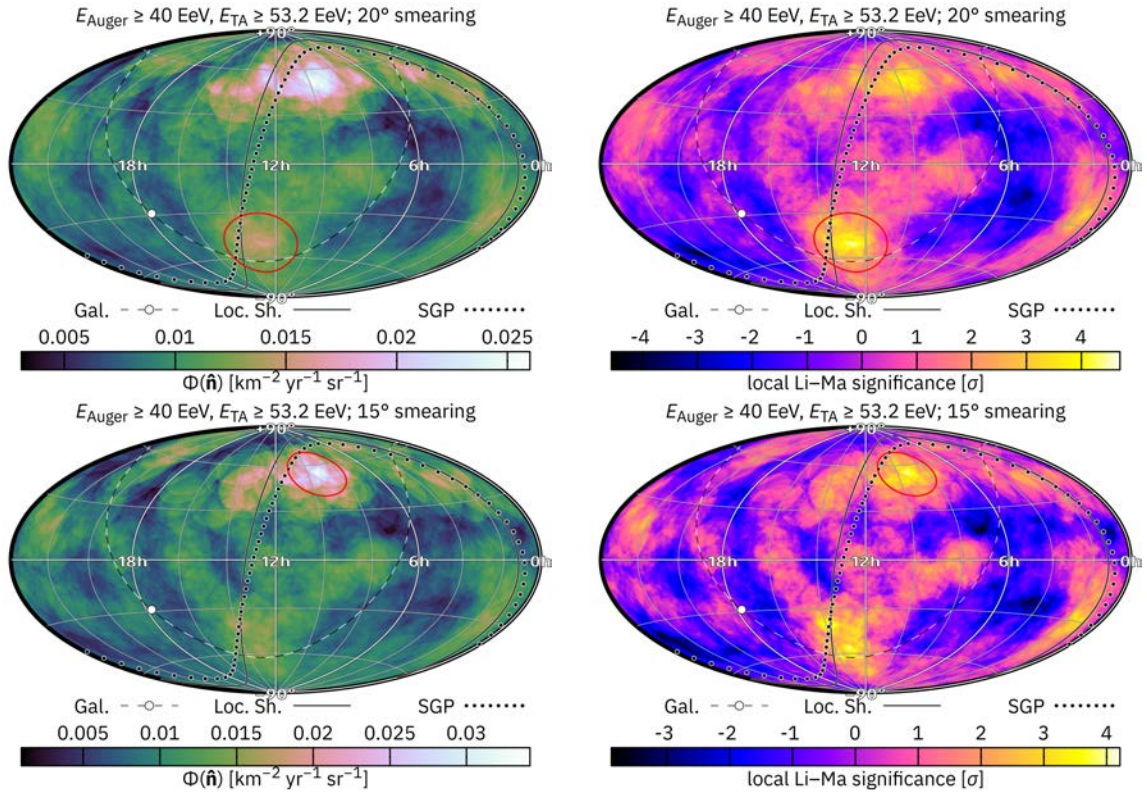

Fig. 1.14. Map of the local flux of cosmic rays within a 20° radius (top), and 15° radius (bottom), measured by the Pierre Auger Observatory and the Telescope Array. The energy cutoff for these events is 40 EeV for the Pierre Auger events, and 53.2 EeV for telescope Array, to account for different energy scales between the two observatories. Flux is shown on the left, with the local significance shown on the right. From [37].

air shower. With a huge number of shower particles spread over a large area, detectors need only cover a small fraction of the total collecting area, with the fraction required getting smaller with increasing cosmic ray particle energy. Detection of cosmic rays via extensive air showers does come at a cost. Indirect detection does not allow for cosmic ray energy and composition to be determined simply. Cosmic ray particle properties must be deduced from the properties of the extensive air shower.

1.2.1 Terminology

In this section, some terminology will be introduced that is commonly used when discussing cosmic ray shower physics.

Particles in a cosmic ray shower typically travel in approximately the same direction as the primary particle. This is especially true at higher energies. This means that the majority of particles are concentrated near a line that the primary particle would have taken had it not

interacted. This line is referred to as the shower axis. Shower development along this axis is referred to as longitudinal development. Since the development of a cosmic ray shower is predominantly caused by interactions with air nuclei, the level of development of a shower is primarily dependent on the depth of matter traversed. The total column density (or "depth") of matter encountered along a path is:

$$X = \int \rho dl \tag{1.10}$$

for a matter density ρ Considering that particles in a cosmic ray shower travel in nearly straight lines, and are generally close to the shower axis, we can define a depth at a given height for an atmospheric shower of zenith angle θ at height h:

$$X(h) = \frac{1}{cos\theta} \int_h^{\text{inf}} \rho(z) dz \tag{1.11}$$

The unit for X typically used in cosmic ray physics is $\mathrm{g\,cm^{-2}}$.

Particles within a shower do not necessarily lie exactly on the shower axis. This is mostly relevant for surface detectors, as it allows showers to be detected without having a detector exactly at the shower core (the location where the shower axis intersects with the ground). The density of particles arriving at the ground is primarily dependent on distance from the shower axis. Since showers are unlikely to be exactly vertical, the distance from the axis is not the same as the distance to the core. Because of this, it is useful to introduce a shower plane coordinate system, where a position on the ground is projected onto a plane perpendicular to the shower axis. Shower plane coordinates are typically expressed as a polar coordinate system, with a distance from the core in the shower plane, r, and an azimuth, ζ, where $\zeta = 0$ is usually chosen to be in the upstream direction (underneath the shower axis). The distribution of particles in the shower plane is often referred to as the lateral distribution.

1.2.2 Electromagnetic component

Electromagnetic showers are cascades initiated by either electrons, positrons, or photons. Such cascades almost exclusively consist of electrons, positrons, and photons. With the composition of cosmic rays at the highest energy being hadronic with only very rare or no exceptions, pure electromagnetic showers are not applicable in most studies of ultra-high energy cosmic rays. However, photons, electrons, and positrons are produced in hadron initiated cascades and so electromagnetic cascades are an important component of hadronic showers. The electromagnetic component of an ultra-high energy cosmic ray shower will typically contain the majority of particles and is responsible for the majority of fluorescence

and Čerenkov light. Electromagnetic cascades can be understood with the Heitler model [53]. In the Heitler model of an electromagnetic cascade, the two dominant particle interactions are considered, pair production and bremsstrahlung radiation. A high-energy photon in the vicinity of a massive charged particle (in this case predominantly air nuclei) can undergo pair production to produce an electron-positron pair:

$$N + \gamma \rightarrow N + e^- + e^+ \tag{1.12}$$

Electrons and positrons at high energy predominantly interact in the vicinity of air nuclei to produce photons by bremsstrahlung radiation:

$$N + e \rightarrow N + e + \gamma \tag{1.13}$$

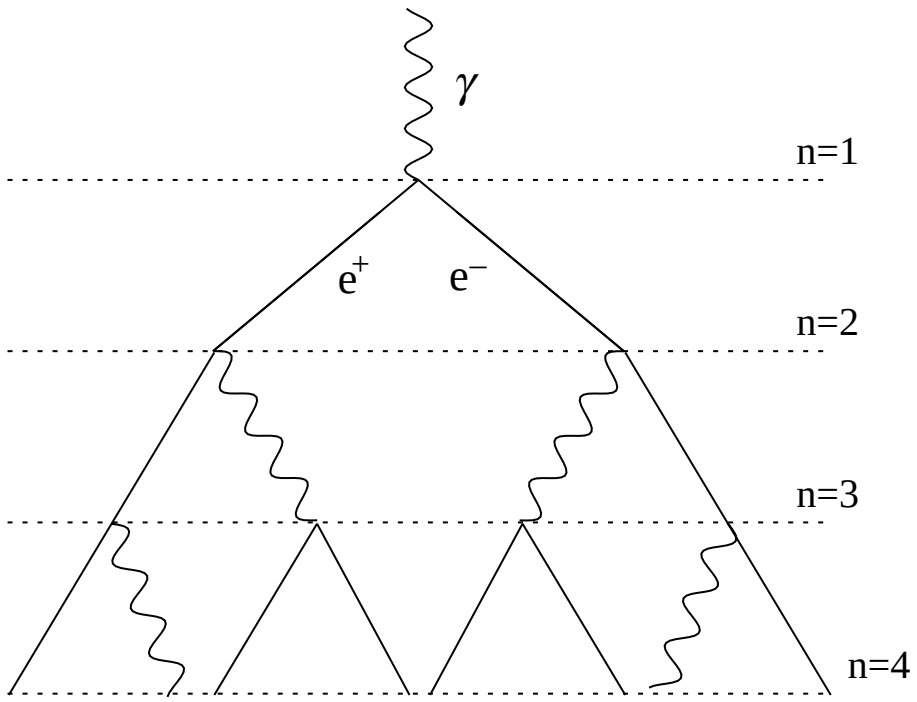

Fig. 1.15. The Heitler model for electromagnetic air showers. Scattering angles have been exaggerated.

At high energy, electrons will give on average about half of their energy to the photon produced by bremsstrahlung. The electron and positron produced by pair production will also each have, on average, half of the energy of the parent photon. Particles will interact with a mean interaction depth λ.

At high energies, the interaction length for pair production and bremsstrahlung are approximately equal. Additionally, the interaction length of these two interactions are roughly independent of energy for high energy particles.

Given these assumptions, an electromagnetic shower can be thought of as having a total number of particles doubling with each interaction length, starting from a single parent particle. With each generation of interactions, the energy per particle is halved. Thus, after n interaction lengths, the total number of particles is:

$$N = 2^n \tag{1.14}$$

and the average energy of each particle is:

$$E = \frac{E_0}{2^n} \tag{1.15}$$

where E_0 is the energy of the primary particle. Figure 1.15 shows an electromagnetic shower with a photon as the primary particle. This process cannot continue indefinitely though. Electrons will lose energy continuously through ionisation loss. This loss is very small over one interaction length for high energy particles but below 81 MeV electrons are more likely to lose their energy through ionisation loss before a bremsstrahlung interaction. This is known as the critical energy, ξ_c^e. An electromagnetic shower will have its maximum number of particles when the average energy is equal to the critical energy with the maximum number of particles being:

$$N_{max} = \frac{E_0}{\xi_c^e} \tag{1.16}$$

The maximum number of particles occurs at the following atmospheric depth:

$$X_{max} = \lambda_r \frac{\ln\left(\frac{E_0}{\xi_c^e}\right)}{\ln(2)} \tag{1.17}$$

With the value of λ_r of about 37 $\mathrm{g\,cm^{-2}}$ in air.

Due to bremsstrahlung interactions converting an electron into an electron and a photon, and pair production converting a photon into two electrons, we expect that the ratio of photons to electrons to be:

$$N_e = 2N_\gamma \tag{1.18}$$

More detailed simulations, as well as observations of electromagnetic showers, do show some discrepancies with this simplified model. During bremsstrahlung, multiple photons may

be produced. Additionally, it is only electrons and positrons that lose energy to ionisation loss, meaning that for particles with energy near or below the critical energy, a deficit of electrons and positrons occurs. At depths near the maximum in shower development, the majority of particles are of low energy, so the number of electrons present is greatly overestimated in the Heitler model. In reality, photons outnumber electrons by an approximate factor of 6 at the maximum [71]. This is quite relevant as many detectors, including scintillation detectors, are much more sensitive to electrons. Despite this inaccuracy of the Heitler model, it does still correctly predict that the maximum shower size is proportional to E_0, and that the depth of shower maximum increases logarithmically with energy.

Particles in an electromagnetic shower can be deflected away from the shower axis by collisions. The scattering angle is smaller for high energy particles so most of the deflection occurs with particles near the critical energy. The scale of the particle distribution is given by the Moliére radius. The Moliére radius is the product of one radiation length of an electromagnetic particle and the scattering angle of an electron at the critical energy. Near sea level, this is approximately 100 m. 90% of all electromagnetic particles are contained within one Moliére radius of the shower axis.

1.2.3 Hadronic component

Hadronic showers, typically initiated by a proton or heavier nucleus, will develop into a larger variety of particles, with the 3 most significant components being the hadronic, electromagnetic, and muonic component. The shower begins as purely hadrons, with decays feeding the electromagnetic and muonic components. When a high energy hadron interacts with an air nucleus, a number of pions are produced, with a smaller number of kaons and more rarely other exotic hadrons.

$$p + N \rightarrow p + \pi^0 + \pi^+ + \pi^- + ... \tag{1.19}$$

The number of pions produced is typically about 10-20 for protons but does show an energy dependence of approximately $E^{1/5}$ [71]. The interaction length for such a collision also depends on energy, and is approximately 40 $\mathrm{g\,cm^{-2}}$ at the highest energies. For heavier primary particles, the interaction length is much shorter. For iron nuclei, the interaction length is approximately 15 $\mathrm{g\,cm^{-2}}$. Additionally, the primary interaction from a heavier nucleus produces many more particles when compared to a proton primary. Of the pions produced, approximately 1/3 of the pions are neutral pions and the other 2/3 charged pions.

π^0 particles have an extremely short half-life, so decay will almost always occur before interaction. π^0 particles decay via the electromagnetic interaction into a pair of photons.

$$\pi^0 \rightarrow \gamma + \gamma \tag{1.20}$$

The photons produced by this decay will then go on to create electromagnetic sub-showers. With each successive generation of hadronic interactions, about 1/3 of the energy remaining in the hadronic component is transferred to the electromagnetic component. For ultra-high energy showers, there will be several generations of hadronic interactions. Because of this, the majority of the shower energy will be transferred to the electromagnetic component.

At high energy, charged pions will most likely interact with another air nucleus. The interaction length for pions in air is approximately 120 g cm^{-2}, though like protons, this also decreases with increasing energy. The number and type of particles produced in a pion-air nucleus interaction are very similar to that of a proton-air nucleus interaction:

$$\pi^{\pm} + N \rightarrow \pi^0 + \pi^+ + \pi^- + ... \tag{1.21}$$

The less commonly produced kaons can also decay into either muons or pions:

$$K^{\pm} \rightarrow \mu^{\pm} + \nu_{\mu}^{\mp} \tag{1.22}$$
$$K^{\pm} \rightarrow \pi^{\pm} + \pi^0 \tag{1.23}$$
$$K_S^0 \rightarrow 2\pi^0 \tag{1.24}$$
$$K_L^0 \rightarrow 3\pi^0 \tag{1.25}$$

Like with the electromagnetic shower, the hadron component also has a critical energy. In this case, the critical energy is the energy that decay is more likely than a nuclear interaction. Charged pions undergo the following decay:

$$\pi^{\pm} \rightarrow \mu^{\pm} + \nu_{\mu}^{\mp} \tag{1.26}$$

In the case of an electromagnetic shower, the interaction rate and the rate of ionisation loss are both proportional to air density, so the critical energy was not dependent on air density. With the hadronic shower, the interaction rate is proportional to density but the decay rate is not density dependent. As a result of this, the critical energy will be dependent on air density. Assuming an ultra-relativistic pion (a reasonable assumption for Earth's atmosphere), the critical energy is inversely proportional to air density. Critical energy will increase with

decreasing shower energy, and also increase with increasing zenith angle, due to the higher altitude of the shower maximum. For ultra-high energy cosmic ray showers the pion critical energy is typically close to 10 GeV.

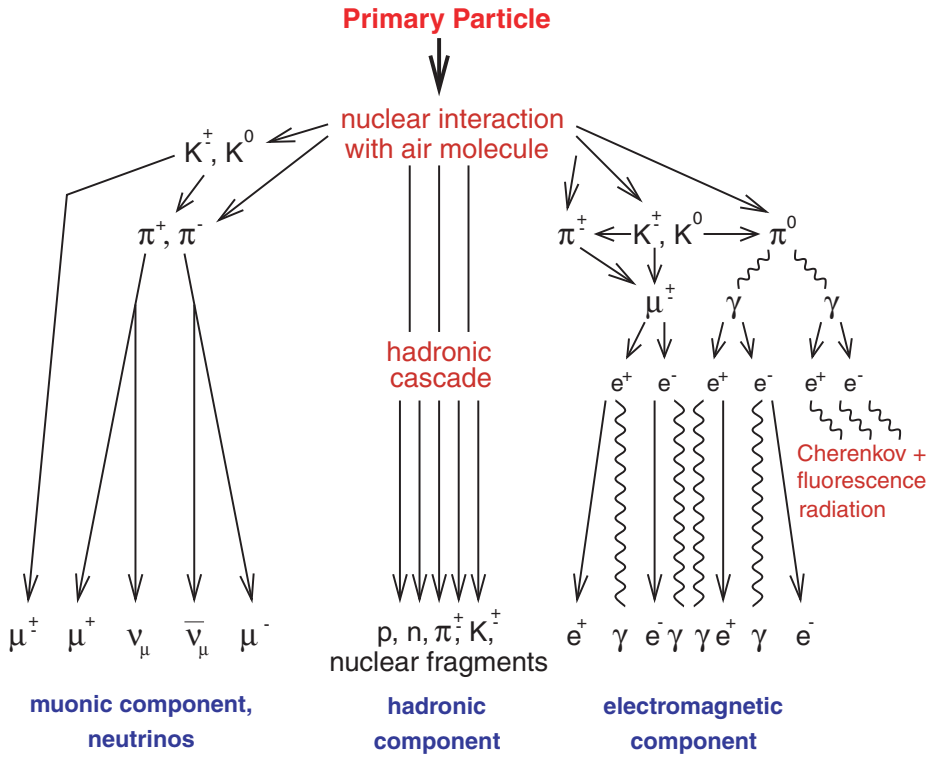

Fig. 1.16. Diagram of the processes involved in a hadron initiated air shower (not to scale). From [50].

The Heitler model can be applied to the hadronic particles in a shower [71]. It will be assumed that the number of charged pions produced in each interaction $N_{ch} = 10$. Thus, there will also be $N_{ch}/2$ neutral pions. After n interactions, we have a total number of charged pions:

$$N_\pi = {N_{ch}}^n \tag{1.27}$$

Since the neutral pions will take away 1/3 of the total energy in the hadronic component with each interaction, the average energy of each pion will be:

$$E_\pi = \frac{E_0}{\left(\frac{3}{2}N_{ch}\right)^n} \tag{1.28}$$

For a given critical energy, ξ_c^π, the number of interactions required for the average pion energy to reach the critical energy is:

$$n = \frac{\ln[E_0/\xi_c^\pi]}{\ln\left[\frac{3}{2}N_{ch}\right]} \tag{1.29}$$

$$= 0.85\log_{10}[E_0/\xi_c^\pi] \tag{1.30}$$

From this, we obtain the maximum number of charged pions $N_{\pi^\pm}$:

$$N_{\pi^\pm} = {N_{ch}}^n \tag{1.31}$$

$$= \left(\frac{E_0}{\xi_c^\pi}\right)^\beta \tag{1.32}$$

where

$$\beta = \frac{N_{ch}}{\ln\left[\frac{3}{2}N_{ch}\right]} \approx 0.85 \tag{1.33}$$

These charged pions decay into muons and thus the number of muons produced, $N_\mu = N_{\pi^\pm}$.

Next, the electromagnetic component can be considered. By conservation of energy, all of the shower energy that does not produce critical energy pions will be in the electromagnetic component. From this, we get the fraction of shower energy contributing to the electromagnetic component:

$$\frac{E_{EM}}{E_0} = \frac{E_0 - N_{\pi^\pm}\xi_c^\pi}{E_0} \tag{1.34}$$

$$= 1 - \left(\frac{E_0}{\xi_c^\pi}\right)^{\beta-1} \tag{1.35}$$

At ultra-high energy, this will be the vast majority of the shower energy. Because of this, and also the lower critical energy, electrons will make up the vast majority of charged particles. This means that fluorescence detection (see section 1.3.2) will predominantly measure electrons. It is therefore relevant to find the depth of maximum development, $X_{\max}$, of the electromagnetic shower. This can be approximated by considering the electromagnetic sub-showers initiated by the first interaction as these will have the largest share of the energy in the electromagnetic component. We assume $\frac{N_{ch}}{2}$ neutral pions are produced in the first interaction and will decay into N_{ch} photons each with energy $\frac{E_0}{3N_{ch}}$. Using the equation for the

depth of shower maximum for these electromagnetic sub-showers, we get:

$$X_{max}^{p} = X_0 + \lambda_r \ln\left[\frac{E_0}{3N_{ch}\xi_c^e}\right] \tag{1.36}$$

Where X_0 is the depth of the first interaction, for a primary proton p. This simple model does show a discrepancy with more detailed simulations. One reason is that only photons from the first generation of hadronic interactions is considered. Another important factor to consider is that energy is not uniformly distributed between the hadrons produced in a hadron-air collision. Though it is not well known at the highest energies, the highest energy particle produced in a collision may take half of the energy of the parent particle. This will cause showers to develop more slowly giving a larger value for $X_{\max}$

The Heitler model can also be extended to handle nuclear primary particles using the superposition model. In the superposition model, a nucleus of mass number A and energy E_0 can be treated as A individual nucleons, each with energy E_0/A. The resulting air shower is then treated as the sum of A separate proton showers. Applying this to the equations for $X_{\max}$ and the number of muons, and comparing to a proton shower of the same energy, we get:

$$N_{\mu}^{A} = N_{\mu}^{p} A^{0.15} \tag{1.37}$$

$$X_{max}^{A} = X_{max}^{p} - \lambda_r \ln A \tag{1.38}$$

In addition to the shallower value of $X_{\max}$, there is also a difference in the shape of the $X_{\max}$ distribution at a given energy. Due to the stochastic nature of nucleon-air collisions, two showers with identical primaries will not necessarily have the same value of $X_{\max}$. Most of this variation between showers is due to the depth of the first interaction, with the multiplicity of particles from the first interaction and secondary interaction lengths having smaller contributions to this variability. Since the interaction length for nuclear primaries is shorter than the proton interaction length, it is expected that the variance in $X_{\max}$ is also smaller. For a width of the proton $X_{\max}$ distribution $\sigma(X_{max})_P$, using the superposition model, we get:

$$\sigma(X_{max})_A = \frac{\sigma(X_{max})_P}{\sqrt{A}} \tag{1.39}$$

Though the width of the $X_{\max}$ distribution does reduce with increasing A, the superposition model overestimates this effect. More detailed simulations typically put $\sigma(X_{max})$ for iron at about 3 times smaller than for protons, whereas the superposition model predicts the width to be approximately 7.5 times smaller. This is due to the assumption in superposition model that

the individual nucleon showers occur independently to each other. In reality, the nucleons are bundled in a nucleus where a collision between a nuclear primary particle and an air nucleus will likely affect many of the nucleons. This results in the shower properties of each nucleon being correlated to each other. Due to this correlation, the variance in shower properties for a heavy nucleus shower will be higher than the superposition model prediction.

1.2.4 Muonic component

The muonic component of an extensive air shower is primarily produced by the decay of hadrons that have an energy near or below the critical energy. Most common are charged pion and kaon decays:

$$K^{\pm} \rightarrow \mu^{\pm} + \nu_{\mu}^{\mp} \tag{1.40}$$

$$\pi^{\pm} \rightarrow \mu^{\pm} + \nu_{\mu}^{\mp} \tag{1.41}$$

It is also possible for muons to be created via pair production when a photon interacts with an air nucleus:

$$N + \gamma \rightarrow N + \mu^{+} + \mu^{-} \tag{1.42}$$

The small cross-section for muon pair production means that this process is negligible in hadronic air showers but can be significant when considering the small number of muons produced in purely electromagnetic showers.

Muons are unstable with a mean lifetime of 2.2 μs at rest. Due to relativistic time dilation, muons produced in hadronic showers are likely to reach the ground. Though muons do lose energy through ionisation loss in air, muons produced by pion decay have an energy in the order of $\sim$10 GeV. A muon produced in a vertical shower near the maximum in muon production may lose $\sim$1 GeV through ionisation before reaching the ground, so ionisation loss will not prevent the majority of muons from reaching the ground. In inclined showers, there will be higher ionisation losses as muons pass through a greater depth before the ground, but the critical energy is higher owing to the lower air density around the maximum depth for muon production.

Since muons are unlikely to transfer a large fraction of their momentum in a collision in air, they generally travel in nearly straight lines. Additionally, the parent hadrons typically do not deviate from the shower axis. When the parent hadron decays into a muon, a neutrino is also produced. This allows muons to have a component of momentum perpendicular to the shower axis. So although muons travel in straight lines, they arrive at the ground spread over a much larger area than hadrons. Due to muons travelling in straight lines it is also possible to

observe a muon at the ground and deduce the production point of the muon, if the geometry of the shower is also known. This can make muons detected at ground level potentially very useful for probing the hadronic component of the shower. Due to their instability, not all muons will make it to the ground. Muons may decay into electrons in the following process:

$$\mu^{\pm} \rightarrow e^{\pm} + \nu_{\mu}^{\pm} + \nu_{e}^{\mp} \tag{1.43}$$

The electron produced in this decay can produce a small electromagnetic shower. This is sometimes referred to as the muon halo. Close to the shower core, the electromagnetic component caused by π^0 decay dominates, with the muon halo being negligible. Due to the narrower lateral distribution of the electromagnetic component caused by π^0 decay, at larger core distances the muon halo can make up a significant fraction of the electromagnetic component.

1.3 Detection of ultra-high energy cosmic ray showers

Considering the increasing rarity of cosmic rays with increasing energy, ultra-high energy cosmic rays require an exceptionally large collecting area, far larger than any apparatus that could be practically built. Cosmic ray showers produced by ultra-high energy cosmic rays can contain many particles at ground level, with the highest energy cosmic ray showers containing over 100 billion particles. This makes it possible do detect and determine properties of showers with detectors that are sparsely distributed over a vast area, with a total collecting area far larger than the detection equipment. For example, the Pierre Auger Observatory covers an area nearly 200,000 times larger than the sum of all of the detection equipment. There are a number of possible ways to detect cosmic ray showers. The two that will be detailed in this thesis are the surface detector array and fluorescence detection.

1.3.1 Surface detector arrays

Surface detector arrays have been around for longer than any other method for detecting cosmic ray showers, dating back to when Pierre Auger first discovered extensive air showers. In 1938, Pierre Auger found that two or three particle counters would on occasion be simultaneously triggered. This would occur at rates much higher than could be explained by random coincidences of unconnected sources triggering each detector. The rate of these simultaneous triggers was highest for separations less than 10 metres and reduced as separation distance increased, with simultaneous triggers still observed with detectors separated by hundreds of metres. This observation of extensive air showers is how the

existence of cosmic rays at ultra-high energy were discovered. Cosmic ray primary particles with energies above approximately 10^{14} eV will produce a sufficiently large number of particles at the ground to allow for a reconstruction of the original properties of the primary particle. At the ground level, muons, electrons, and photons are the 3 types of particle predominantly detected due to their broad lateral distribution. There may still be a significant number of hadrons at ground level, but hadrons usually land within 10 metres of the shower core, making their detection in a sparse detector array difficult. Figure 1.17 shows the lateral distribution of particles for a 10^{19} eV shower. If at least 3 detector stations are able to measure particle density, it is possible to reconstruct both the position of the shower core, and the number of particles in the shower, which can then be used to determine the energy of the shower.

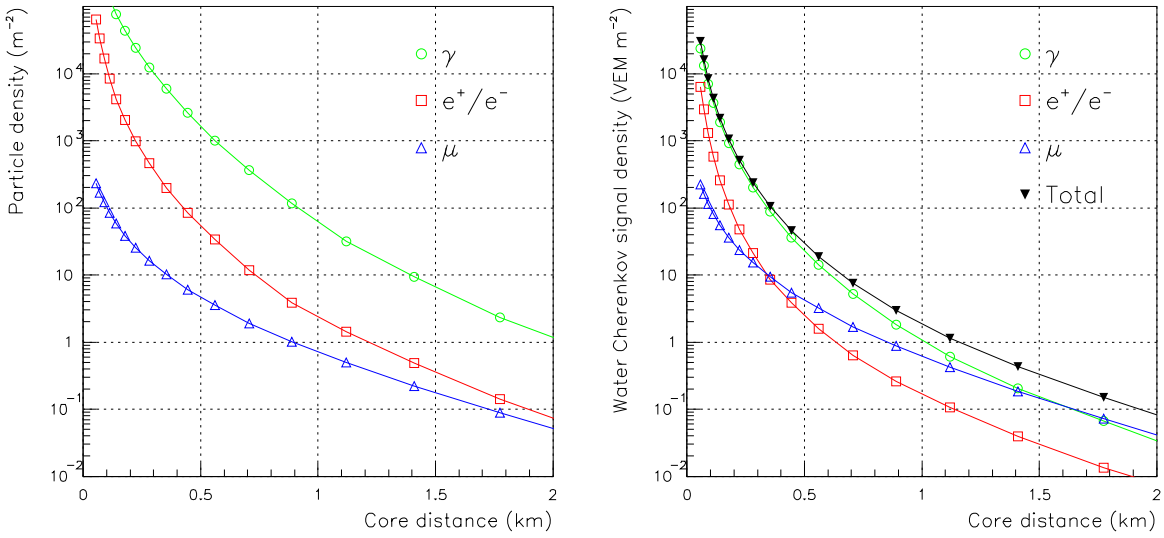

Fig. 1.17. The lateral distribution of particles at ground level due to a 10^{19} eV cosmic ray (left) and the signal in a 1.2 m deep water Čerenkov tank (right). Muons have the greatest water Čerenkov signal per particle because the average energy of a muon is higher than an electron or photon, and muons leave a track through the entire detector. Electrons have a short interaction length and only travel a short distance. Photons contribute by pair producing electrons in the water. From [95].

Since most particles in a shower travel at speeds close to the speed of light, with relatively small angular deflections from the shower core, the particles in a shower will form a front in the shape of a pancake centred about the shower axis. At small core distances, this can be approximated as being flat, but for larger core distances the shower front does have a curvature which must be taken into account. If the arrival time of particles in at least 3 detectors is known, it is possible to reconstruct the direction of propagation of the shower front and hence the direction of the primary particle.

The spacing of the detectors in a sparse array is predominantly based on the energy of showers being observed. The type and size of detectors, and the quality of the reconstruction required, also affects the required detector spacing but to a smaller degree. In order to reconstruct the energy and direction of a cosmic ray shower, at least 3 stations need to have reasonable estimates of both arrival time and particle density. Lower energy cosmic ray showers have too few particles to be reliably detected at large distances from the shower core. Because of this, detector stations must be arranged with a small spacing between detectors to get a reasonable signal in 3 or more detectors. Lower energy showers do have a fairly high arrival rate, so a smaller array area is sufficient to detect a large number of showers. At the highest energies, detectors at a larger core distance can collect a sufficient number of particles to determine timing and density, so a larger detector spacing can still allow the properties of the cosmic ray shower to be reconstructed. A smaller detector spacing would give a more accurate reconstruction of an ultra-high energy cosmic ray shower, but considering the extremely low arrival rate of ultra-high energy cosmic rays, it is usually desirable to have the largest possible detector spacing to maximise the collecting area of the array.

There are different types of detectors that may be used in a surface detector array. The two predominant types will be discussed in this section. They are scintillation detectors, and water Čerenkov detectors. Scintillation detectors rely on a scintillation medium that is luminescent when exposed to ionising radiation. Light is then detected using a photomultiplier tube (PMT). Chemically-doped plastic is typically chosen as the scintillation material due to its relatively low cost and ability to be used for a large detector area. The scintillation medium is usually a few centimetres thick, and is surrounded by reflective materials designed to ensure light produced anywhere in the scintillation medium is detected by a PMT. Scintillation detectors can detect muons and electrons directly, as they are ionising particles. Photons may also be detected if they interact and pair produce in the detector. Sometimes a layer of lead may be used to cause pair production so that photons are more likely to be detected, since photons are the most numerous particles at the ground. Scintillation detectors are equally sensitive to both muons and electrons, but given the higher particle density of the electromagnetic component of a shower, scintillation detector signals are usually dominated by the electromagnetic component.

Another type of detector, currently being used in the Pierre Auger Observatory, is the water Čerenkov detector. In a dielectric medium, light at optical wavelengths travels at a speed slower than the speed of light in a vacuum. For a refractive index n, this is given as:

$$v_n = \frac{c}{n} \tag{1.44}$$

It is therefore possible for a massive particle to have a speed greater than the speed of light in a refracting medium (at optical wavelengths). If the particle is charged, the result of this is that light is emitted in a cone shaped front analogous to a sonic boom. The emission angle of the light cone relative to the particle direction, for a particle velocity v is given as:

$$cos(\theta) = \frac{c}{nv} \tag{1.45}$$

Čerenkov light forms a continuous spectrum, with a spectral intensity approximately proportional to frequency. Considering that this only occurs at wavelengths where the medium is refracting, Čerenkov emission will predominantly be at ultraviolet wavelengths. In water, the refractive index is 1.33, so the minimum particle velocity to produce Čerenkov light is $0.75c$. The majority of muons and electrons in a cosmic ray shower have a velocity greater than $0.75c$, so water Čerenkov detectors will detect most of these. Photons can also be detected when they interact in the water by pair producing electrons, or by Compton scattering. Considering that water depth in a water Čerenkov detector is typically about 1 m, corresponding to 100 g cm^{-2} of matter, these interactions are quite likely. Because of this, water Čerenkov detectors are highly efficient at detecting photons provided the photon energy is sufficient to pair produce electrons with a speed above the Čerenkov threshold velocity. Muons at the ground level have an average energy in the order of a few GeV. With an ionisation loss over the depth of a water Čerenkov detector being a few hundred MeV, most muons will produce Čerenkov light over the entire depth of the detector. Electrons from the electromagnetic component often have a much lower energy, and given a relatively short interaction length for bremsstrahlung, many electrons will not make through the depth of the detector due to energy loss from ionisation and bremsstrahlung. Because of this, water Čerenkov detectors have a higher sensitivity to muons than they do to EM particles.

It is also possible to estimate the composition of the primary particle with a surface detector array. The simplest method of doing this is by determining both the density of EM particles and the density of muons. Considering that the number of muons in a shower is proportional to $A^{0.15}$, for a nucleus of mass number A, it is possible to determine A if both the EM and muon densities are known. This does require an array designed to be able so separate the EM and muon components, which may require additional detectors. Detectors can be made sensitive to only the muon component by shielding them to block out the EM component. Burying detectors below about 1 m of earth is sufficient to block out nearly all of the EM component. It is more difficult to isolate the EM component of a shower, but if a detector above ground is used in conjunction with a buried detector, the muon component determined by the buried detector can be subtracted from the above ground detector. It is

also feasible, though not as straight-forward, to deduce both the EM and muon component with two above ground detectors if the two detectors have a different ratio of EM:muon sensitivity. Examples of this may include stacked scintillation detectors with some shielding in between them to reduce EM sensitivity of the lower detector, segmenting a water Čerenkov detector into two levels so that the bottom level is less EM sensitive than the top, and placing a scintillation detector on top of a water Čerenkov detector.

There are some other ways to deduce composition without detectors that can discriminate muons from EM particles. The lateral distribution of muons is wider than the lateral distribution of EM particles. Additionally, the lateral distribution of each of the particle types may also depend on the specifics of the longitudinal development of a shower. Thus, the lateral distribution of particles can be indicative of the overall muon content, and also may give clues about the longitudinal development of a shower. Another method to deduce composition involves studying the arrival time distribution of particles at the detectors. Muons travel in nearly straight lines at close to the speed of light. Given that the hadrons that decay into muons lie very close to the shower axis, the point of production of the muon can be deduced from the arrival time of the muon at the ground. The timing of the muon will be delayed relative to the plane front of the shower by τ, where:

$$\tau = \frac{\sqrt{d^2 + r^2} - d}{c} \approx \frac{r^2}{2dc} \tag{1.46}$$

for a muon produced at a distance d from the shower core along the axis, at a core distance r.

1.3.2 Fluorescence detection

As charged particles pass through the atmosphere, they excite air molecules, which then isotropically emit fluorescence light. The amount of fluorescence light emitted is proportional to the energy deposited, so if this fluorescence light can be measured, it is possible to get a calorimetric measurement of the energy of an air shower. Most of the fluorescence light is emitted from electronic transitions in N_2 molecules and N_2^+ ions. The majority of fluorescence light emission occurs in the near ultraviolet at wavelengths between 300 nm and 400 nm(see figure 1.18)[10]. Though this emission is small for a single particle, the large number of particles present in the core of an ultra-high energy shower is sufficient for observation at night with sensitive equipment. This method of detection is possible for showers with an energy above approximately 10^{17} eV.

Though the quantity of fluorescence light produced is proportional to energy deposit, there are other factors that affect the observation of fluorescence light. Excited nitrogen molecules are capable of de-excitation through collisions. This collisional de-excitation

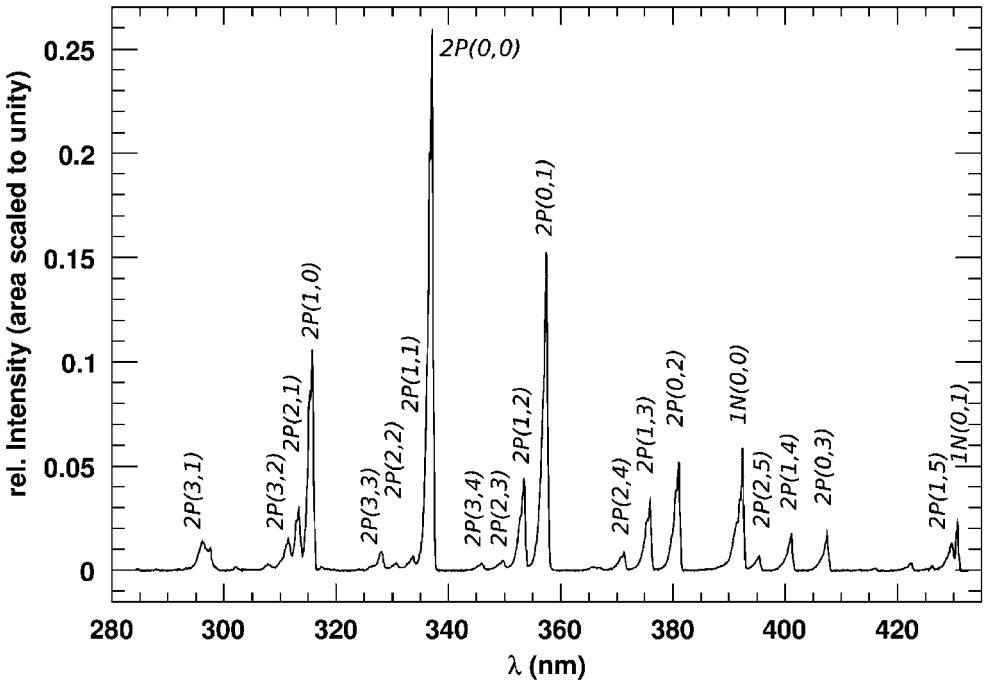

Fig. 1.18. The air fluorescence spectrum excited by 3 MeV electrons at 800 hPa. The labels indicate the transitions associated with the prominent spectral lines. From [10].

occurs predominantly with molecules that are not nitrogen, such as oxygen and water vapour. Thus, at higher atmospheric pressure, the yield of fluorescence light per unit of energy deposit is lower due to the higher rate of collisions between molecules. Humidity will also have an effect on fluorescence light emission, with a 20% difference between dry air and 100% humidity at room temperature and atmospheric pressure [10]. Temperature also plays a role, as at higher temperature, for a constant density, the rate of collisions between molecules will increase. The velocity of molecules colliding will affect the probability of a collisional de-excitation, so temperature will have a further effect on fluorescence yield because of this.

Detecting an extensive air shower can be likened to being able to see a 100 W light bulb, at a distance of 30 km, travelling at the speed of light. This requires a detector that is very sensitive to ultraviolet light as well as having a high temporal resolution. This is usually achieved by using an optical telescope to focus light onto photomultiplier tubes. Filters that only pass UV light are also incorporated into the optical system to reduce the amount of background light. The optical telescopes need to have a large collecting area, preferably at least a few square metres, in order to gather enough light. A fairly wide field of view is also desirable, to observe a long length of shower track, and to observe a large volume of the atmosphere. A good angular resolution is useful for reconstructing the shower geometry, and for reducing the amount of background light collected by each pixel. It is somewhat difficult

to cover a very wide field of view with a large area telescope, so a large number of telescopes are usually used to cover a large solid angle of the sky. Taking into account differences in the observed track direction due to different positions (typically a very small correction), the images from each telescope can be combined to be equivalent to one "eye" with a large field of view. Operation of a fluorescence detector requires a clear, moonless night, so they will typically have a duty cycle of about 10%.

Since the majority of particles lie close to the axis of a shower, the fluorescence signal can be treated as a point source of light, travelling at the speed of light in a straight line. The lateral distribution of particles is only visible in exceptionally close high energy events, and would not ordinarily require consideration. Reconstructing the geometry of the shower is done in multiple steps. The first step is to examine the directions of pixels that observed the fluorescence light. A plane can be defined, centred on the detector, that contains the directions of the pixels observing the shower. This plane is referred to as the SDP (shower-detector plane), within which the shower axis must lie. Reconstructing the position and direction of the shower axis within the SDP requires knowledge of the timing of the pulses observed in each pixel. Given the direction of each pixel and the time that the spot passed through that pixel, a fit can be done to the pixel timing to determine the direction of the shower axis within the SDP, the distance from the shower axis to the detector, and the timing of the shower as it crosses the point of closest distance to the detector. Details of this procedure will be discussed in section 2.4.2.

The timing fit to determine the position and direction of the shower axis can have a relatively low accuracy when compared to the SDP fit. This is especially true if the track is viewed over a short length. Short track lengths are likely when viewing the highest energy showers, where a long distance from the shower to the detector is more likely. A short track length leads to a degeneracy between the direction of the shower axis and the distance between the detector and the shower axis, leading to an inaccurate determination of energy and X_{max} , as well as the primary particle direction. There are however, ways to compensate for this. The first method is stereo detection. If a shower is observed by two fluorescence detectors that are separated from each other, a timing fit may not be required. The shower axis can be found simply by finding the intersection between the two SDP's. The other method is hybrid detection. This method is possible if the fluorescence detector is situated so that it overlooks a surface detector array. The arrival time of the shower front at a surface detector station is able to constrain the geometry of the shower axis, removing the degeneracy from the timing fit. This also has an added benefit for the surface detector array, as the energy determined by the fluorescence detector can be used to calibrate the surface detector.

Once the shower geometry is known, the fluorescence emission from the shower can be deduced along the shower axis. Attenuation in the atmosphere between the shower axis and detector must be taken into account. Particles in a shower emit Čerenkov light as well as fluorescence. Since Čerenkov light is heavily forward directed in air, most of the Čerenkov light is not observed, but a small number of particles moving towards the detector can produce observable direct Čerenkov light, and forward directed light can be scattered toward the detector. The Čerenkov contribution is much smaller than the fluorescence contribution for showers viewed from side on, but the Čerenkov contribution must still be calculated for an accurate reconstruction. Given the fluorescence light emission profile, and the fluorescence yield, the energy deposit profile can be determined. From this, $X_{\max}$ can be found, and the total energy deposit can be deduced by integrating the energy deposit profile. A small fraction of the primary particle energy will not show up in this profile, from particles that do not release their energy in the atmosphere, such as hadrons, neutrinos, and high energy muons. This 'invisible energy' must be added to the total energy deposit to determine the energy of the primary cosmic ray. Though the invisible energy correction is not easy to quantify, relying on either simulations or data from muon detection, the invisible energy as a fraction of total shower energy is small, so inaccuracies in simulations will only contribute a small error to the primary particle energy.

Fluorescence detectors, when compared to surface detectors, are able to obtain a much more direct measurement of primary energy, due to their calorimetric nature. Surface detector arrays rely much more heavily on simulating ultra-high energy particle interactions, which are not accessible by particle accelerator experiments. Though corrections are necessary for fluorescence detectors, they are based on well understood physical processes, with the only exception being small invisible energy correction. The low duty cycle of fluorescence detectors ($\sim$10%) does mean that fluorescence detectors are able to detect far fewer events when compared to a similarly sized surface detector array.

1.4 History of UHECR detectors

1.4.1 Volcano Ranch

The Volcano Ranch array [69] consisted of 19 plastic scintillation detectors, each with a collecting area of 3.3 m^2 (see figure 1.19), operating from 1959 to 1978. The scintillation signals were picked up with a 5 inch photomultiplier. It was initially operated with a spacing of 442 m giving a collecting area of 2 km^2. It was also operated with a spacing of 884 m to give a larger collecting area of 8.1 km^2. In addition to this, there was also an additional 3.3

m^2 detector shielded with 10cm of lead in order to record the muon density for some of the events. The Volcano Ranch array produced an energy spectrum for cosmic ray events above 10^{18} eV, showing a flattening of the spectrum referred to as the ankle [68]. An exceptionally high energy event was also observed, with an energy of 1.4×10^{20} eV [67]. It was not realised at the time that the energy of this event exceeded the predicted spectral cutoff as the cosmic microwave background had not been observed.

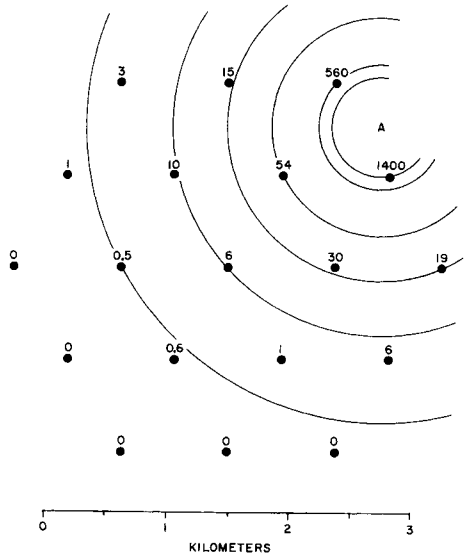

Fig. 1.19. Layout of the Volcano Ranch array in February 1962. The numbers above each of the points are the particle densities (in particles m^{-2}) measured for the highest energy event recorded in the detector. The letter A represents the estimated core position of the event and the circles are contour lines of particle density. From [67].

1.4.2 Haverah Park

The Haverah Park array, unlike its predecessors, relied primarily on water Čerenkov detectors, operating from 1962 to 1987. The array initially started with 4 detectors, each with an area of 34 m^2 [94]. Each of the detectors was made up of fifteen smaller units, made of $1.85 \times 1.24 \times 1.29$ m galvanized steel tanks, filled with 1.2 m of water, with the water sourced from a nearby bore drilled into limestone. The tanks each had a 5-inch photomultiplier, with the bottom of the photomultiplier submerged in the water to improve light collection. The detectors were configured with one in the centre, and three surrounding it in a triangle with a 500m spacing from the central detector to the outlying detectors. For each of these detectors, the signals from the fifteen photomultipliers were combined in a summing circuit to give one signal for each of the 4 stations. In 1968, [66], additional detectors were placed at a distance

of 2 km from the centre. Due to land use restrictions, the detectors were arranged into six sub-arrays of four 13.5 m^2 detectors, with the sub-arrays having 50 m & 150 m spacing. Some additional detectors were placed to fill in the largest gaps in the detector, and also an infill array of thirty 1 m^2 detectors in a lattice with a 150 m spacing. The detectors in the infill array were constructed out of expanded plastic foam, with an depth of 1.2 m, and filled with deionised water. A diagram of the array layout is given in figure 1.20.

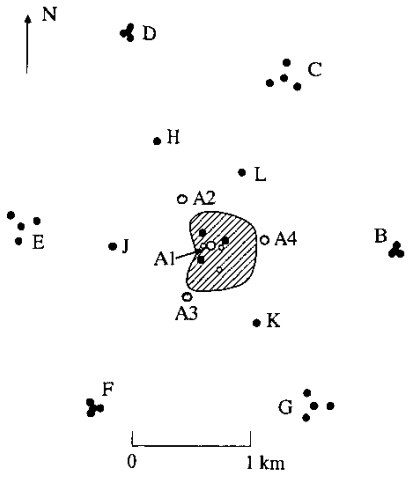

Fig. 1.20. Map of the Haverah Park array, as it was from 1976 onwards. Detectors A1-A4 are the triggering detectors with an area of 34 m^2. Detectors B-G are each made up from four 13.5 m^2 detectors. At H there is a single 13.5 m^2 detector. J-L are 2.25 m^2 detectors. The three points 150 m from A1 are 9 m^2. The shaded area contains an infill array of thirty 1 m^2 detectors. The open circles inside the infill array are additional muon detectors. From [66].

The method of energy reconstruction did evolve over the life of the experiment. The initial method was to estimate the total energy loss of the shower into a 1.2 m layer of water at core distances between 100 m and 1000 m. It was later found that a better energy estimate is to find the detector signal at a fixed core distance. In the case of Haverah Park, this was chosen as the signal at a core distance of 600 m. [66]. Through their 20+ years of operation, the detectors demonstrated that the water quality and lining of water Čerenkov detectors could be maintained over an extended period, with only one of the tanks showing issues caused by contamination from that specific tank being opened repeatedly throughout the experiment. The most notable proof of the quality of the water came when the collaborators drank water from the 20 year old tanks upon decommissioning.

1.4.3 SUGAR

The Sydney University Giant Air Shower Recorder was located near Narrabri, New South Wales, and was the only large cosmic ray detector in the southern hemisphere before the Pierre Auger Observatory [112]. It was in operation from 1968 until 1979. This array differed from others by only having detectors that are buried below ground. There was a total of 54 stations deployed over an area of 60 km^2. The stations were made up of two 6 m^2 liquid scintillation detectors buried 1.7 m below the ground and 50 m apart. Most of the stations were arranged in a square array with a 1600 m spacing, as well as a smaller number with 800 m and 400 m spacing. Unlike previous arrays, which required each detector station to be connected by cables to a central recorder, SUGAR stations operated autonomously. This allowed for a large array without long cable runs. A station would store the timing and intensity of pulses when triggered. The data is then collected and checked against data from other stations for coincidences consistent with a cosmic ray shower. In order to reduce the number of pulses recorded from low energy cosmic rays, a detector station would be triggered when signals were detected in both scintillators within 350 ns of each other. The two scintillators were separated by 50 m for this reason. Accurate timing was maintained by continuously transmitting a radio timing signal to all of the stations.

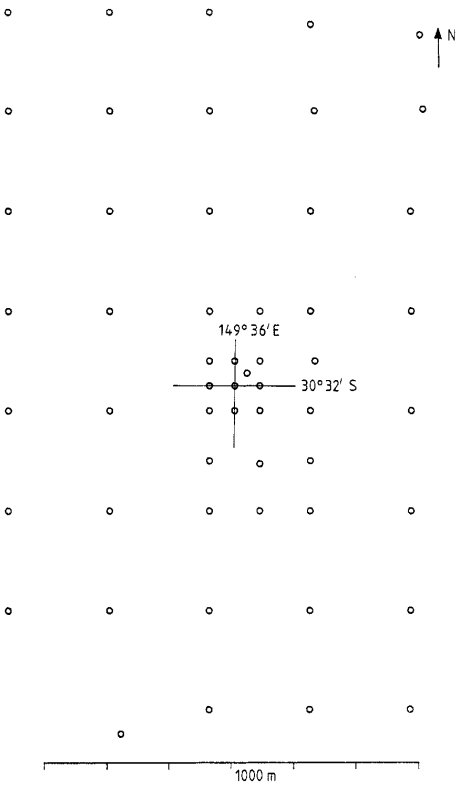

Fig. 1.21. Map of SUGAR showing station positions. From [112].

Since the particle density near the shower core is orders of magnitude larger than the minimum density detectable with detectors designed for a sparse array, it is desirable to have detectors capable of measuring both very high and very low particle densities, thus requiring a high dynamic range. Electronics to detect the magnitude of a pulse from photomultipliers used in cosmic ray shower experiments were not capable of such a high dynamic range. Detectors at SUGAR avoided this problem by using a logarithmic time to height converter. Charge from the photomultiplier anode would be fed into a capacitor in parallel with a resistance to give a decay constant of 3.0 μs. The signal would then be fed through an amplifier to a discriminator which would trigger when voltage was above a certain threshold. Assuming the photomultiplier pulse duration is much shorter than the decay constant, the amount of time that the voltage is above threshold will be proportional to the logarithm of the charge in the pulse. Thus, the stations would simply record the length of time for which the discriminator was triggered, which in turn could be used to deduce the size of the pulse. This meant that the detectors had a very high dynamic range, though with an unfortunate side effect; photomultipliers of this type were capable of afterpulsing. Afterpulsing is an effect whereby the photomultiplier produces a spurious secondary pulse several microseconds after the original signal. On occasion this afterpulse could significantly extend the time that the discriminator was triggered, substantially increasing the estimated charge, leading to a vastly overestimated particle density.

The very large detector spacing meant that for the majority of events, only three stations were triggered. The small number of stations triggered, even for the highest energy events, in addition to the problems caused by photomultiplier afterpulsing meant that the reconstructed energy of events were of poor resolution. SUGAR did contribute to the field with arrival directions of events in the southern hemisphere and pioneered the use of autonomous detector stations.

1.4.4 Yakutsk

The Yakutsk array, located in Russia, began taking data in 1970, and is still in operation to this date [58], [72]. The array is made up of a number of different types of detector. There are 58 above-ground scintillation detector stations each with two scintillation detectors with an area of 2 m^2, and thickness 5 cm. There are also 6 underground scintillation detectors to measure muons. The underground stations are also plastic scintillators with a collecting area of 20 m^2, with one of them having a collecting area of 192 m^2. In addition to the array of particle detectors, there are also a series of air Čerenkov detectors, able to measure the Čerenkov emission from shower particles and give information about the longitudinal development of an air shower. This allows for a better calibration of energy from the surface

detector array, with reduced reliance on shower simulations. There are currently 48 of these detectors spread across the array. The total area of the array has varied over the lifetime of the experiment, with a maximum area of 17 km^2 in 1990. In 1995, the array was contracted to 10 km^2, in order to gather more lateral detail in showers. The array currently has a collecting area of 8.2 km^2. The Yakutsk energy spectrum does show results consistent with a cutoff due

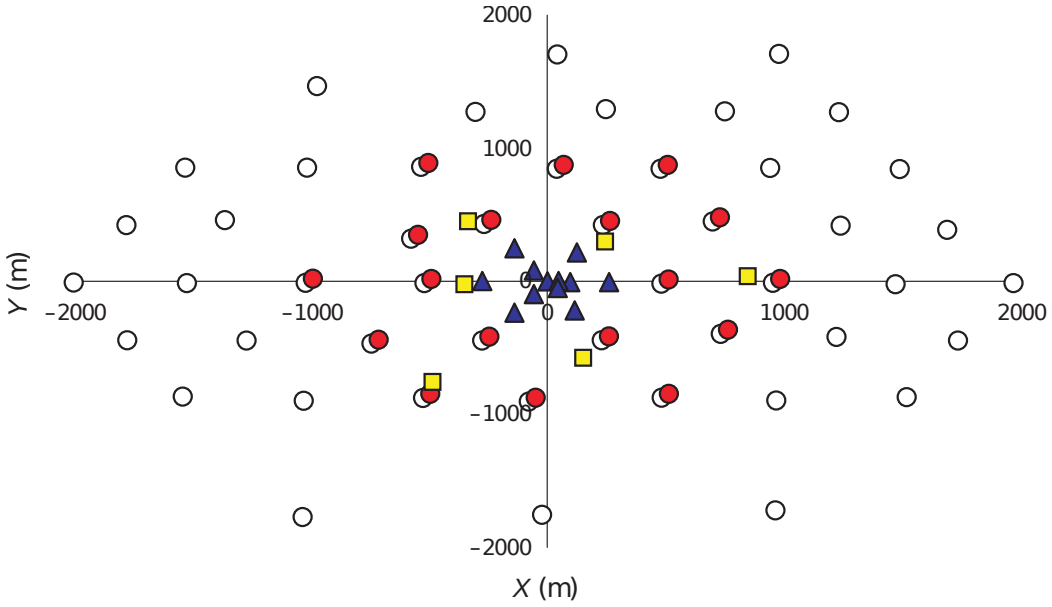

Fig. 1.22. Arrangement of detectors in the Yakutsk array. From [59].

to the GZK effect, though the size of the array means that there is a low statistical significance to this result.

1.4.5 AGASA

The Akeno Giant Air Shower Array ran from 1990 until 2004, and at the time, was the largest cosmic ray observatory in the world [30]. It consisted of 111 2.2 m^2 plastic scintillation detectors, with a spacing between detectors of approximately 1 km. The array had a total collecting area of 100 km^2. The plastic scintillation medium was 5 cm thick and viewed by a 125 mm photomultiplier. In addition to the scintillation detectors, there were also 27 muon detectors. The muon detectors are made up of proportional counters 10 cm wide and 10 cm high, with a length of either 5 m or 2 m. A set of these proportional counters was placed underneath some of the scintillators, as well as a few of larger area placed adjacent to detectors. The proportional counters were shielded by either 1 m of concrete, 30 cm of iron, or 5 cm of lead above 20 cm of iron. There were fifteen with an area of 2.8 m^2, three of 3.6

m^2, one of 7.2 m^2, six of 10 m^2, one of 15 m^2, and one of 20 m^2. A prototype of a water Čerenkov detector for the Pierre Auger Observatory was also tested at this site.

The array was divided into four smaller branches, each having a branch centre to handle the acquisition of data. The detectors were linked to their branch centre by fibre optic cables. Cables had to be hung on utility poles of electric and telecommunication companies, which did lead to long cable runs, and complicated data acquisition. Initially, each of the 4 branches operated independently. This limited the total collecting area of the observatory as events that landed near the boundary between branches may not trigger one or more of the necessary branches, and lack of precise timing between branches made reconstruction difficult. The result was an effective area 1.7 times smaller than the area of the whole array. In 1995, the four branches were unified to allow rapid communication of triggering signals and accurate timing between each branch, bringing the effective collecting area up to 100 km^2.

The energy spectrum of cosmic rays measured by AGASA did not show an expected cutoff in the spectrum due to the GZK effect, with a spectrum continuing well beyond 10^{20} eV, up to the highest energy event recorded at 2.46×10^{20} eV [91]. This is in contradiction with results from other large observatories, that show a substantial suppression at energies above the GZK cutoff.

1.4.6 Cornell experiment

The Cornell experiment was an early attempt at measuring air fluorescence from cosmic ray showers [27]. The experiment was constructed in 1967. The detector was comprised of 10 fluorescence detector modules. Each of the modules had a 0.1 m^2 Fresnel lens covered by a filter to pass UV light. 50 PMT's were placed at the focal plane of each module, with each PMT covering a 6 degree wide section of the sky (see figure 1.24). An event was triggered by two or more adjacent pixels having signals with a delayed coincidence. Pulses were then displayed on a large bank of 3 inch cathode ray tubes and photographed with 70 mm film.

Ultimately, the small collecting area of the detector modules, and the levels of aerosols and water vapour in the atmosphere meant that the experiment was unable to reliably detect cosmic ray showers.

1.4.7 Fly's Eye

The Fly's Eye detector was the first to reliably detect extensive air showers using the atmospheric fluorescence technique [13, 72]. Work began on the detector in the 1970's, with the detector becoming operational in 1981. The detector was situated in the desert at the Dugway Proving Grounds, Utah. The original detector, called Fly's Eye I, was comprised of

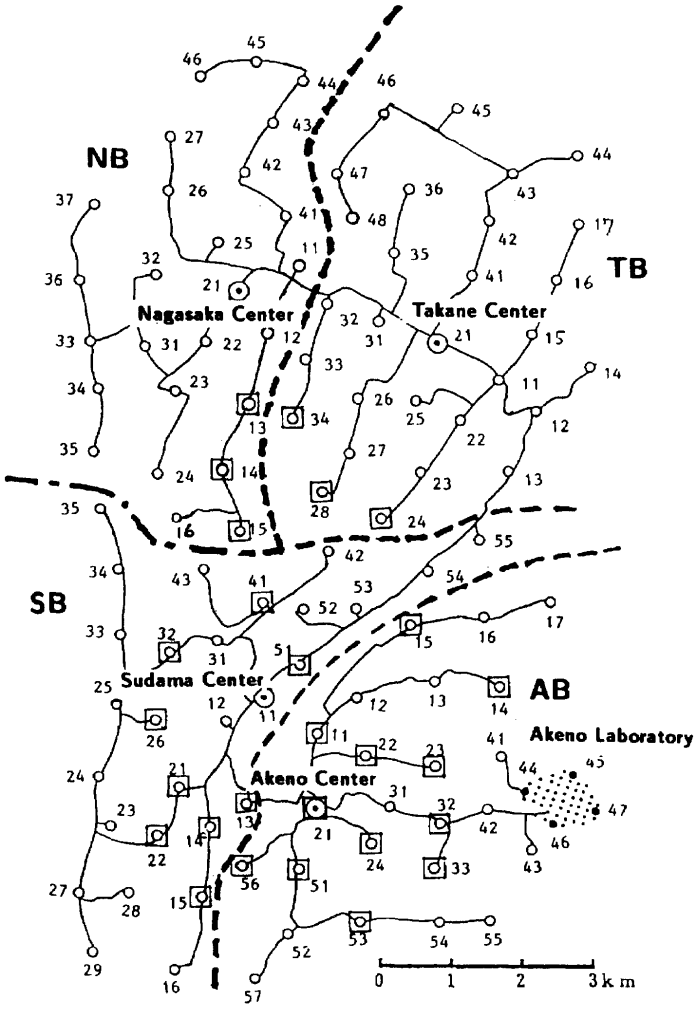

Fig. 1.23. Map of AGASA. The circle points represent the surface scintillation detectors. The squares represent muon detectors. The lines connecting the detectors show the routes of the optical fibers. The dotted lines are the boundaries between the four branches. From [76].

67 telescopes, each with a 1.575 m diameter spherical mirror. Each mirror focused light on to an array of either 12 or 14 photomultiplier tubes with a diameter of 90 mm, giving each pixel an angular diameter of 5°. Hexagonally faced reflective funnels were used to channel light into the photomultipliers that would otherwise go in between them. Each of these modules were housed in a steel drum with a length of 2.13 m and a diameter of 2.44 m. The drums would point downwards to protect the mirror and electronics from light and weather, and turned upwards at night to a pre-determined position. Fly's Eye I had a total of 880 pixels, covering the entire night sky. Fly's Eye had a collecting area of about 1000 km^2, significantly larger than any surface detectors of the time. The detector was only able to operate on clear, moonless nights, so the duty cycle of the detector was only about 10%.

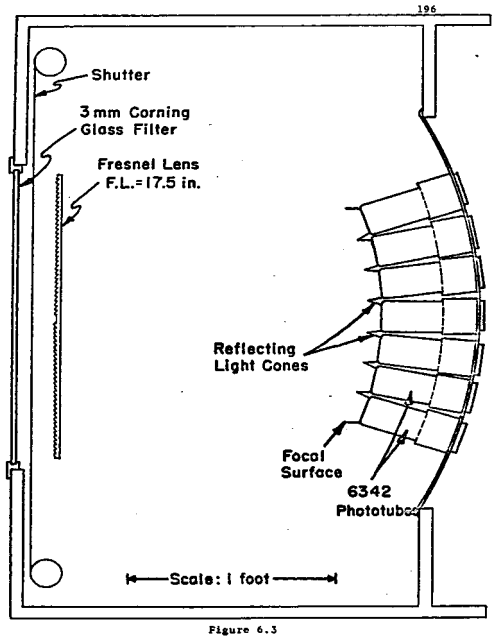

Fig. 1.24. Diagram of one of the fluorescence detector modules in the Cornell experiment. From [27].

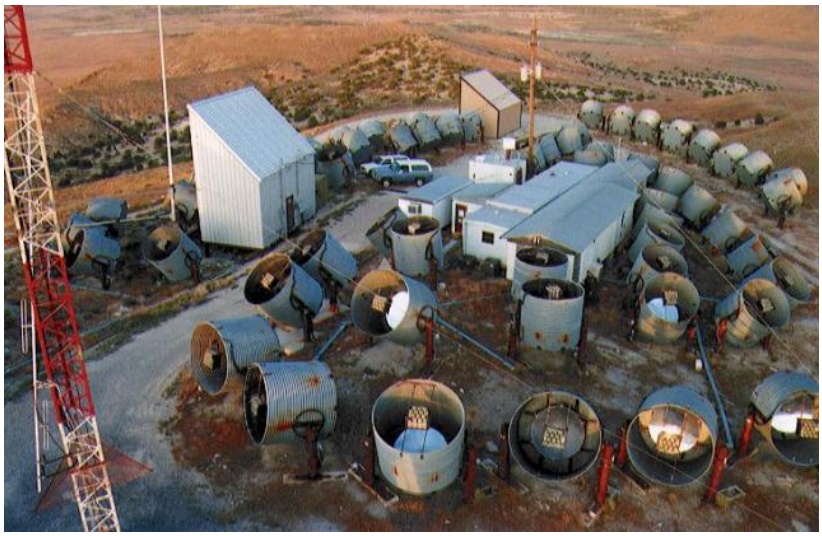

Fig. 1.25. Picture of Fly's Eye I.

Signals from each PMT are connected by cable to a central building, containing the electronics and computers to control the observatory and acquire data. Due to varying levels of background light, triggering levels for each pixel were constantly adjusted to give

a constant trigger rate for each pixel. When the triggering conditions were met for the observatory, the pulse integrals and timing for all triggered pixels were read and stored. To monitor the sensitivity of the detectors, optical pulsers were installed in each telescope. To monitor atmospheric conditions, 28 vertical flashers were installed. Nitrogen lasers were also fired periodically to study the scattering of light in the atmosphere.

A second detector, Fly's Eye II (FE II), began operating in 1986. It was situated at a distance of 3.4 km from Fly's Eye I(FE I), with 36 mirrors and a total of 464 photomultiplier tubes. The telescopes covered half of the sky in the direction facing FE I. This made stereo detection of showers possible, with a substantial improvement in geometric resolution. When an event was triggered in FE I, an infra-red triggering signal would be sent to FE II to record any signal triggered simultaneously.

The Fly's Eye detector provided an energy spectrum which showed a precise measurement of the ankle (discussed in section 1.1.5) in the cosmic ray energy spectrum at $\sim 3 \times 10^{18}$ eV [21]. With the ability to measure $X_{\max}$, composition was also studied. A change in composition with energy was found, with heavy primaries at 0.1 EeV, changing to a lighter composition at 15 EeV [21]. Fly's eye also has the honour of observing the highest energy cosmic ray ever detected to this day, with an energy of $3.2 \pm 0.9 \times 10^{20}$ eV, on October 15, 1991 [20] (see figures 1.26, 1.27). Operation was ceased in 1992 to begin work on a higher resolution fluorescence detector.

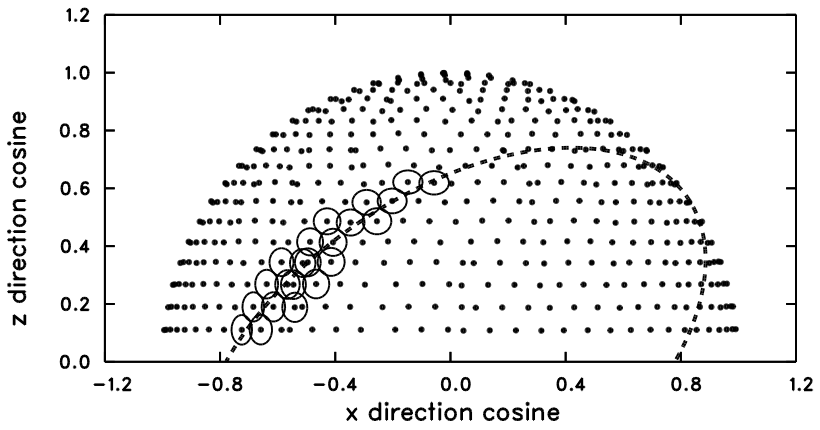

Fig. 1.26. Pointing directions of the pixels triggered from the highest energy cosmic ray ever detected, projected into the xz-plane. From [20].

1.4.8 High Resolution Fly's Eye (HiRes)

HiRes was a significant upgrade over the Fly's Eye experiment, being situated in the same location [56]. There were detectors on two sites, separated by 12.6 km. The telescope mirrors

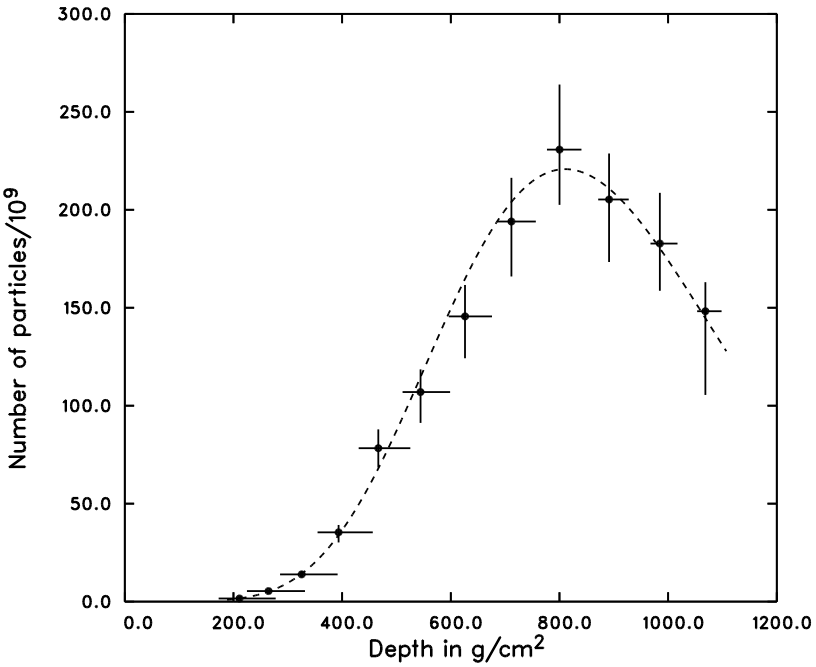

Fig. 1.27. Fit of the shower profile for the highest energy cosmic ray ever detected. From [20].

had an area of 5.2 m^2, translating to an effective area of 3.72 m^2 when considering the obscuration by the central PMT cluster. Each telescope had an array of 256 photomultipliers at the focal plane giving a pixel size of 1 degree. This meant that events could be observed at a much greater distance when compared with the original Fly's Eye. HiRes telescopes were pointed at low elevation in order to observe a large volume of atmosphere, since the highest energy events would be visible at very large distances, in excess of 30 km. Upward pointing telescopes would only observe a comparatively small volume of atmosphere, so would not substantially increase the collecting area of the observatory.

HiRes-1 began operations in 1997, and was situated at the same site as Fly's Eye I. It consisted of 22 telescopes, observing elevations from 3 to 16.5 degrees, and a full 360 degrees in azimuth.

HiRes-2 was completed in 1999, 12.6 km away from HiRes-1. Like HiRes-1, HiRes-2 had 360 degree coverage in azimuth, but utilized a total of 42 telescopes to cover a larger range of elevations, from 3 to 30 degrees. This allowed for more accurate geometric reconstruction of monocular events. Having the second detector operational also allowed for stereoscopic detection of showers, with much more accurate geometry. Though the telescopes and photomultipliers were the same as those in HiRes-1, HiRes-2 had significant upgrades to the electronics [24]. HiRes-1, like Fly's Eye, used ADC's (analogue to digital converters) that would only allow the integrated pulse signal to be read for each pixel, with

the timing of the pulse also being stored as a single value for each pixel. HiRes-2 utilised an FADC (flash analogue to digital converter) that allowed for an instantaneous reading of the photomultiplier with very short time intervals. Signals from each PMT were digitised at a rate of 10 MHz, and passed through a 820 μs buffer. This allowed for better triggering criteria based on information from distributed sources, and signals could then be read out from all pixels in a detector. The full shape of the pulse was also recorded, which allowed for a more accurate reconstruction.

Calibration of PMT sensitivity was done with a portable xenon flash lamp directly illuminating the PMT cluster. Changes in PMT response were also monitored using a frequency tripled YAG laser. The laser could illuminate the PMT cluster directly, as well as by reflecting off of the mirror to monitor mirror reflectivity using optical fibres. Lasers with steerable beams were used at each of the two sites to measure atmospheric extinction, and could also give an indication of any cloud cover. Infrared cloud monitors also gave information on cloud cover. Xenon flashers were also placed between the sites to give information about the atmosphere between sites [56].

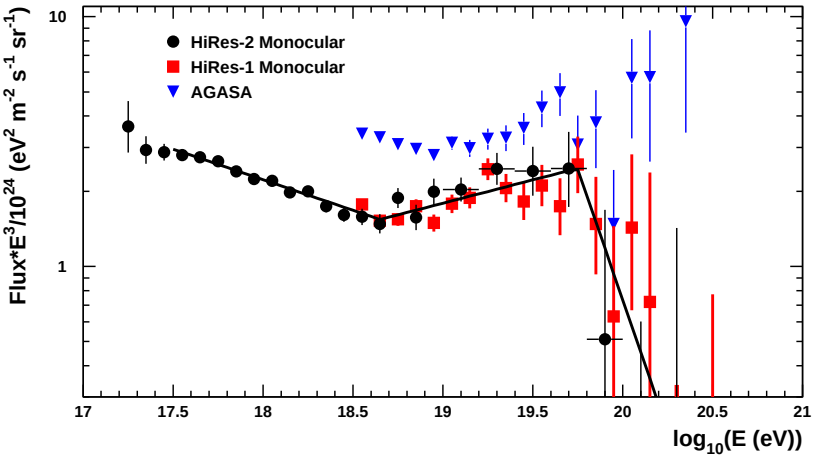

Fig. 1.28. Energy spectrum obtained by HiRes showing the GZK cutoff. From [1].

With the large collecting area of the observatory, in combination with the calorimetric energy measurement from fluorescence detection, HiRes was the first experiment to observe a suppression in flux at energies above 6×10^{19} eV, consistent with the predicted GZK cutoff (see figure 1.28) [1]. Results from the analysis of $X_{\max}$ distribution found that a proton-rich composition is favoured at the highest energies [89]. HiRes ceased operations in April 2006.

1.4.9 Telescope Array (TA)

The Telescope Array Experiment is the most recently constructed observatory designed to detect ultra-high energy cosmic rays, with data taking beginning in 2007 [92]. It is also the largest ultra-high energy cosmic ray experiment in the northern hemisphere. TA is a hybrid detector, consisting of both a surface detector array and fluorescence detectors.

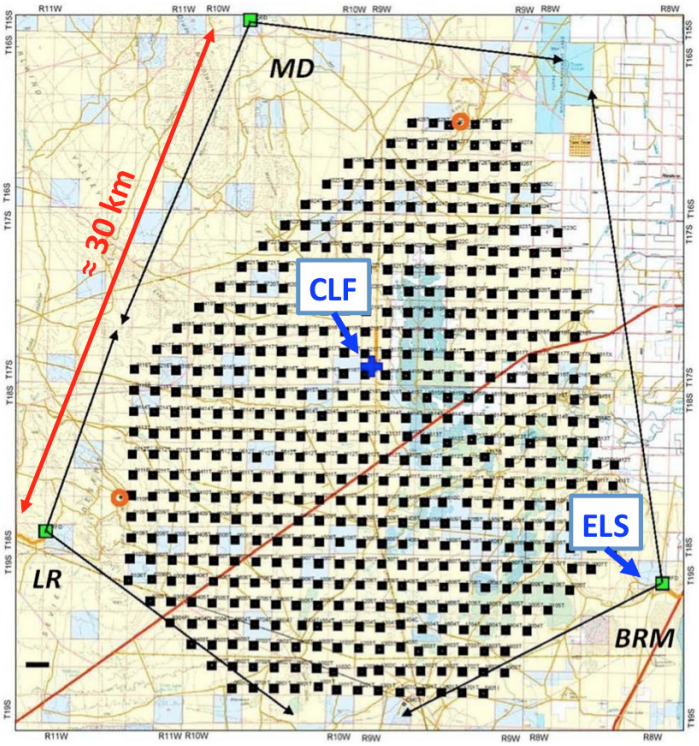

Fig. 1.29. Map of Telescope Array. The arrows indicate the field of view of the fluorescence telescopes.

The surface detector array consists of a total of 507 stations covering an area of 762 km^2, arranged in a square grid with a 1.2 km spacing [2]. The detector stations consist of two layers of plastic scintillators, with an area of 3 m^2 and thickness 1.2 cm for each layer. Light produced by the scintillation medium is directed to a $\frac{9}{8}$ inch photomultiplier via 96 wavelength shifting fibres. The PMT signal is then low-pass filtered with a cutoff frequency of 9.7 MHz and read out at a rate of 50 MHz by a 12 bit FADC. The array is divided into 3 sub-arrays, each controlled wirelessly from 3 communication towers that handle triggering. Individual stations will transmit a signal to the tower if triggered, and if 3 adjacent stations are triggered, the tower will store the event, collecting traces from any station that detected a signal. Synchronisation of stations is handled via GPS. Stations are powered by a 125 W

solar panel and a lead-acid battery. Detector calibration is monitored by observing pulses from minimally ionising particles in background radiation.

The Fluorescence detector consists of 3 sites overlooking the surface detector array, separated by about 35 km [106]. The north-west site, called Middle Drum (MD), contains 14 fluorescence telescopes that were relocated from HiRes-1. These telescopes are described in the previous section. The two southern sites, Black Rock Mesa (BMR), and Long Ridge (LR) each have 12 telescopes newly constructed for TA. The new telescopes are each made from 18 hexagonal segments, with a total diameter of 3.3 m, and a focal length of 3 m. The PMT cameras are composed of 256 PMT's, with a pixel size of approximately 1 degree. Each PMT camera covers 15 degrees in elevation and 18 degrees in azimuth. PMT signals are digitised by a 12 bit FADC at a rate of 40 MHz. Calibration of PMT's is achieved with a N_2 laser, and monitored with a YAP pulser on three PMTs in each camera. The other PMTs are calibrated relative to the three calibrated PMTs by uniformly illuminating the camera with a xenon flasher. Atmospheric monitoring is done using a central laser facility in the center of the array, as well as a LIDAR at each of the three sites. A more complete calibration of the fluorescence detector is also done with a linear particle accelerator fired into the atmosphere in front of the FD sites [93].

An extension called TALE (Telescope Array Low energy Extension) has been added to TA to observe showers at lower energy [107]. TALE consists of additional fluorescence telescopes and surface detectors designed to detect showers down to energies below 10^{17} eV, an order of magnitude lower than TA. The fluorescence detector components consists of 11 telescopes at MD. These telescopes were refurbished telescopes from HiRes-2. The telescopes are pointed at elevations between 31 and 59 degrees, and can operate in conjunction with the low elevation telescopes at MD. Low energy showers are only observable at close distances, where the shower maximum will only be observable at high elevation angles. The surface detector component uses a similar station design to the TA SD. An additional 37 stations were added to extend the surface detector array towards MD. 76 stations were placed at close distance in front of MD, with the closest 45 counters having a 400 m spacing, and the remaining stations having a 600 m spacing.

An expansion of the array is currently in progress called TAx4, which involves increasing the area of the detector to 3000 km^2 [62]. 500 surface detector stations, of similar design to the previous TA SD, will be utilised in a square grid with a 2.08 km spacing. Additional fluorescence telescopes will be installed at Middle Drum and Black Rock overlooking the expanded surface detector array.

1.4.10 FAST

FAST (Fluorescence detector Array of Single pixel Telescopes) is a new design for a fluorescence detector with the ability to achieve a very large collecting area at a lower cost [42, 41]. It is currently being designed, with prototypes undergoing testing. This design utilises smaller telescopes, with a collecting area of $\sim$1 m^2, and much larger pixels, with angular sizes of 15°. This design can be built at a significantly lower cost compared to traditional fluorescence telescopes, making it feasible to build a vast array of these detectors. An array spacing of 20 km is being considered, allowing for a density of stations $\sim$100 times lower than for a surface detector array.

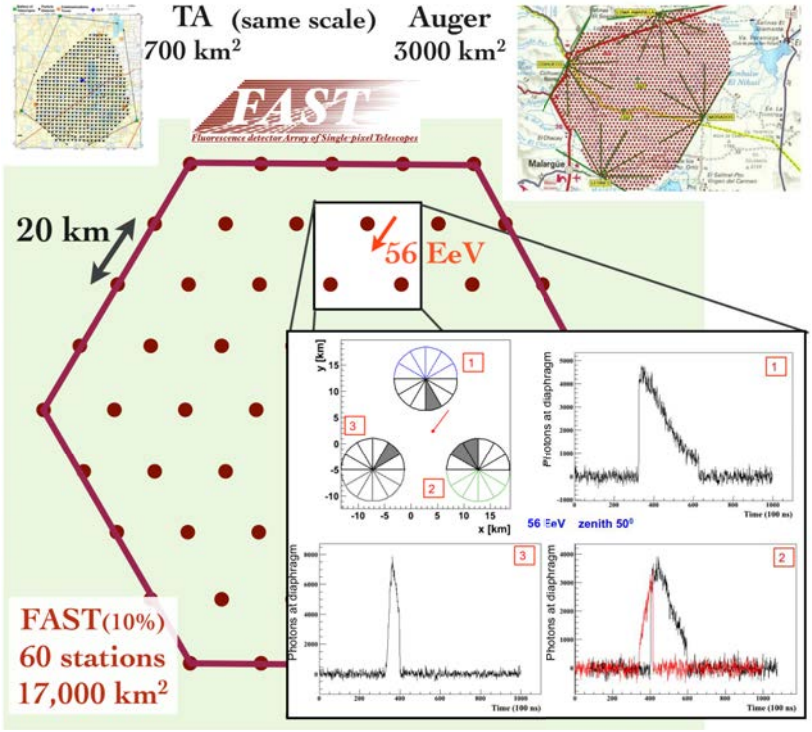

Fig. 1.30. An array of 60 FAST stations with Telescope Array and Pierre Auger Observatory shown for scale. Also included are the simulated signals for a 57 EeV event. From [41].

This design does present some drawbacks, mostly being the lower sensitivity and the difficulty reconstructing geometry. A smaller telescope collecting area means that fewer photons are collected. In addition to this, the larger pixels collect much more of the night sky background light, further reducing sensitivity. This will mean a much higher energy threshold when compared to existing fluorescence detector designs, but the large collecting area of FAST is intended for shower energies above $\sim 10^{19.5}$ eV, which are bright enough to be observed with FAST telescopes.

A more difficult issue to overcome is accurately reconstructing the geometry of the shower. Since a shower is observed by a few pixels (potentially only one), a shower-detector plane cannot be determined. There are possible remedies to this. One is to use a surface detector array to reconstruct shower geometry. The fluorescence light observations could be used to determine an energy deposit profile if the shower geometry is known. A surface array would come at a significant cost though, as a large number ($\sim$100) of surface detector stations would be required for each FAST station. A method of geometry reconstruction without a surface detector array is also being considered. If multiple FAST stations observe a shower, the relative intensities and pulse shapes of fluorescence light observed can be used to determine geometry.

Designs are currently being tested at the Telescope Array site, and at the Pierre Auger Observatory. The design being tested uses reflecting telescopes, each covering a 30 degree by 30 degree field of view with four pixels. These are situated next to the current fluorescence telescopes, and rely on them for triggering and for testing geometry reconstruction.

1.4.11 JEM-EUSO

JEM-EUSO is a space based fluorescence detector currently being planned, to observe cosmic rays with energies above the GZK cutoff with an unprecedented collecting area [40, 3]. The observatory will be located on the Japanese experiment module on the ISS. Due to the $\sim$400 km altitude of the ISS orbit, JEM-EUSO will be able to observe a very large area, orders of magnitude above current cosmic ray detectors. A single telescope will be used, utilising Fresnel lenses, with an area of $\sim$4.5 m^2, and a 60 degree field of view. A substantially smaller pixel size is required when compared to ground based fluorescence detectors. Multi-anode PMTs each containing 64 pixels may be used to give a total of 2304 pixels, with the pixel size corresponding to $\sim$500 m on the ground. A simulated shower image from this camera is shown in figure 1.31. Silicon-based photo-sensors are also being evaluated as a possible alternative to PMT's, with a higher quantum efficiency. With the telescope pointing directly downwards, the instantaneous collecting area will be $\sim 2 \times 10^5$ km^2. The long distance from cosmic ray showers being observed means that the detector will have a very low efficiency for energies below $\sim 5 \times 10^{19}$ eV, but this observatory's purpose is to study cosmic rays above that energy. With an orbital inclination of 51.6 degrees, JEM-EUSO will have a nearly uniform exposure across the northern and southern hemispheres. Tilting the detector can cover a much larger area, as much as 7×10^5 km^2, though the detector would require even higher energies to become fully efficient. Prototype versions are currently being tested, with a ground based version at TA, and additional prototypes being tested on balloons.

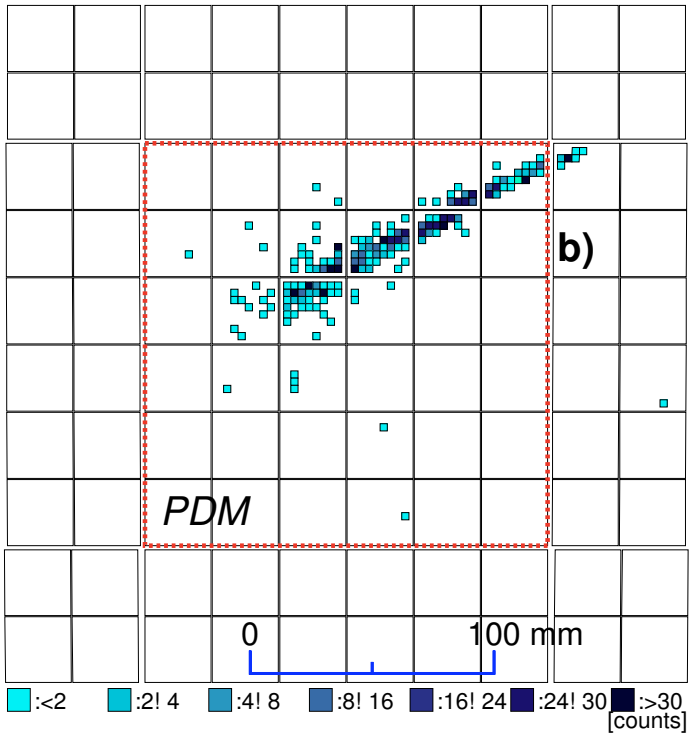

Fig. 1.31. A simulated image of a 10^{20} eV shower seen by JEM-EUSO. From [3].

Chapter 2

Pierre Auger Observatory

2.1 Overview

The origin of the highest energy cosmic rays has been a mystery for many decades, since the earliest experiments with surface detectors discovered cosmic ray showers at exceptionally high energies. Due to the rarity of such high energy events, cosmic ray observatories with increasingly large area are desirable. Many scientists saw the need for a cosmic ray observatory with a collecting area far greater than any previous experiments. With such a great task at hand, a collaboration spanning 18 countries was formed to pursue this goal. It was decided that the observatory should be named after the man who discovered extensive air showers, so from then it was named the Pierre Auger Observatory. Data taking began in 2004, and construction of the observatory was completed in 2008. The site that was selected is in Mendoza Province, Argentina, near the town of Malargüe.

The Pierre Auger Observatory is a hybrid detector, consisting of a 3000 km^2 surface detector, in combination with a series of fluorescence telescopes overlooking the surface detector. The surface detector, with a nearly 100% duty cycle, provides the largest exposure of any cosmic ray observatory in the world. Although the fluorescence detector has a similar collecting area to the surface detector, it can only operate on clear, moonless nights, giving a $\sim$15% duty cycle. The fluorescence detector, even with its far lower exposure, provides a number of important functions for the observatory. The fluorescence detector provides a calorimetric measurement of energy, with low systematic and statistical errors, that can be used to calibrate the surface detector energy. The ability to measure X_{max} also means that the fluorescence detector is far more sensitive to the primary particle composition. The fluorescence detector also benefits from the surface detector, since surface detector stations allow for a hybrid geometry reconstruction.

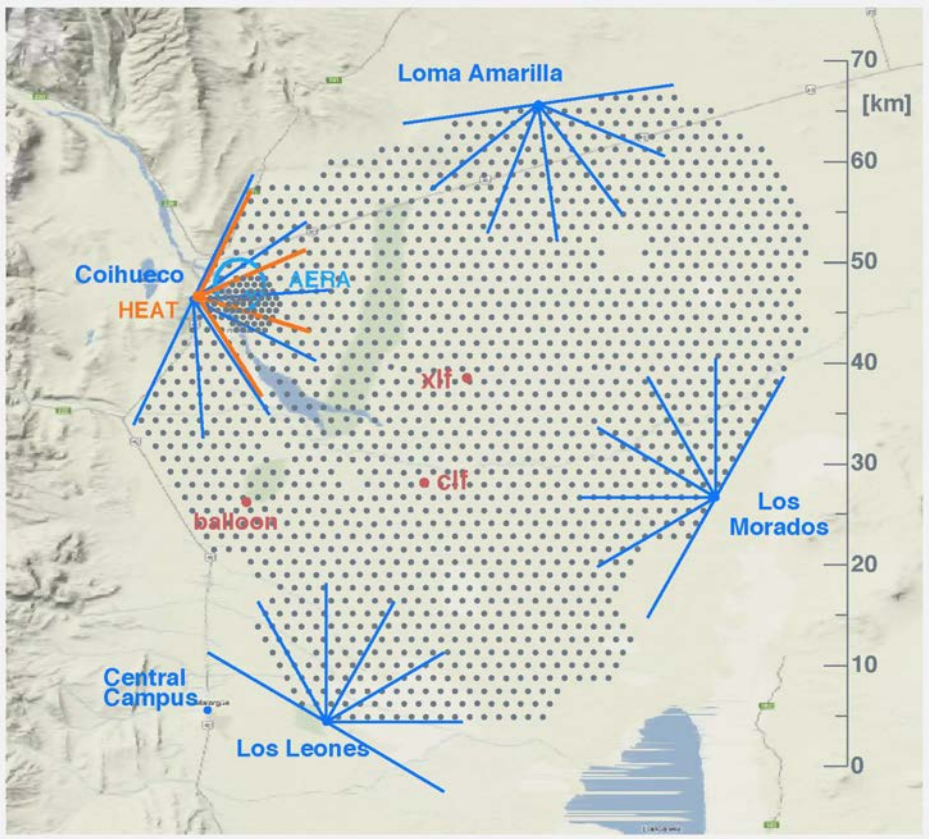

Fig. 2.1. Map of the Pierre Auger Observatory

2.2 Surface detector array (SD)

The surface detector array is comprised of 1660 stations spread over an area of 3000 km^2 [101, 77]. Detector stations are configured in a uniform triangular grid, with a spacing of 1500 m (see figure 2.1). Most of the array is situated on a plane, with an average altitude of $\sim$1400 m, though the altitude for individual stations varies between 1340 m and 1610 m. In addition to this array, there is also an infilled portion of the array, in front of the Coihueco fluorescence detector site. The infill array has 61 detectors with a spacing of 750 m, and is designed to detect lower energy showers, in conjunction with the high elevation fluorescence telescopes at Coihueco.

The detector stations are water Čerenkov detectors, with the water reservoir having a 3.6 m diameter and a height of 1.2 m [77]. The tank is composed of polyethylene, produced by rotomoulding, coloured on the outside to blend in with the environment, with a carbon black pigment on the inside to ensure light cannot penetrate. The total height of a tank is $\sim$1.6 m. Three 9 inch photomultipliers are used to pick up Čerenkov light, and are distributed symmetrically over the water at a distance of 1.2 m from the centre of the tank. The water is

contained within a liner composed of Tyvek and polyethylene films. The liner is also light tight, with a reflective interior. The liners are filled with ultra-pure distilled water, produced locally at a water plant owned by the Auger collaboration. The liner has three clear windows that the PMTs sit in. The PMTs are covered with a light tight plastic casing. Above the three PMTs, there are hatches that allow access to the inside of the tank. The hatches have light tight and water resistant coverings, with one being larger to accommodate the electronics. The stations are powered by two 55 watt solar panels feeding two 105 Ah, 12 V lead-acid batteries wired in series. The solar panels are mounted on top of the tank using aluminium brackets. The brackets also support the communication and GPS antenna mast.

Fig. 2.2. A Pierre Auger surface detector. (Image by the author).

The photomultiplier tubes have a 9 inch photocathode and eight dynode stages, designed to optimise linearity. The anode is operated at a positive voltage, with the photocathode grounded due to the proximity to water. Two signals are recorded from each PMT. One is an AC-coupled anode signal. The other is the last dynode signal inverted and amplified to give a signal with a gain 32 times higher than the anode signal. Each of the 6 channels are fed to a circuit where signals are filtered and read into 10-bit semi-flash ADCs operating at 40 MHz. The use of two signals with a gain difference of 32 gives a dynamic range of 15 bits. An LED flasher is mounted in a test port in the liner, containing two LEDs. The LEDs can be pulsed simultaneously or independently, to allow the linearity of the PMTs to be monitored.

Time synchronisation is achieved with a GPS receiver at each station, with an antenna mounted on top of the communications mast. The GPS receiver outputs a signal once per second. This, together with a custom built timing circuit, allows the synchronisation of data from the ADCs to within a 10 ns RMS. The timing signals from the GPS unit may be offset

from the true GPS time by up to 50 ns, which is periodically corrected for. A programmable logic device analyses the ADC outputs for trigger patterns, stores data in a buffer, and informs the station controller when a trigger occurs.

There are two levels of triggering that occur locally at one station [78]. The first level, T1, is set off by two possible signals. The first, a threshold trigger (TH), is if all 3 PMTs simultaneously record a signal greater than 1.6 times the VEM peak intensity (VEM being the signal equivalent to one vertical muon going through the detector). The second, called time over threshold (ToT), is when at least two PMTs record an intensity greater than 0.2 times the VEM peak for 13 time bins within 3 μs. ToT triggers occur at a lower rate than TH triggers. TH triggers are useful for inclined showers, where muon signals dominate, and may produce a pulse too short for a ToT trigger. ToT only triggers are more likely for low energy showers near the core, or high energy showers of small zenith angle at larger core distance. If a second level trigger (T2) occurs, the timing of the T2 trigger is transmitted to the central data acquisition system (CDAS). While all T1-ToT triggers automatically become T2, T1-TH triggers are only promoted to T2 level if all 3 PMTs record an intensity greater than 3.2 times the VEM peak. Since June 2013, additional triggering conditions have been added, that build upon the ToT condition, to lower the energy threshold of the SD [101]. The first method, time over threshold deconvolved (ToTd), deconvolves the signal, removing the long exponential tails from pulses before applying the ToT condition. This has the effect of reducing the influence of a single muon by compressing its signal to 1-2 time bins. The second new trigger, multiplicity of positive steps (MoPS), counts the number of time bins where at least two PMTs record an increase in signal greater than a small threshold of about 5 times the RMS noise, but smaller than about 0.5 times the size of a vertical muon step (to reduce the influence of muons). Both ToTd and MoPS require a 0.5 VEM integrated signal. There are also additional triggers for signals that are used for recording the scale of background radiation, and for calibration purposes that are only used by the station locally.

Stations must be calibrated so that signals for each station can be found in units of VEM (vertical equivalent muons) [18]. Due to the limited bandwidth available, stations must perform this calibration locally. This is done by examining background pulses from single muons. A histogram of the height of each PMT pulse is made, and the peak of this distribution is found. The gains of each PMT are adjusted so that the peak is at 50 ADC channels. A histogram of the total charge in each pulse is also found. The peak of this distribution (charge-peak) is used to convert the integrated PMT signal into units of VEM, with the relation between the charge-peak and the VEM unit found using a muon hodoscope [101] (see figure 2.3).

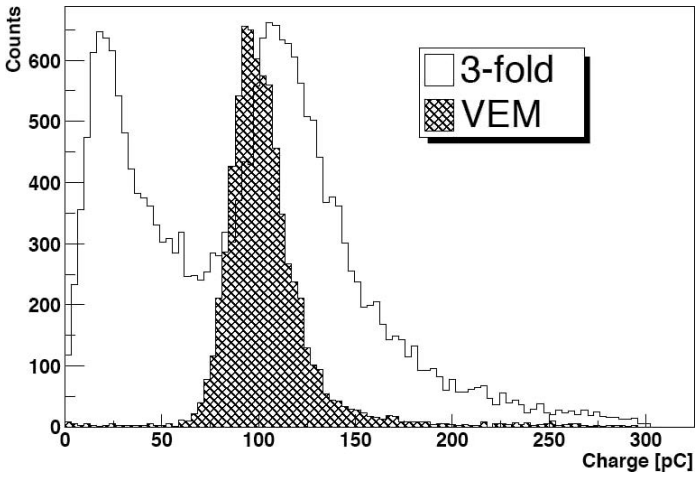

Fig. 2.3. The distribution of charges obtained from a threefold coincidence of photomultiplier triggers. The filled histogram shows the spectrum obtained when triggered by vertically aligned plastic scintillators above and below the centre of the tank, corresponding to a vertical muon, used to relate the peak of the threefold triggered spectrum to a VEM. From [101].

The surface detector stations communicate via a WLAN system, operating in a band from 902 to 928 MHz, to one of four communication towers located at the fluorescence detector stations. These towers communicate via a microwave link to the central data acquisition system (CDAS) [101]. CDAS gathers triggering data from the SD stations and decides on global triggering of the array, and collecting and storing pulses and calibration data from stations. When stations have a T2 trigger, the timing of the trigger is sent to CDAS, where triggering data from stations is combined to decide on a global trigger for the SD array, called a T3 trigger. The main T3 trigger is based on the timing and positions of station T2 triggers. For each T2 triggered station, a series of concentric hexagons of stations are defined centred on that station. If three stations are coincidentally T2-ToT, it is required that for one of the triggered stations, one of the other stations is in the first hexagon, and the third station is no farther than the second hexagon. If four stations display a coincidence of any kind of T2, one other station must be in the first hexagon, the third within the second hexagon, and the fourth may be within the fourth hexagon. A diagram of the hexagons is shown in figure 2.4. Timing is also checked, where timing of trigger must be within $(6+5n)$ μs of each other for a station in the n'th hexagon. If the T3 condition is met, a message is sent to all stations requesting trace data for any T1 or T2 triggers within 30 μs of a T2 trigger that meets the T3 criteria.

T3 triggers may also be from other criteria. There are a small number of doublet stations (two stations about 10 m apart) which cause a T3 trigger if they trigger within 1 μs of each other. A random single tank T2 is also selected about every 30 minutes and elevated to T3 for

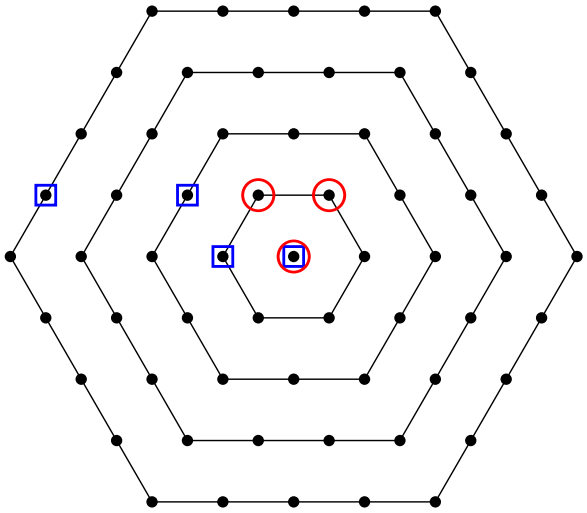

Fig. 2.4. A Diagram showing the hexagons used for SD T3 triggers. The red circles show an example of a 3-fold coincidence, and the blue squares show an example of a 4-fold coincidence. From [101].

monitoring purposes. CDAS will also receive triggering information from the fluorescence detector and will also produce a T3 trigger in order to obtain relevant information for a hybrid event.

2.3 Fluorescence detector (FD)

The main fluorescence detector of the Pierre Auger Observatory consists of 24 telescopes at 4 sites, each site having 6 telescopes covering 180 degrees in azimuth, and 30 degrees in elevation, with a minimum elevation of 1.5 degrees. The four sites sit along the boundaries of the surface detector array and overlook the stations (see figure 2.1). The northern site is named Loma Amarilla (LA), the eastern site is named Los Morados (LM), the southern site is named Los Leones (LL), and the western site is named Coihueco (CO) [97].

The telescopes are located inside climate controlled buildings. The side walls of the buildings contain the apertures through which light can enter, with a radius of 1.1 m. The aperture is covered with a filter which passes UV light. The apertures sit behind shutters, which only open when conditions are suitable for observation. Inside the aperture is a correcting lens ring to reduce spherical aberration near the edges of the aperture, with an inner radius of 850 mm. Light is focussed by a 13 m^2 mirror, of spherical shape with a radius of curvature of 3400 mm. The mirrors are constructed of smaller segments to reduce the cost and weight. The mirrors at Los Morados and Los Leones are made from 36 rectangular segments, and the mirrors at Coihueco and Loma Amarilla are made from 60 hexagonal

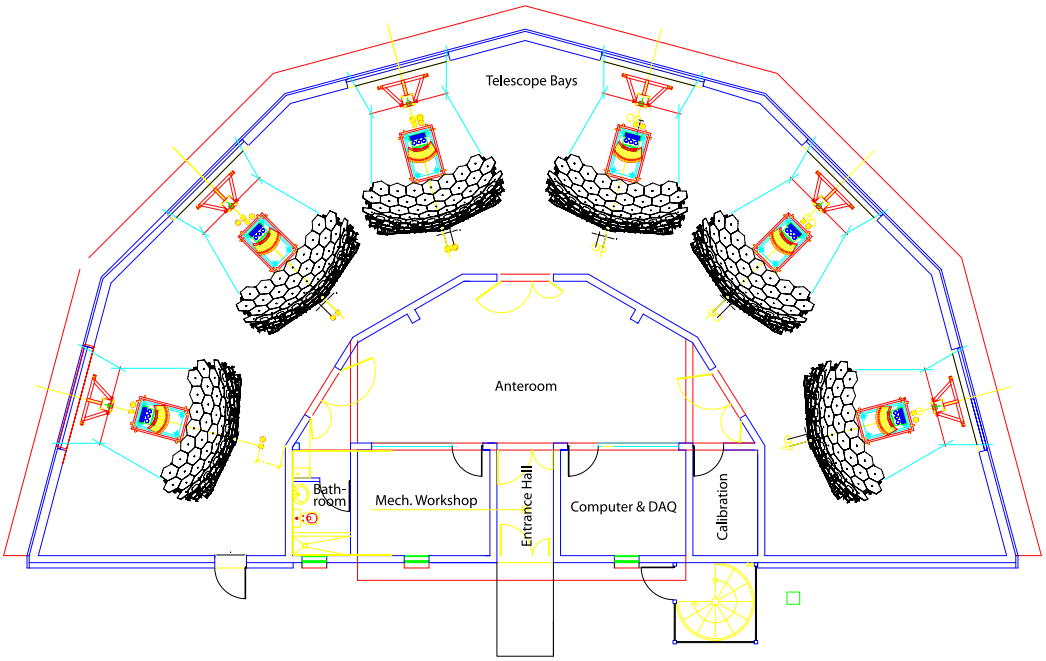

Fig. 2.5. A Schematic of a fluorescence detector station. From [97].

Fig. 2.6. A fluorescence detector station (Los Morados) in operation. Note that there are 6 telescopes at this site, but only 4 are visible due to the proximity of the camera. (Image by the author).

segments. The focal surface has a radius of curvature of 1700 mm. The camera body is machined from an aluminium block, with a curvature to match the focal surface. Each camera contains 440 hexagonal PMTs arranged with 22 rows and 20 columns. Each pixel is a hexagon with a size of about 45.6 mm. PMTs are separated by Winston cones that direct light into the PMTs that would otherwise land in between them. The camera is placed such that the focal surface is at the outer edges of the Winston cones. This gives a pixel angular size of approximately 1.5 degrees.

Fig. 2.7. One of the Fluorescence telescopes at Los Leones. The UV filter and corrector ring are visible in the upper right corner of the image. (Image by the author).

The PMTs are hexagonal with a 40 mm diameter with eight dynode stages. The power supplies for the PMTs each supply a group of 44 PMTs. Since the high voltage is adjusted to maintain the correct gain, PMTs were tested for their gain properties, and grouped in lots of 44 with similar gain properties to be used on the same high voltage supply. PMT signals are fed into analogue boards, with each analogue board managing signals from 22 PMTs. The analogue boards can fine tune the gains of each individual PMT by a factor of up to 1.9. There is also an anti-aliasing filter that is designed for the 10 MHz sampling rate of the ADC. The anti-aliasing filter is a fourth order Bessel filter with a 3.4 MHz cutoff. The final stage in the analogue circuit is designed to extend the dynamic range to 15 bits, using 12 bit ADCs. Virtual channels are made by summing the signals from 11 non-adjacent pixels, with a gain that is a factor of 20 lower than for the individual pixel channels. When a close

enough shower with a sufficiently high energy occurs, pixels may saturate, but at any given time bin, only one pixel in each virtual channel is likely to be saturated, so the saturated pixel's signal can be recovered from the virtual channel. The signals are then passed to the first level trigger (FLT) module.

Each FLT module reads in signals from one 22 channel column. Signals are digitised using a 12-bit pipelined ADC at a rate of 10 MHz. The FLT board stores the digitised signals in a circular buffer with the ability to hold 100 μs of data. This data can be read out if there is a second level trigger. A field programmable gate array is used to handle first level triggers. A moving sum of the last n ADC samples from a pixel is found, where n can be adjusted from 5 to 16, and the sum is compared to an adjustable trigger threshold level. The threshold is adjusted dynamically to give a trigger rate of 100 Hz. A moving sum going above the trigger level causes a first level trigger (FLT) in that pixel. After a pixel moving sum drops below the threshold, a retriggerable mono-flop extends the pixel trigger for a period of 5 μs to 30 μs common to all pixels, to increase the chance of coincident triggers. To analyse background light levels, the variance of each PMT is also found every 6.5 ms using 65536 consecutive ADC samples. The number of pixels above the threshold is tracked and passed on to the second level trigger board (SLT).

Each second level trigger board handles the FLTs from the 20 FLT boards from one telescope. The SLT board examines FLTs for coincident triggers of pixels. A second level trigger (SLT) requires four out of five pixels in a straight line segment to be triggered. The different allowable pixel configurations of straight line segments are shown in figure figure 2.8. A full scan of all FLTs occurs every 1 μs, with FLT information being stored in a ring buffer. The SLT board also creates the time stamp for each event, using synchronisation signals sent from the GPS module.

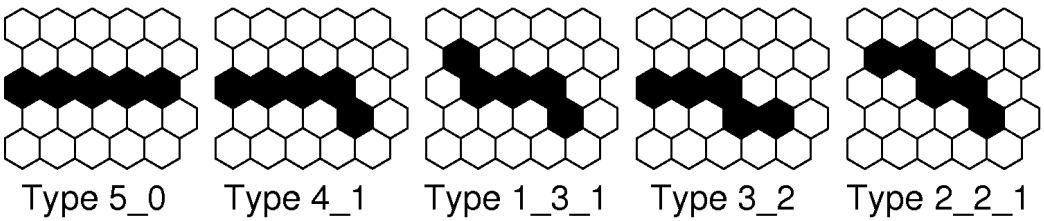

Fig. 2.8. Configurations of five triggered pixels that can cause a SLT. From [97]

Information from the FLT and SLT memory is read out by a MirrorPC. Each MirrorPC is connected to the FLT and SLT boards with a firewire interface and communicate with the EyePC via LAN. Second level triggers from air showers are processed by a third level trigger (TLT). Third level triggered showers, as well as second level triggers triggered externally, are sent to the EyePC, where an event is built and a T3 trigger is generated for the SD array. The

third level trigger examines the time evolution of the FLT multiplicity to reject background events, primarily caused by distant lightning, but also random triggers and muon impacts. This is done in less than 50 μs. A simple reconstruction of events are done to determine an approximate core location and timing, which is sent to CDAS for the T3 trigger to check surface detectors for triggers at an appropriate time.

An absolute calibration of the response of all PMTs in the FD is achieved by doing a drum calibration on each telescope [25]. A drum is placed over the aperture of each telescope to uniformly illuminate the camera (see figure 2.9). The drum contains a UV LED that can be pulsed to illuminate the drum. The drum is designed to internally scatter the light from the LED, and transmit it diffusely at a uniform intensity. The intensity of the drum is calibrated with a PMT, which itself is calibrated against a photodiode calibrated by NIST. Uncertainties resulting from all steps in this calibration result in a 9% uncertainty in the absolute calibration of the FD. This has also been checked against a calibration using vertical laser shots of known intensity.

There is also a system to monitor time variations in telescope calibration. 3 different light sources are used on each telescope for this. One is an LED mounted in the centre of the mirror which directly illuminates the PMTs. Another is a xenon flasher that is sent via optical fibres to the sides of the PMT camera, where they reflect light off the mirror and into the camera. The third source is a xenon flasher whose light is reflected off the inside of the telescope doors, and thus must also travel through the UV filter as well as reflect off the mirror to reach the PMT. A monochromator drum source was also used to calculate the relative spectral efficiency from 270 nm to 430 nm.

There are a number of systems in place for atmospheric monitoring. They include:

- In the centre of the SD array, there is a central laser facility (CLF) [9]. The CLF contains a frequency tripled YAG laser with a wavelength of 355 nm. This laser is pulsed upwards with a light output equivalent to a 100 EeV shower. The observed brightness at the detector sites allows for the atmospheric aerosol profile to be deduced so that atmospheric extinction of light from showers can be compensated for. Another similar facility, called the XLF, has also been installed further north to provide a site closer to Loma Amarilla. Some of the light from the laser is also directed into an adjacent surface detector station to assist in monitoring any time offsets between the FD and the SD. CLF shots for atmospheric monitoring are done every 15 minutes during FD operation. The beam can also be inclined to assist in monitoring of telescope pointing (this is discussed in chapter 3).

- A horizontal attenuation monitor (HAM) [96] also provides an atmospheric extinction measurement, with a high intensity discharge light source at Coihueco, and a filtered

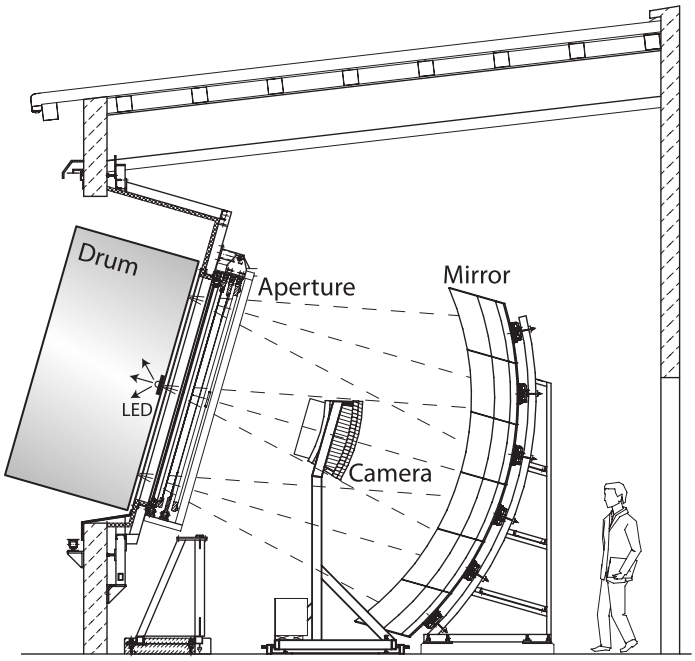

Fig. 2.9. Schematic of a fluorescence telescope showing the calibration drum mounted in front of the Aperture. From [97]

CCD camera at Los Leones, measuring extinction at five wavelengths between 350 nm and 550 nm.

- At each FD site there is a LIDAR to monitor cloud height, cloud cover, and aerosols in the atmosphere around the site (see figure 2.10) [17]. LIDAR stations can also provide ground level aerosol attenuation measurements in the direction of the CLF, and may also be used to scan the atmosphere along the SDP (shower-detector plane) of an interesting cosmic ray shower candidate immediately after it is detected.

- A Photometric Robotic Atmospheric Monitor (FRAM) [98] is installed at Los Leones, consisting of a 0.3 m diameter optical telescope to measure starlight to determine the wavelength dependence of Rayleigh and Mie scattering. FRAM also has a wider angle camera with a 4 degree field of view, that uses stellar photometry to determine atmospheric extinction along a recently detected SDP.

- Infrared cameras are installed at each FD site to monitor cloud cover, that could mask or scatter light from cosmic ray showers (see figure 2.10). The camera pans and tilts to cover the field of view of the FD every 5 minutes, and the full sky every 15 minutes [99].

- A balloon launching station (BLS) [61] is located towards the western side of the array where radiosonde launches have been performed to measure temperature, pressure, and humidity profiles, in order to validate the data from the global data assimilation system (GDAS).

Fig. 2.10. (top) The Central Laser Facility (CLF). (left) An infrared cloud camera in operation, situated on the roof of Los Leones (Image by the author). (right) A LIDAR in operation, located adjacent to Los Leones (Image by the author).

2.4 Shower reconstruction

2.4.1 SD

Reconstruction of a shower measured by the surface detector relies on both the timing and magnitude of signals recorded by the surface detector stations. Firstly, T3 events recorded by the surface detector undergo a selection process to filter out random triggers. This is primarily based on coincidences between adjacent stations having timing consistent with a

propagating shower front. Events that pass this are triggered off-line to the T4 level. Stations with incompatible timing, primarily due to random muons, are rejected as random signals. A fiducial cut is also applied to events to ensure a quality reconstruction. Typically, a cut known as a 6T5 trigger is applied, where the station with the highest signal must be surrounded by 6 operating neighbours, to ensure the event is well contained within functioning stations, and to allow for a simple calculation of detector exposure. Studies without such requirements may use a less strict cut such as 4T5 or 5T5.

To accurately reconstruct the direction of the shower, the position of the shower core must be known, since shower fronts observed with a relatively large array spacing cannot be accurately approximated as planar. Finding the position of the shower core accurately requires the direction of the shower to be known so that station distances from a shower axis can be found for a lateral distribution fit. Since the axis direction and core position fits both rely on each other, a more approximate arrival direction is first found, using a planar approximation. If there are sufficient stations, a simple spherical approximation may be used, where the shower front is approximated as a sphere expanding at the speed of light, giving:

$$c\,(t_i - t_0) = |\vec{x}_{sh} - \vec{x}_i|\,, \tag{2.1}$$

where t_i and $\vec{x}_i$ are station times and positions, and t_0 and $\vec{x}sh$ is the start time and position of virtual origin for the shower.

With this approximate direction, the core position can be found by performing a fit to the lateral distribution function (LDF) of SD station signals. The LDF fit is done using the log likelihood method, which can take into account stations that did not trigger, as well as saturated stations. The function used to fit the lateral distribution is:

$$S(r) = S(r_{opt}) \left(\frac{r}{r_{opt}}\right)^{\beta} \left(\frac{r + r_1}{r_{opt} + r_1}\right)^{\beta+\gamma} \tag{2.2}$$

where r_{opt} is an optimum distance based on the array spacing, and $r_1 = 700$m. $S(r_{opt})$ is the signal at a distance of r_{opt} [73]. For a 1500 m array spacing, r_{opt} is optimally 1000 m, making the shower size $S(1000)$, which is used to determine energy. β and γ can be free parameters if there are sufficient stations, but they may be fixed to a value based on zenith angle and shower size if there are too few stations. Once the position of the shower core is known, the direction of the shower axis can be determined. Given a shower core position $\vec{x}_{gr}$, the direction of the shower axis, $\hat{a}$, can be found:

$$\hat{a} = \frac{\vec{x}_{sh} - \vec{x}_{gr}}{\left|\vec{x}_{sh} - \vec{x}_{gr}\right|} \tag{2.3}$$

The angular resolution achieved is typically better than 1.6 degrees for showers with only three stations, down to 0.9 degrees for showers with six or more stations [22].

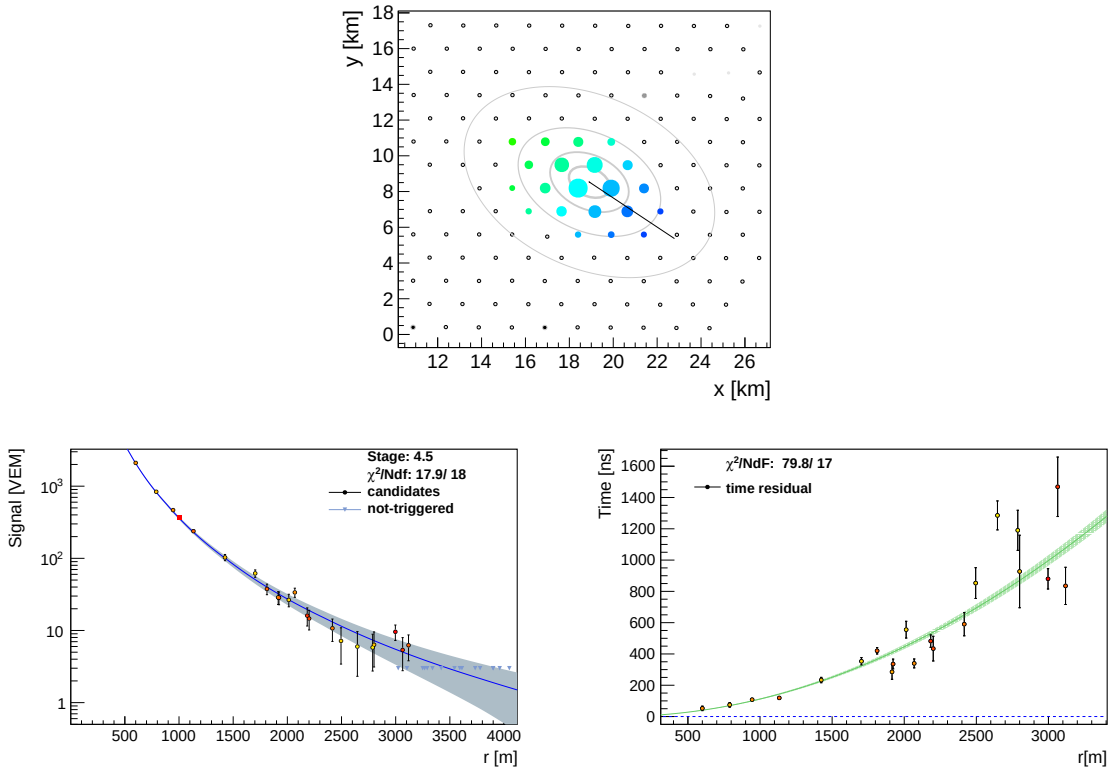

Fig. 2.11. A reconstruction of an SD event. The shower has a reconstructed energy of $(9.52 \pm 0.20 \pm 0.06) \times 10^{19}$ eV, and a zenith angle of (44.5 ± 0.1) degrees. The top figure shows a map of triggered stations coloured according to their time, and sized by signal. The direction of the axis is shown by a black line extending out from the core. The left figure is the LDF fit. The right figure is the timing fit showing the timing residual of each station from a plane fit.

After direction and $S(1000)$ has been determined, the primary energy can be determined. For a given primary energy, $S(1000)$ is dependent on zenith angle, with $S(1000)$ being lower at larger zenith angles due to particle attenuation and geometric effects. To reconstruct energy, an attenuation curve must first be found to compensate for this attenuation. The attenuation curve, $f_{CIC}(\theta)$, is determined by the Constant Intensity Cut (CIC) method [54]. In the CIC method, it is assumed that the arrival rate of cosmic rays above a given energy is not dependent on zenith angle. Given this, at a given zenith angle θ, a value for $S(1000)_{min}$ can be found such that the arrival rate of a larger shower size than $S(1000)_{min}$ is equal to a constant. Applying this constant to all zenith angles allows $f_{CIC}(\theta)$ to be found:

$$S(1000)_{min}(\theta) = f_{CIC}(\theta)S(1000)_{min}(\bar{\theta}) \tag{2.4}$$

where $\bar{\theta}$ is chosen as the median zenith angle, 38 degrees, and $f_{CIC}(\theta)$ is normalised to give $f_{CIC}(\bar{\theta}) = 1$. The fitting function used is $f_{CIC}(\theta) = 1 + ax + bx^2 + cx^3$, where $x = cos^2\theta - cos^2\bar{\theta}$. Originally the parameters a, b, and c had fixed values but have recently been updated to account for an energy dependence. a, b, and c are now expressed as a second degree polynomial in the variable $k = \log_{10}(S_{38}/40\text{VEM})$ [110]. From this $S(1000)$ is converted to a zenith angle independent version known as S_{38}:

$$S_{38} = \frac{S(1000)}{f_{CIC}(\theta)} \tag{2.5}$$

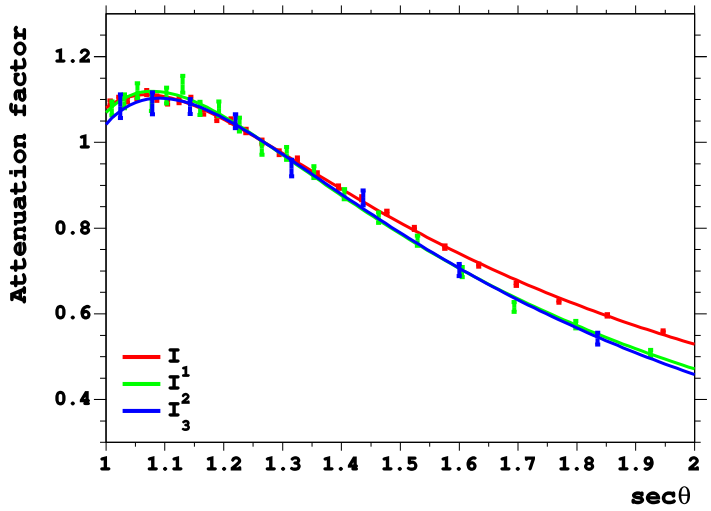

Fig. 2.12. Plot of $S(1000)$ vs $sec(\theta)$ for a constant intensity, for three intensity thresholds corresponding to approximate energies of 3 EeV (I_1), 8 EeV (I_2), and 20 EeV (I_3). From [110].

The final step is to convert S_{38} into primary particle energy. In previous surface detector experiments, the relationship between observed particle densities and primary energy would have relied on methods highly prone to systematic errors, such as shower simulations. With a hybrid detector, a subset of showers detected by the surface detector array are also detected by the fluorescence detector, and thus have an independent calorimetric measurement of energy. To obtain the relationship between energy and S_{38}, high quality hybrid events are selected, with energy above the threshold for full SD triggering efficiency. A maximum

likelihood fit is then performed using a single power law function:

$$E_{FD} = A\left(\frac{S_{38}}{\mathrm{VEM}}\right)^{B} \tag{2.6}$$

for FD energy E_{FD}. The values in use for the parameters are $A = (1.90 \pm 0.05) \times 10^{17}$ eV, and $B = 1.025 \pm 0.007$. This gives the energy determined by the SD as:

$$E_{SD} = A\left(\frac{S(1000)}{f_{CIC}(\theta) \times \mathrm{VEM}}\right)^{B} \tag{2.7}$$

The SD energy systematic error due to this method of calibration is less than 2% over the whole energy range, so the systematic in SD energy is dominated by the systematics in the FD energy scale. The energy resolution of the SD energy can also be determined using hybrid showers. By examining the distribution of $\frac{E_{SD}}{E_{FD}}$, if the resolution of the FD is known, the SD resolution can be deduced. The resolution of the SD obtained by this method is found to be $(16 \pm 1)\%$ at lower energy, and $(12 \pm 1)\%$ at the highest energies.

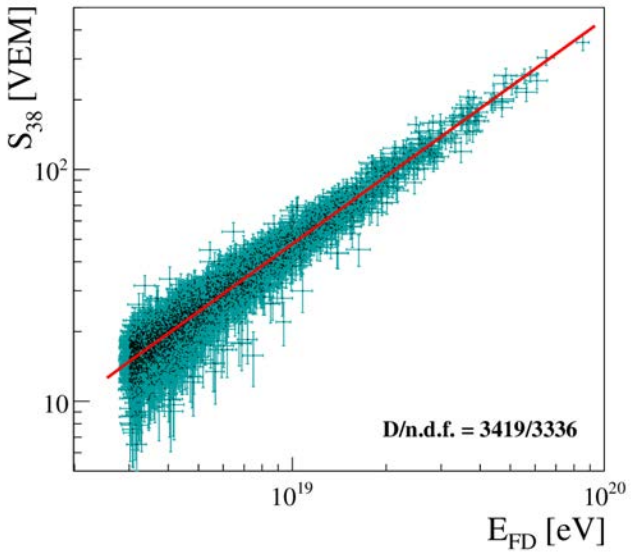

Fig. 2.13. S_{38} vs E_{FD} fit used to determine the SD energy scale. From [110].

The standard SD energy reconstruction is used for zenith angles up to 60 degrees. It is desirable to extend event reconstruction to larger zenith angles, as this can increase the exposure of the observatory by up to 30 %. This has been achieved with a separate method of reconstruction [80]. Showers with zenith angles larger than 60 degrees are called horizontal air showers. Due to the large amount of atmospheric attenuation, horizontal air shower

signals in surface detectors are dominated by muons, and much of the electromagnetic signal is muon halo (electromagnetic particles produced by muon decay and interactions). Though horizontal air shower signals are typically smaller at a given core distance when compared to vertical showers of the same energy, the density of stations in the shower plane is higher, so a large number of stations can be triggered. The lateral distribution of particles in a horizontal air shower can be highly asymmetric, due to there being significant longitudinal development between the early and late stations, as well as muon deflection due to the geomagnetic field. Geomagnetic deflection also means that the lateral distribution of particles is dependent on the azimuth of the shower axis. As a result of this, a more complex 2-dimensional lateral distribution function is used, depending on the azimuth and zenith angle of the shower. From the lateral distribution fit, the shower size parameter obtained is known as N_{19}. The relation between energy and N_{19} is found using hybrid data, with the same method as for vertical events.

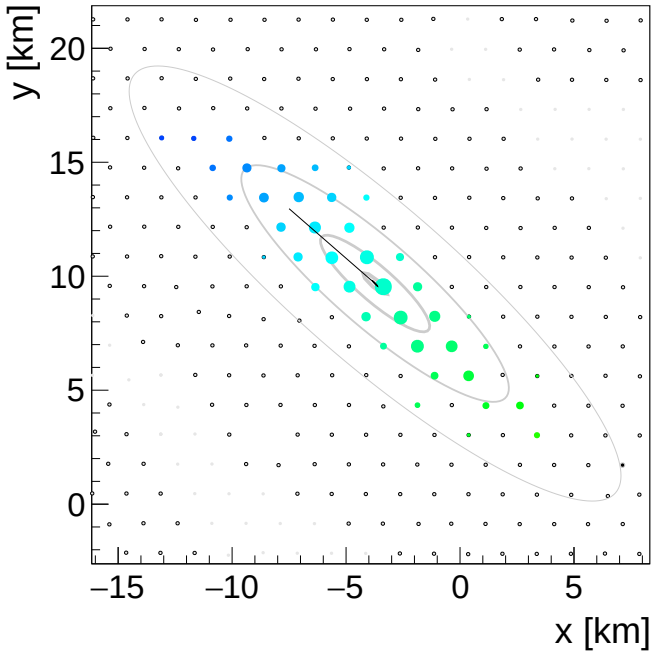

Fig. 2.14. A map of triggered stations for a horizontal air shower. The shower has a zenith angle of (75.7 ± 0.1) degrees, and an energy of $(5.2 \pm 0.26) \times 10^{19}$ eV.

2.4.2 FD

Reconstruction of a shower measured by the fluorescence detector is done in steps, starting with geometry and then continuing to profile and energy reconstruction. The geometry

reconstruction utilises both the magnitude and timing of the signals in each pixel, along with the known pointing direction of each pixel. For energy and profile reconstruction, the calibration of the fluorescence detector, and the properties of the atmosphere must be used.

First, triggered pixels have their traces examined to find a shower signal. The trace is scanned to find a start and stop time for the pulse that maximises the signal to noise ratio (SNR). A pixel is only selected for geometry reconstruction if the SNR is ≥ 5. With this start and stop time, the integrated signal for the i'th pixel is given as:

$$q_i = \sum_k s_k^i \tag{2.8}$$

where s_k^i is the charge of the k'th ADC bin of pixel i, and the sum is run from the previously determined start and stop time. The timing of the centroid of the pulse is:

$$t_i = \frac{\sum_k \tau_k^i s_k^i}{q_i} \tag{2.9}$$

where τ_k^i is the time of the k'th ADC bin. The error in t_i and q_i can be determined by considering the background variance and Poisson fluctuations in the signal.

Next, the SDP (shower-detector plane) is determined using the integrated signal in each pixel, and the pointing directions of each pixel, $\vec{p}_i$. This is done by minimising the offset of pixel pointing directions from the SDP, weighted by integrated signal. The function to minimise is:

$$S = \frac{1}{\sum_i q_i} \sum_i q_i \left(\frac{\frac{\pi}{2} - arccos(\vec{p}_i \cdot \vec{n}_\perp^{\,\mathrm{SDP}})}{\sigma_{\mathrm{SDP}}} \right)^2 \tag{2.10}$$

with the vector $\vec{n}_\perp^{\,\mathrm{SDP}}$ defined as the vector normal to the SDP. The parameter σ_{SDP} is set to allow S to be interpreted as a χ^2 function for error analysis. The value of σ_{SDP} was determined to be 0.35 degrees by studying CLF shots of known geometry. The free parameters for the SDP fit are θ_{SDP} and ϕ_{SDP}, the direction of $\vec{n}_\perp^{\,\mathrm{SDP}}$ in spherical polar coordinates.

The next step in reconstruction is to determine the geometry of the shower axis within the SDP. For this, an angle known as χ is defined for a direction within the SDP as being the angle with respect to the horizontal within the SDP. As there are two opposite horizontal directions within the SDP, the one chosen is in the direction of $\vec{n}_\perp^{\,\mathrm{SDP}} \times \hat{z}$, and the direction of $\vec{n}_\perp^{\,\mathrm{SDP}}$ is chosen (again, from 2 possible opposing directions) such that the cross product is in front of the detector (within the detector field of view). Each triggered pixel has an associated angle, χ_i. Since pixel pointing directions do not necessarily lie exactly on the SDP, pixel directions are projected onto the SDP before χ_i is determined. The geometry of the shower axis within the SDP is defined by three parameters. They are χ_0, R_p, and t_0 (see

figure 2.15). χ_0 is the angle of the direction of origin of the shower. R_p is the distance of the shower axis at its closest point to the FD. t_0 is the time at which the shower passes its closest point to the FD. The expected observation time of the shower t_i at a pixel angle χ_i is derived under the assumption that the shower propagates at the speed of light, while also considering the propagation time of light from a point along the shower axis to the FD. Consider a point S_i along the shower axis, corresponding to an angle χ_i. The distance along the shower axis relative to the shower at time t_0 is:

$$d_{S_i} = \frac{R_p}{tan(\chi_0 - \chi_i)} \tag{2.11}$$

giving an arrival time of the shower at S_i as:

$$t_{S_i} = t_0 - \frac{R_p}{c \cdot tan(\chi_0 - \chi_i)} \tag{2.12}$$

Similarly, the propagation time to the eye from S_i is:

$$t_i - t_{S_i} = \frac{R_p}{c \cdot sin(\chi_0 - \chi_i)} \tag{2.13}$$

This gives an arrival time at the eye, t_i, as:

$$t(\chi_i) = t_0 + \frac{R_p}{c} tan\left(\frac{\chi_0 - \chi_i}{2}\right) \tag{2.14}$$

The parameters χ_0, R_p, and t_0 are determined by minimising the following function:

$$\chi^2 = \sum_i \frac{(t_i - t(\chi_i))^2}{\sigma(t_i)^2} \tag{2.15}$$

Events observed by the Pierre Auger Observatory FD often have only short tracks observed. For a fit based solely on FD pixel timing and directions, there can be a large degeneracy between R_p and χ_0. This is especially true if $d\chi/dt$ does not vary greatly along the observed track. This error in geometry can be quite large, and lead to an inaccurate energy as well. Previous experiments have relied on stereoscopic observations of showers to constrain geometry. Relying on stereoscopic observations does result in a reduced exposure though, with the reduction also depending on the configuration of the FD stations. For the Pierre Auger Observatory, the large detector spacing means that showers must be of exceptionally high energy, and land near the centre of the observatory, making it unsuitable as a reliable method of geometry reconstruction.

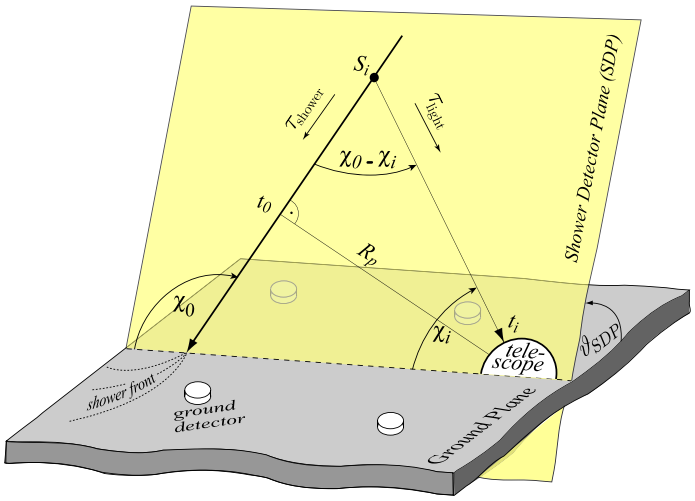

Fig. 2.15. Diagram of the coordinates used in the reconstruction of shower geometry. From [65].

The Pierre Auger Observatory solves the geometry reconstruction in a different way, that does not rely on stereo observation. Since the FD stations are situated along the edges of the SD array, and face inwards with a 180 degree field of view, most events observed by the fluorescence detector will also be picked up by the surface detector. If just one SD station is triggered, the timing of that station can constrain the geometry of the shower, significantly improving the accuracy of the timing fit. The requirement of only one SD station means that a hybrid station can be found at energies far lower than the full trigger efficiency of the SD, as the FD can provide a T3 trigger for the SD. For a given trial shower geometry, the χ angle of the shower as the shower front passes the SD station is found, χ_{SD}, and the expected time that the shower front would pass the SD station is found, $t(\chi_{\mathrm{SD}})$. The determination of $t(\chi_{\mathrm{SD}})$ must take into account a time delay due to shower front curvature. The function to minimise then becomes:

$$\chi^2 = \sum_i \frac{(t_i - t(\chi_i))^2}{\sigma(t_i)^2} + \frac{(t_{\mathrm{SD}} - t(\chi_{\mathrm{SD}}))^2}{\sigma(t_{\mathrm{SD}})^2} \tag{2.16}$$

With the geometry of the shower determined, the longitudinal profile, and hence the energy of the shower can be found. This does require the sensitivity of the detector, the atmospheric attenuation, and contribution of other light sources to be known [108]. The light flux at the detector can be found for each ADC time bin, by adding the signals in pixels detecting light from the shower. Pixels are chosen for this if they are within an angle ζ of the expected position of the shower at the corresponding time. With a profile of light observed by the fluorescence detector, the next step is to determine the energy deposit profile. The light

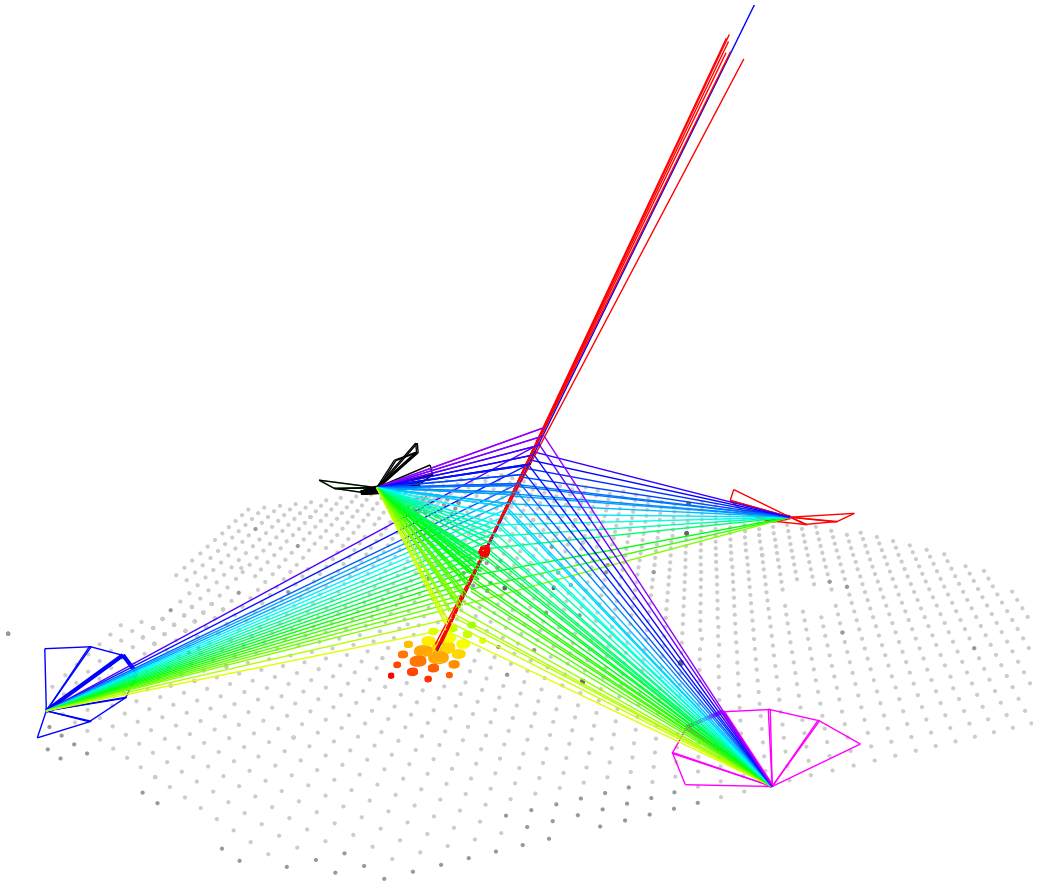

Fig. 2.16. A shower observed by all 4 FD stations. The shower energy is $\sim 8 \times 10^{19}$ eV. The lines emanating from the FD stations represent the directions of triggered pixels, coloured by the pixel timing. The red lines are the shower axes determined by the FD stations. The blue line is the axis determined by the SD. The red spots along the axes are the locations of $X_{\max}$ reconstructed by the FD stations.

observed at the detector can come from a number of different mechanisms. Fluorescence light is produced in an amount proportional to the energy deposited in the atmosphere, and is is emitted isotropically. At a given slant depth, X_i, the number of photons produced in a slant depth interval ΔX_i can be written as:

$$N_\gamma^f(X_i) = Y_i^f w_i \Delta X_i \tag{2.17}$$

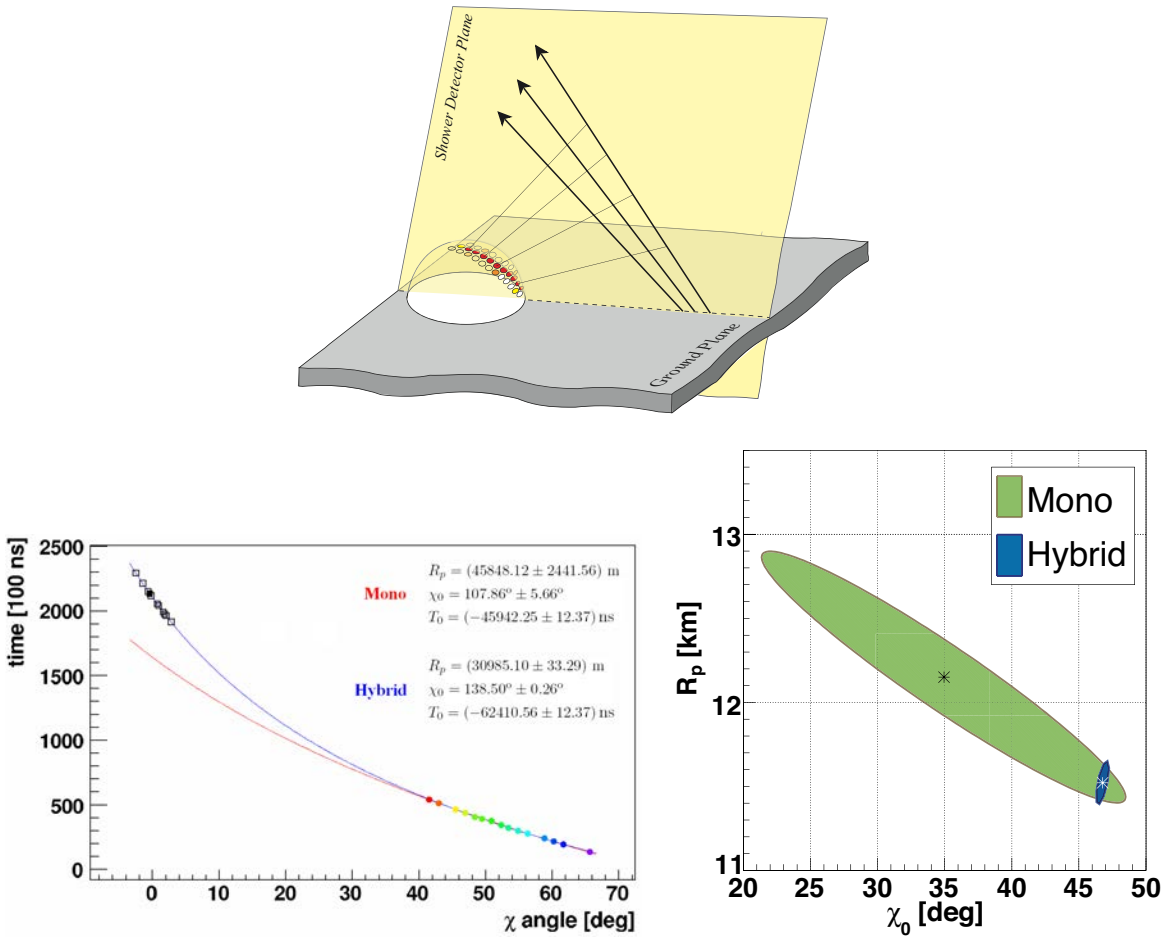

Fig. 2.17. The degeneracy in the geometry reconstruction is shown in the upper figure. The left figure shows a comparison of a mono time fit to a hybrid time fit of the same shower. the right figure shows the allowable values of R_p and χ_0 for a mono vs hybrid reconstruction.

where w_i is the energy deposited per unit depth at a depth X_i, and Y_i^f is the fluorescence yield, which is dependent on the pressure, temperature, and humidity at slant depth X_i. Taking into account atmospheric attenuation, a fraction T_i will make it to the detector. With a detector aperture area A, at a distance r_i from the detector, and a light detection efficiency ε, the measured flux of fluorescence light is given as:

$$y_i^f = d_i Y_i^f w_i \Delta X_i \tag{2.18}$$

$$d_i = \varepsilon T_i \frac{A}{4\pi r_i^2} \tag{2.19}$$

This signal, if isolated is the best measure of energy deposit, but this signal is contaminated by Čerenkov light. Due to the refractive index of air, Čerenkov light is directed in a

very narrow cone (less than 1.5°) in the direction of the particle producing it. Since the vast majority of particles in a shower lie very close to the shower axis, and are directed nearly parallel to the shower axis, the majority of Čerenkov light exists in a narrow beam close to the shower axis. With fluorescence detected showers being viewed side-on, this beam cannot be detected directly, but does contribute to the observed signal when Čerenkov photons in the beam are scattered in the direction of the detector. Both Rayleigh scattering due to air molecules, and Mie scattering due to aerosols, can contribute to this observed signal. A small fraction of particles in a shower can obtain a large transverse momentum and be directed towards the FD aperture producing a direct Čerenkov signal (see figure 2.18).

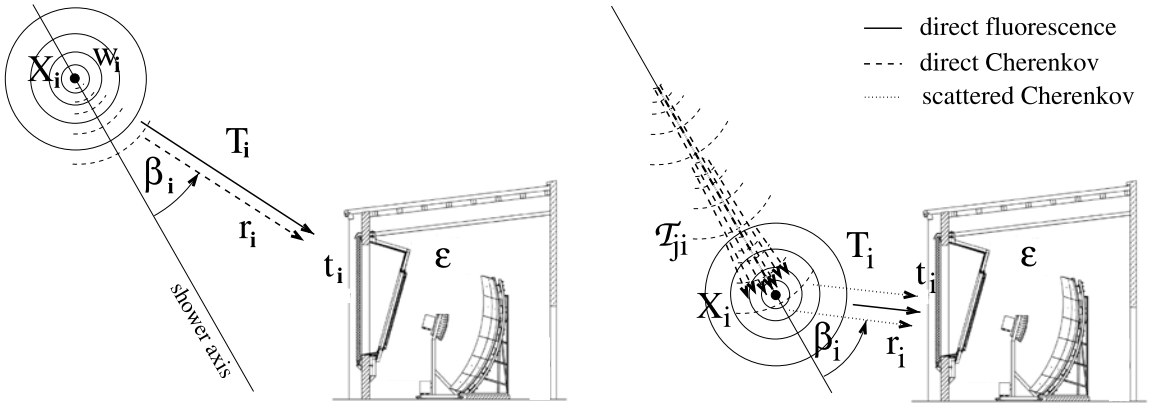

Fig. 2.18. Diagram showing the different light contributions to the observed signal. The left diagram shows the direct fluorescence and direct Čerenkov contributions. The right diagram shows the scattered Čerenkov contribution. From [108].

The direct Čerenkov contribution observed at the detector can be expressed as:

$$y_i^{Cd} = d_i f_C(\beta_i) Y_i^C \Delta X_i N_i^{\mathbf{e}} \tag{2.20}$$

where $f_C(\beta_i)$ is the fraction of Čerenkov photons emitted per unit solid angle at angle β_i with respect to the shower axis, and $N_i^{\mathbf{e}}$ is the number of electrons in the shower at depth X_i above the Čerenkov threshold energy. The number of Čerenkov photons in the beam depends on the number of electrons at shallower depths as the beam is built up as the shower progresses. The number of Čerenkov photons in the beam is:

$$N_\gamma^{\text{beam}} = \sum_{j=0}^{i} \tau_{ji} Y_j^C \Delta X_j N_j^{\mathrm{e}} \tag{2.21}$$

giving an observed scattered Čerenkov signal:

$$y_i^{Cs} = d_i f_s(\beta_i) N_\gamma^{\text{beam}} \tag{2.22}$$

where τ_{ji} is the fraction of light transmitted from the j'th position to the i'th position, and $f_s(\beta_i)$ is the fraction of photons scattered at angle β_i with respect to the shower axis per unit solid angle. From this, the total signal observed at the FD can be expressed as:

$$y_i = y_i^f + y_i^{Cd} + y_i^{Cs} \tag{2.23}$$

Since there are two unknowns that need to be deduced, energy deposit and number of electrons, and only one observable, photons at the detector, an additional assumption must be made. Since the vast majority of energy deposited in the atmosphere is by electrons, it can be assumed that the number of electrons and the energy deposit are related. This relation is found to be dependent on shower age, and is universal. With this, the solution can be written in matrix form. Let **y** be a vector of light observed at the detector y_i, and let **w** be a vector of the corresponding energy deposits w_i. The energy deposit profile can be found using the expression:

$$\mathbf{y} = \mathbf{C}\mathbf{w} \tag{2.24}$$

where **C** is the Čerenkov - fluorescence matrix [108]. The coefficients of this matrix are obtained from the above equations for fluorescence and Čerenkov light. Inverting **C** allows the energy deposit profile to be found (see figure 2.19). There is also wavelength dependence to consider. The atmospheric transmission and scattering coefficients are both dependent on wavelength, as is the detector response. To handle this wavelength dependence, this method is done in a number of wavelength bins.

The energy of the shower could be found by integrating the energy deposit profile, but this requires a very large range of depths to be observed. Since only a limited range of depth is typically observed, the energy deposit profile is fit to the Gaisser-Hillas function:

$$f_{\text{GH}} = w_{\text{max}} \left(\frac{X - X_0}{X_{\text{max}} - X_0} \right)^{(X_{\text{max}} - X_0)/\lambda} e^{(X_{\text{max}} - X)/\lambda} \tag{2.25}$$

The free parameters are w_{max}, the maximum rate of energy deposit, X_{max} , the depth of maximum energy deposit rate, and two parameters that describe the shape of the energy deposit profile, X_0 and λ. Since some showers only observe a small range of depths, the shape parameters can have a large uncertainty. This was previously handled by placing constraints on the fit to fix the values of X_0 and λ to their average values, determined from showers with

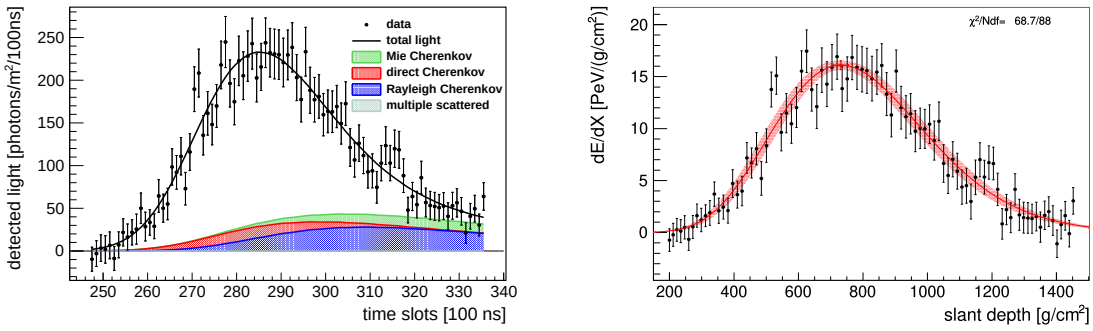

Fig. 2.19. Profile reconstruction for a shower with an energy of $1.10 \pm 0.04 \times 10^{19}$ eV. The left plot is of the light profile at the FD, showing the estimated Čerenkov contributions. The right plot is the reconstructed energy deposit profile.

a high quality profile. Recently, the Gaisser-Hillas function has been re-parameterised to the following function:

$$f_{\mathrm{GH}} = (dE/dX)_{\max} \left(1 + \frac{R}{L}(X - X_{\max})\right)^{1/R^2} (exp) \left(-\frac{X - X_{\max}}{RL}\right) \tag{2.26}$$

with L and R representing a shower profile width and asymmetry, respectively. With this new parameterisation, all four parameters (including the two shape parameters, R and L) are both fitted with loose constraints on R (0.257 ± 0.055) and L $((227.3 + 7.44 \log(E_{cal}/\mathrm{EeV})) \pm 11.5$ g cm^{-2}), with the central values determined from showers with a high quality profile, and the ranges determined from simulations to account for shower-shower fluctuations and different mass compositions [33].

Determination of the primary particle energy must also take into account invisible energy. Some of the energy in the shower goes into particles that do not deposit energy in the depths associated with atmospheric showers, such as high energy muons, and neutrinos. The invisible energy fraction is dependent on primary energy, as well as composition, and interaction model. The uncertainty due to composition and interaction model can be reduced if the number of muons in a shower is known, since the number of muons is related to the invisible energy universally. The invisible energy fraction used for the Pierre Auger Observatory reconstruction has been parameterised as a function of calorimetric energy from a combination of inclined shower reconstructions (where muon signals dominate), and also vertical golden hybrid showers, comparing SD and FD signals [104]. The invisible energy fraction used is shown in figure 2.20.

With suitable quality cuts applied, the energy resolution is 8%, and $X_{\max}$ resolution is 20 g cm^{-2}, for energies of 1-10 EeV [34].

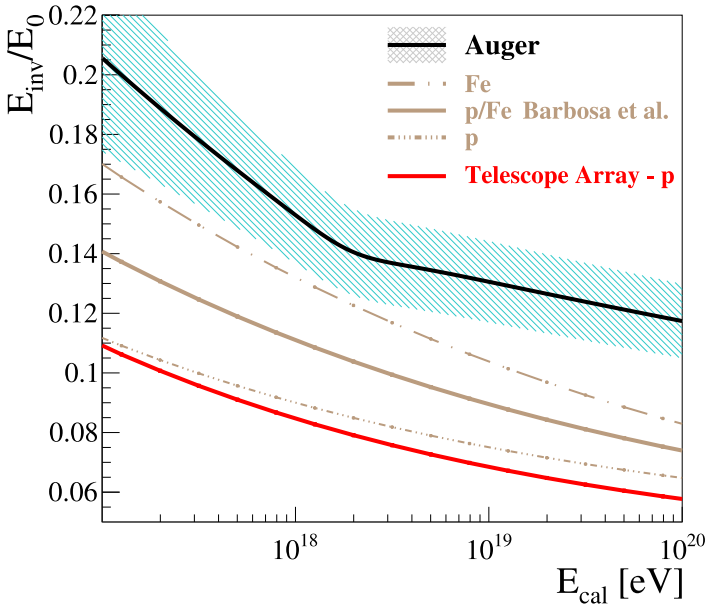

Fig. 2.20. Invisible energy parameterisation used by the Pierre Auger Observatory, determined by data-driven methods, compared to model predictions and the TA parameterisation. From [104].

The FD is capable of detecting events with a far lower energy if they are directed toward the telescope due to the high Čerenkov light emission. These events are more difficult to reconstruct, as these events are not hybrid. With the shower being dominated by Čerenkov light, even small errors in geometry can propagate into large errors in energy deposit due to the angular dependence of Čerenkov emission. To reconstruct the shower geometry, a profile constrained geometry fit (PCGF) can be used, where a fit is done simultaneously to both the geometry and energy deposit profile, with a constraint that the energy deposit profile must be compatible with a Gaisser-Hillas function [75].

2.4.3 Systematics

With many steps involved in calibration and reconstruction of showers, there are systematic errors incurred [33], which must be accounted for in the FD reconstruction, the possible sources are:

- The fluorescence yield. This includes uncertainties in the scale of the fluorescence yield, and the relative spectrum. There are also uncertainties in atmospheric conditions, such as humidity, that contribute to this uncertainty in fluorescence yield.
- Atmospheric attenuation and scattering. Uncertainties in aerosol optical depth, and atmospheric density profile, contribute to uncertainties in atmospheric attenuation and

Systematic uncertainties in energy scale	
Fluorescence yield	3.6 %
Atmospheric uncertainty	3.4 - 6.2 %
FD calibration	9.9 %
FD profile reconstruction	6.5 - 5.6 %
Invisible energy	3 - 1.5 %
SD Energy scale stability	5 %
Total	**14 %**

Table 2.1 Summary of the systematics in the energy scale. Where errors are shown as a single value, the errors are not strongly dependent on energy. Where there is a strong energy dependence, the uncertainties are given at energies of 3×10^{18} eV and 10^{20} eV. From [33].

particulate scattering. There are also uncertainties in the phase function and wavelength dependence of aerosol scattering.

- Errors in the calibration of the FDs. The steps in performing the absolute drum calibration, and also in the relative calibrations performed nightly. The optical efficiency of the telescope also contributes to this error.

- Errors in the energy deposit profile reconstruction. Some of the light from the shower is spread onto pixels that are not selected for the reconstruction by both the telescope optics, and spread of light in the shower. Uncertainties in this lead to systematic uncertainty in the energy scale.

- Invisible energy. Though this error has been reduced with muon detection studies, there is still a small uncertainty in the invisible energy fraction. Any uncertainty in the invisible energy fraction will systematically propagate onto the energy scale.

Since the SD energy scale is calibrated using the FD, the SD inherits the systematics in the FD energy scale. This also means that the SD calibration and reconstruction steps done before the calibration fit do not affect the SD energy scale systematic. There is an additional source of systematic error in the SD energy associated with the stability of the SD energy scale. Results from measuring the stability of the energy scale can be used to give an estimate of energy scale uncertainty due to stability. The total uncertainties are summarised in table 2.1.

2.5 Composition

2.5.1 FD

The fluorescence detector measures the energy deposit profile of a shower, and can determine the depth of maximum energy deposit, $X_{\max}$. $X_{\max}$ is the best available indicator for determining composition, and is used for determining the overall changes in composition at a given energy. Due to fluctuations in the first few generations of interactions, the $X_{\max}$ value of an individual event cannot be used to determine the composition of that event, but the distribution of $X_{\max}$ can be used to infer the composition of a large set of showers.

Many events observed by the FD only have a limited portion of the shower track in the field of view of the FD telescopes. Some events may also be of low quality, due to a low signal to noise ratio, high levels of aerosols, and clouds. These can result in biases in the $X_{\max}$ distribution. The Pierre Auger Observatory prevents this by applying cuts to the events used to find the $X_{\max}$ distribution, to remove events that may cause a bias [100]. The cuts that are applied are:

- Hardware status. Events are only selected if they occur during good data taking conditions. There must be a good calibration, the timing relative to SD timing must be within acceptable limits to ensure a good geometry reconstruction, and the telescope optics must be properly aligned.

- Aerosols. There must be a measurement of aerosols in the atmosphere within one hour of the observed shower. The VAOD (vertical aerosol optical depth) from the ground to an altitude of 3 km must be less than 0.1, to reduce possible biases due to poor viewing conditions.

- Hybrid geometry. For an accurate reconstruction, it is required that there is a hybrid geometry reconstruction. This also cuts events caused by spurious signals, such as distant sheet lightning.

- Clouds. Cloud layers can cause inaccurate profile reconstruction by reflecting or shadowing light. Information from lidars, the two laser facilities, the cloud cameras, and cloud data from GOES (Geostationary Operational Environmental Satellites) are used in determining if a profile is likely affected. Events are selected if no cloud is detected in the shower direction as seen by the FD station (using cloud camera data), as well as having no cloud visible in the ground level projection of the shower (seen by GOES). Sufficiently high clouds will not have a significant effect on profile reconstruction if the majority of shower light production is below the cloud layer.

Events during cloudy conditions are therefore accepted if both the lidars and the laser facilities measure a cloud height above the geometrical field of view or 400 g cm^{-2} above the fiducial field of view (fiducial field of view will be discussed shortly).

- Energy. For analysis with the standard FD telescopes (not including HEAT), an energy threshold is applied so only events with $E > 10^{17.8}$ eV are accepted. For the analysis using HeCo, the energy threshold is lowered to $10^{17.2}$ eV.

- Hybrid probability. At low energies, the SD may not trigger a detector for hybrid analysis with full efficiency. If not fully efficient, there may be composition biases, since trigger probability may be composition dependent.

- $X_{\max}$ observed. It is required that $X_{\max}$ is within the field of view of the telescope, since profile reconstructions using only the tails of the energy deposit profile may lead to inaccurate $X_{\max}$ reconstructions.

- Quality cuts. Events must have an expected $X_{\max}$ resolution of better than 40 g cm^{-2}, determined by propagating statistical uncertainties from photo-electrons in expected PMT signals, geometry, and atmospheric errors to an $X_{\max}$ uncertainty. Geometries where the shower light is observed at small angles with respect to the shower axis are also rejected, due to the large contribution of Čerenkov light, that is highly dependent on geometry, and therefore sensitive to small geometry errors, at small observation angles.

- Fiducial field of view. The fiducial field of view is defined by the minimum and maximum values of $X_{\max}$ for which a shower is expected to pass the quality and $X_{\max}$ observed cuts. The minimum and maximum observable $X_{\max}$ are referred to as X_{low} and X_{up}. The values of X_{low} and X_{up} are required to encompass the majority of the $X_{\max}$ distribution, to reduce biases caused by a differing acceptance of events with $X_{\max}$. The fiducial cuts will be further discussed shortly.

For the fiducial cuts, the values of X_{low} and X_{up} are initially not known as the true $X_{\max}$ distribution is not yet known. X_{low} and X_{up} are found for each energy bin by analysing the differential behaviour of $\langle X_{\max} \rangle$ as X_{low} and X_{up} are adjusted. The values of X_{low} and X_{up} are chosen to give a value of $\langle X_{\max} \rangle$ that is within 5 g cm^{-2} from the asymptotic value (see figure 2.21). This method produces a flat $X_{\max}$ acceptance for values of $X_{\max}$ between X_{low} and X_{up}. This leaves the $X_{\max}$ distribution with minimal detector bias, so that the $X_{\max}$ distribution can be directly compared to the distributions predicted by various composition mixes and interaction models [100].

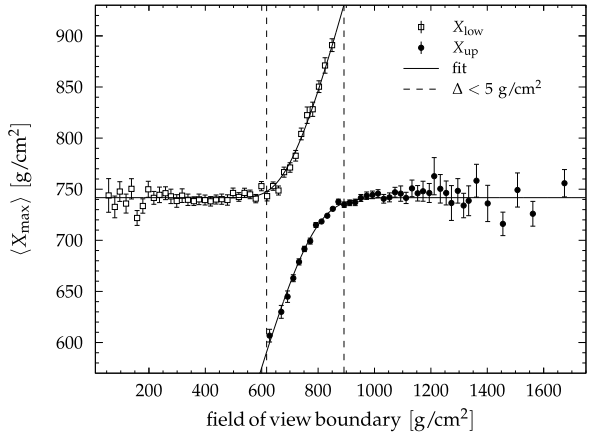

Fig. 2.21. $\langle X_{\rm max} \rangle$ for showers in the energy interval from $10^{18.1}$ to $10^{18.2}$ eV, with differing values of $X_{\rm low}$ and $X_{\rm up}$. The dashed lines indicate the chosen values of $X_{\rm low}$ and $X_{\rm up}$ corresponding to a 5 g cm^{-2} bias in $\langle X_{\rm max} \rangle$ from the asymptotic value. From [100].

For values of $X_{\rm max}$ outside of the interval from $X_{\rm low}$ to $X_{\rm up}$, the acceptance is not constant, reducing for values of $X_{\rm max}$ values farther outside the flat acceptance range. To compensate for this, the detector acceptance is determined by a detailed simulation, and events are weighted by the inverse of their acceptance (see figure 2.22).

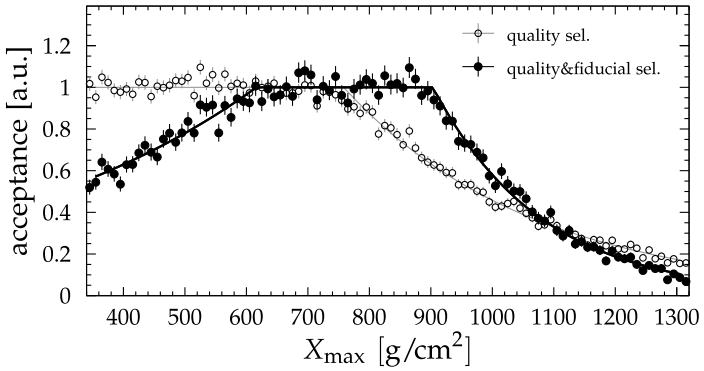

Fig. 2.22. The simulated detector acceptance as a function of $X_{\rm max}$ in the energy interval from $10^{19.0}$ eV to $10^{19.1}$ eV. The open points show the simulated detector acceptance without fiducial cuts, and the filled points show the simulated acceptance with fiducial cuts applied. Note that both have been normalized to have a peak acceptance of 1. From [100].

The simplest method for extracting overall composition information from the $X_{\rm max}$ distribution is to look at the mean and width of the distribution, $\langle X_{\rm max} \rangle$ and $\sigma(X_{\rm max})$. A heavier composition will correspond to a shallower $\langle X_{\rm max} \rangle$, with $\langle X_{\rm max} \rangle$ being linearly related to $\langle \ln A \rangle$, where A is the nuclear mass, though this is also dependent on the interaction model used. The rate of change of $\langle X_{\rm max} \rangle$ with increasing energy, known as the elongation rate, is also indicative of composition changes. For a constant composition, the elongation rate

is expected to be ~ 60 g cm^{-2} per decade in energy, and is roughly independent of the composition and interaction model.

For a pure composition, $\sigma(X_{\rm max})$ is larger for lighter composition, due primarily to the longer first interaction length, and the larger variance in the multiplicity of particles produced in the first interaction. Mixed compositions are a more complicated matter. Unlike with $\langle X_{\rm max}\rangle$, $\sigma(X_{\rm max})$ does not just depend on the average composition $\langle \ln A\rangle$, but also the variance of the composition $\sigma^2(\ln A)$. For a given $\langle \ln A\rangle$, $\sigma(X_{\rm max})$ will be the smallest for a pure composition ($\sigma^2(\ln A) = 0$), and become larger with a more mixed composition (increasing $\sigma^2(\ln A)$). For the $X_{\rm max}$ distributions obtained by the Pierre Auger Observatory, the detector resolution must be considered, as the observed $\sigma(X_{\rm max})$ will be made larger than the true value. To deal with this, the $X_{\rm max}$ resolution has been carefully studied, and the detector resolution is subtracted in quadrature from the observed $\sigma(X_{\rm max})$ to give a true $\sigma(X_{\rm max})$.

The $\langle X_{\rm max}\rangle$ for a given composition is dependent on the hadronic interaction model used, and it is uncertain which, if any, correctly predict $\langle X_{\rm max}\rangle$. Because of this, it is difficult with the $X_{\rm max}$ distribution alone to differentiate between a more pure but lighter mass composition, and a heavier but more mixed mass composition. By including data from the SD, it is possible to differentiate these cases with a lesser dependence on the interaction model. For a pure composition, a shower of a given energy with a deeper $X_{\rm max}$ will have a larger $S(1000)$, due to the shower developing closer to the ground. When considering a mixed mass composition, heavier primary particles have a higher muon content, meaning that a larger $S(1000)$ is expected. Heavier primaries will, on average, also have a shallower $X_{\rm max}$. This means that in a mixed mass composition, deeper showers can have a smaller $S(1000)$. Thus, by examining the correlation between $X_{\rm max}$ and $S(1000)$, it is possible to deduce the purity of the composition mix [81, 117]. To compensate for the dependence of $S(1000)$ on energy and zenith, and $X_{\rm max}$ on energy, the values of $X_{\rm max}$ and $S(1000)$ are scaled to a reference energy of 10 EeV, and $S(1000)$ is scaled to a zenith angle of 38°. These scaled values are known as $S^{\star}_{38}$ and $X^{\star}_{\rm max}$.

2.5.2 SD

The surface detector array offers a vastly increased data set when compared to the FD, being a factor of 30 larger at energies above 3 EeV. The surface detector does not provide a composition measure that can be directly compared with other detectors or shower simulations, like the measured $X_{\rm max}$ from the FD. The SD observations could be compared against detector simulations to infer composition, but this relies heavily on hadronic interaction models, but the models currently available do not describe showers well at the highest energies, especially when considering the muon density at the ground. Despite this, there are useful

measurements of composition information extending to higher energies than the FD can provide.

Risetime

Particles produced at different depths will take a different path to get to an off-axis detector. As a result of this, not all particles in a shower will arrive at a detector at the same time. It is therefore possible to extract information about the longitudinal development of a shower by examining the time distribution of the observed signal in a surface detector station.

The signal observed by the Pierre Auger Observatory surface detector stations consists of both a muon and electromagnetic component. Muons are typically energetic enough that they can be approximated as traveling in straight lines at the speed of light. As muons are produced very close to the core, and are not likely to be scattered traveling from their production point to the ground, the arrival time of a muon at the ground is dependent only on geometrical effects (see figure 2.23). Away from the core, the electromagnetic component consists of particles at lower energies, that are likely to undergo multiple scatterings before reaching a detector, so the electromagnetic component arrives at the detector later than the muon component.

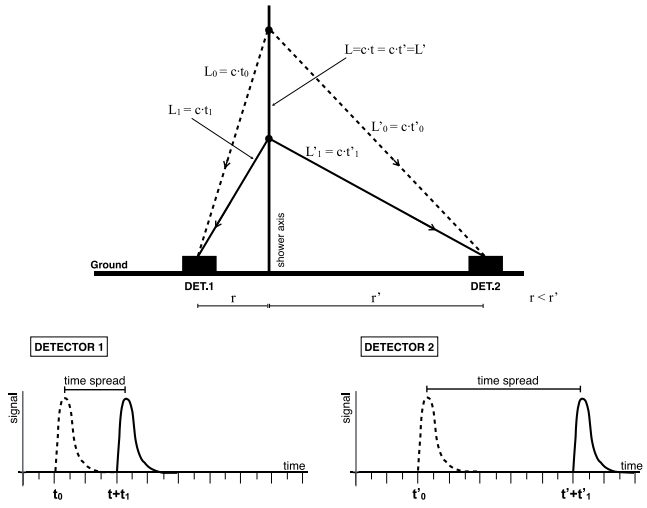

Fig. 2.23. Diagram showing the arrival time difference between muons produced at different depths. From [103].

A measure that has been found to be useful for composition analysis is known as risetime ($t_{1/2}$), the time taken for the integrated signal to increase from 10% to 50% of the final value [103, 105]. Risetime will depend on zenith angle, as the longer distance from muon production to the ground will produce smaller risetimes for more inclined showers. There is

also an asymmetry that must be accounted for, where stations with the same core distance in the shower plane will have a risetime dependent on azimuth, as stations underneath the shower axis sample an earlier part of the shower development. Most importantly, showers that develop earlier, with $X_{\max}$ occurring at a higher altitude, will have a smaller risetime when compared to a later developing shower, as the time spread of muons due to geometric effects is smaller. The last effect allows for the determination of the depth of shower development, giving a measure of composition.

Currently, risetimes measured by the SD are analysed using the Delta method. In this method, a risetime benchmark, $t_{1/2}^{bench}$ is found in a narrow energy range, as a function of zenith angle and core distance, as well as containing corrections for asymmetry. A parameterisation of the uncertainty, $\sigma_{1/2}$, is also found, using measurements from twin stations (two stations that are separated by 11 m), and pairs of stations with a similar core distance. Thus for a given station, we define Δ_i as:

$$\Delta_i = \frac{t_{1/2} - t_{1/2}^{bench}}{\sigma_{1/2}} \tag{2.27}$$

This is also illustrated in figure 2.24. For an event where there are N stations with a risetime measurement, a shower Delta, Δ_s can be obtained as an average of each of the station estimates:

$$\Delta_s = \frac{1}{N} \sum_{stations} \Delta_i \tag{2.28}$$

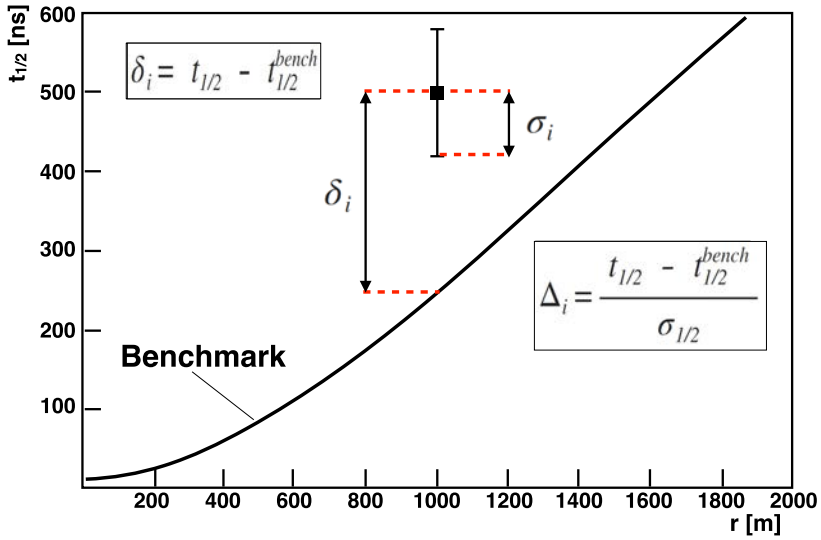

Fig. 2.24. Diagram of how Δ is obtained in the Delta method. From [103]

For the Delta method analysis, a number of selection criteria are applied to events. They are:

- 6T5. These events have the detector with the highest signal surrounded by 6 working detectors to ensure an accurate reconstruction.
- Energy cuts. There is a lower bound on energy to ensure a 100% triggering efficiency to avoid a composition related triggering bias. The lower energy bound is $10^{18.5}$ eV for the 1500 m array and $10^{17.5}$ eV for the 750 m array.
- Zenith angle. At large zenith angles, $t_{1/2}$ becomes too small for the 25 ns resolution of the FADCs. The maximum value of $sec\theta$ is 1.30 for the 750 m array. Initially the maximum $\sec\theta$ was 1.45 for the 1500 m array, but this has recently been extended to 2.0.
- Bad periods. Events from data taking periods where the array performance was not optimal are rejected.
- 3 stations. Events were required to have 3 stations that fulfilled the selection criteria for a risetime analysis. Stations were required to have signals of a least 3 VEM for the 750 m array, and at least 5 VEM for the 1500 m array. Stations must also not be saturated since the risetime cannot be determined for a saturated station.

After cuts are applied, the benchmark functions are determined. Benchmark functions are done for the low gain and high gain electronics channels separately. After testing a number of functions, the following functions are used:

$$t_{1/2}^{low-gain} = 40\text{ns} + \sqrt{A(\theta)^2 + B(\theta)r^2} - A(\theta) \tag{2.29}$$

$$t_{1/2}^{high-gain} = 40\text{ns} + N(\theta)\left(\sqrt{A(\theta)^2 + B(\theta)r^2} - A(\theta)\right) \tag{2.30}$$

$$\tag{2.31}$$

where A and B are free parameters, determined with a fit to the low gain channels. A fit to the high gain channels is then used to determine N. The benchmark fits are done in the energy range from $10^{17.7}$ eV to $10^{17.8}$ eV for the 750 m array and $10^{19.1}$ eV to $10^{19.2}$ eV for the 1500 m array. This energy range is chosen as it contains data over a good range of core distances for both low and high gain channels. An example of this fit is shown in figure 2.25. Finally, using these fits applied over numerous zenith angles, A, B, and N are parameterised

as a function of θ:

$$A(\theta) = a_0 + a_1(sec\theta)^{-4} \quad (2.32)$$

$$B(\theta) = b_0 + b_1(sec\theta)^{-4} \quad (2.33)$$

$$N(\theta) = n_0 + n_1(sec\theta)^2 + n_2 e^{sec\theta} \quad (2.34)$$

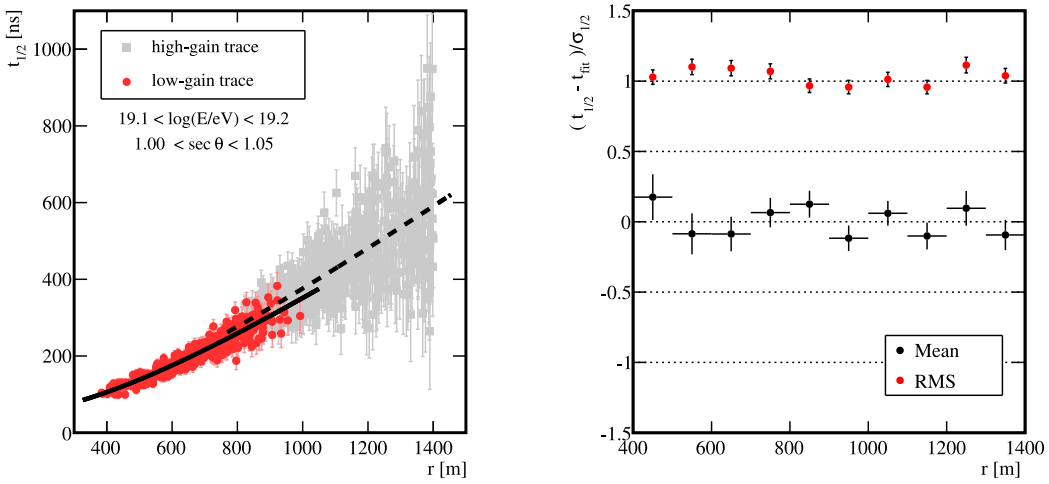

Fig. 2.25. (left) An example of a benchmark fit to risetimes. The solid line shows the fit for the low-gain trace, and the dashed line shows the fit to the high gain trace. (right) residuals to the example benchmark fit. From [103]

Muon production depth

Since muons travel in approximately straight lines at near the speed of light, the arrival time of a muon can be traced back to the production point, if the shower geometry is well known. For vertical showers, the electromagnetic component makes it difficult to do this with a surface water Čerenkov detector. For heavily inclined events, the electromagnetic component is strongly attenuated, while the muons are not. This makes it possible to determine a profile of muon production depth without the requirement for underground muon detectors[31, 70].

Muons will have a time delay relative to the plane front due to a number of possible factors, shown in figure 2.26. At larger core distances, the geometric contribution is dominant, which is desirable for determining production height. For a muon produced at a position z along the shower axis, travelling a distance l to reach the ground, they reach a point (r, ζ), where r and ζ are shower plane distance and azimuth (see figure 2.26). The muon production

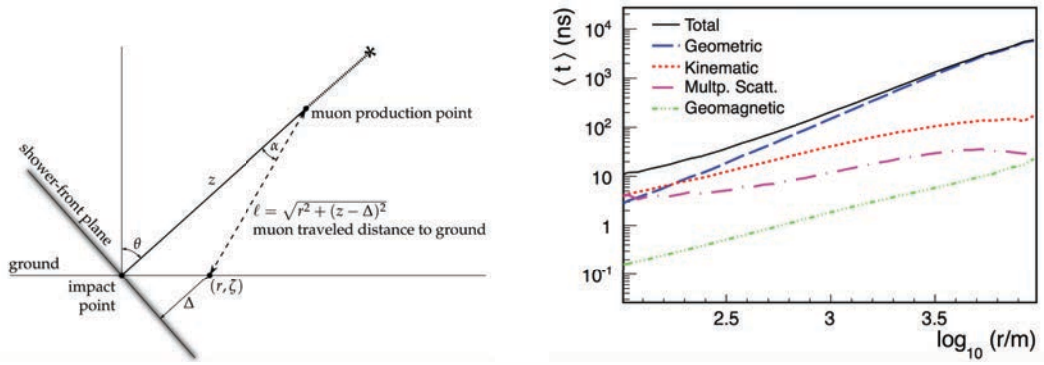

Fig. 2.26. (left) Diagram showing the geometry causing the time delay. (right) Contributions to the muon delay from the plane front, as a function of distance. From [31]

position z can be found with the following equation.

$$z \simeq \frac{1}{2}\left(\frac{r^2}{ct_g} - ct_g\right) + \Delta - \langle z_\pi \rangle \tag{2.35}$$

where t_g is the geometric delay, with:

$$t_g \simeq t - \langle t_\varepsilon \rangle \tag{2.36}$$

where t_ε is the kinematic delay due to the muon travelling slower than the speed of light. Δ is the distance from the muon ground impact point to the the shower plane, given by:

$$\Delta = r \tan\theta \cos\zeta \tag{2.37}$$

$\langle z_\pi \rangle$ is to take into account the decay length of the parent pion. The kinematic delay is dependent on the muon energy, which is not directly measurable with the surface detectors. A parameterisation is used to estimate the kinematic delay. With the muon production position determined, a muon production depth can be found:

$$X^\mu(z) = \int_z^\infty \rho(z')\mathrm{d}z' \tag{2.38}$$

The distribution of muon production depth (MPD) contains information about the development of the hadronic component of the cascade. The maximum of this distribution is known as $X^\mu_{\max}$, and can be used similarly to $X_{\max}$, measured with the FD.

Due to the time resolution of the detector, and the large contribution of kinematic delay, core distances smaller than 1200 m are not used. At small zenith angles, this could introduce a bias, since the muons produced deeper are produced close to the ground and will not spread

out to large core distances. For more inclined events, almost all muons are produced far from the ground, and cover a large area on the ground.

The Function used to fit the MPD distribution is:

$$\frac{\mathrm{d}N}{\mathrm{d}X} = \left(1 + \frac{R}{L}(X - X^{\mu}_{\max})\right)^{R^{-2}} \exp^{-\frac{X - X^{\mu}_{\max}}{LR}} \tag{2.39}$$

for a total number of muons produced N, at depth X. $X^{\mu}_{\max}$, R, and L are the fit parameters. Due to the small number of muons detected ($\sim$50 at $10^{19.5}$ eV), the parameter R is fixed, and L is given an initial value. The R and L values used are dependent on zenith angle, so a parameterisation is used for the fits. To take into account a dependence of $X^{\mu}_{\max}$ on zenith angle, the value of $X^{\mu}_{\max}$ for each event is normalised to $\langle\theta\rangle = 55^{\circ}$.

A number of quality cuts are applied to ensure reliable MPD reconstructions. They are:

- 6T5. The detector with the highest signal must have all six closest neighbours operating, to ensure a good reconstruction.
- Number of stations. At least 5 stations with a signal greater than 3 VEM must contribute to the reconstruction, to avoid trigger fluctuations, and to minimise the impact of accidental signals.
- Fit uncertainty. The MPD fit must converge and have an uncertainty $\delta X^{\mu}_{\max}/X^{\mu}_{\max}$ smaller than a certain threshold $\varepsilon_{\max}$. This value varies from 28 % at low energy, to 18 % at the highest energy.
- L. The value of the parameter L must be between 130 g cm^{-2} and 415 g cm^{-2}. Values outside of this range are associated with the first part or the tail of the MPD being very poorly reconstructed.

2.6 Upgrades

2.6.1 High Elevation Auger Telescopes (HEAT)

The standard FD configuration, observing elevations of up to 30°, is well suited to observing the highest energy showers. At energies below $\sim 10^{18}$ eV, showers can only be observed at a close distance. At a close distance, the standard FD will only observe a limited range of depths, with $X_{\max}$ being above the field of view. HEAT was added to the observatory to extend the field of view of the FD to a 60° elevation, extending the range of observable energy down to $\sim 10^{17}$ eV [101, 63].

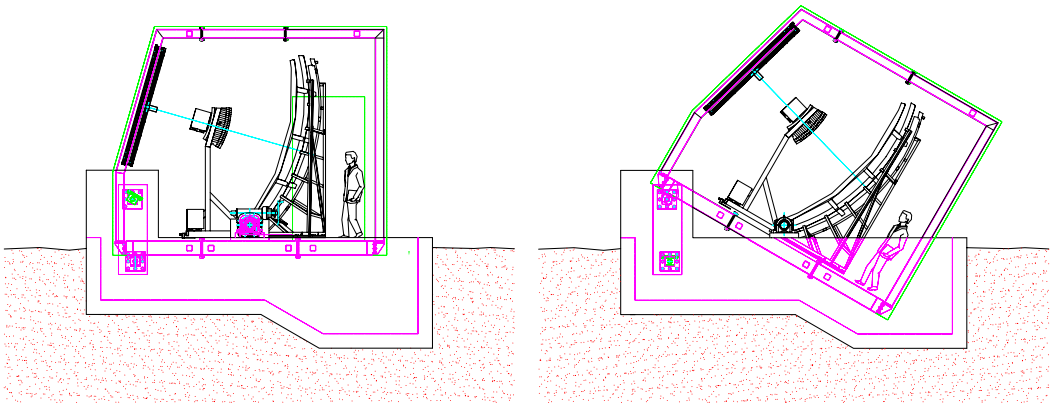

Fig. 2.27. Diagram of HEAT in horizontal mode and in tilted mode. From [101]

Fig. 2.28. HEAT in operation. (Image by the author).

HEAT consists of three telescopes similar in design to the other FD telescopes, with one container for DAQ, slow control, and calibration hardware. One notable difference is that the electronics are capable of sampling at up to 40 MHz, compared to 10 MHz for the other FD telescopes, to better reconstruct showers with high angular velocities. Each telescope is housed in a separate building, located 180 m away from Coihueco (see figure 2.28). The buildings can be tilted using a hydraulic system (see figure 2.27). The telescopes are kept in the horizontal position to allow maintenance, and to allow for a cross calibration with Coihueco. HEAT is designed to operate normally in the tilted mode, observing elevations

up to 60°. HEAT is designed to be used in conjunction with the infilled array of the surface detector, allowing fully efficient hybrid triggering at low energies. HEAT began operations in 2009.

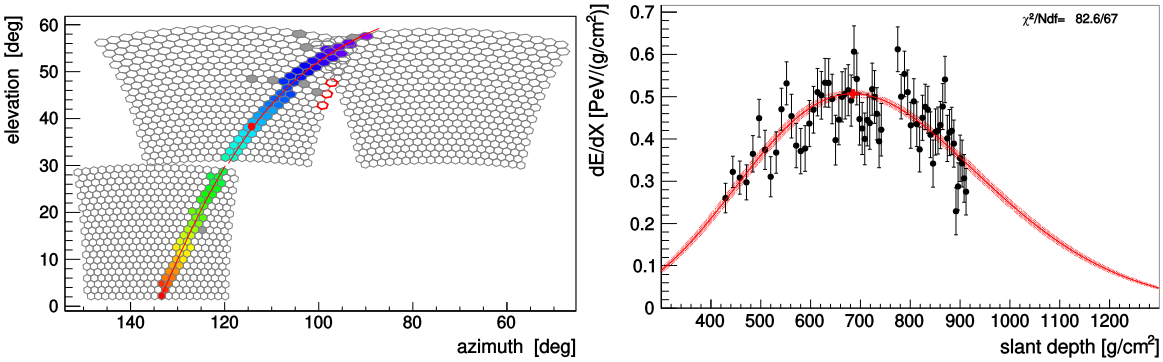

Fig. 2.29. A $3.72 \pm 0.18 \times 10^{17}$ eV shower seen by Heat and Coihueco.

2.6.2 AugerPrime upgrade

A series of upgrades are being applied to the Pierre Auger Observatory [102]. The main motivation for this is to determine the composition mix at the very highest energies. A much larger dataset is required than the current set available with the FD. The best way to substantially increase the number of events with composition measurements is to make the surface detector sensitive to composition. The upgrades include scintillation detectors on top of every SD station for μ-EM discrimination, improved electronics for the SD array, buried muon detectors in the infilled array for direct measurements of muon content, radio detection for inclined showers, and a new operation mode for the FD to increase duty the cycle.

Auger Muon and Infilled Ground Array (AMIGA)

AMIGA is a detector designed to directly measure the muon content of extensive air showers [101, 23]. It consists of a denser array of water Čerenkov surface detectors (known as the infilled array), and a series of buried scintillator detectors. The infilled array is nested within the 1500 m array, with a spacing of 750 m, and is situated 6 km in front of Coihueco, to allow hybrid reconstruction at lower energies for HEAT. The infilled array is fully efficient down to 3×10^{17} eV for zenith angles below 55°. The area of the infilled array is 23.5 km^2. Though this area is small, the flux of cosmic rays increases rapidly with decreasing energy, so the event rate at lower energies is more than adequate. An additional array has also been

constructed with a 433 m spacing covering an area of 1.9 km^2, lowering the energy threshold down to $10^{16.5}$ eV.

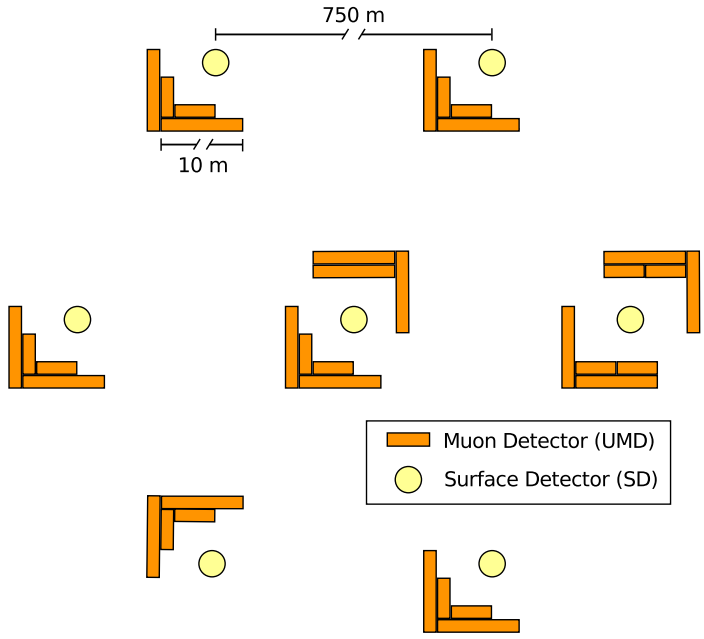

Fig. 2.30. Map of the AMIGA engineering array. From [23].

Adjacent to each SD station in the infilled array, 30 m^2 of plastic scintillators will be buried underground, to be sensitive only to muons. These are currently undergoing testing, with units installed at 7 stations operating since March 2015. The plastic scintillators are buried under 2.3 m of soil corresponding to $\approx$ 540 g cm^{-2} of vertical mass overburden. This means that there is a cutoff of 1 GeV for vertical muons. The 30 m^2 of scintillators at each station is made up of 10 m^2 and 5 m^2 units. Each unit is made up of 64 polystyrene strips 4.1 cm wide and 1.0 cm thick. Each strip has a wavelength shifting optical fibre to direct the light to a photo-detector at the center of the module. For detection of the scintillation light, 64 channel multi-anode PMTs, and arrays of 64 silicon photomultipliers (SiPMs) were tested, with the SiPMs being chosen for production. Two of the stations have two sets of 30 m^2 stations, to analyse the experimental accuracy of the detectors. There is also an additional 20 m^2 detector buried under 1.2 m of soil to better analyse the shielding properties of soil.

Each photomultiplier and SiPM channel is digitised at 320 MHz with just 1 bit per channel, being either 1 or 0 depending on whether the signal is above a set threshold. With the detector being highly segmented, and with a fast readout the detectors act as muon counters. Counting muons means that there is no need to carefully calibrate the gain of each detector. Signals from the muon detectors are transmitted via a dedicated system based on a

WiFi 802.11g standard. Data from the muon detectors is sent to CDAS only when there is a T3 trigger.

Radio research program

Individual particles in an air shower will often travel at a speed very close to the vacuum speed of light, producing Čerenkov light. Čerenkov light emission is proportional to λ^{-2}, so most Čerenkov emission is expected near the shortest wavelengths for which the medium refracts light (typically UV wavelengths). Čerenkov emission at radio wavelengths due to individual particles would be expected to be virtually impossible to detect. However, in a cosmic ray shower, there can be a charge excess induced at the shower front, also travelling at very near the vacuum speed of light. At wavelength scales longer than the size of the charge excess, the charge excess acts like one particle with a very large charge. With Čerenkov light emission also being proportional to q^2, where q is the charge, Čerenkov emission is greatly boosted at longer wavelengths. This charge excess can be caused by photons in the shower front scattering electrons from air molecules. This is known as the Askaryan effect [11]. Magnetic deflection of shower particles can also form charge excesses perpendicular to the direction of shower propagation. The formation of these charge excesses also mean that electric currents will be produced in a shower. The electric currents also produce electromagnetic radiation at radio wavelengths. Recent studies have found that the geomagnetic deflection of shower particles is the dominant source of radio emission in extensive air showers, though the Askaryan effect must still be accounted for [79]. Radio detection of extensive air showers is possible during both day and night, and is not dependent on weather. Radio detection is primarily sensitive to the electromagnetic component of a shower, and can be used to determine a longitudinal profile.

A test array, known as the Auger Engineering Radio Array (AERA) has been constructed, and has been measuring the radio properties of extensive air showers [102]. AERA consists of 153 stations, spread across an area of 17 km^2 (see figure 2.31). Each station has a dual polarisation antenna, able to observe electric fields in the north/south and east/west direction. Nine stations also have a vertically aligned antenna. AERA stations are sensitive between 30 and 80 MHz, chosen due to this range being fairly radio quiet. AERA is capable of a self-trigger, as well as an external trigger.

Since the radio emission is highly forward directed, vertical air showers have only a very small radio footprint on the ground, requiring a very dense array to detect air showers. For highly inclined showers, the long distance from $X_{\max}$ to the ground means that the radio footprint is very large, making radio detection possible with a large array spacing [46]. As part of the Auger Prime upgrade, radio detectors will be placed on all of the surface detector

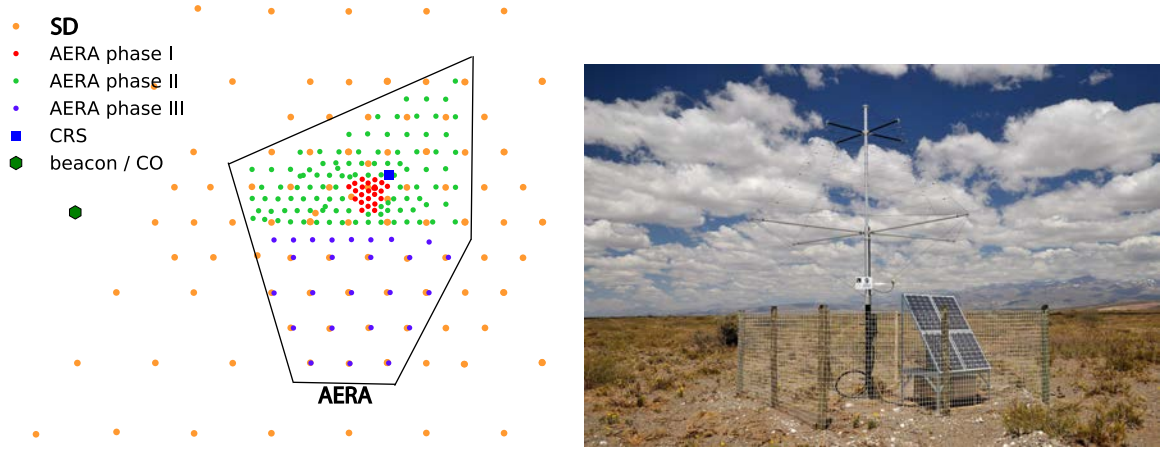

Fig. 2.31. (left) Map of AERA. (right) Picture of an AERA station. From [102].

stations [83]. This will allow for measurements of both the electromagnetic (radio) and muonic (SD) component for inclined air showers, while the surface scintillation detector provides this for vertical events. A 1.2 m diameter short aperiodic loop antenna (SALLA) will be installed on top of each SD station, with electronics integrated with the other detector components (see figure 2.32). The energy threshold for full efficiency is dependent on zenith angle, ranging from $10^{18.3}$ eV for the highest zenith angle, and increasing with decreasing zenith angle.

SD station upgrades

A number of upgrades to the surface detector array are being undertaken, to allow for better mass composition sensitivity for the SD array. As well as the previously discussed radio detector, a small PMT will be added to the WCD, and a scintillation detector will be installed above the detector.

It is desirable to extend the dynamic range of the water Čerenkov detector (WCD), to allow measurements to be made closer to the shower core [74]. Near the center of the tank, there is a 30 mm window in the liner, originally intended for a spare LED. A small PMT (SPMT), with a much smaller cathode can be placed over this window. The SPMT will have a greatly reduced sensitivity compared to the 3 large PMTs (LPMTs). The SPMT is not sensitive enough to record a single muon, so a calibration based on a VEM is not possible. Instead, the SPMT will be cross-calibrated to the LPMTs using pulses that are below the saturation threshold for the LMPTs low gain channel.

The electronics are also being upgraded for the surface detector stations, with a factor of 10 increase in processing power and memory, allowing for the handling of the additional

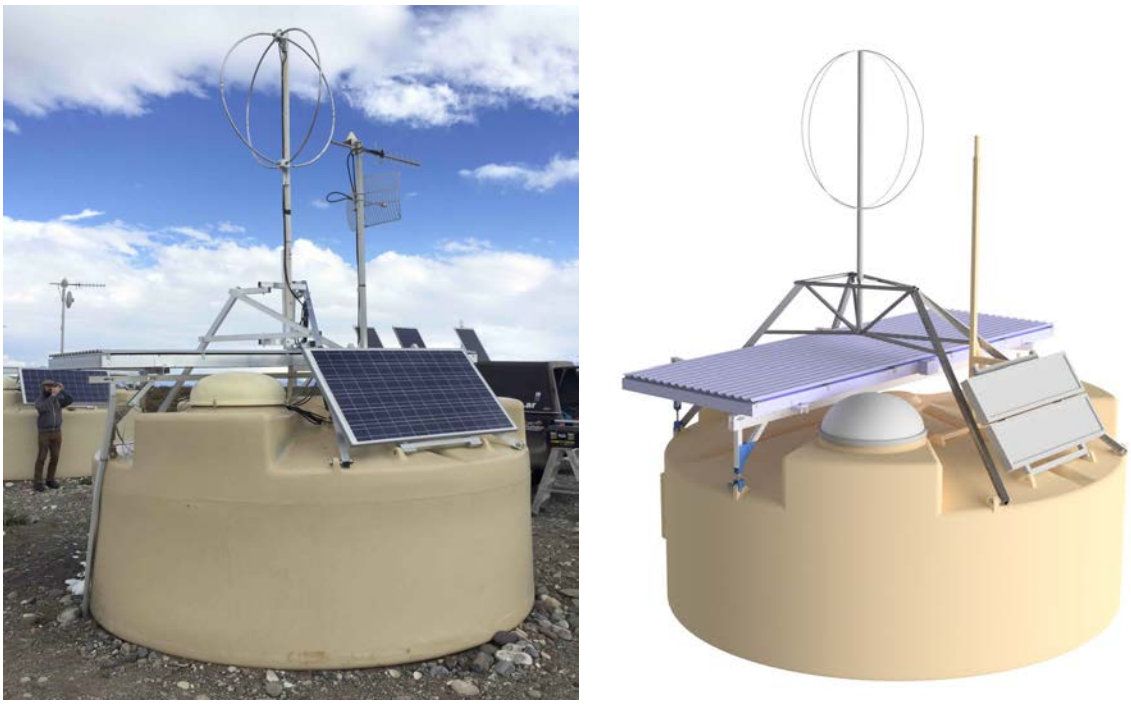

Fig. 2.32. An upgraded SD station. From [83].

hardware, as well as more advanced local processing. The ADCs for the surface detector are also being upgraded, operating at 120 MHz as opposed to the original 40 MHz. The LPMT high gain channel was previously derived from the last dynode stage, but this signal is too noisy for the upgraded dynamic range, so both low and high gain signals will be derived from the anode with two parallel amplifiers. The dynamic range of the upgraded stations will be extended to 20,000 VEM.

The most significant upgrade to the SD station is the scintillator surface detector (SSD) [82, 102]. To provide better composition sensitivity, it is desirable to be able to separate the electromagnetic and muon component from each other. After a number of proposals were evaluated, it was decided that the best way to achieve this is by placing a scintillator on top of the existing WCD. The WCD is more sensitive to muons than it is to the electromagnetic component, whereas the scintillator is equally sensitive to both muons and electrons. With the electron density being higher than the muon density for vertical showers, the scintillator is more sensitive to the electromagnetic component of a shower. A combination of WCD and SSD signals allows for the two components of the air shower to be disentangled. The SSD is composed of 48 plastic bars of dimensions 160 cm long, 5 cm wide, and 1 cm thick. The scintillators are surrounded by a layer of reflective TiO_2. Wavelength shifting fibres are used to direct light into a single PMT. The detector area of the SSD is approximately 3.84 m^2

(see figure 2.33). The PMT signal is split to a high and low gain channel, with a gain ratio of 128. Each channel is digitised with a 12 bit 120 MHz ADC. Calibration is achieved in a similar fashion to the WCD, by measuring signals from single particles passing through the detector. The units in this case are MIPs (Minimum Ionising Particles). The dynamic range of the SSD extends to 20,000 MIP. The SSD is mounted on top of the detector with a rigid aluminium frame (see figure 2.32). Deployment of the SSDs should be completed in 2020.

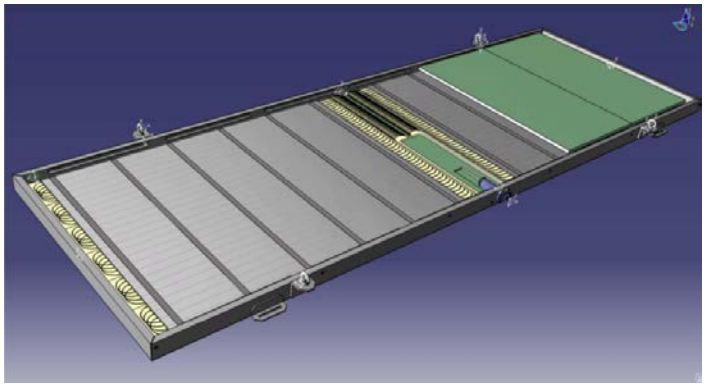

Fig. 2.33. Drawing of an AugerPrime SSD. From [82].

Extended FD operation

The FD is capable of the most direct measurement of the energy deposit profile, but suffers from a big problem. The duty cycle of the FD is approximately 15 %, as operations currently only occur on dark, moonless nights. Excessive levels of background light, with high anode currents, can lead to the deterioration of the PMTs.

If FD operation can be extended into periods with higher night sky background, when the moon is up or during twilight, the duty cycle may be increased by up to 50 % [102]. To compensate for the high night sky background, the high voltage supply can produce a lower voltage, reducing the gain of the PMTs. This does reduce the sensitivity of the detector, meaning only the highest energy events are detected, but the upgrade is primarily to increase the number of events at the highest energy, so this operation mode is still very useful. Tests of this show good quality data can be obtained at energies above $10^{19.5}$ eV, and that the PMTs will not be aged to an excessive degree. With the higher allowed night sky background, the FD duty cycle will be increased to a theoretical maximum duty cycle of 29 % up from 19 % (these do not take into account weather and malfunctions).

2.7 Current results

2.7.1 Energy Spectrum

There are a number of different spectrum measurements, covering differing energy ranges. The largest exposure belongs to the 1500 m SD array for vertical events, with an exposure greater than 60,000 km^{2}sr yr, covering energies above $10^{18.4}$ eV. The spectrum obtained with the 1500 m SD array has also been unfolded to compensate for energy resolution effects. Results are shown in figure 2.34. The spectrum shows the transition at the ankle and the cutoff at high energy. The spectrum is best described with an additional transition between the ankle and the cutoff, with the J_{1234} function, as opposed to the $J_{12\Delta}$ function describing a smooth transition in the spectral index from the ankle to the cutoff.

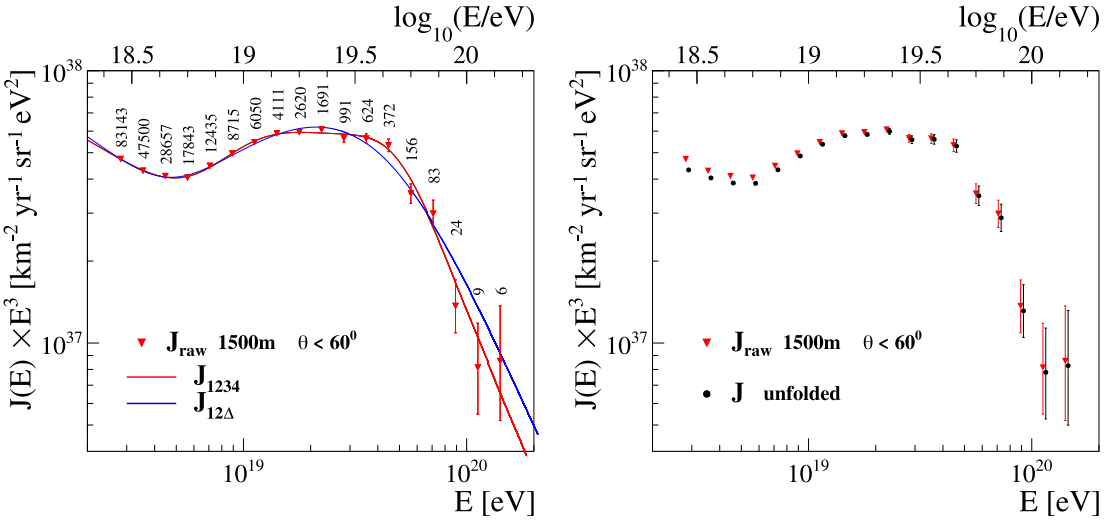

Fig. 2.34. (left) The energy spectrum measured by the SD. (right) The SD energy spectrum unfolded to compensate for energy resolution effects. From [110].

The data from the other observation modes of the observatory can also be combined with the 1500 m SD vertical results to extend the energy range and exposure [110]. The additional modes are:

- SD horizontal air showers, with $\theta > 60$ deg. This has the second largest exposure, at 17,447 km^{2}sr yr, and covering energies above $10^{18.6}$ eV.
- FD hybrid, with an exposure of 2248 km^{2}sr yr at 10^{19} eV (increasing with increasing energy), and a minimum energy threshold of 10^{18} eV.
- SD 750 m array, with an exposure of 105.4 km^{2}sr yr, and a minimum energy threshold of 10^{17} eV.

- FD Čerenkov events, with PCGF used for geometry and energy determination. The exposure for this mode is just 2.86 km^{2}sr yr, but with a minimum energy threshold of $10^{16.5}$ eV.

The results of these observation are shown in figure 2.35.

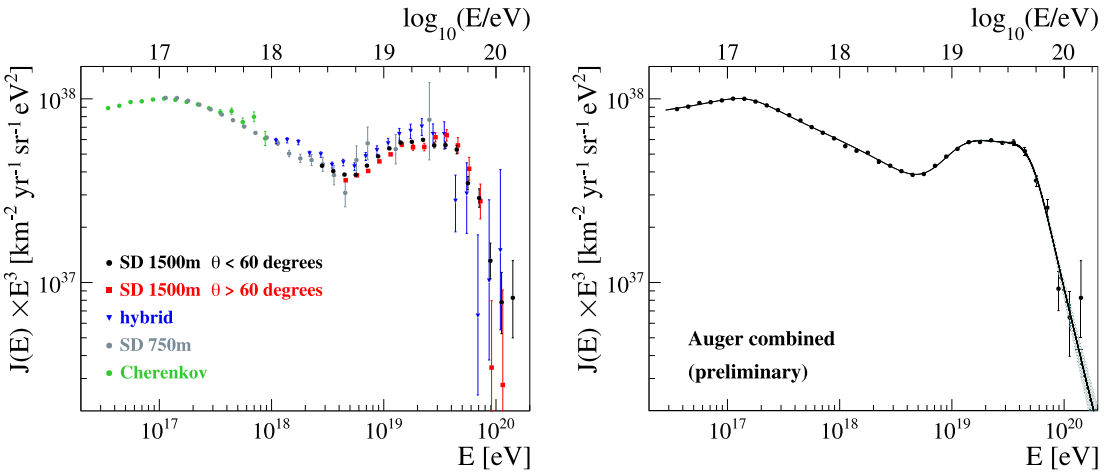

Fig. 2.35. (left) The energy spectrum of the different observation modes. (right) The combined energy spectrum, with a J_{01234} fit. From [110].

With the extension into lower energies covering the second knee, the spectrum is well described by a J_{01234} fit, with changes in spectral index at the second knee, ankle, and cutoff, as well as the additional change between the knee and cutoff. The equation for this fit is:

$$J_{01234} \propto E^{-\gamma_0} \frac{1+(E/E_{01})^{\gamma_0}}{1+(E/E_{01})^{\gamma_1}} \frac{1+(E/E_{12})^{\gamma_1}}{1+(E/E_{12})^{\gamma_2}} \frac{1+(E/E_{23})^{\gamma_2}}{1+(E/E_{23})^{\gamma_3}} \frac{1+(E/E_{34})^{\gamma_3}}{1+(E/E_{34})^{\gamma_4}} \tag{2.40}$$

The values of the parameters are: $E_{01} = 0.15 \pm 0.02$ EeV, $E_{12} = 6.2 \pm 0.9$ EeV, $E_{23} = 12 \pm 2$ EeV, $E_{34} = 50 \pm 7$ EeV, $\gamma_0 = 2.92 \pm 0.05$, $\gamma_1 = 3.27 \pm 0.05$, $\gamma_2 = 2.2 \pm 0.2$, $\gamma_3 = 3.2 \pm 0.1$, $\gamma_4 = 5.4 \pm 0.6$. These results are the first to show the point of inflection at $\sim$12 EeV, between the ankle and the cutoff.

Comparing the Pierre Auger energy spectrum results to those obtained by Telescope Array, there is a notable discrepancy between the two, as seen in figure 1.8. With one of the experiments being in the southern hemisphere and one in the northern hemisphere, differences due to anisotropy have been considered, by comparing spectra in a common declination band, observed by both experiments, but the differences still persist in this band [35]. Most of the discrepancy can be attributed to differences in FD energy scale between the two observatories, due to the use of different fluorescence yield and invisible energy corrections. Even with this rescaling, the spectra require an additional energy dependent

rescaling to bring the spectra into agreement. The placement of Auger detectors at TA, and the use of scintillation detectors at Auger will allow for a cross checking of the two detectors in the future.

[35]

2.7.2 Anisotropy

Anisotropy has been measured over a range of energies. At the lowest energies, magnetic deflection means that the direction of an incoming cosmic ray cannot be traced back to the point of production. However, anisotropy at lower energies may still be expected. For cosmic rays of galactic origin, a dipole anisotropy would be expected as cosmic rays diffuse out from the galactic centre. For cosmic rays of extra galactic origin, the galactic magnetic fields may reduce the flux of cosmic rays coming from the direction of the galactic centre. The full dipole moment has been examined for energies above 4×10^{18} eV, where the array is fully efficient [86]. The exposure, including both vertical and horizontal air showers, is 92,500 km^{2}sr yr. For energies below this, the array is not fully efficient, and it is difficult to determine the declination dependence to a sufficient accuracy. As the array has a near 100 % duty cycle, the exposure is highly uniform in right ascension, so at lower energies, the component of the dipole moment perpendicular to Earth's axis of rotation can be found. Using the denser infill array, it is possible to extend the right ascension anisotropy study down to 3×10^{16} eV.

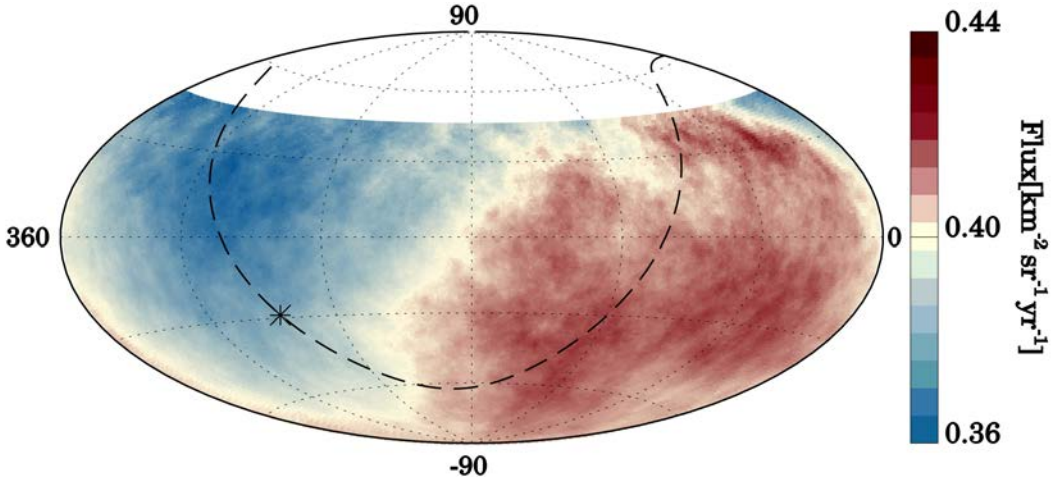

Fig. 2.36. Map of cosmic rays above 8×10^{18} eV, averaged with a 45° radius. From [86].

Events with energy above 4×10^{18} eV show a dipole moment with an excess pointing away from the galactic centre. The dipole moment shows an increasing amplitude with increasing energy with a significance of 5.1 σ over a constant amplitude. This suggests an

extra galactic origin for cosmic rays at this energy. The results at low energies, looking at anisotropies in right ascension, smaller dipole moments are observed at low energies. The phase of the dipole moments at low energies consistently indicate a small excess in the direction of the galactic centre, switching to an excess pointing away from the galactic centre at $\sim 10^{18}$ eV (see figure 2.37). This suggests a transition from galactic to extra-galactic origin at $\sim 10^{18}$ eV.

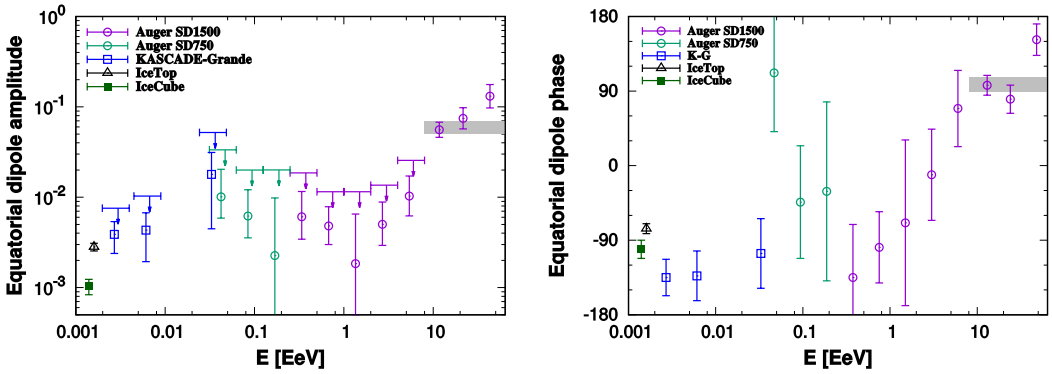

Fig. 2.37. Amplitude and phase of the equatorial dipole moment measured by Auger, along with other EAS experiments. From [86].

At higher energies, the magnetic deflections may be small enough that cosmic ray arrival directions can be used to determine a source. Additionally, at energies above $\sim 10^{19.5}$ eV, any cosmic rays observed must be from a nearby source (within ~100 Mpc), meaning that sources may be visible (This has been discussed in section 1.1.4). In the latest study by the Pierre Auger collaboration [28], both vertical and horizontal SD events are used at energies above 32 EeV, with a total exposure of 101,400 km^{2}sr yr. 2157 events meet the selection criteria. Since the magnetic deflection of cosmic rays is not known, the angular spread of cosmic ray events due to a source is also not known. Due to this, a blind search is performed over the whole sky, searching for an excess in a circular region in 1° increments for both position and size of the region, and also for varying minimum energies. The greatest significance was found for a cutoff energy of 38 EeV, and a radius of 27°. A map of the significance is shown in figure 2.38. The pre-trial significance is 5.6σ, with a p-value of 0.025 accounting for the scan. The excess is within 2° of Centaurus A.

Considering that Centaurus A is an excellent candidate for an ultra high energy cosmic ray source, the significance for an excess at the position of Centaurus A can be found. Scanning through the size of the region and minimum energy gives a maximum pre-trial significance of 5.1σ, with a post trial significance of 3.9σ, for a minimum energy of 37 EeV and radius of 28° (see figure 2.39).

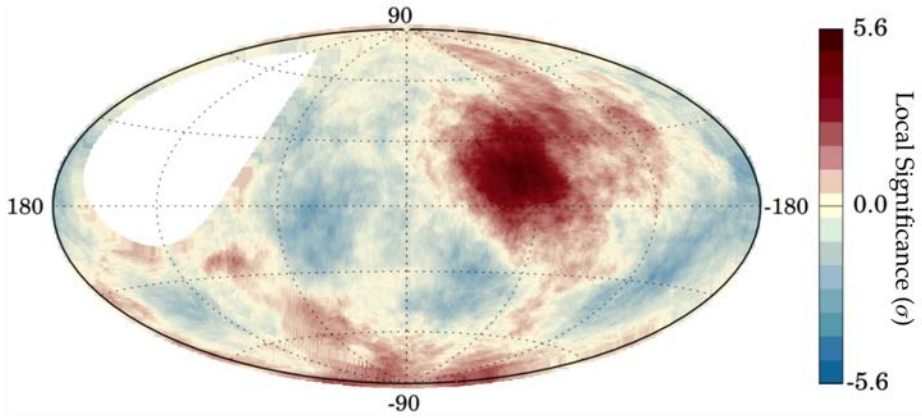

Fig. 2.38. Map of the local significance for an excess with a 27° radius, and a minimum energy of 38 EeV. From [28].

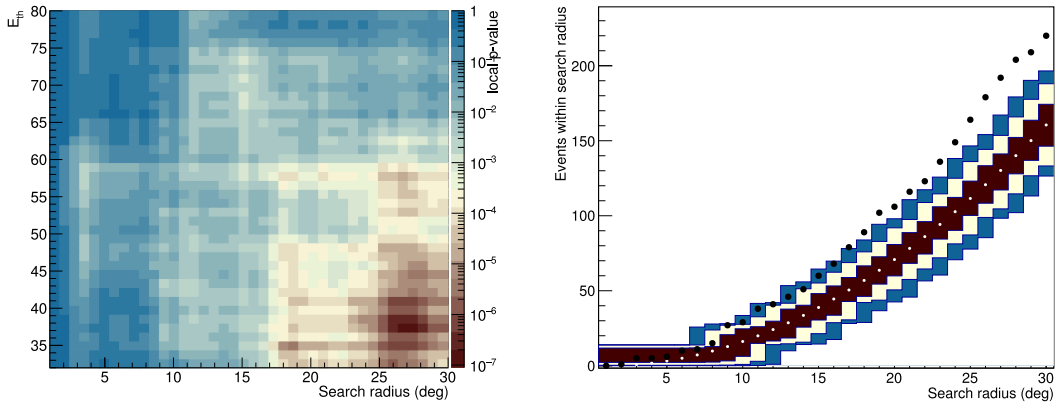

Fig. 2.39. (left) significance for Cen A against radius and minimum energy. (right) number of events vs search radius for Cen A for a minimum energy of 37 EeV with the expectation and 1, 2, and 3 σ significance. From [28].

The directions of observed cosmic rays can also be tested against object catalogues for possible sources of UHECRs. When comparing the observed cosmic ray distribution with the catalogues, the brightness of each object, and attenuation of cosmic rays due to CMB interactions are taken into account to give an expected number of cosmic rays observed at Earth. The brightness and distance of catalogue objects are used to make a probability map for cosmic ray arrival directions, that also has angular distribution width and an isotropic fraction as free parameters. A likelihood fit is performed and compared to an isotropic distribution. The 4 catalogues used for the likelihood analysis are:

- The 2MRS infra-red catalogue, tracing the nearby matter, with sources closer than 1 Mpc removed. The flux in the K-band is used as a proxy for UHECR flux.

- Swift-BAT AGNs, both radio loud and radio quiet, within 250 Mpc. The X-ray flux from 14 keV to 195 keV is used as a proxy for UHECR flux.
- γ-AGNs, measured by Fermi in the 3FHL catalogue. The flux from 50 GeV to 1 TeV is used as a proxy for UHECR flux.
- Starburst galaxies, with the continuum emission at 1.4 GHz used as a proxy for UHECR flux.

The results are shown in figure 2.40, with the best fit being obtained with the starburst galaxies for a cutoff energy of 38 EeV, and angular width of 15°. The 15° angular width is equivalent to a ∼24° radius using the top-hat function in the blind search. The p-value of this maximum is 4×10^{-7}, corresponding to a post-trial significance of 4.5 σ. For the other three catalogues, the maximum post-trial significance is: 3.1 σ for γ-AGNs, 3.7 σ for Swift-BAT, and 3.7 σ for 2MRS. For all four catalogues, the object with the largest contribution to the expected UHECR flux is very near the largest excess from the blind search. The largest predicted contribution for the starburst galaxies is from NGC 4945, 6° away from the centre of the maximum excess. For the other three catalogues, the largest contribution is predicted to be Cen A, 2° from the centre of the maximum. The second largest contribution in the starburst model is NGC 253, near the southern galactic pole, where there is also a smaller excess in UHECR flux (see figure 2.38).

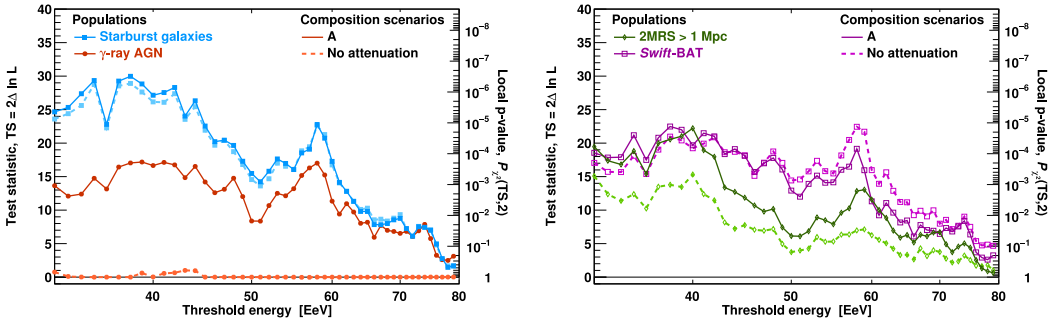

Fig. 2.40. Maximum likelihood vs energy threshold for the four catalogues. The dashed lines show the maximum likelihood if attenuation is not considered. From [28].

2.7.3 Composition

Depth of shower maxumum, X_{max}

The $\langle X_{\mathrm{max}} \rangle$ result (see figure 2.41) suggests a composition initially becoming lighter with energy, but becoming heavier with increasing energy for higher energies [117]. The data is

well described by a broken linear fit, having an elongation rate of 80 ± 1 g cm^{-2} per decade for $E < E_0$, where $E_0 = 10^{18.32 \pm 0.02}$ eV, and 26 ± 2 g cm^{-2} per decade for higher energies, with the higher elongation rate indicating composition becoming lighter with increasing energy, and the lower elongation rate indicating composition becoming increasingly heavy with increasing energy. The measurements of $\sigma(X_{\max})$ made by the Pierre Auger Observatory show a large value for energies up to E_0, with $\sigma(X_{\max})$ gradually decreasing with increasing energy above E_0 (see figure 2.41).

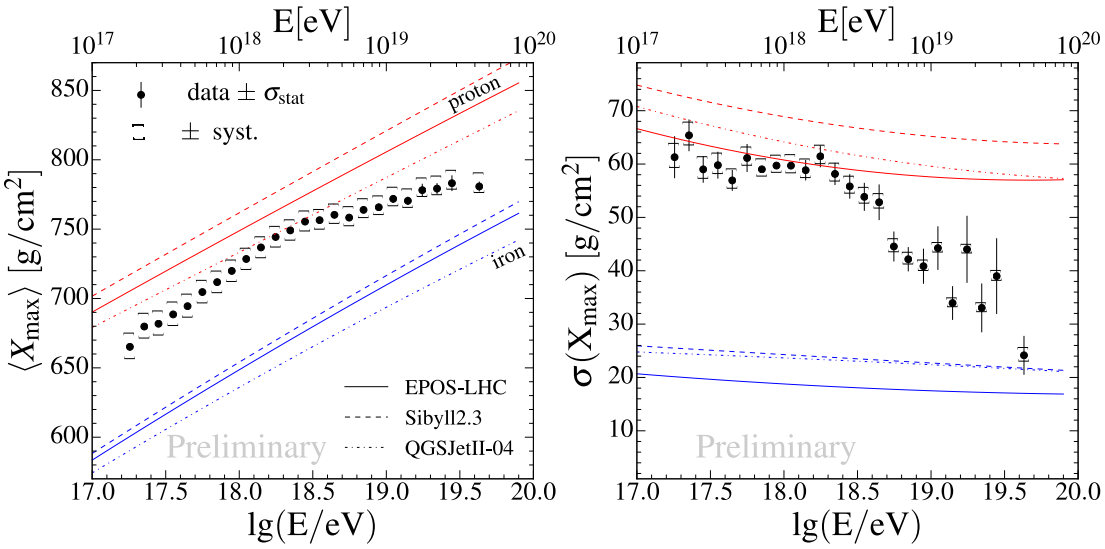

Fig. 2.41. (left) $\langle X_{\max} \rangle$ vs energy measured by the Auger FD. (right) $\sigma(X_{\max})$ vs energy measured by the Auger FD. The lines shown are the predictions from three interaction models for proton and iron primaries. From [117].

The Pierre Auger Observatory results for $\langle X_{\max} \rangle$ and $\sigma(X_{\max})$ appear highly inconsistent with the results from Telescope Array, with Telescope Array showing results consistent with a lighter composition at the highest energies. A possible explanation for the inconsistency lies in the differing analysis methods used. The Pierre Auger data has fiducial field of view cuts applied to produce unbiased $X_{\max}$ distributions, which can then be compared to simulations. Telescope Array does not apply fiducial cuts, therefore producing biased $X_{\max}$ distributions. These biased $X_{\max}$ distributions are then compared to detector simulations of differing composition and interaction models, that simulate the detector bias. A comparison has been made by comparing Telescope array data to a composition mix compatible with the Pierre Auger $X_{\max}$ distributions. This comparison shows Telescope array data is consistent with the Pierre Auger data [48].

Using the $X_{\max}$ distributions from simulated showers, it is possible to determine $\langle \ln A \rangle$ and $\sigma^2(\ln A)$, from $\langle X_{\max} \rangle$ and $\sigma(X_{\max})$. This has been done for three different interaction models.

The results are shown in figure 2.42. As expected, the results for $\langle \ln A \rangle$ show the lightest composition at E_0, with heavier composition at lower and higher energies for all models, though the three models are offset with respect to each other. All of the models also indicate a $\sigma^2(\ln A)$ decreasing with energy, indicating a transition from a mixed composition to a more pure composition. The QGSJETII-04 model has a $\sigma^2(\ln A)$ below zero at the highest energies, an unphysical result. The correlation between $S_{38}^{\star}$ and $X_{\max}^{\star}$ has been examined

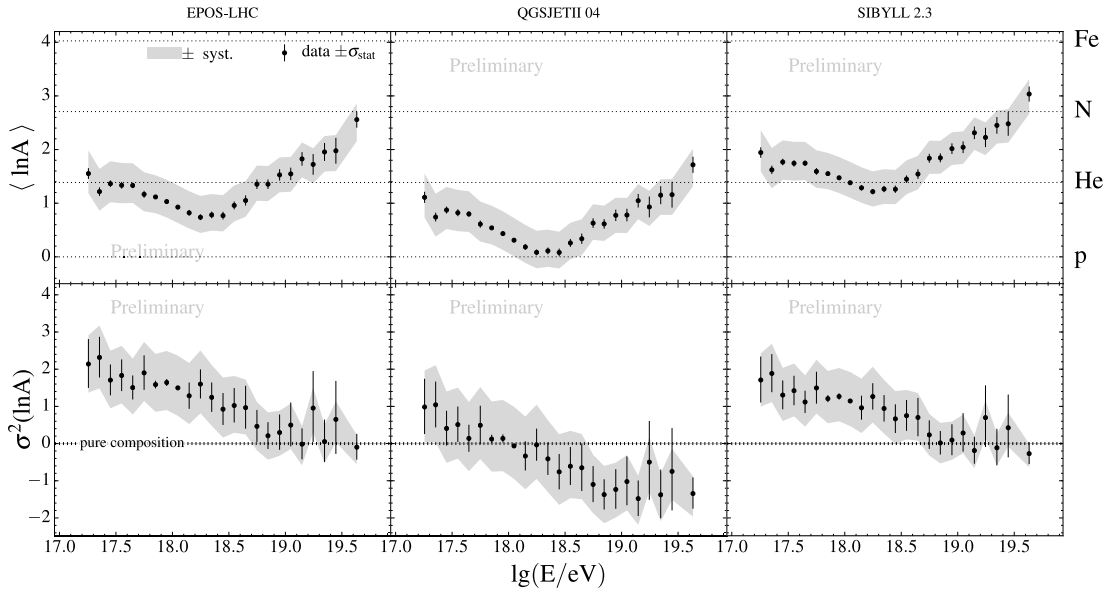

Fig. 2.42. $\ln A$ moments determined from the Auger $X_{\max}$ distributions, using three different interaction models. From [117].

in the energy range from $10^{18.5}$ to 10^{19} eV, to determine the purity of the composition mix. with results shown in figure 2.43.

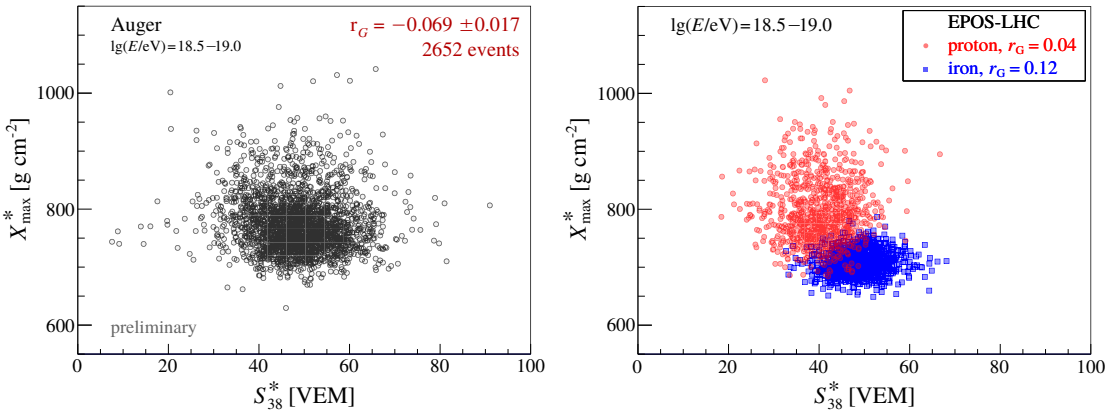

Fig. 2.43. (left) $X_{\max}^{\star}$ vs $S_{38}^{\star}$ for events with energy between $10^{18.5}$ and 10^{19} eV. (right) predictions for iron and proton primaries. From [117].

The correlation found using a ranking correlation coefficient is $r_G = -0.069 \pm 0.017$, suggesting a mixed mass composition. Since any mixture of p and He is also predicted to show a positive correlation, this means that the composition mix must also include nuclei heavier than helium. This result has been compared against simulations spanning all possible fractions of p, He, O, and Fe, in steps of 0.1 (see figure 2.44), suggesting a value for $\sigma(\ln A)$ between 0.85 and 1.6.

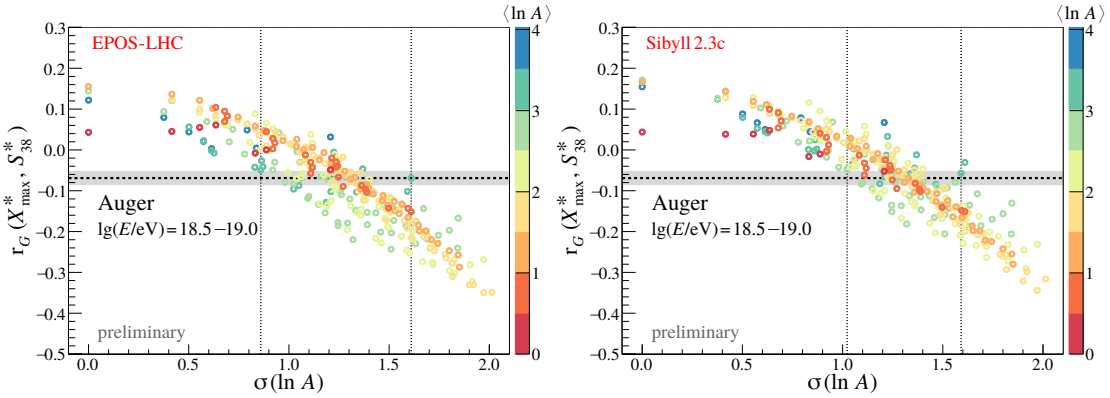

Fig. 2.44. Correlation coefficient r_G vs $\sigma(\ln A)$ for different mixes of p, He, O and Fe. From [117].

The correlation between $S^{\star}_{38}$ and $X^{\star}_{\mathrm{max}}$ has also been examined in different energy bins. Results of this are shown in figure 2.45, compared to predictions for pure and mixed compositions. The results suggest a more mixed composition at energies up to $10^{18.7}$ eV, with composition becoming more pure at higher energies. This is consistent with the results obtained from the X_{max} distribution measured by the FD.

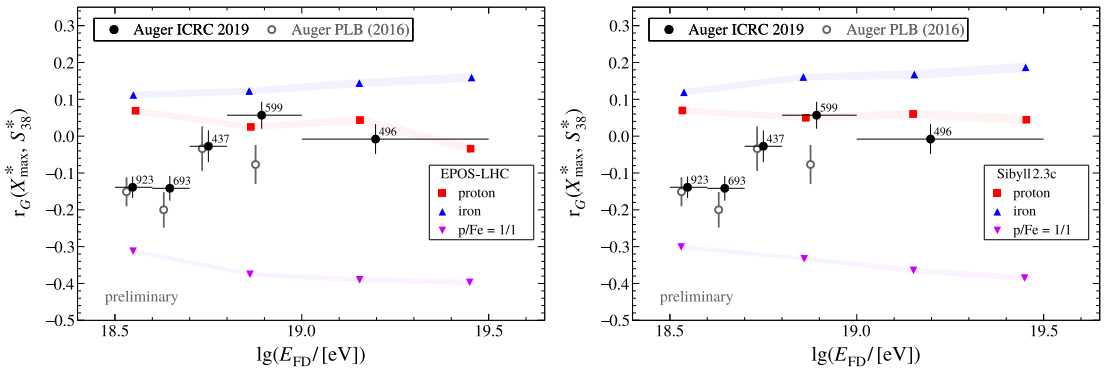

Fig. 2.45. Correlation coefficient r_G vs energy, with model predictions for protons, iron, and a 50/50 mix of proton and iron. From [117].

Risetime

Risetime data is available for 125,005 events, with 237 events above 50 EeV. This provides the largest data set available for studying composition at the highest energies. When comparing the data obtained with detector simulations, the observed $\langle \Delta_s \rangle$ indicates a composition becoming heavier with increasing energy (see figure 2.46). The $\langle \Delta_s \rangle$ data can also be converted to $\langle \ln A \rangle$ for a given interaction model for comparison with other composition measurements (see figure 2.47). When comparing the data with the $X_{\max}$ data from the FD, there is a disagreement between the two. This indicates that the interaction models used in simulations do not adequately reproduce the physics of extensive air showers.

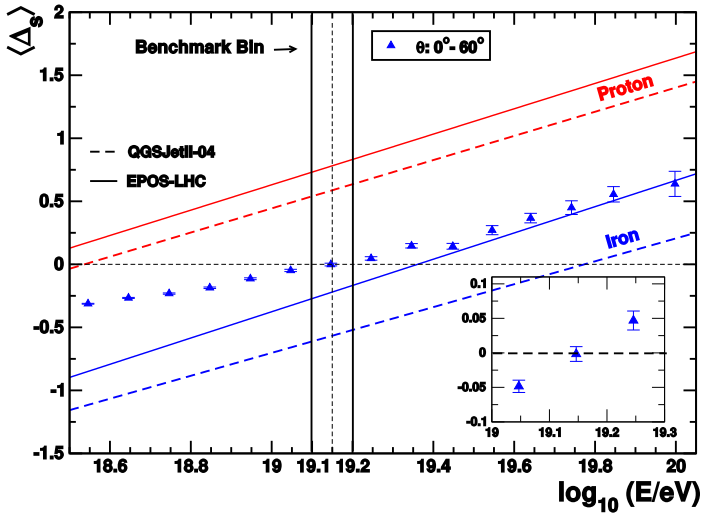

Fig. 2.46. Results for the Δ method for the 1500m array, with lines indicating the interaction model predictions. The inset plot is a zoom in of the results near the benchmark energy. From [105].

Since Δ_s is dependent on the depth of maximum in shower development, it is expected that Δ_s will be correlated to $X_{\max}$ observed by the fluorescence detector. This is shown for the hybrid data in figure 2.48. It is therefore possible to use Δ_s to get an estimate of $X_{\max}$. Due to the larger exposure of the SD, this can allow $X_{\max}$ data to be extended to higher energies. The smaller hybrid dataset allows for a calibration using $\langle X_{\max}^{\mathrm{FD}} \rangle$, to calculate $\langle X_{\max}^{\mathrm{Delta}} \rangle$. The following relation is used to calculate $\langle X_{\max}^{\mathrm{Delta}} \rangle$:

$$\langle X_{\max}^{\mathrm{Delta}} \rangle = a + b \cdot \langle \Delta_s \rangle + c \cdot \log_{10}(E_{SD}/\mathrm{eV}) \tag{2.41}$$

A plot of $\langle X_{\max}^{\mathrm{Delta}} \rangle$ against energy, along with the values of $\langle X_{\max}^{\mathrm{FD}} \rangle$, are shown in figure 2.49. As expected, the values obtained by the SD show a good agreement with the FD data, and show the trend of increasing mass with energy continues up to 10^{20} eV.

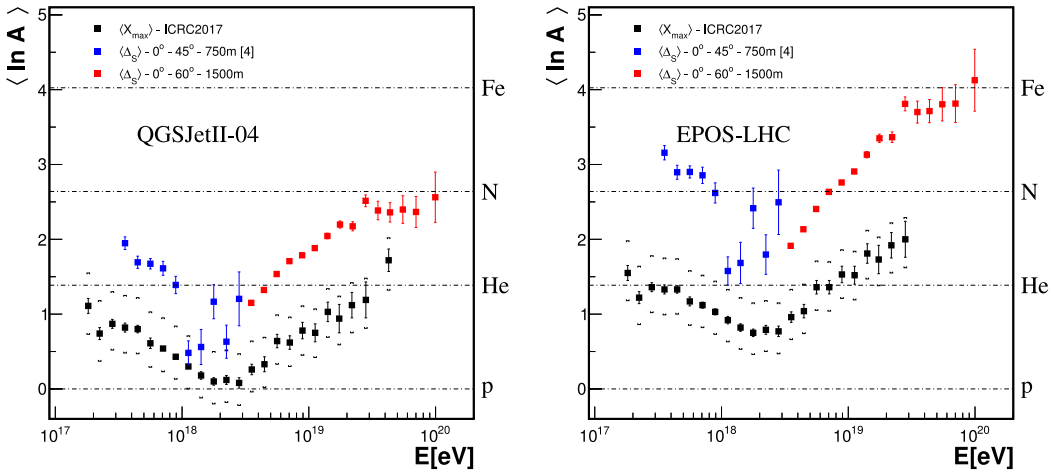

Fig. 2.47. $\langle \ln A \rangle$ deduced from the delta method, compared with $\langle \ln A \rangle$ deduced from the FD $X_{\max}$. From [105]

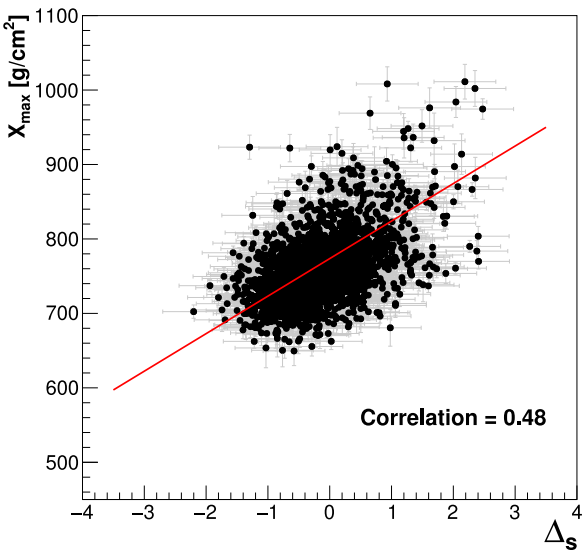

Fig. 2.48. Plot showing correlation of Δ_s to $X_{\max}^{\mathrm{FD}}$. From [105]

Muon production depth

The muon production depth has been determined for over 2000 events, with energies above 1.5×10^{19} eV, and zenith angles between 45° and 65° [70]. Some bias is introduced in the $X_{\max}^{\mu}$ reconstruction, which is dependent on the energy, as well as composition and interaction model. This bias could be corrected for but it would introduce a large systematic uncertainty due to the mass and model dependence. Due to this, results are given as $X_{\max}^{\mu}$ folded with the reconstruction bias, $X_{\max}^{*\mu}$. The results are given in figure 2.50.

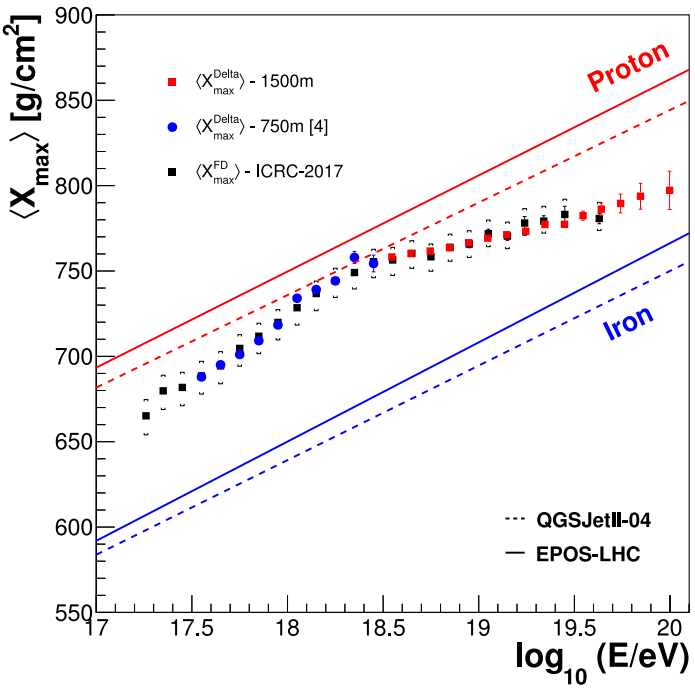

Fig. 2.49. $\langle X_{\mathrm{max}}^{\mathrm{Delta}} \rangle$, with model predictions for proton and iron. $\langle X_{\mathrm{max}}^{\mathrm{FD}} \rangle$ is also shown for comparison. From [105]

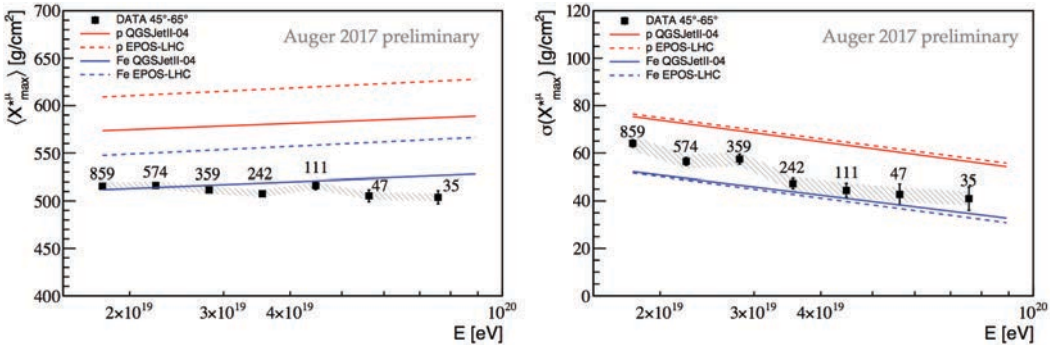

Fig. 2.50. (left) $\langle X_{\mathrm{max}}^{*\mu} \rangle$ as a function of energy. (right) $\sigma(X_{\mathrm{max}}^{*\mu})$. The error bars show the statistical uncertainties, while the shaded area shows the systematic uncertainties. From [70]

The results for $\langle X_{\mathrm{max}}^{*\mu} \rangle$ suggest increasing mass as energy increases, in line with other composition measurements. When comparing $\langle X_{\mathrm{max}}^{*\mu} \rangle$ with the model expectations, results are highly inconsistent with all reasonable mass values for EPOS-LHC, and somewhat inconsistent at higher energies for QGSJetII-04. Better compatibility is observed with $\sigma(X_{\mathrm{max}}^{*\mu})$, with a smaller dependence on hadronic interaction models. These results are compared with X_{max} results from the FD in figure 2.51, for $\langle \ln A \rangle$ derived from $\langle X_{\mathrm{max}}^{*\mu} \rangle$. The X_{max} and $X_{\mathrm{max}}^{*\mu}$ results are highly incompatible, highlighting the inadequacies in current hadronic interaction models.

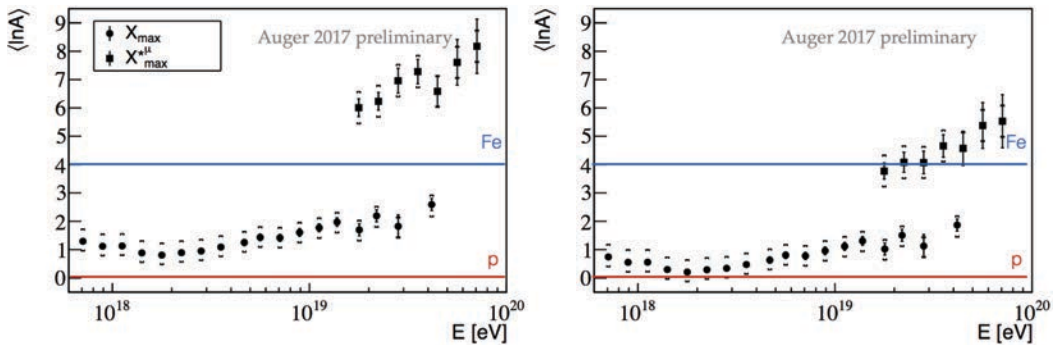

Fig. 2.51. $\langle \ln A \rangle$ derived from $\langle X^{*\mu}_{\max} \rangle$, with the $\langle X^{\mathrm{FD}}_{\max} \rangle$ result shown for comparison. The error bars show statistical errors, while the square brackets show systematic uncertainties. From [70]

Muon density

The engineering array of AMIGA has gathered data on the muon density of showers with energy above $10^{17.5}$ eV. Muon densities, measured in conjunction with energy, can be an indicator of composition, and also a test for hadronic interaction models. With the 750 m spacing of detectors, the muon density at 450 m, ρ_{450} is used for a muon density measure [87]. The analysis is done for zenith angles below 45°. Similar to the SD array, the CIC method is used, giving a muon density corrected for zenith angle effects, normalised to 35°, ρ_{35}. The results for ρ_{35} vs energy are shown in figure 2.52. The measured muon densities suggest muon densities slightly above the prediction for iron primaries. This result is highly incompatible with $X_{\max}$ results, which suggest a lighter composition.

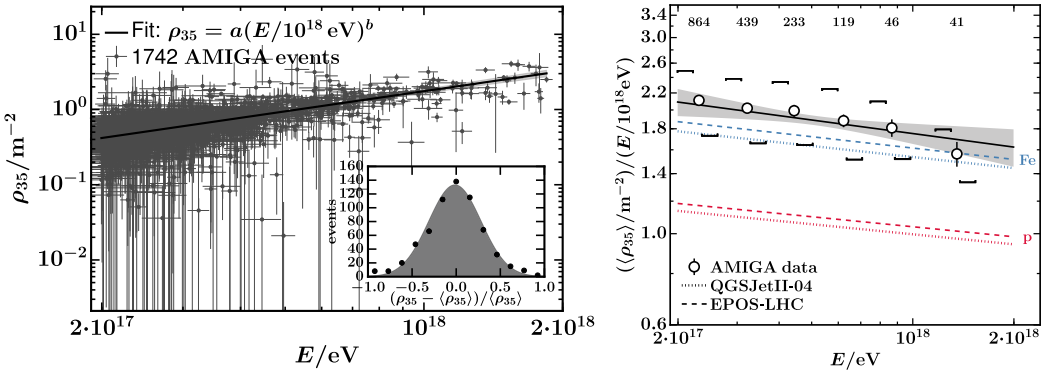

Fig. 2.52. (left) Muon density ρ_{35} measured by AMIGA vs energy, with the insert showing the normalised residuals. (right) comparison of the muon densities to the interaction model predictions, with error bars showing the statistical uncertainty, and square brackets showing systematic uncertainty. From [87].

The muon density can also be measured using the 1500 m SD array with HAS (horizontal air showers). This gives a measurement at higher energies with a much larger exposure. To compare the AMIGA and HAS density results with FD $X_{\max}$ observations, a z-factor is introduced:

$$z = \frac{\langle \ln \rho_{35} \rangle - \langle \ln \rho_{35} \rangle_{\mathrm{p}}}{\langle \ln \rho_{35} \rangle_{\mathrm{Fe}} - \langle \ln \rho_{35} \rangle_{\mathrm{p}}} \tag{2.42}$$

This can also be similarly applied to N_{19}, measured with HAS, as well as for $X_{\max}$, measured with the FD. A plot of z vs energy, for AMIGA, HAS, and $X_{\max}$ is shown in figure 2.53.

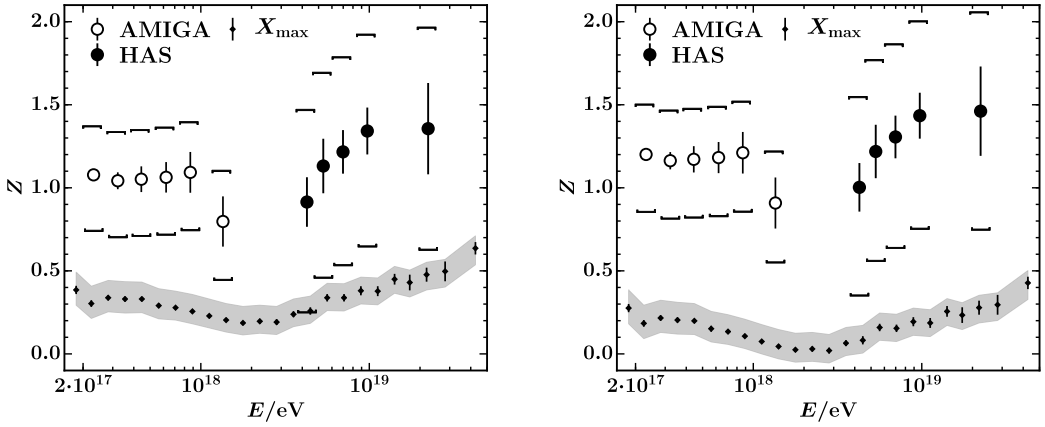

Fig. 2.53. z-factor vs energy, for AMIGA, HAS, and $X_{\max}$ measurements, using EPOS-LHC (left), and QGSJetII-04 (right). From [87].

Muon density measurements at ultra high energies indicate a much higher muon density when compared to the hadronic interaction models. The z-factor obtained by both HAS and AMIGA show a good agreement with this discrepancy, though the energy ranges do not overlap. The trends in z-factor with energy obtained by HAS and AMIGA show a reasonable agreement with the $X_{\max}$ data. The excess in muon densities is also shown in figure 2.54, showing expected muon densities vs $\langle X_{\max} \rangle$ for energies of $10^{17.5}$ eV and 10^{18} eV. To match observations, the simulated muon density would have to be increased by 38% at both energies for EPOS-LHC, while it would have to be increased by 50% at $10^{17.5}$ eV and 53% at 10^{18} eV for QGSJetII-04 [87]. This indicates that current hadronic interaction models show a large deficit in muon density, consistent with numerous other experiments at the highest energies [29].

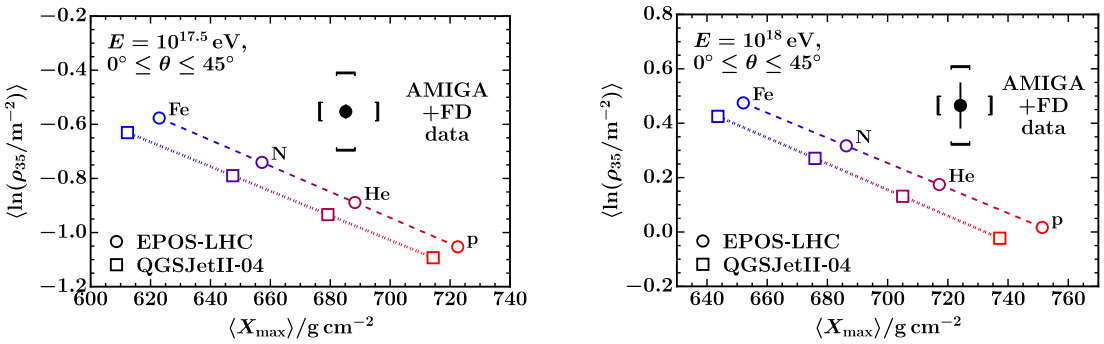

Fig. 2.54. ρ_{35} vs $\langle X_{\max} \rangle$, with model predictions for EPOS-LHC and QGSJetII-04, at energies of $10^{17.5}$ eV (left) and 10^{18} eV (right). From [87].

Chapter 3

FD telescope alignment study

Telescope alignment: the methods

To accurately determine the arrival direction of cosmic rays, the pointing directions of the fluorescence telescopes must be known. Uncertainties in the elevation angles of the telescope also affect the energy and X_{max} reconstruction. It is desirable to determine the telescope pointing directions to within 0.1°. The first section of this chapter describes the methods used by others to determine the pointing directions of the fluorescence telescopes. The next two sections describe my method for finding the pointing directions.

3.1 Previous methods

3.1.1 Using star trails

The directions of stars in the sky are known very accurately. The ultraviolet light from stars is bright enough to be detected by the Auger telescope PMTs. To detect only cosmic ray showers, the signal is high-pass filtered to subtract any background signal, making it difficult to detect stars. However, because the PMTs are counting photons, there is a variance in the signal proportional to n, where n is the number of photoelectrons in a given time bin. The amount of light entering a pixel can then be estimated as being proportional to variance. As a star passes across a pixel (see figure 3.1(a)), the variance rises as the light spot is entering the pixel, then remains constant while the spot is completely inside the pixel, then lowers back to the background level (see figure 3.1(b)). A star will cause a variance increase across a trail of PMTs (see figure 3.2). The timing of the increases in variance from stars can be used to determine the pointing directions of the telescopes. Studies have been done by the Auger collaborators from the Milan group [38] and the Czech group [85]. The Milan method found

the pixel offsets individually, comparing the time at the centre of the signal plateau with the expected time. The Czech method performed a fit over the whole telescope to minimise the difference between the observed and expected signal. There is some disagreement of up to 0.3 degrees in derived telescope pointing directions between the two studies.

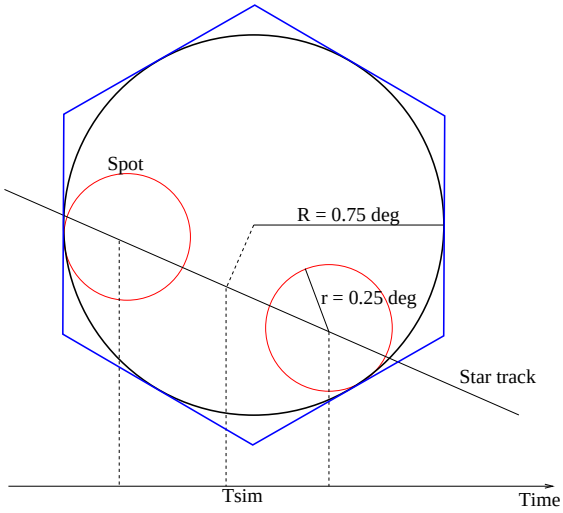

(a) Spot from a star crossing a PMT.

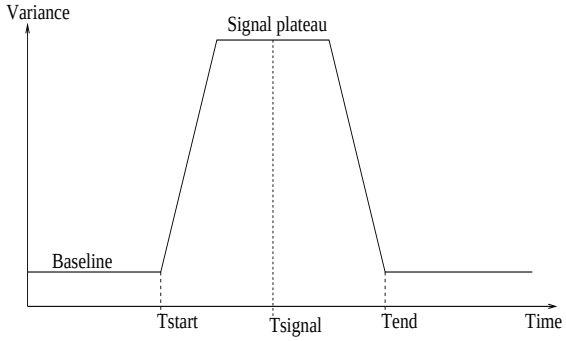

(b) Variance signal increase from a star crossing a PMT.

Fig. 3.1. Detection of a star crossing a PMT. From [38].

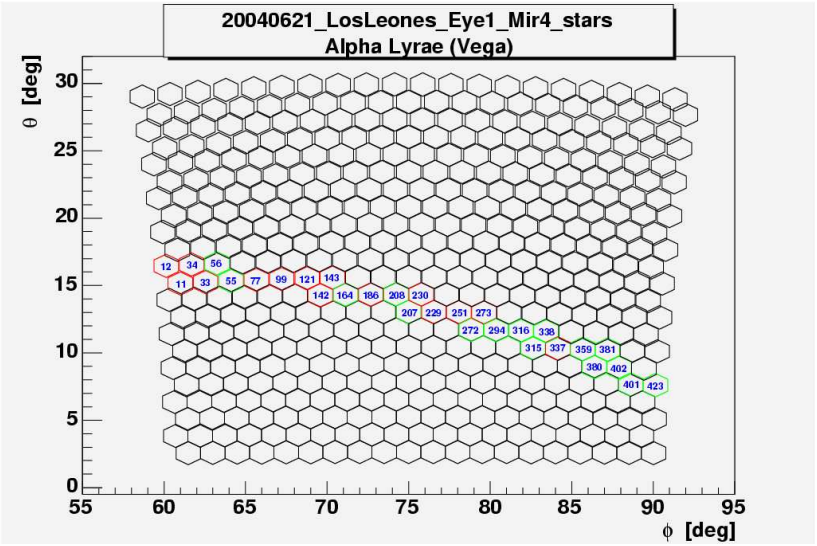

Fig. 3.2. Simulated track from Vega crossing telescope 4 of Los Leones. A signal was found in the red pixels. No signal was found for green pixels but the star did cross the pixels [38].

3.1.2 Using CLF laser shots

Numerous studies have been done to test the alignment of the telescopes using the Central Laser Facility (CLF). Most studies involve comparing the reconstructed SDP (defined in 2.4.2) to the direction of the CLF. Using the SDP allows for detection of telescope misalignment perpendicular to the direction of the laser track. By using laser shots at different inclinations it is possible to determine the pointing direction of the fluorescence telescopes.

Patrick Younk and Brian Fick [115] used inclined CLF shots to find the pointing directions of the telescopes for Los Leones, Los Morados and Coihueco. To do this accurately, tracks are required over a broad range of inclinations. This is only possible for the 1 or 2 telescopes pointing towards the CLF. Figure 3.3 shows the tracks from the CLF shots used in one of the eyes.

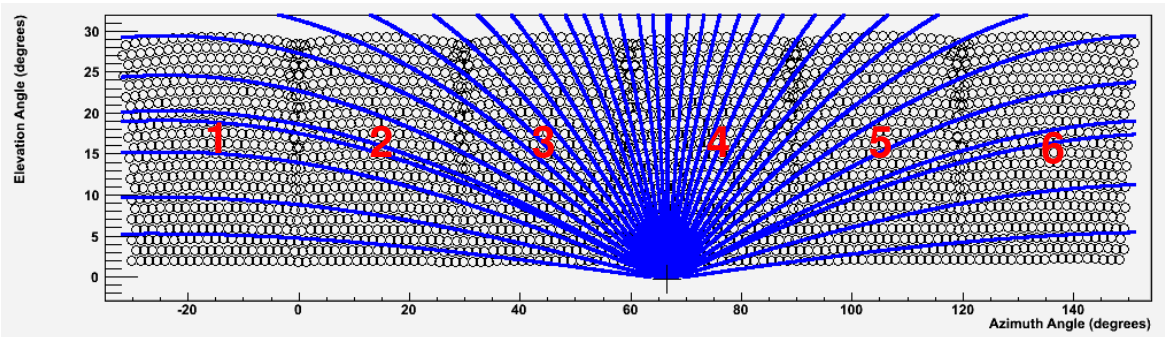

Fig. 3.3. CLF Tracks used to determine pointing directions of telescopes for Los Leones [115].

The estimated precision of the technique was about 0.1 degrees for telescopes pointing towards the CLF. The pointing directions agreed with the star trail methods to within error. For telescopes not pointing towards the CLF, the uncertainty of this method was too large.

Misalignment of the telescopes can also be detected using the timing of the CLF light arriving at the pixels. Timing is sensitive to misalignment in the direction of the laser track. This is most noticeable when the track crosses two telescopes and they have a different alignment relative to each other. This will cause a discontinuity in the timing fit at the transition between the two telescopes. Thomas Harrison, Jose Bellido and Bruce Dawson [49] used the timing to test the alignment of telescope 6 of Coihueco. Figure 3.4(b) shows the time fit residuals for a CLF event which crosses into telescope 6. If the mirrors are properly aligned, the residual would be flat. There is a clear discontinuity between telescope 5 and 6 (the two leftmost telescopes) with the light arriving at the pixels in telescope 6 later than expected when compared to telescope 5. The timing in telescope 5 is consistent with telescope 4. The pixels from Telescope 5 have mostly been rejected as outliers because of the

discontinuity. It appears that telescope 6 is misaligned. The timing discontinuity observed corresponds to a misalignment of 0.7 ± 0.2 degrees in azimuth and -0.2 ± 0.3 degrees in elevation for telescope 6 [49].

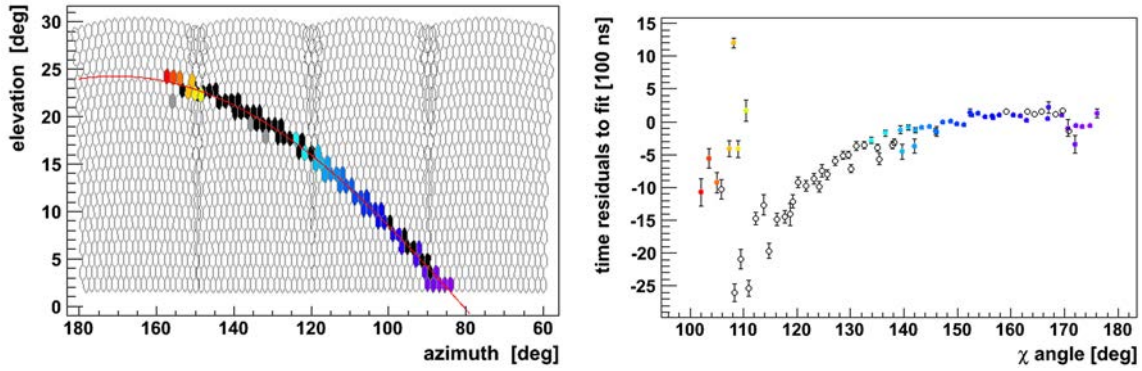

(a) Shower track for CLF event 4404871

(b) Time fit residuals for the event.

Fig. 3.4. CLF event 4404871. The black pixels in (a) were rejected from the time fit. The rejected pixels are the uncoloured points in (b). From [49].

3.2 Determining relative offsets with cosmic ray showers

To test if any of the telescopes are misaligned, the telescopes alignment can be checked against adjacent telescopes (unless they are all misaligned by the same amount). This is possible using CLF laser shots, however the CLF is in a fixed location and can only offer a limited range of track directions. Cosmic ray showers have random arrival directions & core locations giving a wide range of track directions in all telescopes, so showers can be used to determine relative offsets between any adjacent telescopes.

3.2.1 Timing

If there is a relative pointing error between two telescopes, there will be a discontinuity in the timing of the pixel pulses between the two telescopes. This will cause a discontinuity in the timing fit, which is a plot of pixel time versus the χ angle defined in 2.4.2. A plot of the time residuals (see figure 3.5(b)) can clearly show the discontinuity in the pixel timing.

Since the timing of the pixel pulse is a function of the χ angle, only offsets which shift the χ angle of pixels will have an effect on the timing. Hence, this timing method will detect the component of the offset in the direction along the shower track.

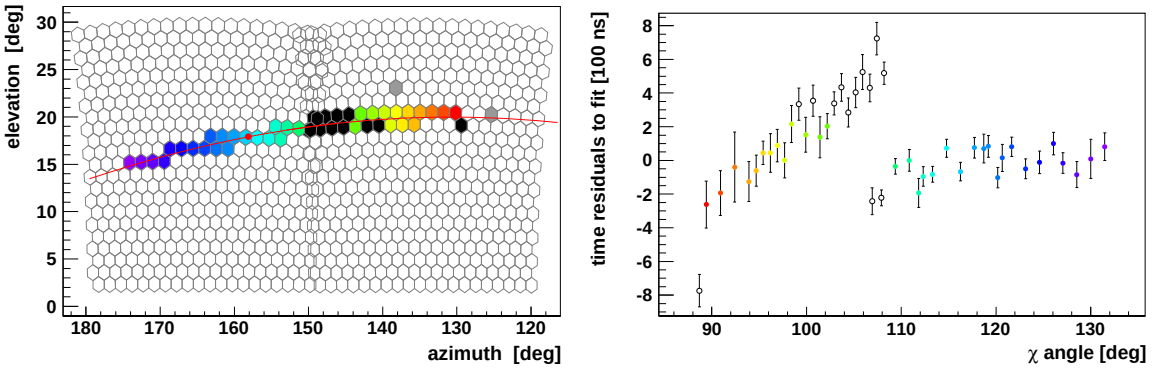

(a) Shower track for event 6872384

(b) Residuals to the timing fit. uncoloured pixels were rejected from the time fit.

Fig. 3.5. Event 68723824. The shower track crosses Coihueco telescopes 5 and 6.

To find the the χ offset, $\Delta\chi$, from the timing offset, Δt, we use the equation first described in 2.4.2

$$t(\chi) = t_0 + \frac{R_p}{c}\tan\left(\frac{\chi_0 - \chi_i}{2}\right) \tag{3.1}$$

inverting this equation gives

$$\chi(t) = \chi_0 + 2\arctan\left(\frac{(t_0 - t)c}{R_p}\right) \tag{3.2}$$

Taking the derivative we get

$$\frac{d\chi}{dt} = \frac{2c}{R_p}\frac{1}{1+\left(\frac{(t_0-t)c}{R_p}\right)^2} \tag{3.3}$$

The χ offset can be approximated as

$$\Delta\chi = \frac{2c}{R_p}\frac{1}{1+\left(\frac{(t_0-t)c}{R_p}\right)^2}\Delta t \tag{3.4}$$

Using multiple cosmic ray showers with tracks appearing in different orientations on the camera, a fit can be applied to determine the relative pointing offset between two telescopes. If we define the relative pointing offset between the telescopes as $\overrightarrow{S}$ with magnitude $|S|$, direction β, and we define the direction of the cosmic ray shower track to be α, we get

$$\Delta\chi = |S|\cos(\alpha - \beta) \tag{3.5}$$

These angles are defined in figure 3.6.

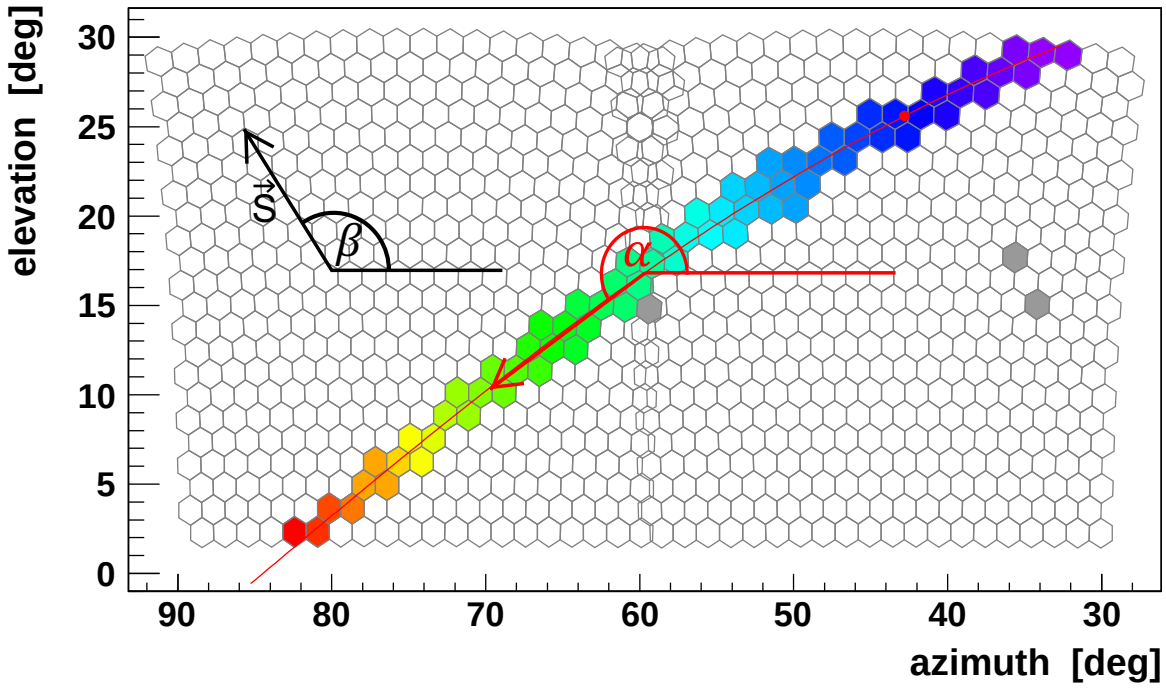

Fig. 3.6. Definition of shower and telescope offset directions. The black vector $\vec{S}$ (exaggerated in magnitude) is the pointing offset of a telescope from its nominal direction, relative to the offset of the adjacent telescope. Angles α and β are measured from the horizontal. The horizontal is the vector defined as the cross product of the direction of the shower spot at the boundary between the telescopes, and the zenith.

Event Selection

The method will be discussed below, but first a comment on selecting the shower events to be used. An accurate time fit is needed in both telescopes. Events with a track length greater than 15 degrees in each of two telescopes were selected. Since the main source of error is the error in the timing fit, we want events with a large value of $\frac{\Delta t}{\Delta \chi}$ to maximize the timing sensitivity. $\frac{\Delta t}{\Delta \chi}$ is large for large values of the shower impact parameter, R_p. Events with R_p greater then 15000 m were selected. There was a total of 164 of these events. Considering that these events are divided across 20 telescope boundaries, this is not a very large number of events. To get more events, an additional set was selected that had a minimum track length of 20 degrees in one telescope and 5 degrees in the other. For these events, instead of comparing the two time fits, the pixel times from the telescope with the short track would be compared to the time fit expectations from the telescope with the long track. 441 events met these criteria (without meeting the first criterion). The first set of events will be referred to as type I events and the second set as type II events.

Determining Offsets

Timing fits had to be done individually in each telescope to find the relative pointing offset between the two telescopes. To do this, events were reconstructed twice using Offline, once with the pixels in even numbered telescopes removed from the fit and again with the pixels from odd numbered telescopes removed. The events had to be "mono" reconstructed (i.e. without surface detector information) because if the telescopes are misaligned the SD station may have the wrong time relative to the telescope pixel times and could affect the timing fit.

For type I events, the two fits were compared to obtain an offset $\Delta\chi$. Figure 3.7 illustrates two telescope time fits overlaid onto the residuals in the timing of each pixel's pulse. The times are displayed as residuals to the global fit (the fit using all of the pixels in the event). The most accurate way to determine the offset was to compare the two fits at the boundary between the two telescopes. The time when the shower was at the boundary was defined as the average of the arrival time of the latest pixel time from the first telescope and the earliest pixel time from the second telescope. Using the equation for $\chi(t)$ (equation 3.2), the χ angles for the two were found and the difference between the two was taken to get $\Delta\chi$. The two fits had slightly different SDPs which means the χ angle is defined differently for each of the fits so the χ angles had to be translated to a common shower-detector plane.

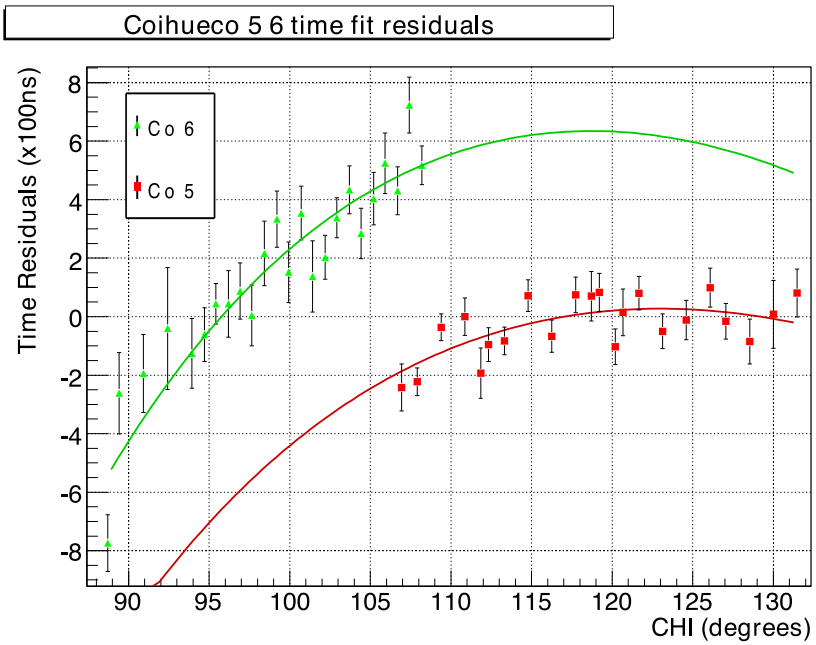

Fig. 3.7. Time fit for a type I event crossing Coihueco telescopes 5 and 6. The pixel times are plotted as a residual to the Global time fit. The green points are pixels from telescope 6 and the red points are from telescope 5. The two lines are the time fits for each individual telescope relative to the global time fit.

Because the fits are mono, there is a strong correlation between errors in χ_0 and R_p. This correlation must be taken into account when calculating an error in $\Delta\chi$ to avoid a huge overestimation of the error. $\overline{\text{Off}}\underline{\text{line}}$ calculates correlation coefficients between the errors in R_p and χ_0. For a function $f(X_i)$, dependent on variables X_i, the error in f for correlated errors is:

$$\sigma(f) = \sum_{i,j} \sigma_i \sigma_j \frac{df}{dX_i} \frac{df}{dX_j} Corr_{ij} \tag{3.6}$$

where σ_i is the error in X_i and $Corr_{ij}$ are the correlation coefficients between X_i and X_j. The correlation coefficients are between -1 and 1 with $Corr_{ii} = 1$.

For type II events, only one of the fits is used. The fit from the telescope with the long track is compared to the pixel times in the telescope with the short track (see figure 3.8). The residual of each pixel's χ angle is found to the $\chi(t)$ fit. The pixel's error is a timing uncertainty so the χ uncertainty is approximated as:

$$\delta\chi_i = \delta t \frac{d\chi}{dt} \tag{3.7}$$

$$= \delta t \frac{2c}{R_p} \frac{1}{1 + \left(\frac{(t-t_0)c}{R_p}\right)^2} \tag{3.8}$$

A chi-squared fit is then done on the pixel χ residuals in the telescope with the short track to get the weighted mean of the residual to the $\chi(t)$ fit, $\Delta\chi$.

3.2.2 SDP

Using cosmic ray shower SDP fits is another method capable of finding the relative misalignment between two telescopes. The shower-detector plane is sensitive to misalignments perpendicular to the track direction. With sensitivity in a different direction to the timing method above, the SDP method can improve the accuracy of the pointing offset determination and can also be cross-checked against timing as this method is independent of timing.

Event selection

The SDP accuracy is typically not as good as the geometrical accuracy from timing fits with a large R_p. Events had to be selected to minimize error in the SDP normal vector. The error in the SDP normal is very different in different directions. The error in the SDP is best defined in the shower track coordinate system (see figure 3.9). The centroidal error is the error of the position of the centroid perpendicular to the shower track. The angular error is the error in a rotation of the track about the centroid. The error in the centroid of the track is less than the

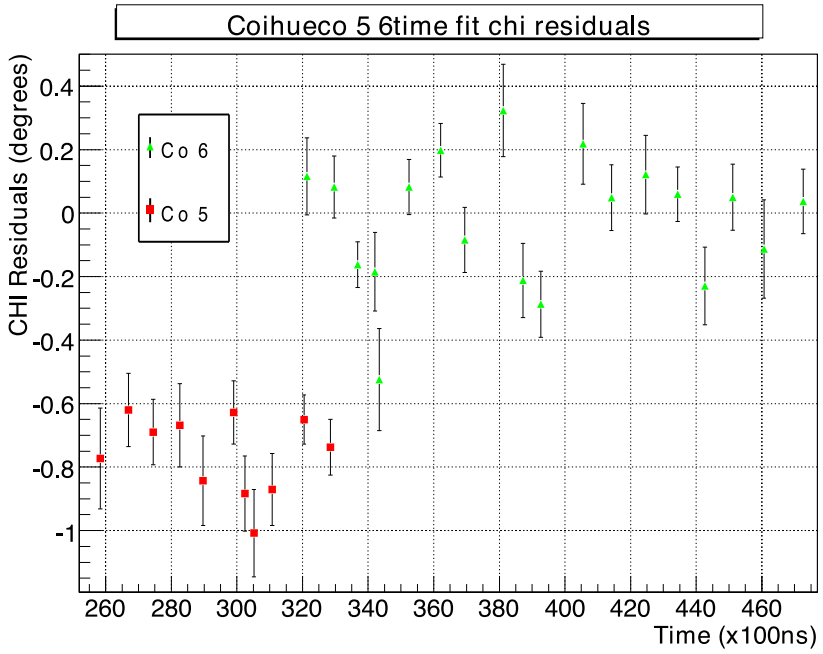

Fig. 3.8. Time fit to a type II event. Instead of displaying residuals to $t(\chi)$, the plot is inverted to show the residuals to $\chi(t)$. The residuals are with respect to the fit to the pixels in the telescope with the long track. The red points are the χ residuals from the PMTs in telescope 5 and the green pixels are from telescope 6.

angular error in the SDP. The angular error is also a lot more dependent on the angular track length.

The direction in which the telescope pointing offset is being measured is perpendicular to the shower track, so the error in that measurement is roughly equal to the centroidal error. A minimum track length of 20 degrees was chosen. At this track length, the typical centroidal error is 0.07 degrees and the angular error is 0.44 degrees [116]. Since no timing is involved, there were no cuts on R_p.

Determining offsets

The relative offsets were found using the SDP normal vectors for each individual telescope. The events were reconstructed separately for each telescope using the same procedure as the timing method. The relative offset between the telescopes in the direction perpendicular to the shower track is the angular offset between the telescopes SDPs near the centroids. For a centroid in the $\hat{x}$ direction, the offset will be:

$$\Delta\phi = (\overrightarrow{n_2} - \overrightarrow{n_1}) \cdot \hat{x} \tag{3.9}$$

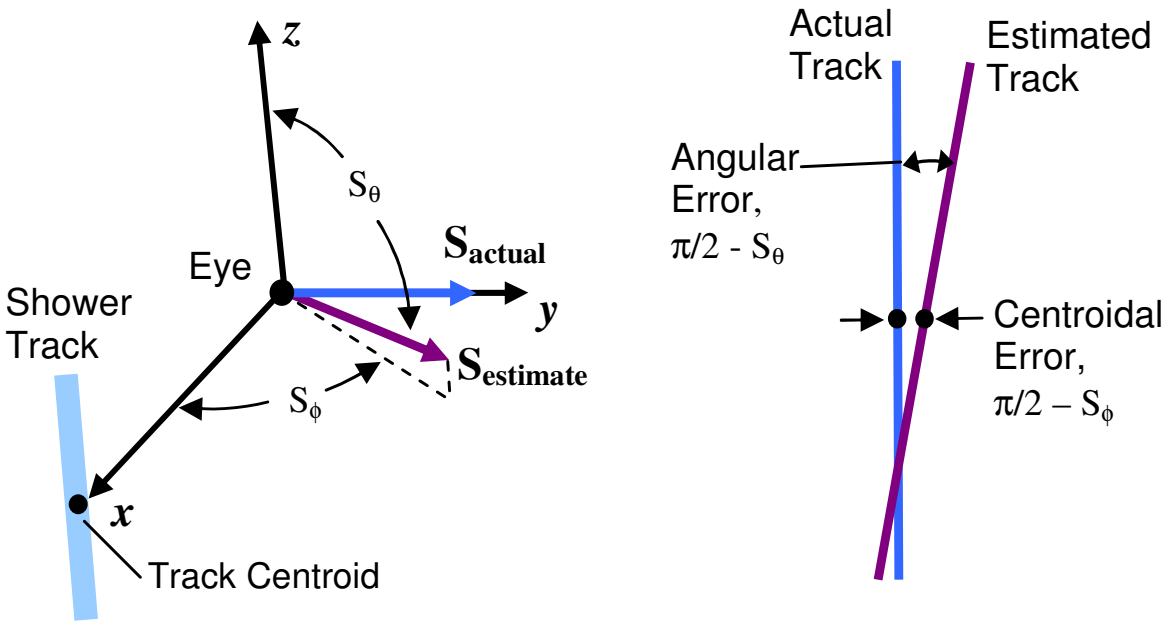

Fig. 3.9. Diagram of the shower track coordinate system (left) and the definitions of angular and centroidal error (right). The centroid is the "centre of gravity" of the triggered pixel positions, weighted by signal. The vector $\overrightarrow{S}$ in this diagram is the normal vector to the shower-detector plane, not to be confused with the relative telescope pointing offset in equation 3.10. From [116].

where $\overrightarrow{n_2}$ and $\overrightarrow{n_1}$ are the SDP normal vectors for the fits in the two telescopes (see figure 3.10). The vector $\hat{x}$ can be anywhere on the SDP, however the error is minimized close to the centroid where sensitivity to angular error is minimized. Since the error from both SDP normals have to be taken into account, the error is minimized when $\hat{x}$ is chosen to be between the centroids.

The errors in the SDP normal vectors are given in altitude and azimuth directions which are not the same as the centroidal and angular directions, so the errors in altitude and azimuth will be highly correlated. This correlation must be taken into account to avoid overestimating errors.

For compatibility with the timing method above, we want the equation to fit the offsets to have the same form as the timing method. Since the component of the offset being measured is perpendicular to the shower track, the angle α is chosen to be an angle between the horizontal and the direction perpendicular to the shower track (see figure 3.11). This is also the direction of the SDP normal vector. The component of the offset will be:

$$\Delta\phi = |S|cos(\alpha - \beta) \tag{3.10}$$

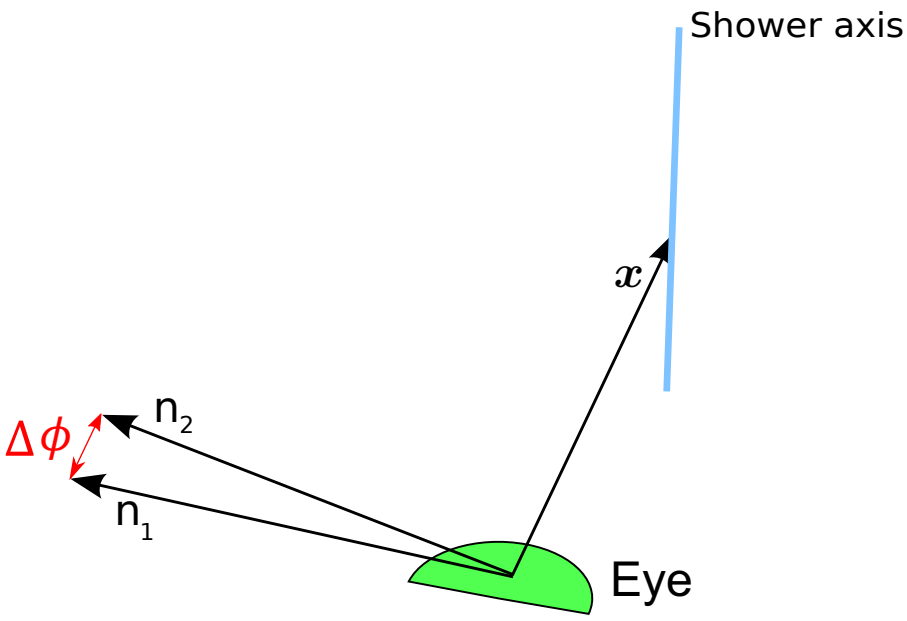

Fig. 3.10. Diagram of the vectors used to find the pointing offset using SDP normal vectors.

where $\vec{S}$ is the relative pointing offset in the direction β, and $\Delta\phi$ is the relative SDP offset.

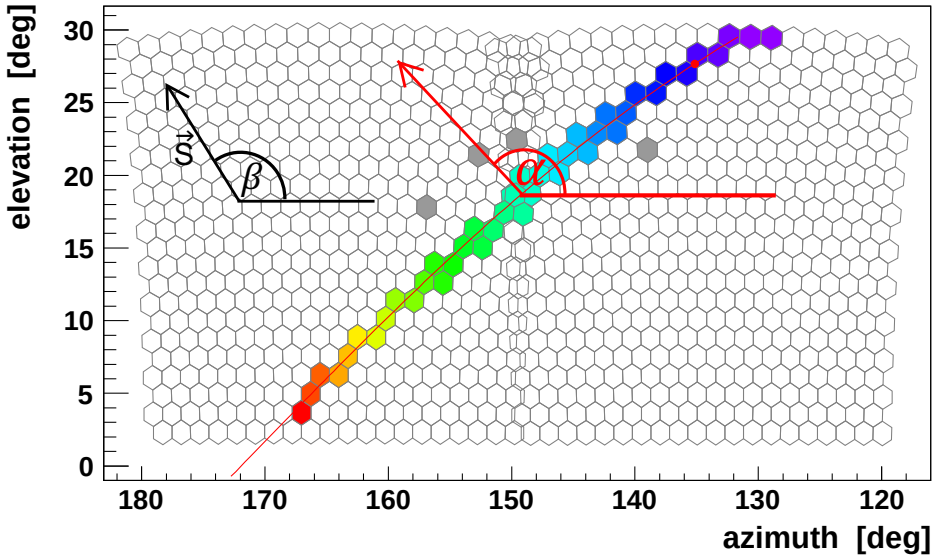

Fig. 3.11. Definition of the SDP offset geometry.

3.3 Determining absolute offsets with hybrid showers

The pointing directions of the telescopes can be checked by comparing the shower reconstructed in the telescope to the surface detector reconstruction. The surface detectors can determine the position and timing of the shower core. Using hybrid cosmic ray showers is similar to using the CLF, except that the core location is not fixed at the centre of the array and the core location and timing are not known quite as accurately. Because the core locations are randomly scattered throughout the SD array, there will be a good variety of track directions for every telescope, unlike the case for the CLF tracks.

Patrick Younk [113] has used golden hybrid showers (golden hybrids trigger 3 tanks so the shower has an SD reconstruction) to determine the azimuth of the telescopes by comparing the SD core to the FD core (see figure 3.12). An azimuth offset in a telescope would cause the angular core difference to have a non-zero mean. The longitudinal core differences could be used to find the elevation offsets but was not considered in the study.

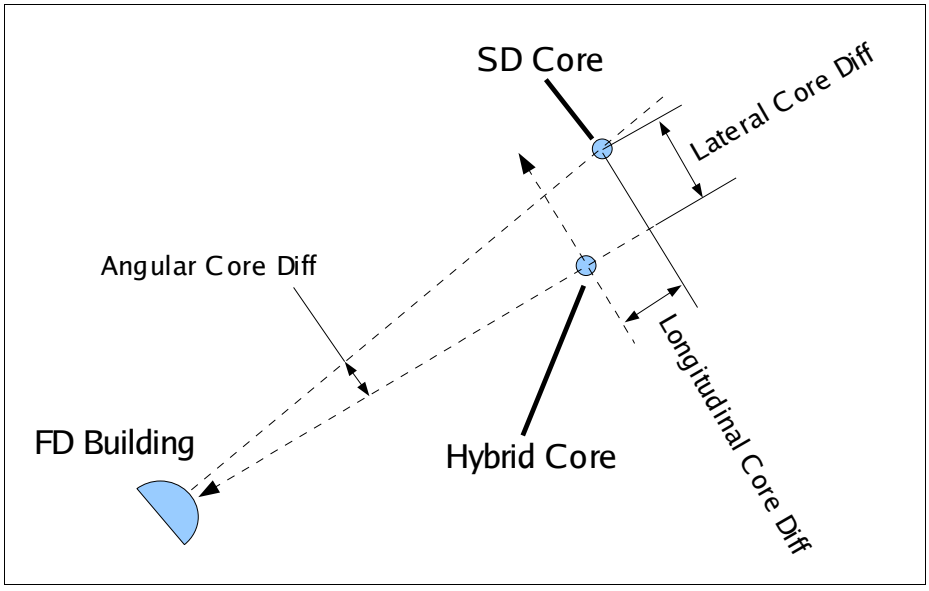

Fig. 3.12. Diagram of the angular and longitudinal differences between the hybrid and the SD core. From [113].

S. Falk et al. [39] previously used the SDP reconstruction of Golden Hybrids to determine both azimuth and elevation offsets. This was done by minimising the angular difference between the SDP and the SD core direction seen from the FD eye. For a single shower, there is a degeneracy in azimuth and elevation offsets. Combining multiple showers with different geometry removes this degeneracy (see figure 3.13).

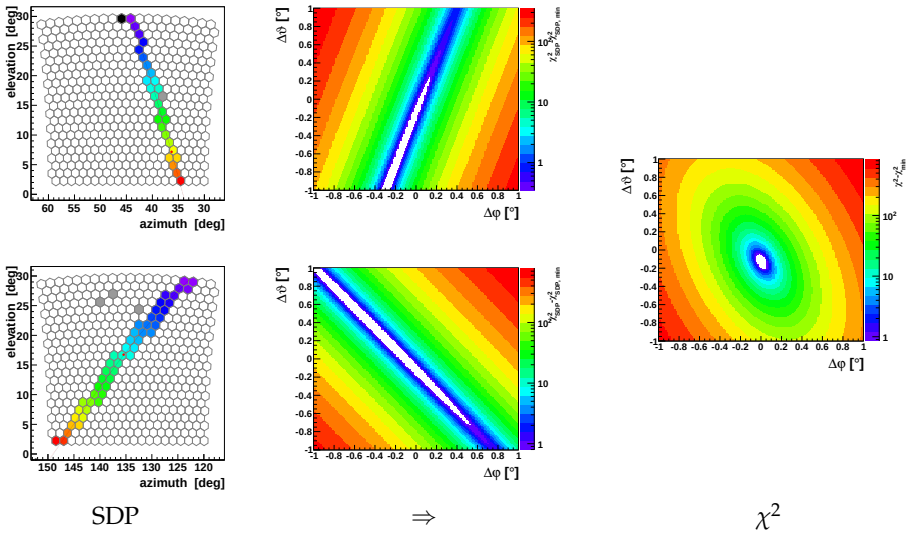

Fig. 3.13. (left) Two different SDPs projected onto the FD camera; (center) χ^2 SDP in parameter space $\Delta\phi - \Delta\theta$; (right) combined χ^2 of the two events. $\Delta\phi$ is the azimuth offset an $\Delta\theta$ is the elevation offset. From [39].

The remainder of this section describes the use of hybrid showers to determine both elevation and azimuth offsets of the fluorescence telescopes. In this study, two methods are used - one comparing the SD core with that predicted from the SDP fit, and one comparing the core time predicted by the SD and FD fits.

3.3.1 SDP method

Event selection

Events had to be golden hybrids with the SD axis and core reconstructed. For an accurate SDP, events with a 20 degree track in one telescope were selected. Although the SDP accuracy does not depend on distance, the angular error from the SD core uncertainty does. SD core errors are typically around 100 m. Events with a large core to eye distance were needed. There were about 2000 events with a core distance of more than 15 km but at that distance, there are very few vertical shower tracks. This is because, at a 20 degree altitude, and a large core distance, the depth of the atmosphere is too shallow for the vertical shower to have developed and is not visible. Since a 20 degree track length is required for a good time fit, a core distance of greater then 10 km was chosen so that vertical tracks of sufficient angular length were included. Because there were so many events, an additional cut was made to only select showers that had triggered 25 or more pixels. Over 3000 events were selected.

Determining the telescope pointing offset

The component of the telescope pointing offset perpendicular to the shower track can be determined by finding the angular deviation of the SD core from the SDP. The angular offset of the core from the SDP will be:

$$\Delta\phi = \hat{n} \cdot \overrightarrow{Core} \tag{3.11}$$

where $\hat{n}$ is the SDP normal and $\overrightarrow{Core}$ is the unit vector in the direction of the SD core from the eye. The core location was given in the site coordinate system and had to be converted to a coordinate system specific to the eye. Events were reconstructed once with only pixels with even numbered telescopes and once with odd numbered telescopes to avoid pixels from other telescopes with different offsets from contaminating the SDP fit. Information from many shower events were combined by fitting the equation:

$$\Delta\phi = |S| cos(\alpha - \beta) \tag{3.12}$$

to extract the absolute telescope pointing offset $\overrightarrow{S}$. α is the angle between the horizontal and the direction perpendicular to the shower track and β is the angle between the horizontal and the direction of the telescope pointing offset $\overrightarrow{S}$ defined in Figure 3.14. So for each shower $\Delta\phi$ and α are known, and a fit of equation 3.12 for a sample of showers results in an estimate of $|S|$ and β.

3.3.2 Timing method

In SD reconstruction, the arrival time of the shower core at the ground is calculated so the core direction and time can be compared to those parameters from the FD time fit.

Event selection

For an accurate monocular FD time fit, a long angular track length is required as well as a small value of $\frac{d\chi}{dt}$. Events with a track length of 20 degrees and a core distance of at least 10 km were selected. These are the same criteria as those for the SDP method so the same set was used.

Determining the offset

The SD core time and location was converted into an FD time and χ angle. Light propagation time must be taken into account when determining the time that the eye sees the shower arrive at the core. The SD-FD time offset must also be taken into account. This is a small

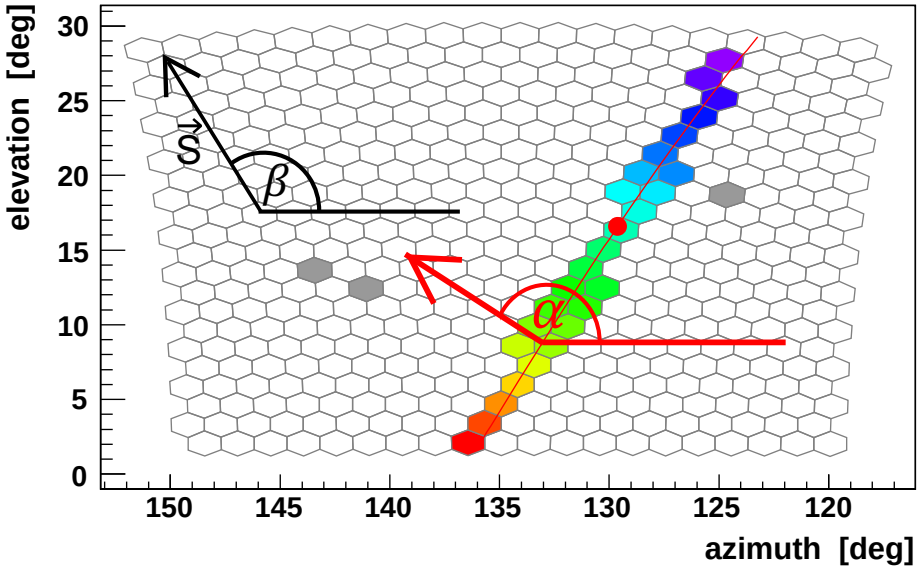

Fig. 3.14. Definition of shower and telescope offset directions. The black vector $\vec{S}$ (exaggerated in magnitude) is the offset of a telescope. Angles α and β are measured from the horizontal. The horizontal is the vector defined as the cross product of the direction of the shower core and the zenith.

time offset beteen the clocks in the Flourescence detector and the Surface detector stations. This offset was found by using horizontal laser shots from the central laser facility [15]. The SD-FD time offset used in this study is 300 ns for all eyes (this is discussed in 3.4.3). The component of the χ offset in the direction of the core will be:

$$\Delta\chi = \chi_{FD}(t_{core}) - \chi_{core} \tag{3.13}$$

where χ_{core} is the chi angle of the core derived using the SD fit and $\chi_{FD}(t_{core})$ is the FD time fit's χ angle at the core time (accounting for light propagation). The contributions to error come from both the FD and SD. The error contribution from the FD is predominantly from the timing fit, as described in section 3.2.1. The error contribution from the SD is not due to error in the timing of the core, but rather the position of the core, as the position of the core will affect propagation time to the FD, and uncertainties in core position are typically much larger than the timing uncertainties (multiplied by the speed of light).

The offsets $\Delta\chi$ are then fitted to determine the pointing offset $\vec{S}$ using the equation

$$\Delta\chi = |S|cos(\alpha - \beta) \tag{3.14}$$

where β is the angle between the horizontal and the direction of the telescope offset and α is the angle between the horizontal and the direction of the shower track defined in figure 3.15. Again $\Delta\chi$ and α are known for each event, and estimates of $|S|$ and β result for each fit.

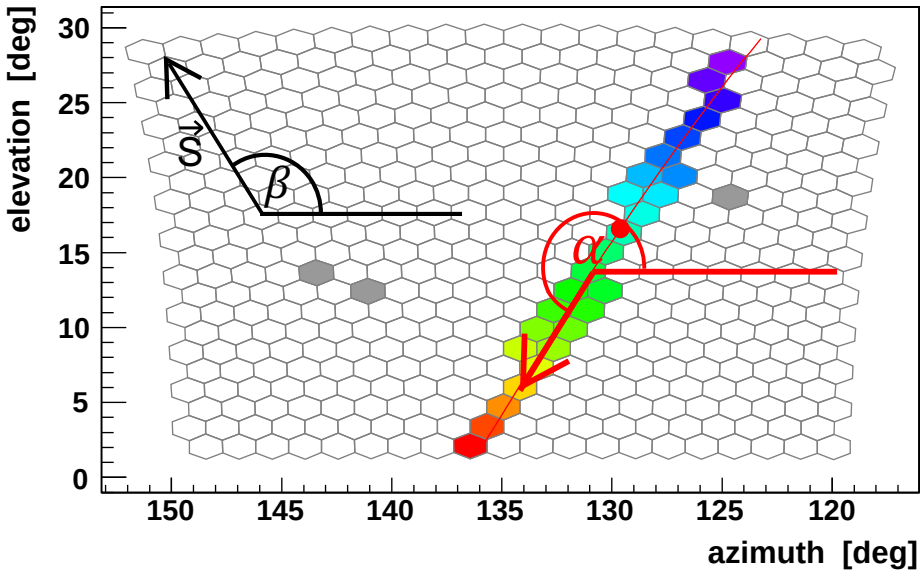

Fig. 3.15. Definition of the timing offset geometry.

3.3.3 Core bias effect on SDP method

In inclined showers, there is a bias in the SD core position [39]. This is because at a given core distance, a station on the upstream side of the shower will have a larger signal, as particles heading to the downstream station have to traverse a greater atmospheric depth (see figure 3.16). This results in a core position biased towards the upstream side of the shower, and due to a curved front being considered for axis fitting, the reconstructed axis direction is shifted to a smaller zenith angle. The bias in core position can be up to 100 m depending on zenith angle and primary composition, as the difference in depth between upstream and downstream stations is dependent on zenith angle, and the shower age and contribution of the electromagnetic component relative to the muon component are dependent on both zenith angle and composition.

The effect of the SD core bias is to create an apparent telescope elevation offset. Due to the dependence of the core bias on composition, a method for correcting the effect on alignment was chosen to be independent of the magnitude of the asymmetry. The angular size of the SD core bias seen by an FD eye is inversely proportional to the core-eye distance. The apparent elevation offset ΔY can be expressed as

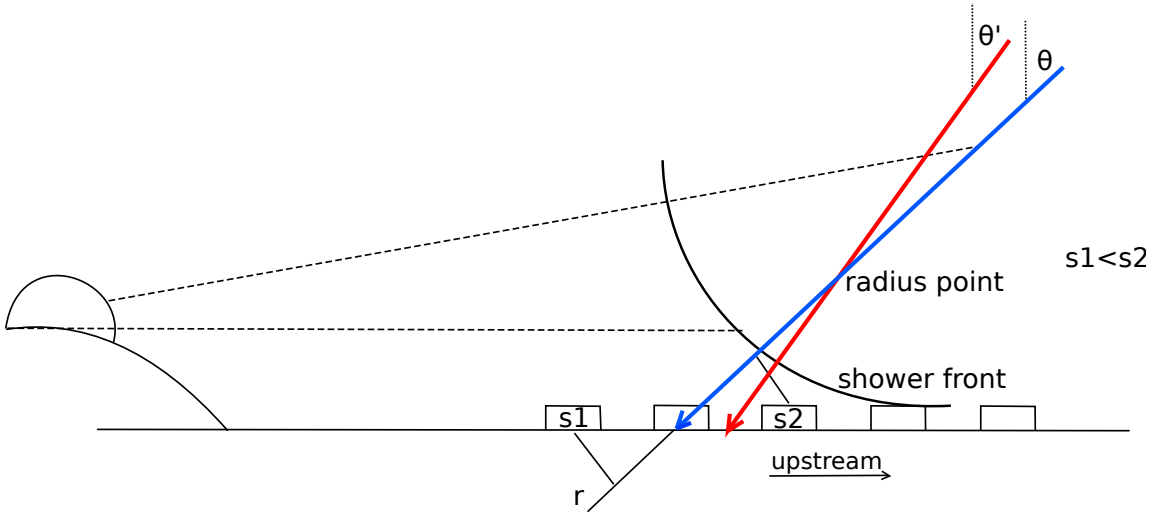

Fig. 3.16. Diagram of an inclined shower showing the effect of asymmetry on the reconstructed axis. In this case, s2 has a higher signal than s1, despite having the same core distance. The reconstructed shower geometry is shown with a core shifted towards s2. The reconstructed zenith angle (θ') is smaller than the true zenith angle (θ), due to the shower front curvature. From [39].

$$\Delta Y = a + b\frac{1}{r} \tag{3.15}$$

where r is the core-eye distance of the shower used. The parameter a is the true offset of the telescope and b measures the effect of asymmetry. In the current study, the apparent offset was found using showers from 9 different distance bins to perform a linear fit of apparent offset vs $\frac{1}{r}$. Since the effect is the same for every telescope, the average slope was found and this average was used to obtain the corrected elevation offsets. Because the elevation offsets were used, the fit parameters for the apparent telescope offset in each distance bin were changed from $|S|$ and β to the azimuth and elevation offsets, ΔX and ΔY where $\Delta X = |S|\cos(\beta)$ and $\Delta Y = |S|\sin(\beta)$. The fit for the offset then becomes

$$\Delta\phi = \Delta X\cos(\alpha) + \Delta Y\sin(\alpha) \tag{3.16}$$

The method of fitting ΔY vs $\frac{1}{r}$ can also be used in the timing method to test for a residual FD-SD time offset since a time offset would cause an apparent elevation offset proportional to $\frac{1}{r}$.

3.3.4 SDP resolution

It has been observed in the results from the relative offsets, that errors in SDP fits may be overestimated. The SDP fit involves minimising L^2, for the following function:

$$L^2 = N\frac{\sum_{i=1}^{N} q_i \Omega_i^2}{\sigma^2 \sum_{i=1}^{N} q_i} \tag{3.17}$$

for N pixels, with the i'th pixel having an integrated signal q_i, and angular distance from the trial SDP Ω_i. The value of σ is chosen as 0.35°, to give L^2/N a unit mean for laser events. L^2 is thus used as a χ^2 estimate. It has been found [111] that for error determination, the use of L^2 as a χ^2 estimate only holds if pixel offsets Ω_i are normally distributed. Due to pixels being distributed in a regular grid, Ω_i values follow a uniform distribution. For the majority of events, this means that errors in SDP geometry are smaller than the estimate currently used. A plot of the $\text{Pull}_{\text{SDP}_\theta}$ distribution from simulated events is shown in figure 3.17, with the difference between reconstructed and true values of SDP_θ, divided by the estimated error. Most geometries show an error 2-3 times smaller than the estimate. Events with $\text{SDP}_\theta \approx 60^\circ$ show an error much larger than the estimate. This is because $\text{SDP}_\theta = 60^\circ$ corresponds to an axis of symmetry of the camera grid, where showers may trigger a single line of pixels. As a result of this, showers with a true SDP_θ near (but not necessarily exactly equal to) 60° may be reconstructed as $\text{SDP}_\theta = 60^\circ$, with all $\Omega_i^2 = 0$, resulting in a greatly underestimated error. To compensate for this, events with $55^\circ < \text{SDP}_\theta < 60^\circ$ are excluded from the offset fits, and the remaining events have errors rescaled by a factor of 0.5.

3.4 Results

The results for absolute offsets are shown relative to previously estimated pointing directions, shown in table 3.1.

3.4.1 Relative offsets

Figure 3.18 shows some of the fits for the relative pointing offsets (defined in 3.2). Coihueco telescopes 5 & 6 and Loma Amarilla telescopes 3 & 4 have the two largest relative pointing offsets, which are shown in figures 3.18(a) and 3.18(b). The parameters of the fit are the offset, $|S|$, and the angle, β defined in 3.2. The blue points are from the SDP method, defined in 3.2.2. The red points are from type I events, and the green points are from type II events, both for the timing method defined in 3.2.1. The plots give the offset of the first telescope

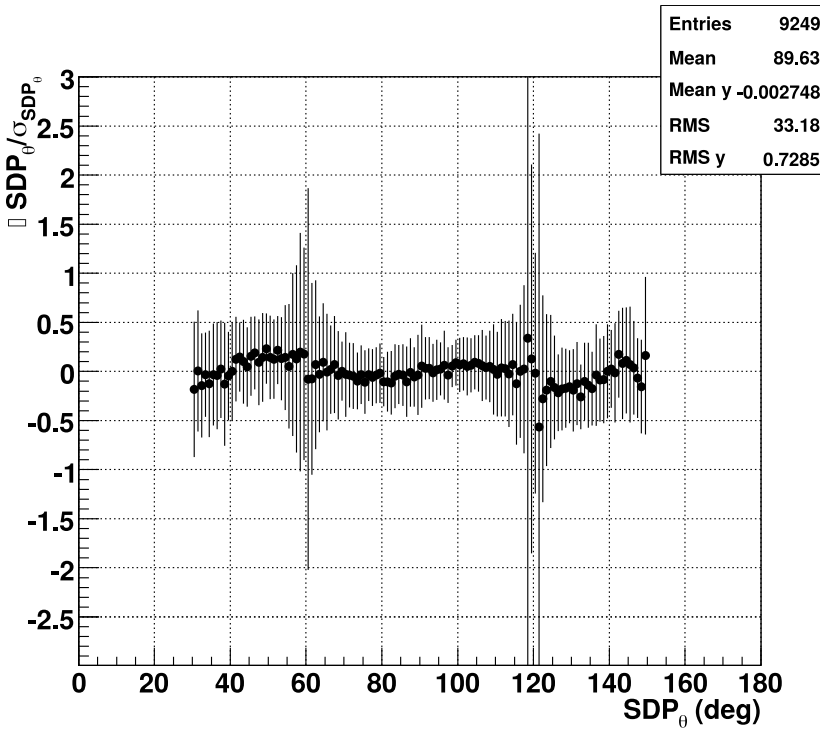

Fig. 3.17. $\text{Pull}_{\text{SDP}_\theta}$ distribution for a series of simulated events, with points representing mean values and error bars representing RMS. From [111].

relative to the second (e.g. the pointing offset for Coihueco 5 6 is the pointing offset of telescope 5 relative to telescope 6).

It appears that the SDP method and the timing method agree with each other. The timing method and SDP method are independent methods with different systematic uncertainties giving confidence in the results.

The estimated errors for each event determined using the method described in section 3.2 seem to be overestimated as the χ^2/ndf for the fits is less then 1 (e.g. figure 3.18). It is quite noticeable that most of the points have error bars much larger then their average deviation from the fit. This may be due to the error estimates for SDP and timing fits being too large when applied to the ends of a shower track. As fitting methods and error estimates were not tested for this specific application, this could be the case even if the error estimate for the core positions and axis direction are reasonable. The error overestimate for individual data points is likely to propagate to overestimated errors in $|S|$ and β from the fit. This is discussed and corrected for when determining the absolute offsets.

Table 3.2 gives the relative pointing offsets for all of the telescope interfaces. The offsets have been converted to azimuth and elevation offsets.

Table 3.1 Pointing directions from FTelescopeList.xml.

eye	telescope	azimuth	elevation
LL	1	15.13	16.04
LL	2	45.00	16.06
LL	3	74.94	15.96
LL	4	104.96	16.14
LL	5	134.93	15.96
LL	6	164.90	15.85
LM	1	14.94	15.97
LM	2	44.80	15.81
LM	3	74.79	15.82
LM	4	104.99	15.75
LM	5	135.02	15.84
LM	6	164.92	15.89
LA	1	15.32	16.20
LA	2	45.07	16.07
LA	3	75.08	16.12
LA	4	104.9	15.75
LA	5	135.15	16.07
LA	6	165.11	15.90
Co	1	15.13	15.94
Co	2	45.06	16.19
Co	3	74.91	16.21
Co	4	104.92	16.26
Co	5	134.96	16.17
Co	6	164.78	16.23

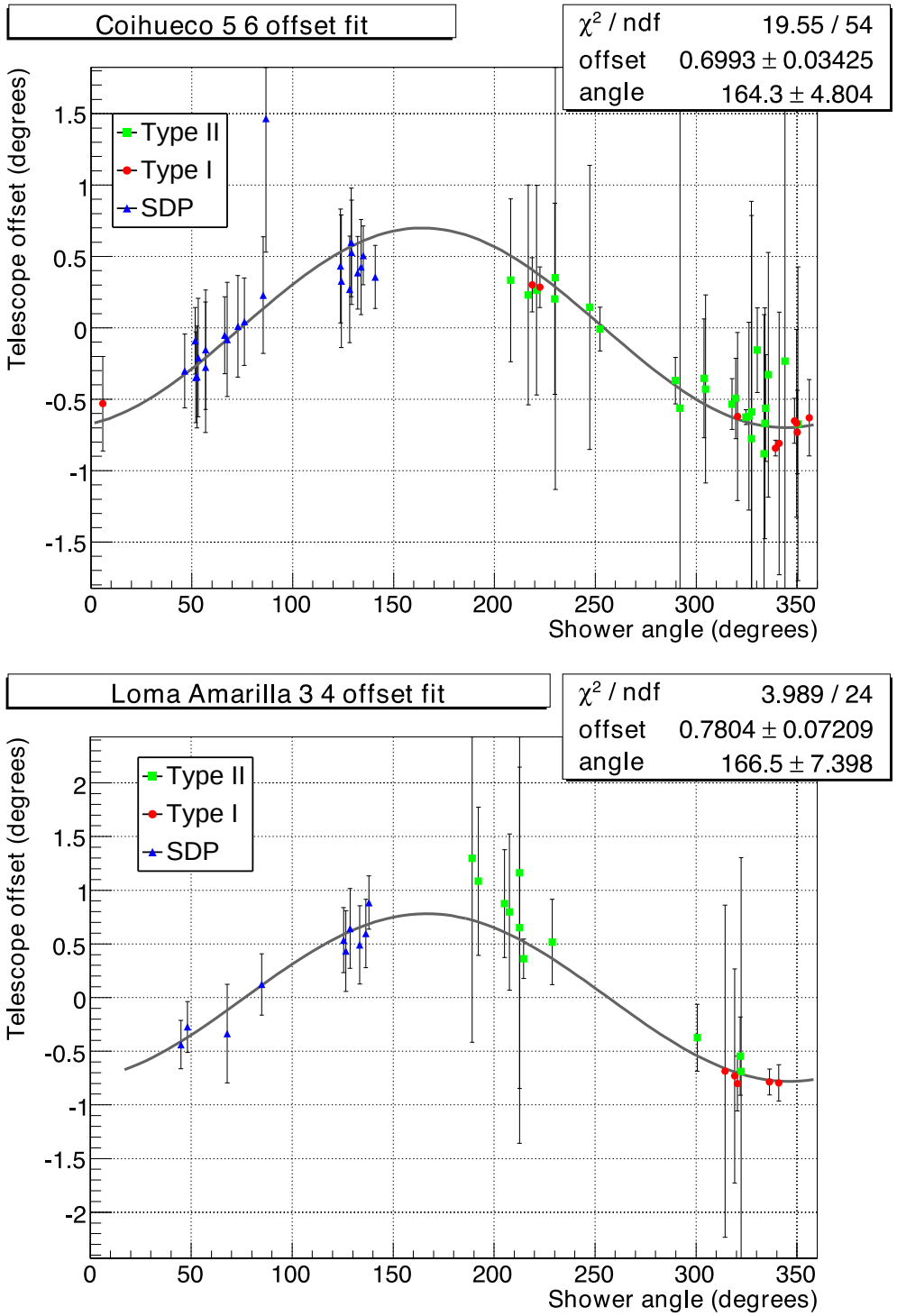

Fig. 3.18. Relative pointing offset fits for the two telescope boundaries with the largest offset. These are for Coihueco telescopes 5 and 6, and Loma Amarilla telescopes 3 and 4. The "offset" parameter (in the box at the top right of each plot) is the magnitude of the pointing offset, $|S|$ and the angle is the angle of the offset, β from equations 3.9 & 3.10, in units of degrees. The "Telescope offset" on the y-axis is $\Delta\phi$, and the "Shower angle" on the x-axis is α, both from equations 3.9 & 3.10.

Table 3.2 Relative pointing offsets. The highlighted values are the two largest measured offsets, with fits shown in figure 3.18.

Eye	Telescope	Azimuth offset (deg)	Elevation offset (deg)
LL	1-2	-0.127±0.024	0.087±0.035
LL	2-3	0.028±0.045	0.269±0.016
LL	3-4	0.183±0.011	-0.0011±0.7861
LL	4-5	0.0020±0.0266	0.126±0.005
LL	5-6	0.245±0.132	0.308±0.105
LM	1-2	-0.148±0.018	0.072±0.034
LM	2-3	0.142±0.041	0.111±0.052
LM	3-4	0.268±0.017	0.236±0.019
LM	4-5	0.342±0.017	0.087±0.062
LM	5-6	-0.184±0.031	0.085±0.065
LA	1-2	-0.434±0.027	0.057±0.072
LA	2-3	-0.045±0.050	-0.101±0.023
LA	3-4	**-0.759±0.060**	**0.182±0.099**
LA	4-5	0.141±0.031	0.160±0.028
LA	5-6	-0.180±0.010	0.0038±0.0767
Co	1-2	-0.187±0.012	-0.047±0.044
Co	2-3	-0.327±0.011	0.030±0.046
Co	3-4	-0.194±0.027	0.121±0.042
Co	4-5	-0.0070±0.0380	0.070±0.005
Co	5-6	**-0.673±0.028**	**0.190±0.057**

3.4.2 SDP method for absolute offsets

Both the azimuth and elevation offsets were examined for a dependence on core distance. As expected, azimuth offsets did not show a dependence on core distance. Due to the bias in core position for inclined events, elevation offsets did show a dependence on core distance, requiring a correction. Figures 3.19-3.22 show the fits of apparent elevation offset ΔY vs $\frac{1}{r}$, for the method of compensating for core position bias mentioned in section 3.3.3. The weighted average of the fitted slopes was obtained to use as a final correction for fits to telescope offsets. Telescopes 1 and 6 for each eye overlook the edge of the SD array, with lower statistics, and a more limited range of shower geometries, so these telescopes were not considered for the calculation of the average slope. The average slope was found to be 1700 ± 100 deg·m. The core bias effect is expected only to affect elevation offsets. Fits for apparent azimuth offset ΔX vs $\frac{1}{r}$ were also done, confirming that core distance had a negligible effect on apparent azimuth offset. With the slope obtained, the observed offset can be expressed as:

$$\Delta\phi = \Delta X \cos(\alpha) + \Delta Y(r) \sin(\alpha) \tag{3.18}$$

where:

$$\Delta Y(r) = a \cdot \frac{1}{r} + \Delta Y_0 \tag{3.19}$$

with the slope a, fixed to the previously determined value 1700 ± 100 deg·m, and the true elevation offset of the telescope ΔY_0. This function was used to determine the corrected pointing offset for each telescope. An example of this fit is shown in figure 3.23. To minimise the systematic error due to the uncertainty in the slope, events were only used with a core distance greater than 8000 m. Due to the lower statistics for telescopes 1 and 6, these fits to these telescopes included events at a distance greater than 6000 m. The systematic error due to the uncertainty in the slope is $\approx 0.01^\circ$. Table 3.3 lists the corrected elevation and azimuth offsets of the telescopes. The χ^2/ndf in table 3.3 is for the final fit to determine the corrected offset. All offsets shown are relative to the telescope pointing directions listed in table 3.1. Most pointing offsets are small ($\sim 0.1^\circ$), but there are several much larger offsets, the largest being telescope 1 of Loma Amarilla, with an azimuth offset of over 0.7°. Telescope 4 of Loma Amarilla received a re-alignment of its mirror segments (see section 3.6). Since the realignment may have altered pointing direction, this telescope has been analysed both before and after the realignment, shown in figure 3.21.

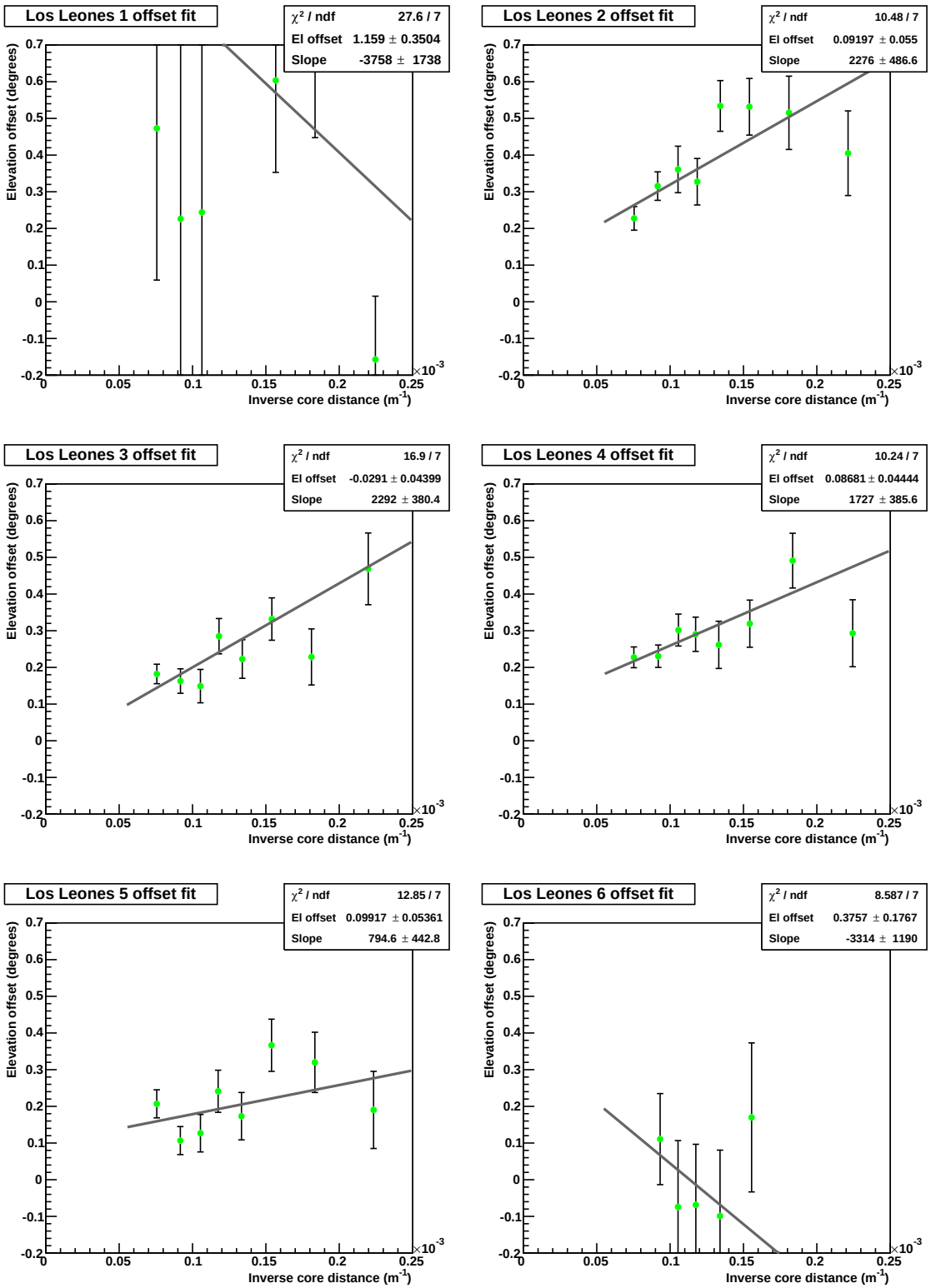

Fig. 3.19. SDP fits to the elevation offsets for the Los Leones telescopes.

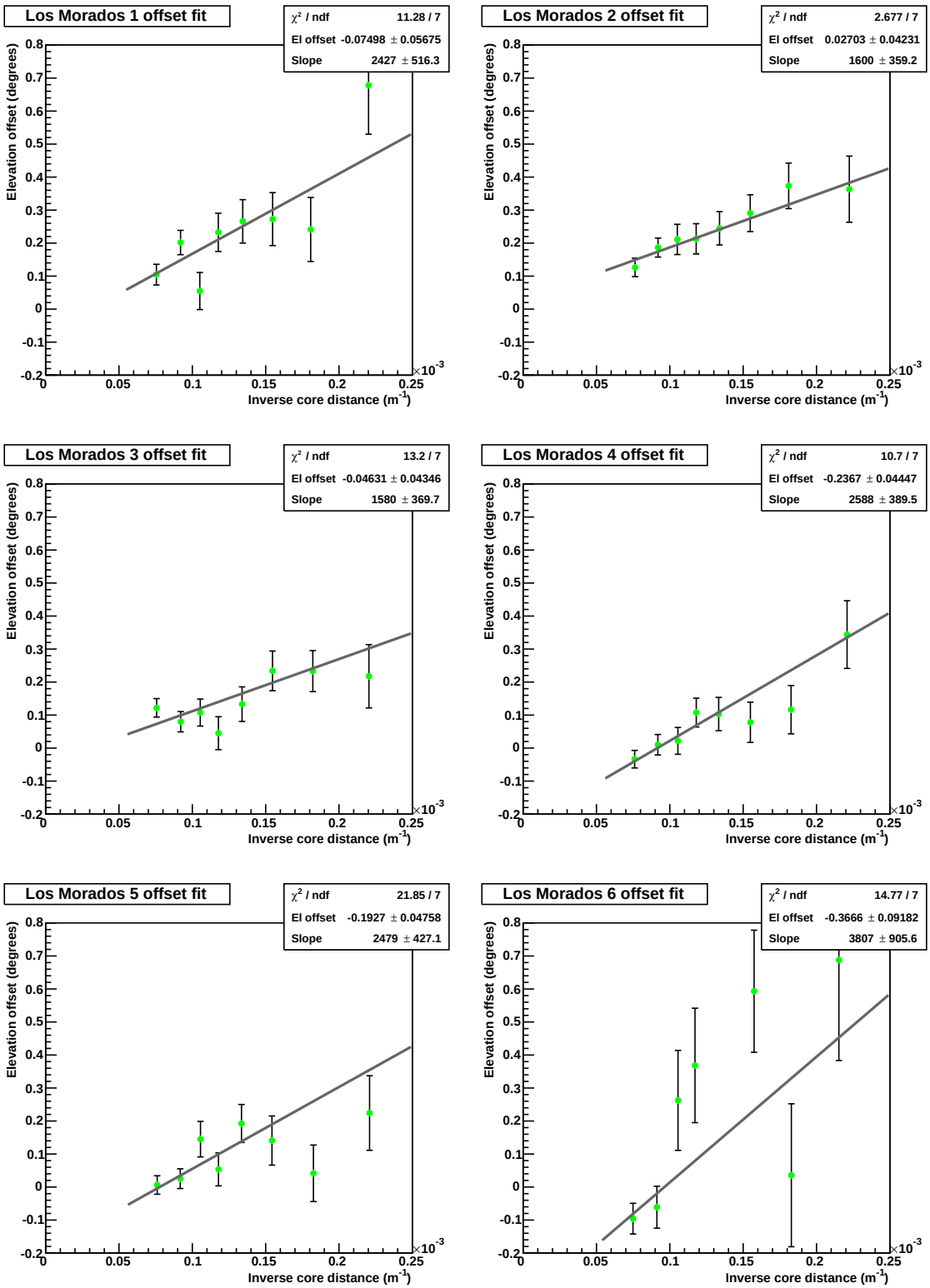

Fig. 3.20. SDP fits to the elevation offsets for the Los Morados telescopes.

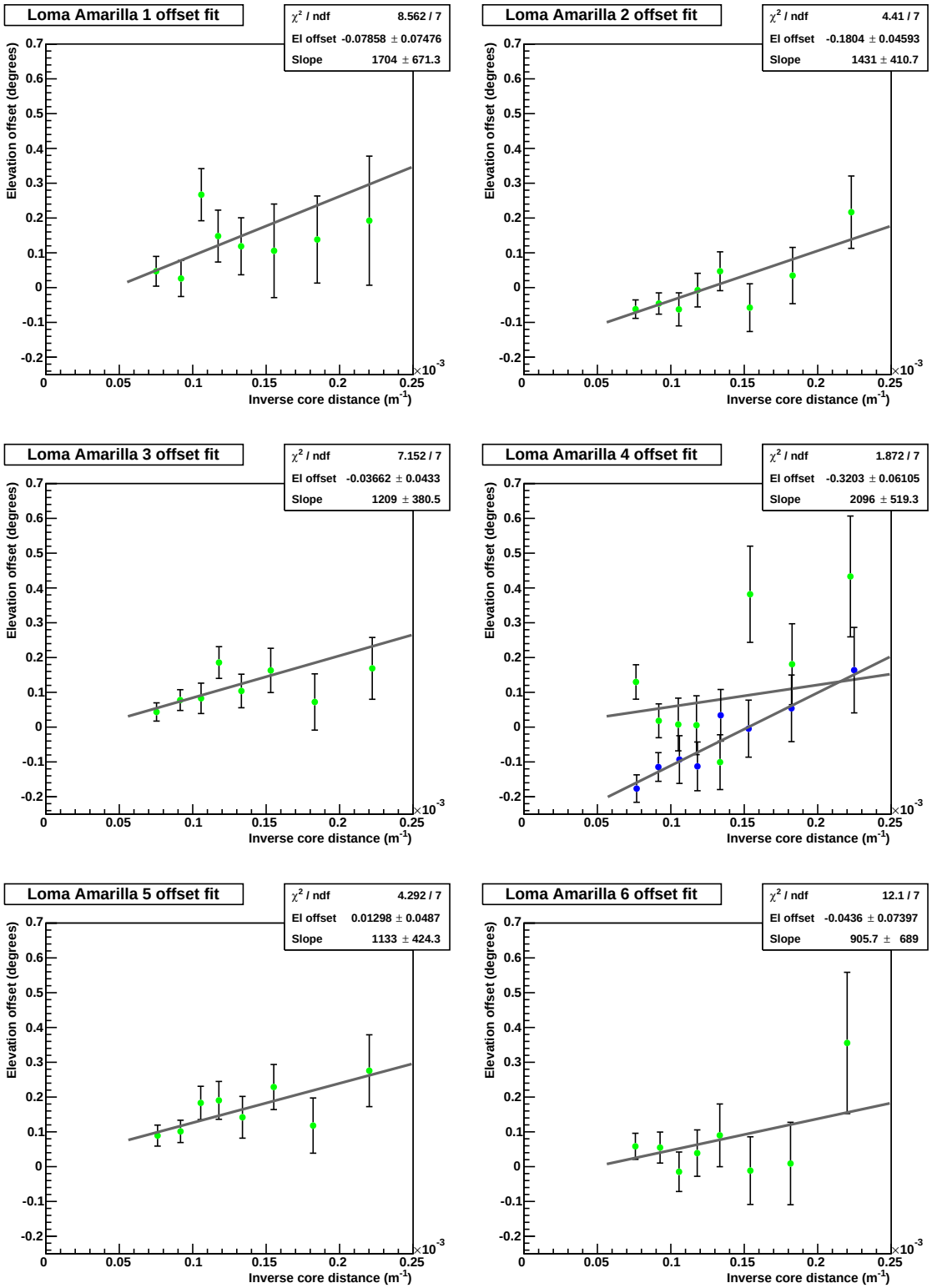

Fig. 3.21. SDP fits to the elevation offsets for the Loma Amarilla telescopes. The blue points for telescope 4 are after the mirror re-alignment.

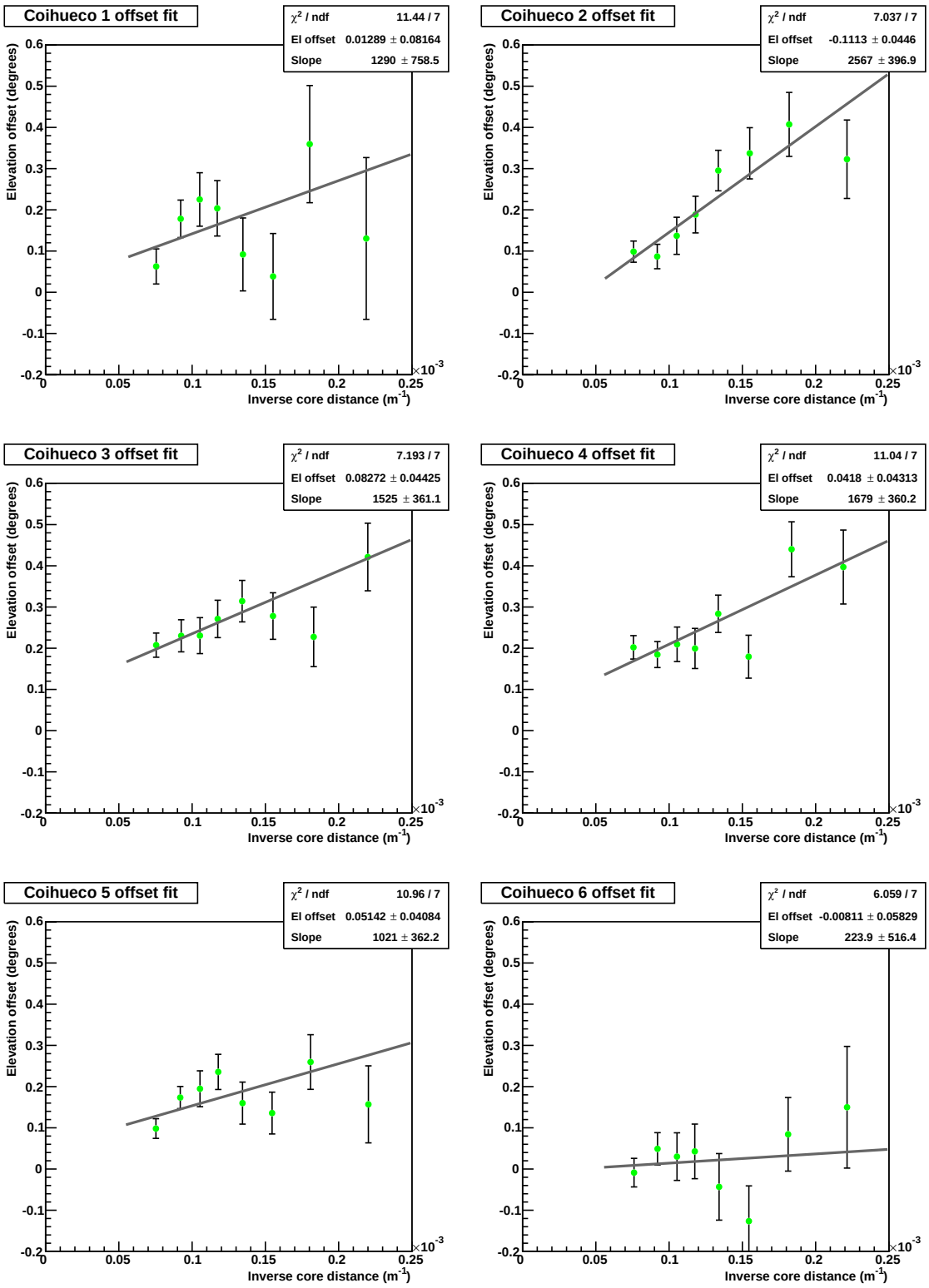

Fig. 3.22. SDP fits to the elevation offsets for the Coihueco telescopes.

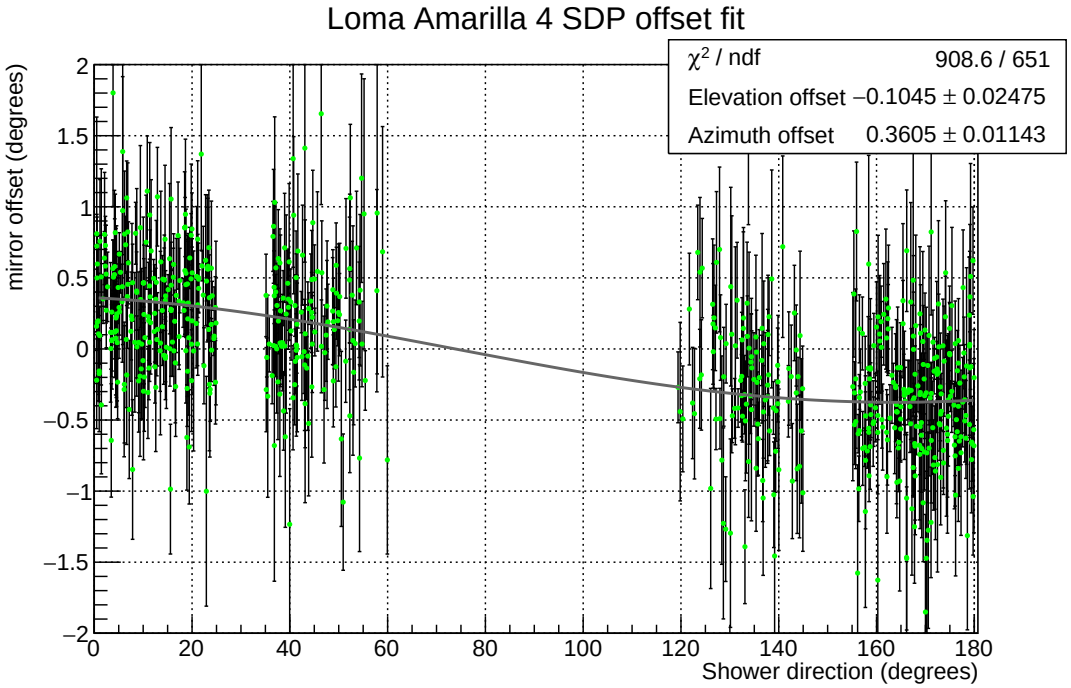

Fig. 3.23. The SDP fit to the apparent offset $\Delta\phi$ against the direction of the shower track α for Loma Amarilla telescope 4, with each data point corrected for core distance.

Table 3.3 Results from the SDP method. The most notable offset have been highlighted. LA telescope 4* is the offset obtained after a realignment of the mirror segments. There is an additional systematic error of 0.01° from the core bias correction.

Eye	Telescope	Elevation offset (deg)	Azimuth offset (deg)	χ^2/ndf
LL	1	0.41±0.13	-0.21±0.13	146/160
LL	2	0.143±0.017	-0.150±0.007	1326/1239
LL	3	0.037±0.014	0.011±0.006	1959/1729
LL	4	0.102±0.014	-0.050±0.006	1955/1746
LL	5	0.007±0.018	0.073±0.007	1511/1276
LL	6	-0.21±0.06	0.11±0.03	312/260
LM	1	0.003±0.016	-0.046±0.007	2456/2177
LM	2	0.003±0.014	0.255±0.006	2281/2007
LM	3	-0.053±0.015	0.282±0.006	2155/1880
LM	4	-0.131±0.014	-0.041±0.006	2103/1873
LM	5	-0.104±0.014	-0.251±0.006	2079/1876
LM	6	-0.15±0.02	0.012±0.012	664/709
LA	1	**-0.07±0.02**	**-0.739±0.009**	1511/1329
LA	2	-0.194±0.014	-0.194±0.006	2572/2088
LA	3	-0.078±0.013	-0.103±0.006	2119/1999
LA	4	**-0.10±0.02**	**0.361±0.011**	909/651
LA	4*	**-0.28±0.02**	**-0.187±0.009**	992/893
LA	5	-0.033±0.016	-0.254±0.007	1830/1665
LA	6	-0.12±0.02	-0.167±0.008	1905/1643
Co	1	-0.02±0.02	-0.320±0.010	1411/1259
Co	2	-0.018±0.014	-0.252±0.006	2100/1904
Co	3	0.080±0.015	-0.039±0.007	1868/1695
Co	4	0.049±0.014	0.113±0.006	2104/1972
Co	5	0.001±0.013	-0.128±0.006	2594/2119
Co	6	**-0.14±0.02**	**0.327±0.008**	1811/1639

3.4.3 Timing method

Though a bias in the offsets obtained with the timing is not expected, the same method was applied for timing offsets as for the SDP offsets to check for a dependence on distance. This method will be effective at detecting and compensating for any bias in timing offsets due to biased core positions, as well as any systematic time offsets between core timing and FD timing not previously accounted for, as both would show a bias proportional to $1/r$. Azimuth offsets are not found to depend on core distance, as expected. Figures 3.24-3.27 show the fits of apparent elevation offset ΔY vs $\frac{1}{r}$. There is a clear dependence of apparent elevation

offset with respect to core distance, though the dependence is not as strong as for the SDP offsets. The average slope, excluding telescopes 1 and 6, is -575 ± 50 deg·m. It is not known whether this is due to a bias in core position, or an unaccounted for time offset, but if it were a time offset, this slope would correspond to a time offset of ≈ 30 ns. A time offset between the FD and the SD is known [15, 114], and is currently accounted for in geometry reconstructions, and also in this study. There is evidence of ≈ 100 ns monthly fluctuations in SD-FD time offsets, and a 30 ns is within error of the SD-FD time offset currently in use. If uncertainties in the SD-FD time offset are assumed to be the cause of the distance dependence of the apparent elevation offset, the fitted slopes determined here may be used to provide a more accurate SD-FD time offset. This slope was then used in a fit to determine offsets, with the same method as for the SDP offsets. The systematic error due to uncertainty in this slope is 0.005°. An example of this fit is shown in figure 3.28. Table 3.4 shows the azimuth and elevation offsets using timing. Results are similar to the SDP offsets, with most telescopes showing a small offset, but several much larger offsets. The largest is once again telescope 1 of Loma Amarilla, with an offset slightly larger than 0.7°, though telescope 4 of Loma Amarilla shows an offset nearly as large.

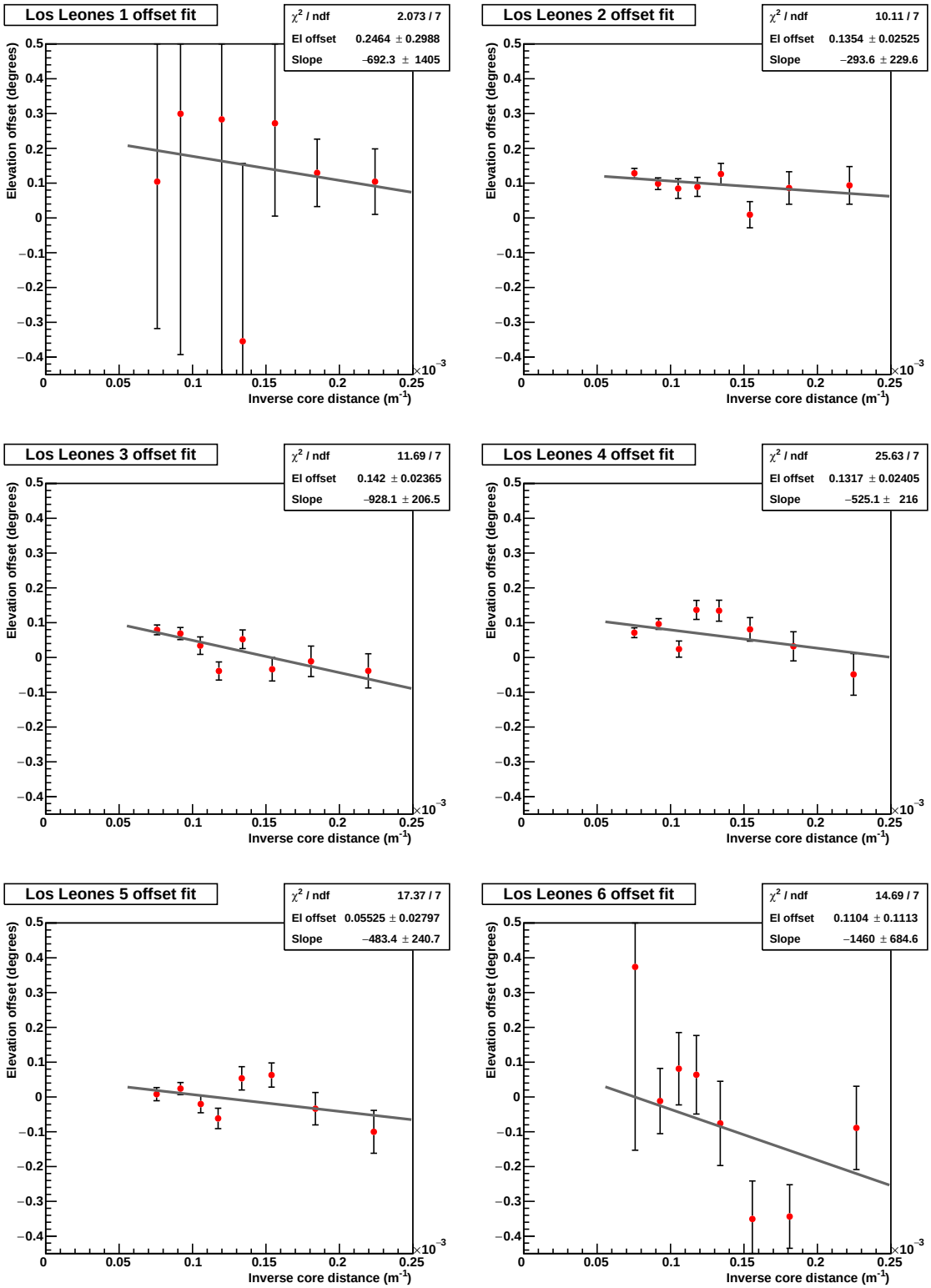

Fig. 3.24. Timing fits to the elevation offsets for the Los Leones telescopes.

Table 3.4 Results from the timing method. The most notable offset have been highlighted. LA telescope 4* is the offset obtained after a realignment of the mirror segments. There is an additional systematic error of 0.005° from the core bias correction.

Eye	Telescope	Elevation offset (deg)	Azimuth offset (deg)	χ^2/ndf
LL	1	0.16±0.17	-0.27±0.18	99/148
LL	2	0.138±0.008	-0.122±0.019	1267/1236
LL	3	0.102±0.008	0.079±0.017	1846/1761
LL	4	0.125±0.008	-0.039±0.016	1885/1793
LL	5	0.037±0.009	0.04±0.02	1207/1234
LL	6	-0.02±0.05	0.16±0.10	224/255
LM	1	0.062±0.009	-0.043±0.019	2042/2200
LM	2	0.042±0.008	0.270±0.017	1892/1966
LM	3	0.010±0.007	0.273±0.017	1863/1835
LM	4	-0.042±0.007	0.067±0.016	2203/1893
LM	5	-0.053±0.007	-0.248±0.015	2158/1885
LM	6	-0.072±0.013	0.14±0.02	965/714
LA	1	**-0.156±0.011**	**-0.73±0.03**	1163/1217
LA	2	-0.149±0.008	-0.216±0.018	2160/1899
LA	3	-0.163±0.008	-0.137±0.018	2030/1805
LA	4	**-0.592±0.015**	**0.38±0.03**	873/755
LA	4*	**-0.291±0.014**	**-0.23±0.03**	597/609
LA	5	-0.101±0.008	-0.263±0.019	1802/1530
LA	6	-0.160±0.010	-0.01±0.02	1830/1485
Co	1	-0.136±0.013	-0.39±0.03	1352/1423
Co	2	-0.001±0.008	-0.219±0.017	1904/1857
Co	3	-0.005±0.008	-0.027±0.018	1646/1686
Co	4	-0.033±0.007	0.084±0.015	2199/1994
Co	5	-0.191±0.007	-0.067±0.015	2363/2107
Co	6	**-0.292±0.012**	**0.41±0.02**	2176/1912

3.4.4 Comparison of timing and SDP methods

Figures 3.29 and 3.30 show a comparison of the absolute elevation and azimuth offsets determined by the SDP and timing methods.

The offsets determined by the SDP and timing methods are very close to each other in most telescopes. The azimuth offsets show good consistency between the two methods, with some ($\approx 0.1^\circ$) inconsistencies in Los Morados telescopes 4 and 6. For the elevation offsets, there are more inconsistencies. Los Morados shows higher elevation offsets for the timing

method across all telescopes, while Loma Amarilla shows the opposite trend. This may be due to differences in the SD-FD time offset between the FD stations. There is also a much larger disagreement for Loma Amarilla telescope 4, nearly 0.5°. This suggests that there is an additional error in telescope geometry, which was identified and corrected (this will be discussed later in section 3.6).

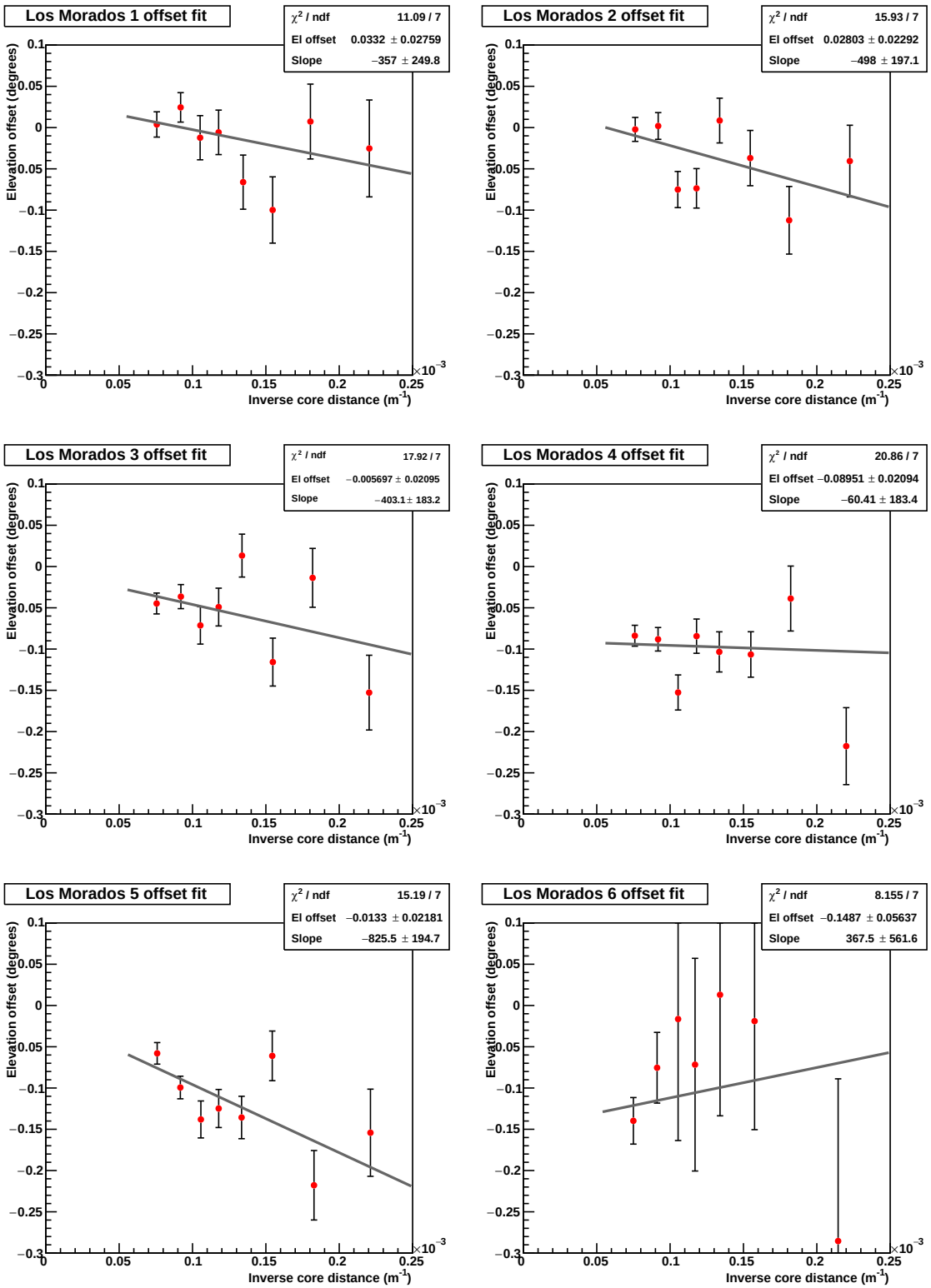

Fig. 3.25. Timing fits to the elevation offsets for the Los Morados telescopes.

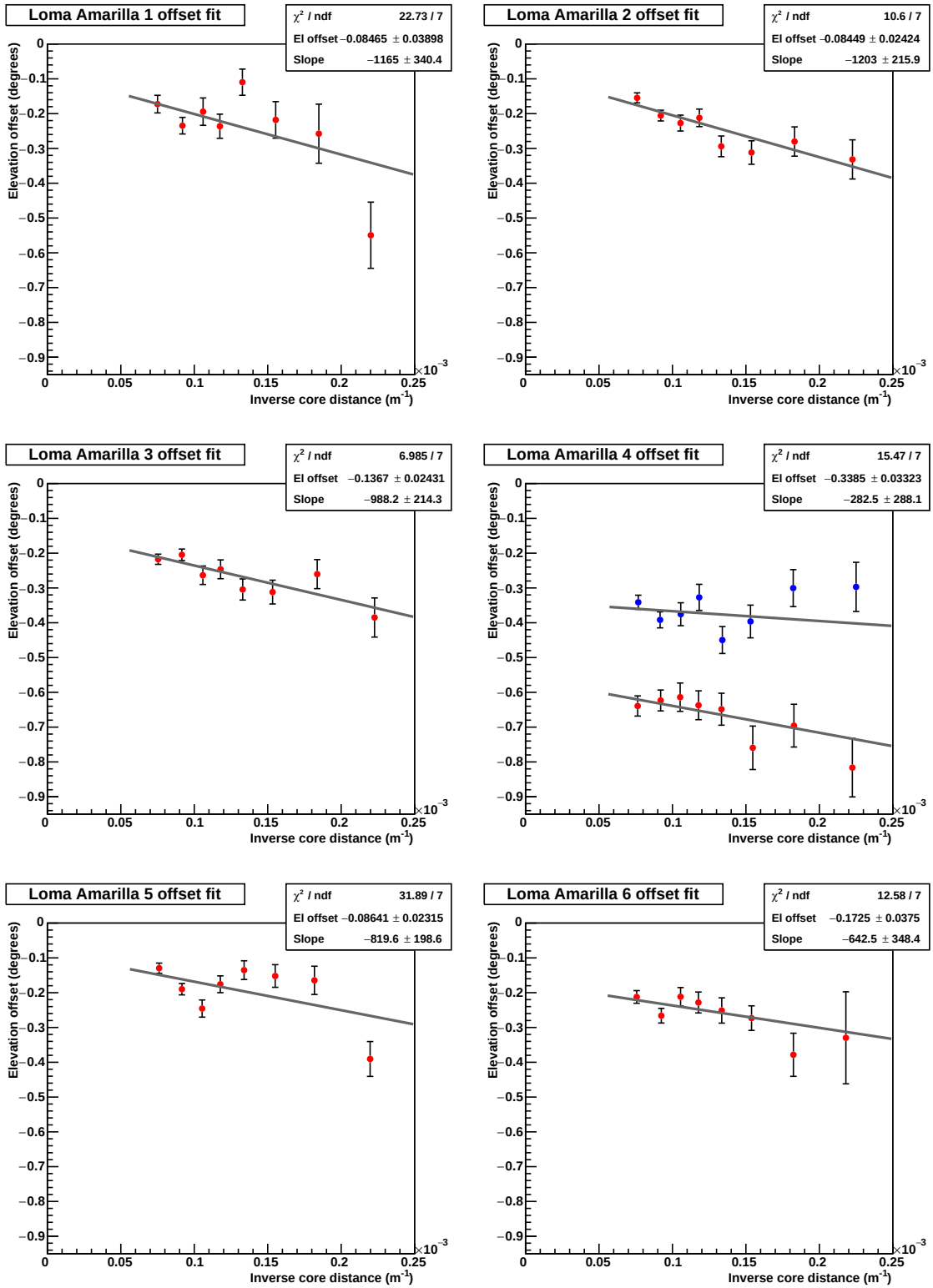

Fig. 3.26. Timing fits to the elevation offsets for the Loma Amarilla telescopes. The blue points for telescope 4 are after the mirror re-alignment.

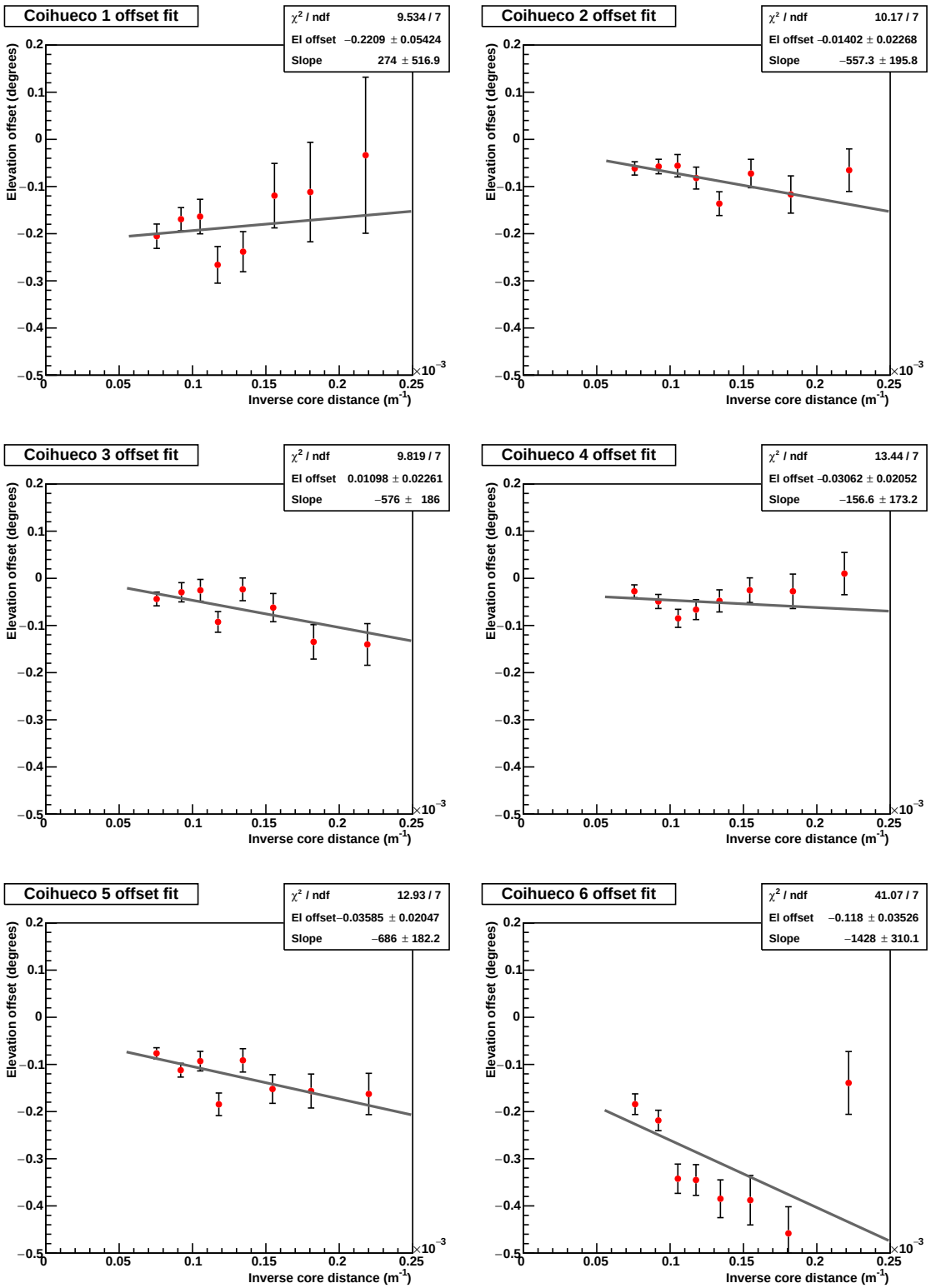

Fig. 3.27. Timing fits to the elevation offsets for the Coihueco telescopes.

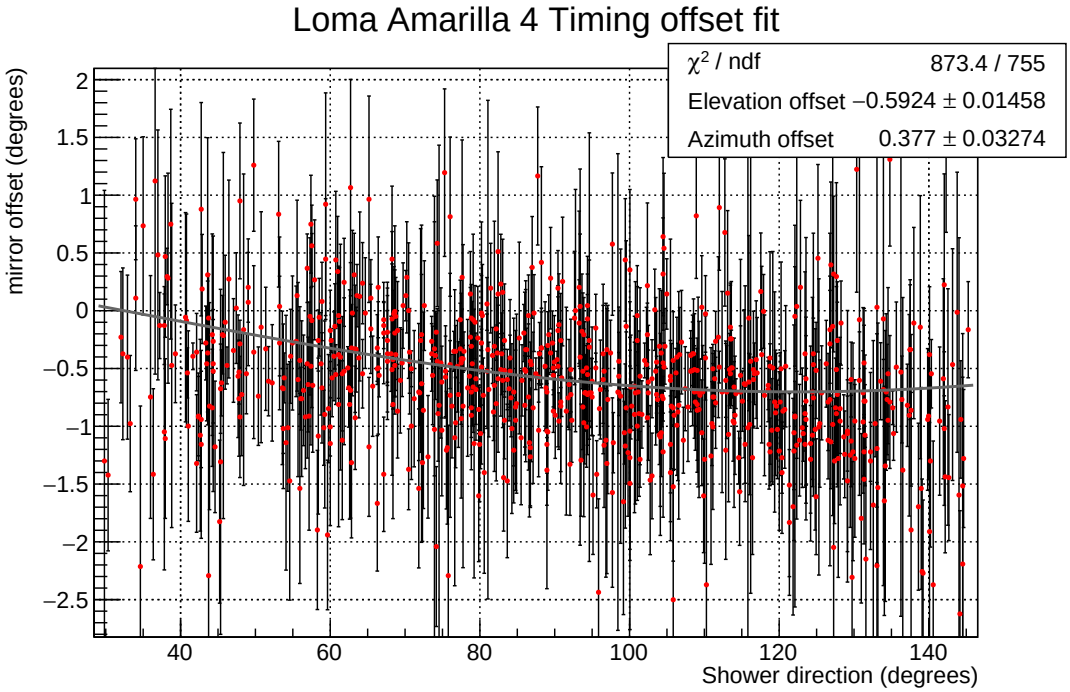

Fig. 3.28. The timing fit to the apparent offset $\Delta\chi$ against the direction of the shower track α for Loma Amarilla telescope 4, with each data point corrected for core distance.

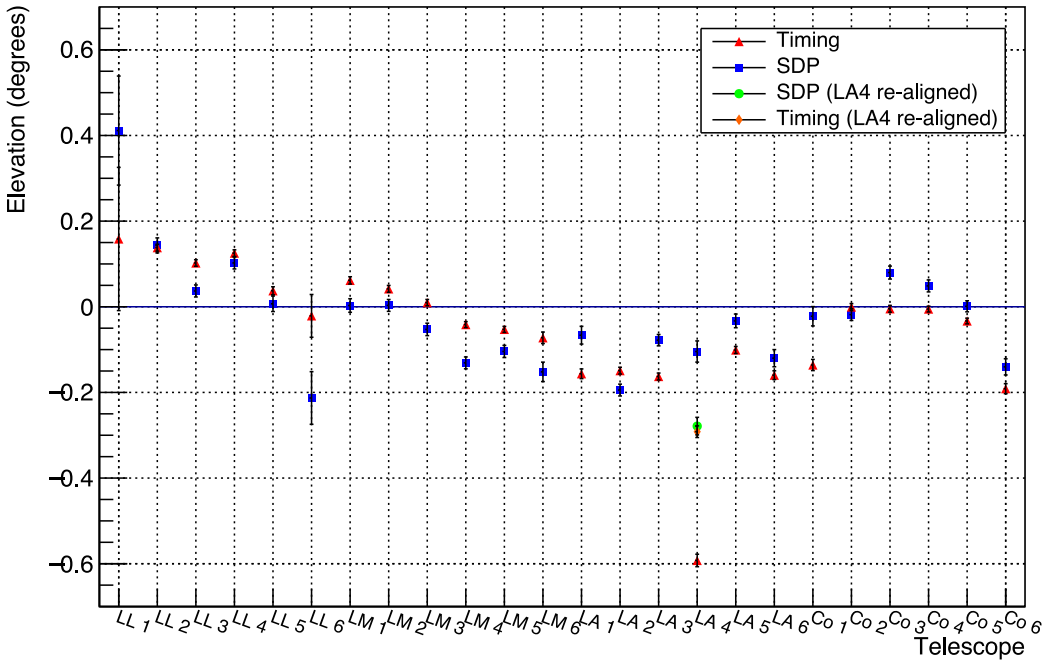

Fig. 3.29. Comparison of elevation offsets found using the SDP and timing methods. Offsets are relative to the values in the current version of Offline. The red triangles are the timing method offsets and the blue squares are the SDP method offsets. The orange diamond and green circle points are the respective timing and SDP offsets for telescope 4 of Loma Amarilla after the mirror re-alignment.

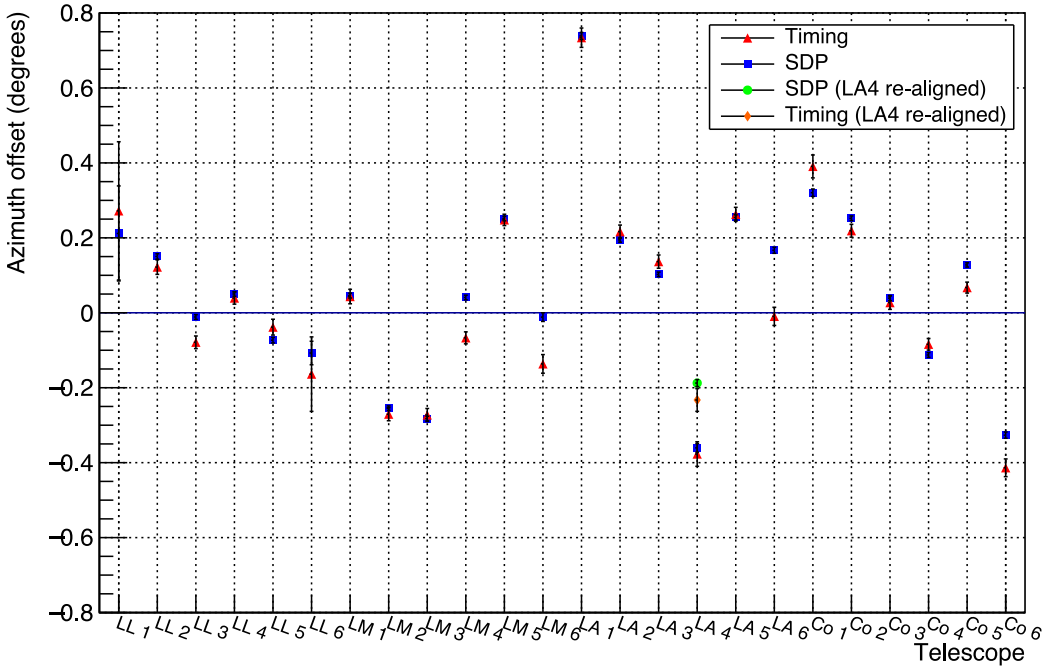

Fig. 3.30. Comparison of azimuth offsets found using the SDP and timing methods. The red triangles are the timing method offsets and the blue squares are the SDP method offsets. The orange diamond and green circle points are the respective timing and SDP offsets for telescope 4 of Loma Amarilla after the mirror re-alignment.

3.4.5 Comparison between relative and absolute offsets

It is useful to check on the accuracy of the absolute telescope pointing offsets by utilising the relative pointing results. The methodology for finding the relative offsets between two adjacent telescopes is less likely to be affected by systematic errors since it does not rely on the surface detector array. Figures 3.31 & 3.32 show a comparison between the relative offset results and the difference between the two absolute offsets, which are expected to be equivalent to each other. The elevation results show a reasonable agreement for most telescope pairs, with a notable exception being Loma Amarilla telescopes 3-4, and 4-5. Azimuth results show a good agreement, once again with Loma Amarilla telescopes 3-4, and 4-5 being the exception. This also suggests an additional error in the geometry of telescope 4.

It is possible that the telescope optics are different from the specifications, most notably the angular field of view of the telescopes. Using both absolute and relative offsets, it is possible to test if the field of view of telescopes across an eye are systematically different to expectation. The sum of all relative azimuth offsets across an eye is expected to be equal to the difference in azimuth offsets between telescopes 1 and 6. If the field of view of all telescopes in an FD station are larger of smaller than expected, the boundaries between two adjacent telescopes will show a systematic azimuth misalignment, while not affecting the azimuth offsets. since relative offsets are measured at the boundaries of the field of view. The sum of relative azimuth offsets and the difference between telescope 1 and 6 azimuth offsets are consistent for Los Leones and Los Morados, but not for Loma Amarilla and Coihueco. For Loma Amarilla, the sum of relative azimuth offsets is $-1.28^\circ \pm 0.09^\circ$, while the difference between absolute azimuth offsets for telescope 1 and 6 is $-0.572^\circ \pm 0.012^\circ$ for the SDP method, and $-0.72^\circ \pm 0.04^\circ$ for the timing method. For Coihueco, the sum of relative azimuth offsets is $-1.39^\circ \pm 0.06^\circ$, while the difference between absolute azimuth offsets for telescope 1 and 6 is $-0.647^\circ \pm 0.013^\circ$ for the SDP method, and $-0.80^\circ \pm 0.04^\circ$ for the timing method. This shows that an error in the telescope field of view is likely, and will be discussed later.

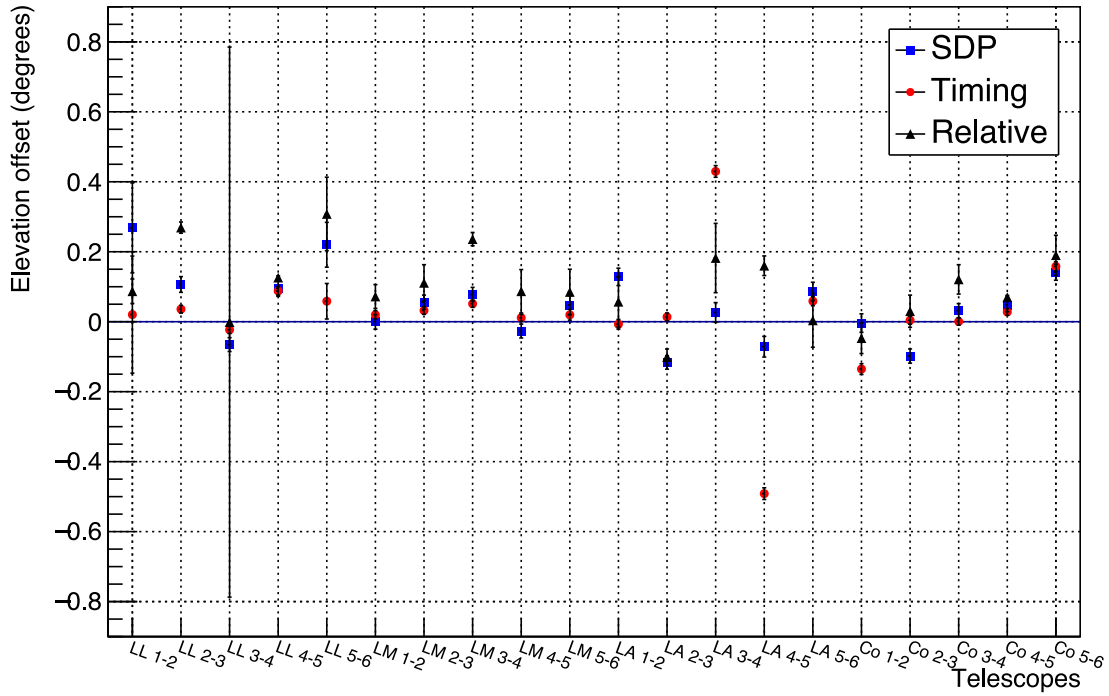

Fig. 3.31. Comparison of relative elevation offsets with the difference between adjacent absolute offsets.

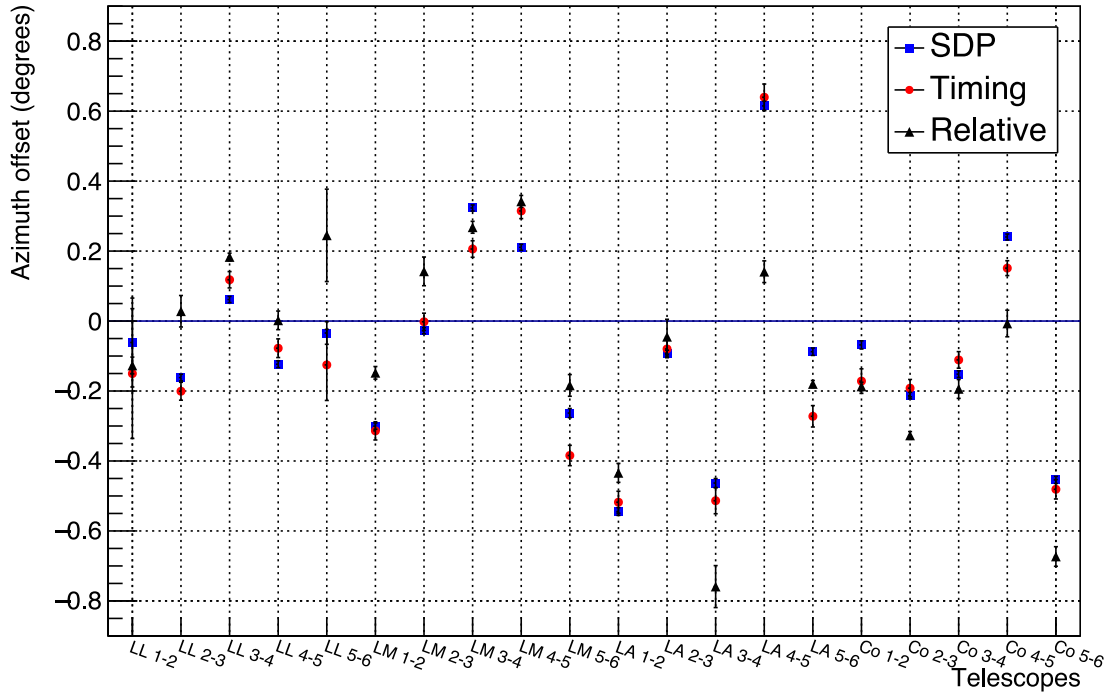

Fig. 3.32. Comparison of relative azimuth offsets with the difference between adjacent absolute offsets.

3.5 Comparison with other alignment studies

Figures 3.33 and 3.34 show a comparison between the values obtained in this study and those obtained in the previously mentioned alignment studies.The two methods observing cosmic ray showers (this study and [39]) show reasonable agreement for Los Leones and Los Morados. In Coihueco and Loma Amarilla there are much larger discrepancies, also indicating that there may be issues other than pointing directions. If this is the case, the different methods for determining pointing may be affected differently and give different pointing directions. The two methods using stars [38, 85] do not show results as consistent, likely owing to the very different methods of determination, but inconsistencies in elevation offsets are greater for Coihueco than for Los Leones. The methods used to determine absolute offsets in this study measure the offsets at the bottom of the telescope field of view, whereas the star methods measure across tracks passing thorough the telescope field of view, so any error in the angular size of the telescope field of view is likely to show as inconsistencies between the different methods.

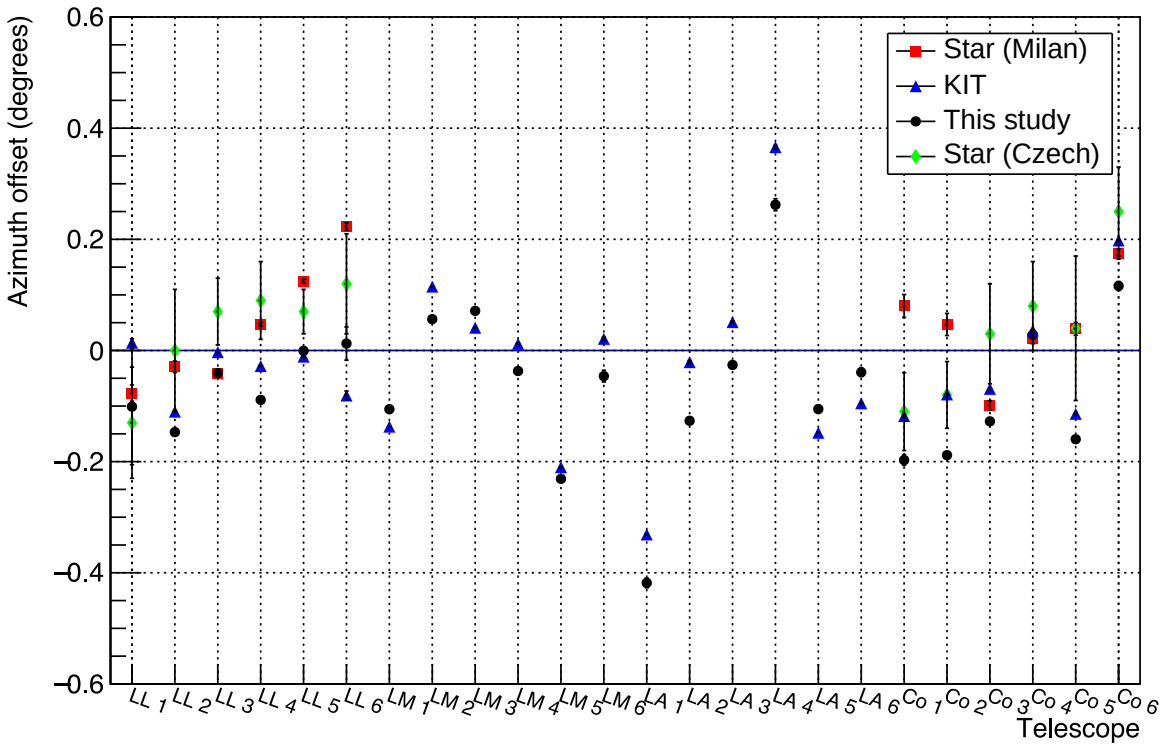

Fig. 3.33. Comparison of azimuth offsets with values found in other studies. Azimuth offsets are measured from the nominal pointing directions. The black points are the offsets found in this study, the blue triangles are from [39], the red squares are from [38], and the green diamonds are from [85].

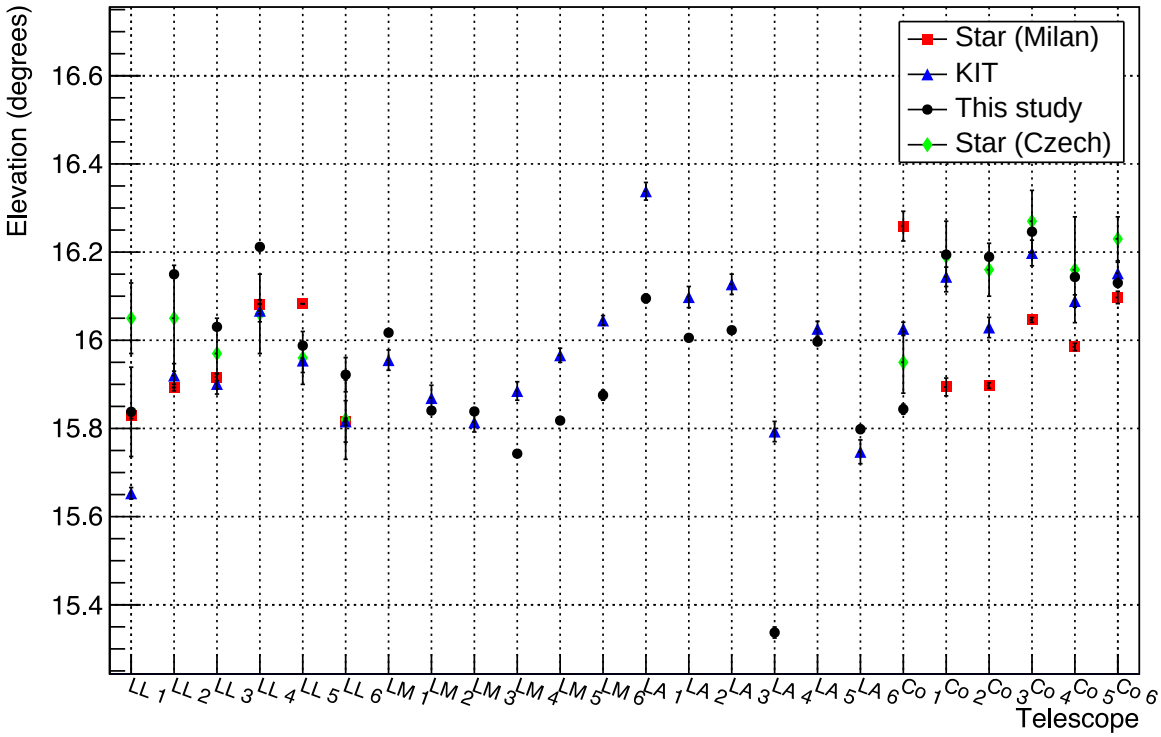

Fig. 3.34. Comparison of elevation with values found in other studies. The black points are the offsets found in this study, the blue triangles are from [39], the red squares are from [38], and the green diamonds are from [85].

3.6 Additional errors in telescope geometry

Discrepancies between pointing directions found using different methods suggest that there may be errors in telescope geometry other than pointing. The most probable source of this error is the telescope field of view. If the PMT array is placed too close or far from the telescope, the field of view will be affected. Of particular interest is telescope 4 of Loma Amarilla as it shows the greatest discrepancies in pointing directions. Figure 3.35 shows a time fit residual to a CLF shot across Loma Amarilla telescopes 3,4,and 5 with and without corrections from the present work to the pointing directions.

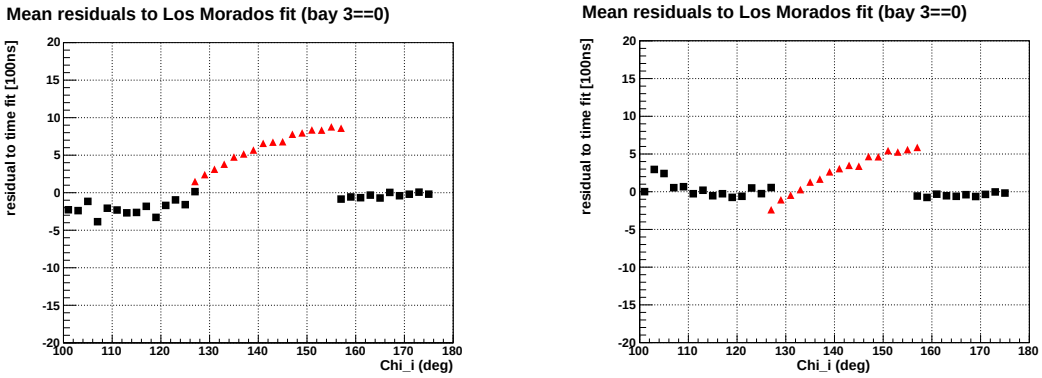

Fig. 3.35. Time residuals to a CLF track across LA 3,4 & 5 with timings averaged over 70 events. The red points are the residuals for telescope 4. The left plot shows the residuals when using the nominal pointing directions, and the right plot with the corrected pointing directions.

If the misalignment was only in pointing directions, the time residuals would be close to 0 with the corrected pointing direction. Additionally, if the new pointing is still incorrect, the time residual across a single telescope would be expected to be proportional to $\frac{d\chi}{dt}^{-1}$. This is inconsistent with residuals changing from positive to negative values over a single telescope. Josè Bellido found significant differences between the FD (hybrid) and SD reconstructions for Loma Amarilla telescope 4 of up to 1.5 degrees in χ_0 [16]. This is not likely due to a misalignment because a misalignment that large was not found. With the telescope field of view being the most plausible explanation for the observed discrepancies, residuals to timing fits were then found trialling different values for the telescope field of view. This was done by adjusting the pixel angular size. Figure 3.36 shows the timing residuals for a series of laser shots with differing assumptions for pixel sizes.

Upon physical inspection of telescope 4 of Loma Amarilla, it was found that the mirror segments were misaligned, giving an incorrect radius of curvature for the telescope. The mirror segments were then re-aligned on September 13th, 2012. After the re-alignment,

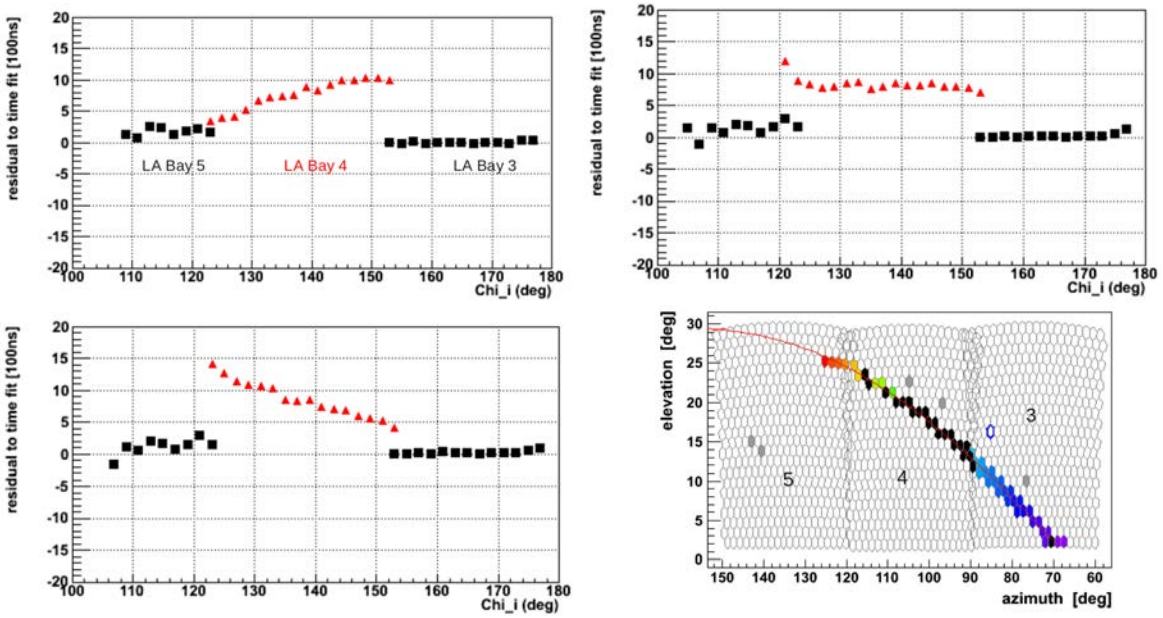

Fig. 3.36. Average time fit residuals for 50 laser tracks. The top left plot is with the standard pixel size of 1.5°. The top right plot is assuming a pixel size of 1.475° and the bottom left plot 1.455°. From [16].

the difference in χ_0 between the SD and telescope 4 changed from 1.5°to 0.5°. It is also interesting that the majority of telescopes in Coihueco and Loma Amarilla show a similar 0.5°discrepancy in χ_0 when compared with SD geometry while the telescopes in Los Leones and Los Morados do not show this discrepancy. The differences between the SD and FD χ_0 before and after the realignment of Loma Amarilla telescope 4 are shown in figure 3.37. Pointing directions for Loma Amarilla telescope 4 have also been found, and are included in the previous results section for absolute offsets. The pointing directions for Coihueco and Loma Amarilla also show larger discrepancies between different methods. This suggests that all of the telescopes in these two sites may have an incorrect pixel angular size. It is also notable that the telescopes at Coihueco and Loma Amarilla share the same design, being composed of hexagonal segments, whereas the mirrors in Los Morados and Los Leones are composed of square segments. This may explain why the discrepancy is only observed in Coihueco and Loma Amarilla, as any issues causing an incorrect pixel angular size would not be expected to be replicated in a different design.

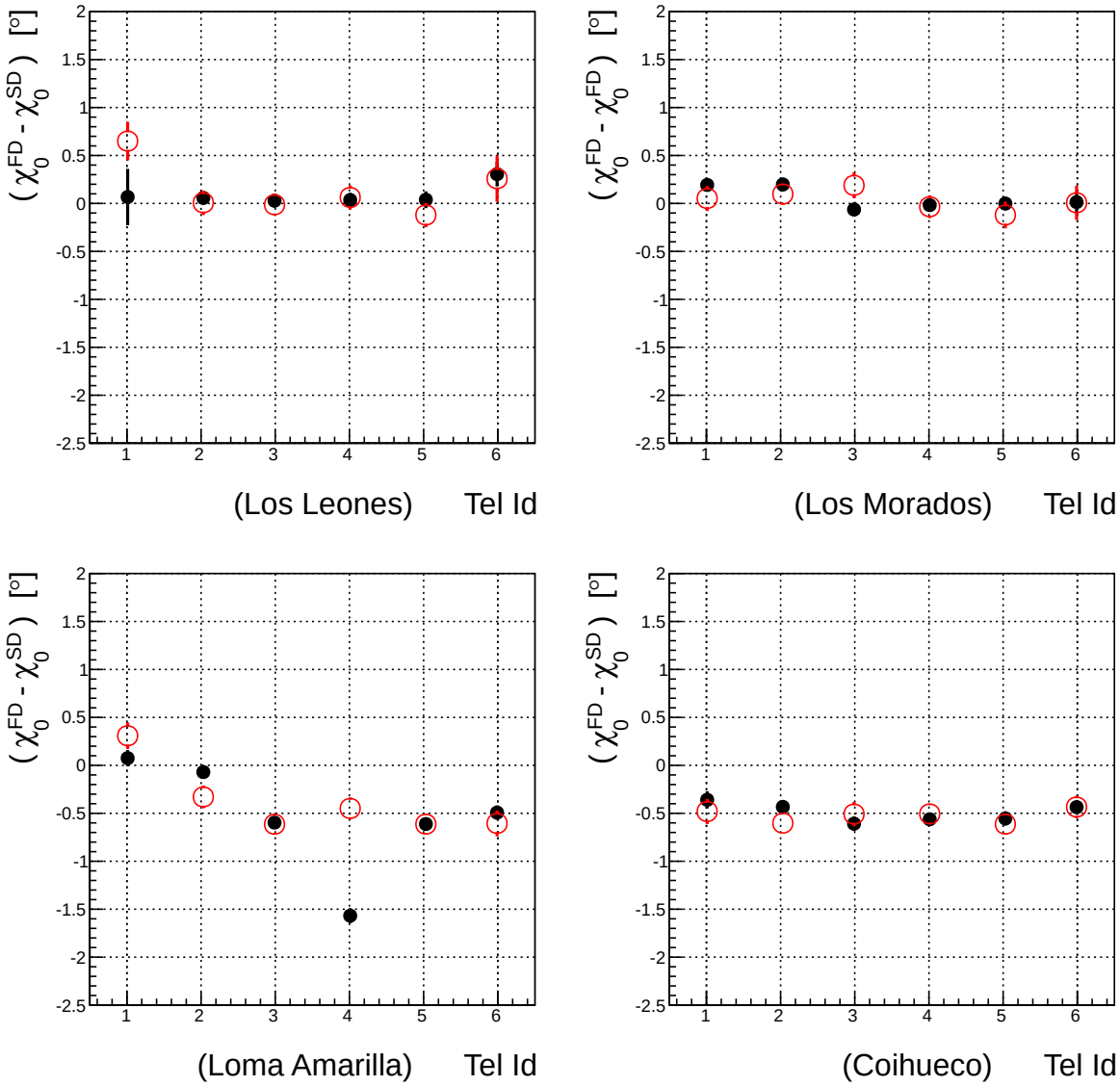

Fig. 3.37. Difference between FD and SD χ_0 for each telescope. The filled circles include events before the realignment of Loma Amarilla telescope 4, and the hollow circles are for events after the realignment. From [16].

3.7 Conclusions

After it was observed that timing fits for certain events showed discontinuities when crossing between mirrors, a method was developed that examined these discontinuities, as well as data from the SDP fits, to determine the pointing offsets of telescopes relative to adjacent telescopes. Using hybrid events (events seen by both the SD and FD), absolute pointing offsets of individual telescopes were found by comparing the SD core position and timing against the FD timing and SDP fits. The timing and SDP methods generally agree well

with each other. There were some discrepancies observed for telescope 4 of Loma Amarilla, which suggested that there may be additional errors in telescope geometry. Results show some agreement with other studies, with agreement being better for Los Morados and Los Leones. It was also found in further research [16] that telescope 4 of Loma Amarilla had an issue with the optics affecting the telescope field of view. It may also be the case that the pixel angular size in all telescopes in Coihueco and Loma Amarilla are incorrect by a small amount. Differences in pointing directions between different methods is likely due to the assumption that the pixel angular sizes were correct. It may be necessary to consider the different angular size in geometry reconstructions in order to accurately reconstruct showers, and also to obtain the true telescope pointing directions. Nonetheless, the uncertainties in telescope geometry are likely to only propagate to small errors in observed shower parameters such as direction, energy, and X_{max}, and would be far smaller than their overall systematic errors.

Chapter 4

Simulation of extensive air showers

The accurate simulation of an extensive air shower is an ongoing and complex problem. Many different types of particles and their interactions must be known in order to track the progress of numerous primary and secondary particles. The highest energy particles in cosmic ray showers far exceed those available in collider experiments and thus the interaction properties of particles at the highest energies are not well known. Additionally, the majority of particles produced in a high energy collision are extremely forward directed. Forward directed particles produced in the highest energy collider experiments can not be all detected as the detectors are not able to be placed in the beam. As a result of this, the interaction properties of high energy particles must be extrapolated from the experimental data. There are a number of different interaction models that these extrapolations are based upon. As new data comes out of collider experiments, interaction models are updated to be consistent with the new data.

4.1 CORSIKA

CORSIKA (COsmic Ray SImulations for KAscade) is a software package designed to simulate extensive air showers [51, 52]. It was originally written to simulate showers for the KASCADE array experiment. Due to the complexity involved in developing new simulation software for an extensive air shower, it has since been used for numerous cosmic ray experiments, including the Pierre Auger Observatory. CORSIKA simulates the interactions and decay of nuclei, hadrons, muons, electrons, and photons in the atmosphere, and is designed to operate with primary particle energies from 10^{11} eV up to 10^{20} eV. Any particles that pass through a selected observation level have their properties such as position, momentum, type, and arrival time recorded. There are 4 main parts to the CORSIKA program. The first part handles the input and output of the program as well as performing decays of unstable

particles, and tracking particles through the atmosphere taking into account ionisation losses and deflections by magnetic fields and multiple scattering. The second part handles the interactions of hadronic particles at higher energies. The third part handles hadronic interactions at lower energies. The fourth part handles the propagation and interactions of the electrons, positrons, and photons. For the high & low energy hadronic and electromagnetic interactions, many different interaction models are available. These models are often updated when new data from accelerator experiments becomes availble. There is also an option to generate Čerenkov light in the atmosphere, to track electronic & muonic neutrinos, and to handle showers with a flat incidence.

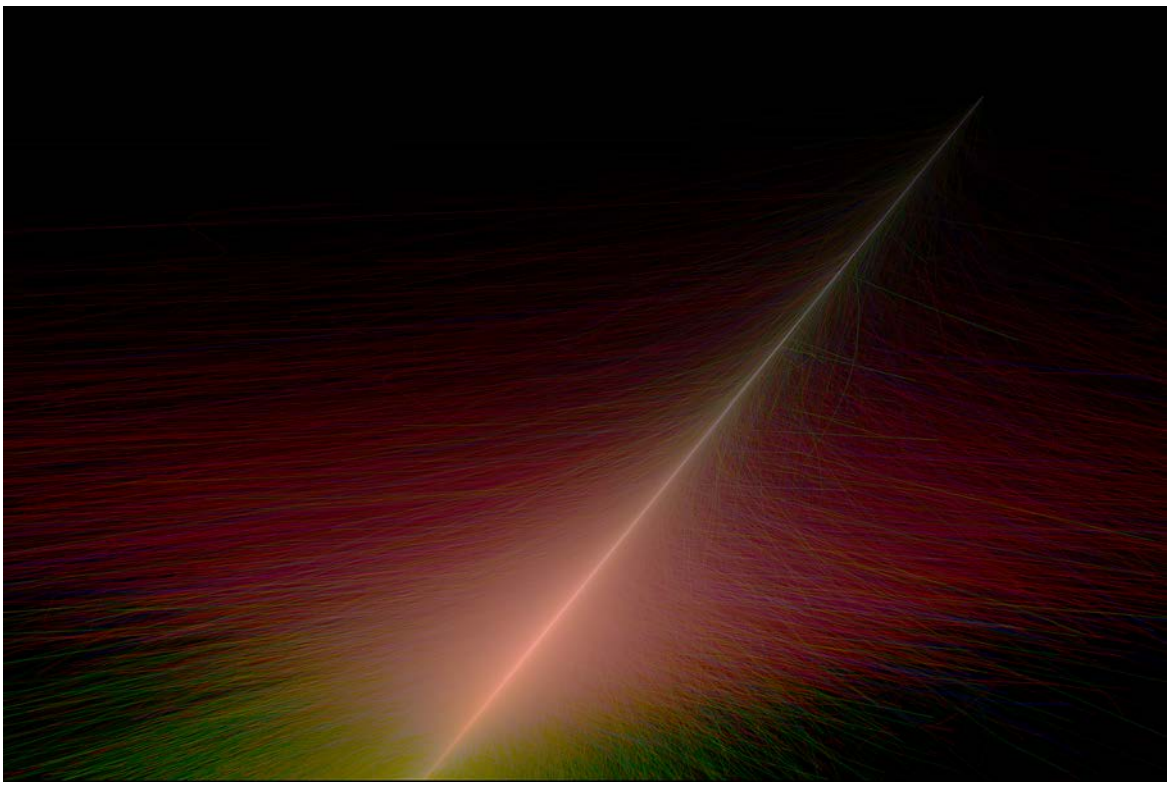

Fig. 4.1. A graphic of a CORSIKA shower obtained using the PLOTSH2 option. Hadrons are given blue tracks, Muons are given green tracks, and electrons & photons are given red tracks.

Another option, thinning, is extremely important for simulating showers at the highest energy. With thinning enabled, only a fraction of particles are tracked. With a sparse array of detectors, such as the Pierre Auger surface detector, only a small fraction of particles that hit the ground will hit a detector so this can be compensated for by feeding particles into a detector from a larger area around the detector (this will be discussed in detail below). Without thinning, the computational requirements for simulating showers at energies above

10^{20}eV are enormous, and would only allow very few showers to be simulated. Thinning can vastly reduce computational requirements especially for the highest energy showers allowing for a large number of showers to be simulated.

4.2 Thinning

The simulation of an ultra-high energy cosmic ray shower, if done fully, requires huge computational resources. Showers at the highest energies develop into hundreds of billions of particles. Tracking every single particle in such a simulation requires an infeasibly large computation time, as well as storage space if many showers are to be simulated. In order to simulate the most energetic showers, a method called thinning is employed, where only a representative sub-sample of particles is tracked.

In a shower simulation with thinning, an energy E_t is chosen as a threshold energy for thinning. Below this energy, whenever a particle interacts, not all of the particles produced by this interaction are kept. The surviving particles are then given a weight w depending on the particle's probability of being chosen. Typically, particles with higher energy are preferred over lower energy particles to most accurately retain the shower's overall properties. In the most commonly used methods, the following acceptance factors are used:

$$F_i(E_i) = \begin{cases} 1 & E_i \geq E_t \\ \dfrac{E_i}{\sum_k \tilde{E}_k} & \text{otherwise} \end{cases} \tag{4.1}$$

where $\tilde{E}_k$ are the energies of particles at the interaction with energy below E_t, and E_t for particles with energy above E_t. Surviving particles are given the following weight:

$$w_i = \frac{w_i'}{F_i} \tag{4.2}$$

where w_i' is the weight of the parent particle, starting at 1 for the primary particle.

If no additional constraints are placed on thinning, there may be low energy particles with extremely high weights, introducing artificial fluctuations in shower properties. Optimizations to this method were introduced by Kobal [64] to enhance statistical precision of shower simulations. With the optimized thinning method, a weight limit is applied to prevent large artificial fluctuations caused by high weight particles. If a particle's acceptance factor causes the particle's weight to exceed w_{max} the acceptance factor is adjusted so that the particle weight will equal w_{max} if accepted. Any particle with a weight equal to w_{max} is not subjected to any further thinning. The value of w_{max} is given a larger value for photons and electrons

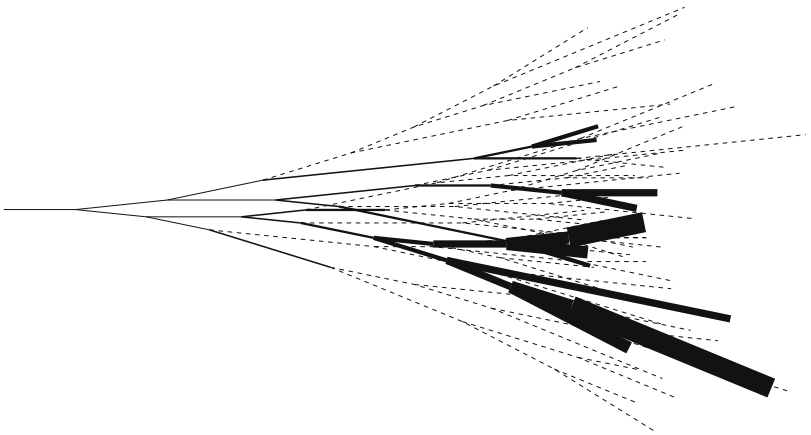

Fig. 4.2. Diagram representing the thinning procedure. The solid lines are particles kept with a thickness proportional to their weight. Dashed lines represent particles not kept.

than for muons and hadrons due to muons having a higher average energy than photons and electrons. The ratio of these maximum weights, ε, typically used is $\varepsilon = 10^2$. The optimal weight limit for a given thinning fraction $t_f = \frac{E_t}{E_0}$, where E_0 is the primary energy, is:

$$w_{max,EM} = \frac{E_t}{GeV} = \frac{E_0 t_f^{-1}}{GeV} \tag{4.3}$$

$$\varepsilon = \frac{w_{max,EM}}{w_{max,\mu}} = 100 \tag{4.4}$$

The optimal weight limit is approximately independent of composition, zenith angle and interaction model so only the primary energy and thinning fraction is needed to specify the weight limit. Additionally, when weight limiting is used at the optimum setting, the computation time to simulate an ultra-high energy cosmic ray shower is nearly independent of primary energy, instead being dependent on the thinning fraction.

4.3 Dethinning

The output of a thinned shower simulation is made up of particles of varying weights at ground level. In determining the average properties of a shower, this is typically dealt with fairly easily, using the particle's weight in any statistical analysis. This may introduce some artificial fluctuations in shower properties, with a smaller number of particles being sampled. If a thinned shower is to be used to simulate the response of a sparse detector array, weighted particles become a much larger problem. A small detector such as a Pierre Auger Observatory

surface detector station may only detect a limited number of particles. If only particles hitting the surface detector stations are considered in a thinned simulation, there may be very few or no particles in stations where there should be many, and with each particle having a high weight, detector signals will have a much higher variance. To get a better representation of signals in each detector station, particles must be injected with a unity weight. This is done by sampling simulated particles from an area that is much larger than the detector station. There are a number different ways this can be done.

Dethinning methods

A method developed by P. Billoir [19] was previously used in the Pierre Auger simulation software. For each detector, a sampling area is defined around the detector station. The station and particle position are found in the shower plane coordinate system defined in section 1.2.1 with r as the distance from the shower core and ζ the azimuth angle. A particle is within the station sampling area if the following constraints are met:

$$\frac{|r - r_s|}{r_s} < \delta \tag{4.5}$$

$$|\zeta - \zeta_s| < \alpha \tag{4.6}$$

for a particle core distance and azimuth of r and ζ, and a station core distance and aziumith of r_s and ζ_s (see figure 4.3).

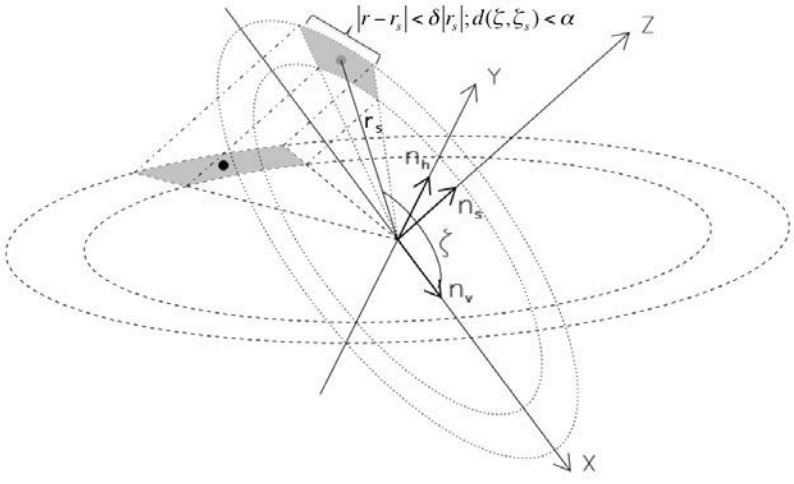

Fig. 4.3. Definition of the sampling area [19]. The sampling area is an area in the shower plane with the detector at core distance r_s and azimuth ζ_s. The sampling area extends out for a radial distance δr_s and azimuth angle α.

The values of δ and α are chosen to provide a large enough sampling region to reduce artificial fluctuations, while being small enough that particle densities in the sampling region are approximately uniform to avoid bias in particle density being injected in the station. Typically for the Pierre Auger Observatory surface detector, values of $\delta = 0.1$ and $\alpha = 0.15$ radians are chosen.

For each particle within the sampling area the projected area of both the detector and the sampling area A_d & A_s are found when projected in the direction of motion of the particle. The particle is then given a resampled weight w_r:

$$w_r = w\frac{A_d}{A_s} \tag{4.7}$$

for a particle weight w. Ideally, it is desirable to have a resampled weight $w_r << 1$. If this is not the case, the particle may require cloning. n copies of the particle are then injected into the detector where n is drawn from a Poisson distribution with a mean $\bar{n} = w_r$.

The particle timing has to be adjusted to account for differences in shower front propagation time between different points in the sampling region. The simplest method is to preserve the time delay of the particle from the shower front, τ. For particle and detector positions $\vec{r}_p$ and $\vec{r}_d$, particle time t_p and shower axis direction $\vec{n}_s$, the corrected time t' is:

$$t' = t_p + \vec{n}_s \cdot \frac{(\vec{r}_p - \vec{r}_d)}{c} \tag{4.8}$$

When $n > 1$, multiple copies of the same particle are injected into the detector. To avoid a large signal spike from multiple particles arriving at the same time, the arrival times of cloned particles are smeared using a log-normal distribution:

$$\tau' = \tau e^{\sigma G} \tag{4.9}$$

where τ is the time delay of the particle from the shower front plane, and G is drawn from a Gaussian distribution with mean of 0 and standard deviation of 1. σ is typically chosen to be 0.1-0.2.

Some biases will arise from using a large sampling area [45]. Most notably, the strong dependence of particle density on core distance. If in the area around the detector, density is proportional to $r^{-\eta}$, the relative excess in the density at the detector station will be $\eta(\eta-1)\delta^2/6$. Since η is typically between 3-4, the excess is in the range of δ^2 to $2\delta^2$. This is much smaller than any natural fluctuations in detector signal, so it is not usually an issue for single events.

The density distribution of particles can also lead to a bias in particle arrival times at the ground. Particles within the sampling area that are nearer the core are overrepresented relative to particles farther from the core. Since particles nearer the core also arrive earlier (with a smaller time delay from the plane front), the distribution of arrival times at the detector is biased towards particles arriving earlier. This effect is small, but can become noticeable for studies which average over a large number of showers, such as the muon production depth estimates [26].

Corrections can be applied to reduce the biases in particle number and timing caused by the steep particle density distribution. A simple adjustment [19] is to correct the weights of the particles to compensate for the dependence of density with core distance:

$$w' = w\left(\frac{r_p}{r_d}\right)^{\eta-1} \tag{4.10}$$

This correction does rely on prior knowledge of the lateral distribution to work, though the correction is fairly insensitive to the chosen value of η. Using a value of $\eta = 3.5$ gives good results for all shower types [45].

Another de-thinning method has been developed by Stokes et al. [90] and is utilised for simulations with Telescope Array. Instead of sampling over a large area for a detector, this method creates a number of copies of the particle on the ground, with the position and timing of each of the copies scattered depending on the original particle's timing and geometry. First a vertex point is chosen along the trajectory of the particle at a distance D from the ground. Copies of the particle are then generated emerging from this vertex with a two dimensional Gaussian distribution centred on the original particle trajectory (see figure 4.4).

There is a maximum distance D_{max} that can be chosen to avoid the possibility of particles arriving before the shower front (propagating at the speed of light from the time and place of first interaction, t_0 and $\mathbf{x_0}$). For a first interaction coordinates $\mathbf{x_0}$, t_0 and particle coordinates $\mathbf{x_i}$, t_i with particle trajectory $\hat{\mathbf{p}}_i$:

$$D_{max} = \frac{c^2\left(t_i - t_0\right)^2 - \left|\mathbf{x_i} - \mathbf{x_0}\right|^2}{2\left(c\left(t_i - t_0\right) - \left(\mathbf{x_i} - \mathbf{x_0}\right)\cdot\hat{\mathbf{p}}_i\right)} \tag{4.11}$$

The angle of the Gaussian cone must be carefully selected. It has to be small enough to avoid introducing a bias in the particle distribution while being large enough to avoid creating small areas of high particle density around higher weight particles. This angle is set to βd where d is the distance of the particle from the shower core. For a thinning ratio $t_f = 10^{-6}$ the value of $\beta = 3\,\text{deg}/\text{km}$ for electromagnetic particles, and $1\,\text{deg}/\text{km}$ for muons and hadrons. The energy of the copied particles is varied to avoid any spikes in the energy

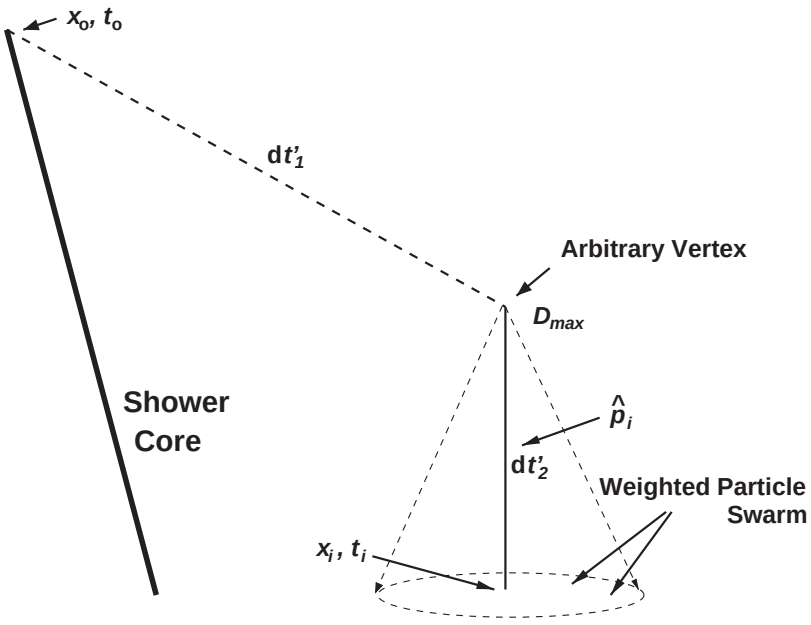

Fig. 4.4. Diagram of the vertex used for dethinning. From [90].

spectrum of particles at the ground. The energy is varied in a Gaussian distribution with standard deviation of 10% in the original particle energy. In showers with a high zenith angle, copied particles can have much longer trajectories than the original particle and would be less likely to make it to the ground. To compensate for this, an acceptance factor for copied particles is introduced. The acceptance probability is:

$$P = e^{-\frac{\Delta X}{\varepsilon}} \tag{4.12}$$

where ΔX is the difference in slant depth between the original particle and the copied particle, and ε is set to 50 gcm^{-2}

The height of the vertex is usually set at D_{max} but this may be far too high for particles such as muons produced later in the shower's development. This may give an excessively wide distribution in the positions of copied particles. This is solved by limiting the vertex distance to the smaller of D_{max} and:

$$D' = |\mathbf{x_i} - \mathbf{x_0}| - X^{-1}(\mathbf{x_i}, \mathbf{x_0}, \alpha \mathbf{h}) \tag{4.13}$$

where h is the hadronic generation from which the particle originated, $\alpha = 30$ gcm$^-2$, and $X^{-1}(\mathbf{x_i}, \mathbf{x_0}, \alpha \mathbf{h})$ is the distance corresponding to a a slant depth of αh on a straight line from $\mathbf{x_0}$ towards $\mathbf{x_i}$.

This method has been found to reproduce the original shower properties for a thinning ratio $t_f = 10^{-6}$ at core distances of up to 4500m without introducing artificial fluctuations.

4.4 Simulation of detector response for the Pierre Auger Observatory

An accurate simulation of the detector response to simulated showers is essential to deduce the properties of observed cosmic ray showers. For this, the $\overline{\text{Off}}\underline{\text{line}}$ software framework was designed to handle both reconstruction of observed cosmic ray showers and the propagation of simulated showers into the detector (and subsequent reconstruction) [8]. The $\overline{\text{Off}}\underline{\text{line}}$ framework is modular in construction, where the series of modules run can be chosen by the user to suit a specific task. $\overline{\text{Off}}\underline{\text{line}}$ was developed in C++, with a framework that consists of 3 main parts (also shown in figure 4.6):

- The sequence of modules. These are assembled by the user to suit a specific task. Modules do not typically pass data to other modules directly but rather communicate through the event data, in a format common to all modules. This simplifies developing and updating modules individually for use in a long sequence of modules. The sequence of modules is controlled by a run controller, with sequencing instructions specified using an XML-based language. An example of the sequencing instructions is shown in figure 4.5.

- Event data. This is the principal way in which modules relay data. It contains all raw, calibrated, reconstructed, and simulated data. The Event data is arranged in a hierarchy structure typically associated with observatory instruments. Modules are able to both read from and write to the event data.

- Detector description. This provides an interface to allow modules to access information about the detector such as the detector configuration, current detector performance, and atmospheric conditions.

Event data is held in memory in a transient event. When data is to be written to a disk, it is stored as a persistent event via a file interface. File input/output in $\overline{\text{Off}}\underline{\text{line}}$ is handled by a ROOT toolkit to store each event and read various file formats. These formats include raw event and monitoring formats produced by the observatory, in addition to simulated data produced by programs such as AIRES, CORSIKA, CONEX, and SENECA.

Another important component of $\overline{\text{Off}}\underline{\text{line}}$ is the geometry package. Since the observatory is spread over a large area, with multiple detector types, there are a number of different

```
<!-- A sequence for hybrid reconstruction -->
  <enableTiming/>
  <moduleControl>
    <loop numTimes="unbounded" pushEventToStack="yes">
      <module> EventFileReaderOG </module>
      <module> EventCheckerOG </module>
      <try>
        <module> FdCalibratorOG </module>
        <module> SdQualityCutTaggerOG </module>
        <module> SdPMTQualityCheckerKG </module>
        <module> TriggerTimeCorrection </module>
        <module> SdCalibratorOG </module>
        <module> SdBadStationRejectorKG </module>
        <module> FdPulseFinderOG </module>
        <module> FdSDPFinderOG </module>
        <module> FdAxisFinderOG </module>
        <module> HybridGeometryFinderOG </module>
        <module> FdApertureLightOG </module>
        <module> FdProfileReconstructorKG </module>
      </try>
      <module> RecDataWriterNG </module>
    </loop>
  </moduleControl>
</sequenceFile>
```

Fig. 4.5. An example of the module sequencing file for reconstruction of a hybrid event.

preferred coordinate systems. These could include a system relative to a Fluorescence detector station, or even a shower coordinate system dependent on the reconstructed shower geometry. The geometry package provides abstract geometrical objects such as points and vectors. The objects internally track the coordinate system used and allow for operations on these objects to be written independent of the coordinate system used.

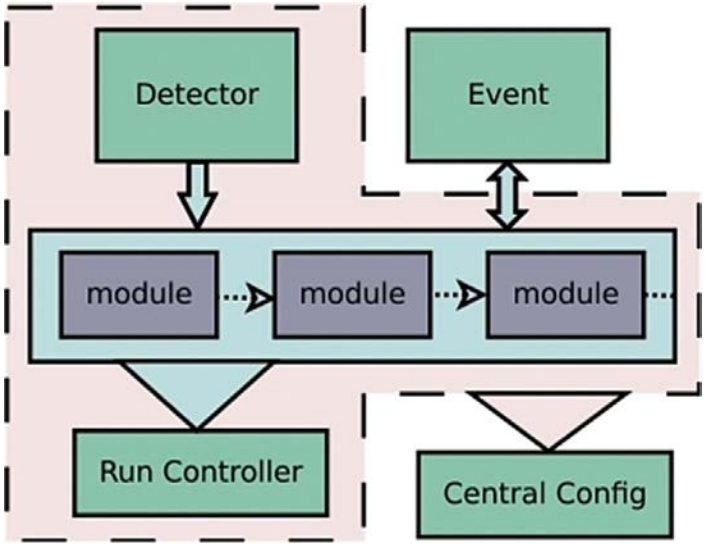

Fig. 4.6. Diagram of the general structure of the $\overline{\text{Off}}\underline{\text{line}}$ framework. From [101]

Chapter 5

An improved dethinning method to reduce biases in detector simulations

5.1 Introduction

Simulations of extensive air showers and the response of detectors to these showers play a vital role in deducing the properties of the primary cosmic ray particle. A major problem with this is that extensive air showers at the highest energy contain billions of particles. A full simulation of such a large number of particles is a computationally intensive process, making the simulation of large numbers of showers difficult. To simulate a large number of showers, a process known as thinning is employed, where only a fraction of particles are tracked in a simulation (details in 4.2). With appropriate weightings applied, overall properties of a shower can be preserved, with only small artificial fluctuations introduced by the statistics of sampling a smaller number of particles. Simulation of a detector response is more difficult, requiring dethinning.

5.1.1 Dethinning

If thinning is employed in an air shower simulation, only a fraction of particles are tracked to the ground with each particle given a weighting which is inversely proportional to the probability of that particle surviving the thinning procedure. Assigning this weight to particles allows the average particle densities in a shower to be determined without bias. However, problems arise when attempting to simulate a detector of limited area. A detector simulation from a thinned shower without resampling would have fewer particles hit but with higher weights introducing artificial fluctuations in detector signals. This is corrected by resampling

where particles are sampled from a larger area than the detector so that particles can be injected into the detector with unity weight.

The resampling method currently used in Offline defines a sampling region around each detector [19]. This sampling area is given a radial width as a fraction of detector core distance δ and an azimuthal angle α in the shower plane (See figure 5.1). Particles can then be given a resampled weight $w_r = wA_d/A_s$, for a particle of weight w, a detector area A_d and a sampling area A_s. The particle is then accepted into the detector n times where n is drawn from a Poisson distribution with $\bar{n} = w_r$. For particles with $w_r << 1$ this is equivalent to accepting the particle with a probability of w_r. If $n > 1$, clones of the particle will be made and are given a time smearing to prevent spikes in detector signals.

The values of δ and α must be chosen carefully. If δ and α are too large, particles being sampled from regions of the shower far away from the detector may introduce biases in particle density and arrival times. If δ and α are too small, larger resampled weights will result in more particle cloning. If the particles injected into a detector are cloned, the variance in the number of particles being injected is higher than the variance expected from Poisson statistics, potentially introducing artificial fluctuations into detector signals. Artificial fluctuations are most noticeable when individual particles contribute a significant fraction of the total signal. Values of about $\delta = 0.1$ & $\alpha = 0.15$ rad are typically chosen for Auger detector simulations. Sampling areas of this size typically have $w_r << 1$ for lower weight particles such as muons. Resampled weights are more likely to be larger than 1 for lower energy EM particles and/or at distances very close to the core, but in both of these cases these particles are very numerous and the artificial fluctuations introduced are not as significant.

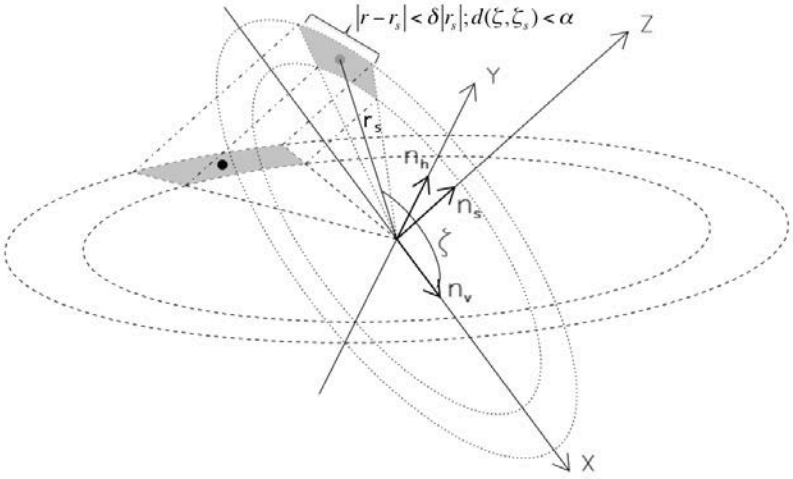

Fig. 5.1. Definition of the sampling area [19]. The sampling area is an area in the shower plane with the detector at core distance r_s and azimuth ζ_s. The sampling area extends out for a radial distance $\delta \cdot r_s$ and azimuth angle α.

5.2 Biases caused by resampling

For the resampling procedure, it is assumed that changes in particle density over small distances are linear. Under this assumption, variations in particle density within a sampling region would cancel out if the detector is in the center of the sampling region. This assumption holds well azimuthally since variations in density are fairly small and roughly linear for values of α around 0.15. Radially however, the density varies much more steeply and its non-linear slope can have an effect on the density simulation at the typically used $\delta = 0.1$.

Biases in the timing of particle arrivals are also possible. The primary cause of timing bias is due to the steep LDF. Because of the steep LDF, there are more particles accepted from closer to the core within the sampling area. Due to the shape of the shower front, particles closer to the core arrive earlier on average so particle timing has an early bias. Recent studies in [45] have found a bias in the timing of muons in 60 degree showers that is independent of primary composition, energy, and hadronic model used (see figure 5.2). This bias is very strongly dependent on the value of δ chosen. Corrections were suggested to reduce this bias where the weighting of particles is scaled depending on their core distance relative to the detector. If it is assumed that the particle density follows an $r^{-\eta}$ trend, weight is rescaled by a factor of $(r_p/r_s)^{\eta-1}$ where r_p & r_s are the particle and detector core distances. A value of $\eta = 3.5$ is suggested. To compensate for biases caused by curvature in the shower front, a correction can also be applied to the particle timing. This can be implemented as an adjustment to the time delay from the plane front, τ, to $\tau' = (\tau - \tau_f(r_p))(r_s/r_p) + \tau_f(r_s)$, where $\tau_f(r) = r^2/(2Rc)$ with R as the radius of curvature.

The biases in timing and density are not likely to be noticeable for individual showers but can introduce significant biases for studies averaging large numbers of showers. Recent work on biases in $X^{\mu}_{\max}$ (defined in section 2.5.2) has found that the timing bias caused by resampling does affect the simulated $X^{\mu}_{\max}$. Figure 5.3 shows the effect of correcting for this bias on $X^{\mu}_{\max}$. The negative time bias caused by resampling will ultimately lead to shallower reconstructed depths in the simulations. Since $X^{\mu}_{\max}$ bias corrections are based on biases in simulations, this will lead to an overestimate of $X^{\mu}_{\max}$ in the real data. Correcting for this bias in the simulation has ultimately led to a shallower $X^{\mu}_{\max}$ in the real data.

5.3 The new resampling method

With biases in density and timing strongly dependent on the extent of the sampling area, it is highly desirable to minimise the sampling area. For a fixed sampling area, the area chosen must be relatively large to account for the higher weight particles to reduce artificial

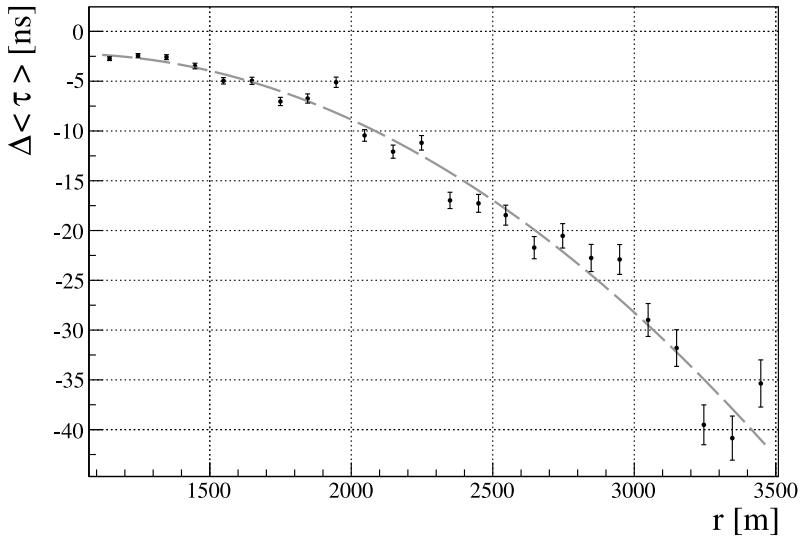

Fig. 5.2. Muon timing bias for $\delta = 0.1$ in a $10^{19.5}$ eV 60 degree shower [45]. $\Delta < \tau >$ is the bias in the mean muon arrival time.

fluctuations, but this means that the majority of particles are being sampled from an unnecessarily large area (see figure 5.4). This problem can be solved by introducing a variable size sampling area for each particle, which is dependent on a particle's weight. This has the advantage of sampling lower weight particles from a small area but allowing a larger area for higher weights, reducing both biases and artificial fluctuations.

With the new resampling method, a sampling area is created around the detector for a given particle with $A_s = wA_d$. For very high weight particles, this sampling area may be excessively large resulting in particles being sampled from too far away. To avoid this, a limit is placed on the size of the sampling area. The maximum allowable sampling area is defined as $A_{max} = 4r_d^2\delta\alpha$ where δ and α are the largest relative radial distance and azimuthal angle allowed. For particles which are overweight, i.e. $wA_d > A_{max}$, cloning is required.

For particles that are not overweight, the sampling area is given a radial and azimuthal size $\delta' = \delta\sqrt{\frac{A_s}{A_{max}}}$, $\alpha' = \alpha\sqrt{\frac{A_s}{A_{max}}}$. If the particle is within the new sampling area, a single copy of the particle is accepted into the detector.

Overweight particles are treated in a way similar to the original $\overline{\text{Off}}\underline{\text{line}}$ method. The particle is cloned n times, where n is drawn from a Poisson distribution with $\bar{n} = wA_d/A_{max}$.

5.4 Performance comparisons

To compare the performance of the two resampling methods, 7200 proton showers were generated in total at energies of 10^{19}, $10^{19.5}$, and 10^{20} eV and zenith angles of 0, 38, and 60

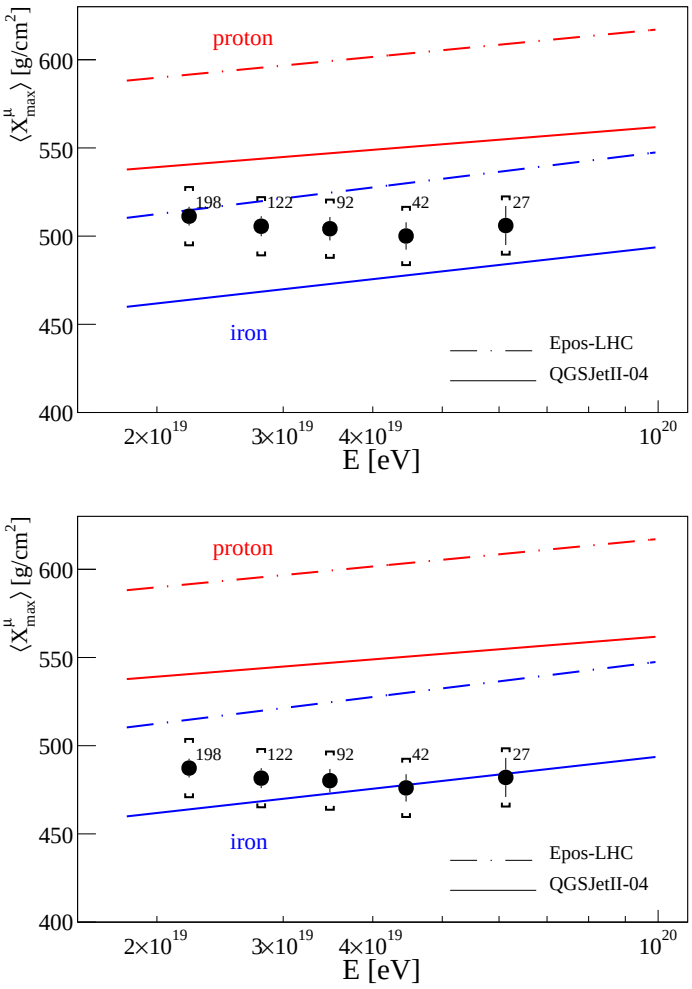

Fig. 5.3. Bias in the real X^{μ}_{max} estimate caused by resampling with the uncorrected (top) and corrected (bottom) X^{μ}_{max} [26].

degrees. The biases are found at the CORSIKA level by determining each particle's mean acceptance $< n >$ into a detector for a series of detector core distances r_d averaged over all azimuths. Using the Offline resampling method, particles can be accepted into the detector if the particle's core distance r_p, and azimuth ζ_p, obey the following criteria:

$$\begin{aligned} \left| r_p - r_d \right| &< r_d \delta \\ \left| \zeta_p - \zeta_d \right| &< \alpha \end{aligned} \tag{5.1}$$

For particles that fit both of these criteria, the mean number of copies accepted for detector area A_d is:

$$\bar{n} = \frac{wA_d}{A_s} \tag{5.2}$$

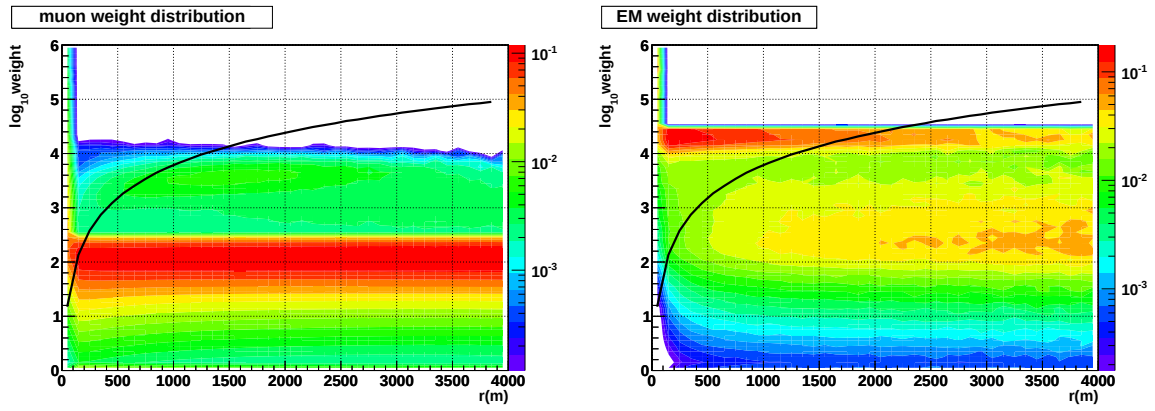

(a) (b)

Fig. 5.4. Contour plot of weight vs core distance for muons (left) and EM (right) for $10^{19.5}$ eV showers. The black line is the weight where $wA_d = A_s$ for $\alpha = 0.15$, $\delta = 0.1$. Below this line particles could be sampled from a smaller area. Above the line particles require cloning. Most muons are at, or slightly below, the hadronic weight limit (the maximum weight hadrons and muons are thinned to in CORSIKA). There is also a smaller number of muons above this limit which are created by pair production from photons, which inherit a higher weight limit (the EM weight limit is a factor of 100 higher for an optimised simulation [64]). The EM component also has most of its particles close to the weight limit at smaller core distance. However a second peak appears in the weight distribution at larger core distances. The second peak is likely muon halo particles (EM particles from decayed muons).

If this is averaged over all detector azimuths, the mean number of copies accepted is:

$$\begin{aligned} < n > &= \bar{n}\frac{2\alpha}{2\pi} \\ &= \frac{wA_d}{A_s} \times \frac{2\alpha}{2\pi} \\ &= \frac{wA_d}{4\delta\alpha r_d^2} \times \frac{2\alpha}{2\pi} \\ &= \frac{wA_d}{4\pi r^2 \delta} \end{aligned} \tag{5.3}$$

With the new method if $wA_d < A_s$ the particle is accepted with $n = 1$ if the core distance is within:

$$\begin{aligned} \left|r_p - r_d\right| &< \delta' \\ \text{i.e. } \left|r_p - r_d\right| &< \delta r_d \sqrt{\frac{wA_d}{A_s}} \\ \text{i.e. } \left|r_p - r_d\right| &< \delta r_d \sqrt{\frac{wA_d}{4r_d^2 \delta \alpha}} \end{aligned} \tag{5.4}$$

And if the azimuth is within:

$$\begin{aligned} \left|\zeta_p - \zeta_d\right| &< \alpha' \\ \text{i.e. } \left|\zeta_p - \zeta_d\right| &< \alpha \sqrt{\frac{wA_d}{4r_d^2 \delta \alpha}} \end{aligned} \tag{5.5}$$

The probability of a particle within the core distance criteria being accepted, and hence the mean number accepted, when averaged over all azimuths is:

$$\begin{aligned} < n > &= \frac{2\alpha'}{2\pi} \\ &= \frac{\alpha}{\pi} \sqrt{\frac{wA_d}{4r_d^2 \delta \alpha}} \\ &= \frac{1}{\pi} \sqrt{\frac{wA_d \alpha}{4r_d^2 \delta}} \end{aligned} \tag{5.6}$$

Similarly to the $\overline{\text{Off}}\underline{\text{line}}$ method , particles with $wA_d > A_s$ have a mean number of copies accepted:

$$\begin{aligned} < n > &= \frac{wA_d}{A_s} \times \frac{2\alpha}{2\pi} \\ &= \frac{wA_d}{4\pi r^2 \delta} \end{aligned} \tag{5.7}$$

Figures 5.5-5.8 show biases for $\delta = 0.1$, $\alpha = 0.15$ for both resampling methods. The plots show differences in density and timing against a reference value of $\delta = 0.02$, which is assumed to be the true density and time. Biases are given for both the muon and EM components. For the EM component, particle contributions to density and timing were weighted by their energy to better represent signals seen in a WCD.

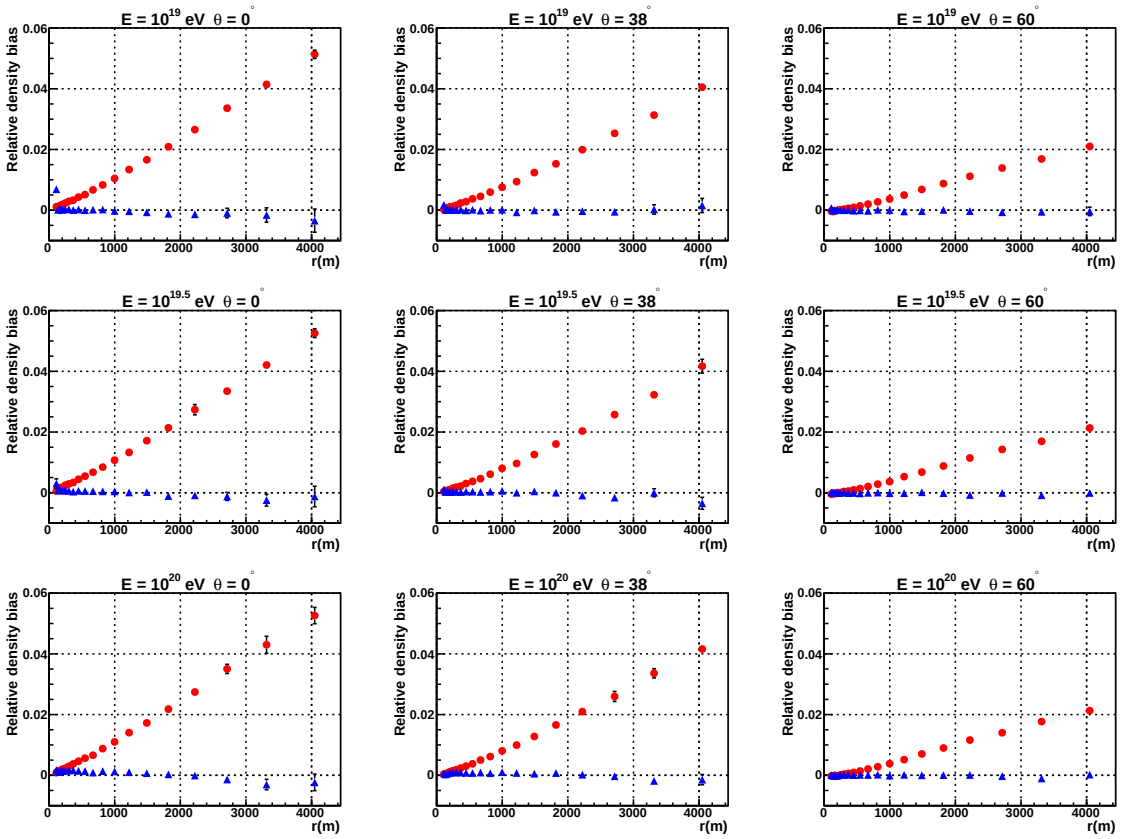

Fig. 5.5. Biases in the **muon density**. The bias in these plots is the difference between the resampled density and the reference density as a fraction of the reference density. The red circular points are for the Offline method and the blue triangular points are for the new method. The energies from top to bottom are 10^{19}, $10^{19.5}$, and 10^{20} eV. The zenith angles from left to right are 0, 38 and 60 degrees.

Biases in both particle density and timing exist for both EM and muons for the Offline method. For the muons, the new resampling method shows almost no biases in both. This is because of the lower weights of muons and hence the smaller sampling distances with the new method. The particle weights in the EM component are typically much larger than those for muons so at smaller core distances ($\lesssim$ 1000 m). EM particles usually utilise the maximum allowable sampling area, so the new and old resampling methods are equivalent. For larger core distances the maximum sampling area is larger so EM particles are more likely to utilise sampling areas smaller than the maximum, reducing biases. This effect is dependent on primary energy, with biases continuing out to larger core distances at higher energy due to the average weight of particles being proportional to primary energy for a given thinning level.

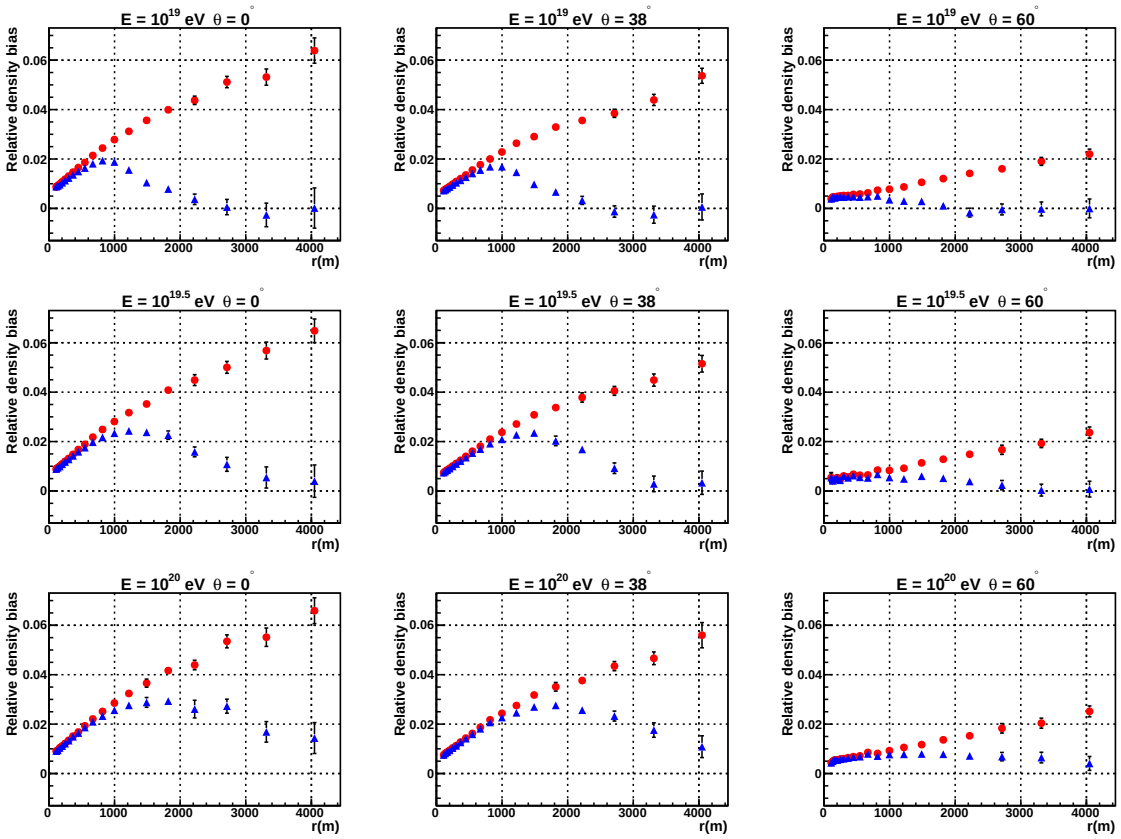

Fig. 5.6. Biases in the **EM density**. The bias in these plots is the difference between the resampled density and the reference density as a fraction of the reference density. The red circular points are for the Offline method and the blue triangular points are for the new method. The energies from top to bottom are 10^{19}, $10^{19.5}$, and 10^{20} eV. The zenith angles from left to right are 0, 38 and 60 degrees.

5.5 Conclusions

It has been shown that this new resampling method can substantially reduce the biases associated with large sampling areas by sampling from the smallest possible area for each individual particle. This minimises the distance from the detector that particles are being sampled from, but also allows for larger sampling areas for particles with higher weights and/or smaller core distances. This minimises the artificial fluctuations caused by particle cloning. For showers thinned at the 10^{-6} level, biases in the muon density and arrival time are almost completely removed because of the low average weight of muons. The EM component still shows some bias at smaller core distances, reducing for distances $\gtrsim 1000$ m. The EM bias worsens with increasing energy due to higher particle weights. The reduced biases are especially useful for applications with a high sensitivity to particle timing, such as

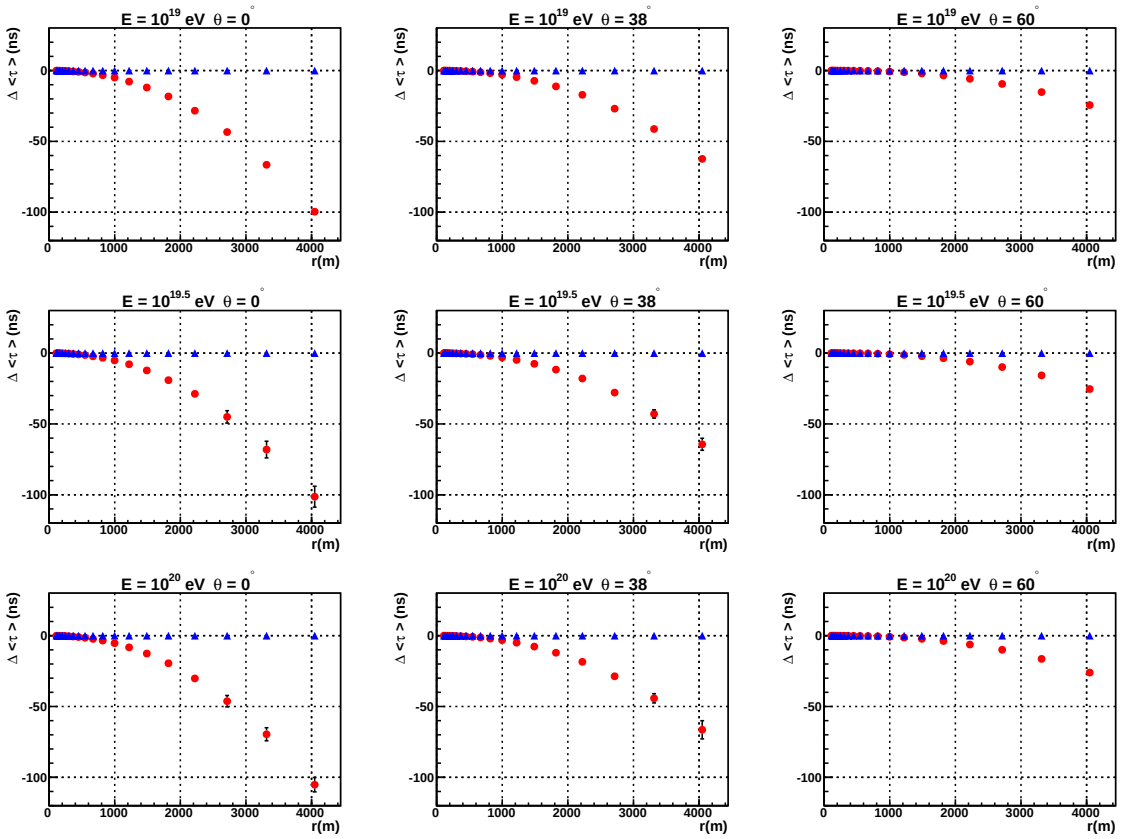

Fig. 5.7. Biases in the **muon mean arrival time**. The red circular points are for the Offline method and the blue triangular points are for the new method. The energies from top to bottom are 10^{19}, $10^{19.5}$, and 10^{20} eV. The zenith angles from left to right are 0, 38 and 60 degrees.

the muon production depth (see section 2.5.2) analysis. The new resampling method is now the default method used in Offline for surface detector simulations.

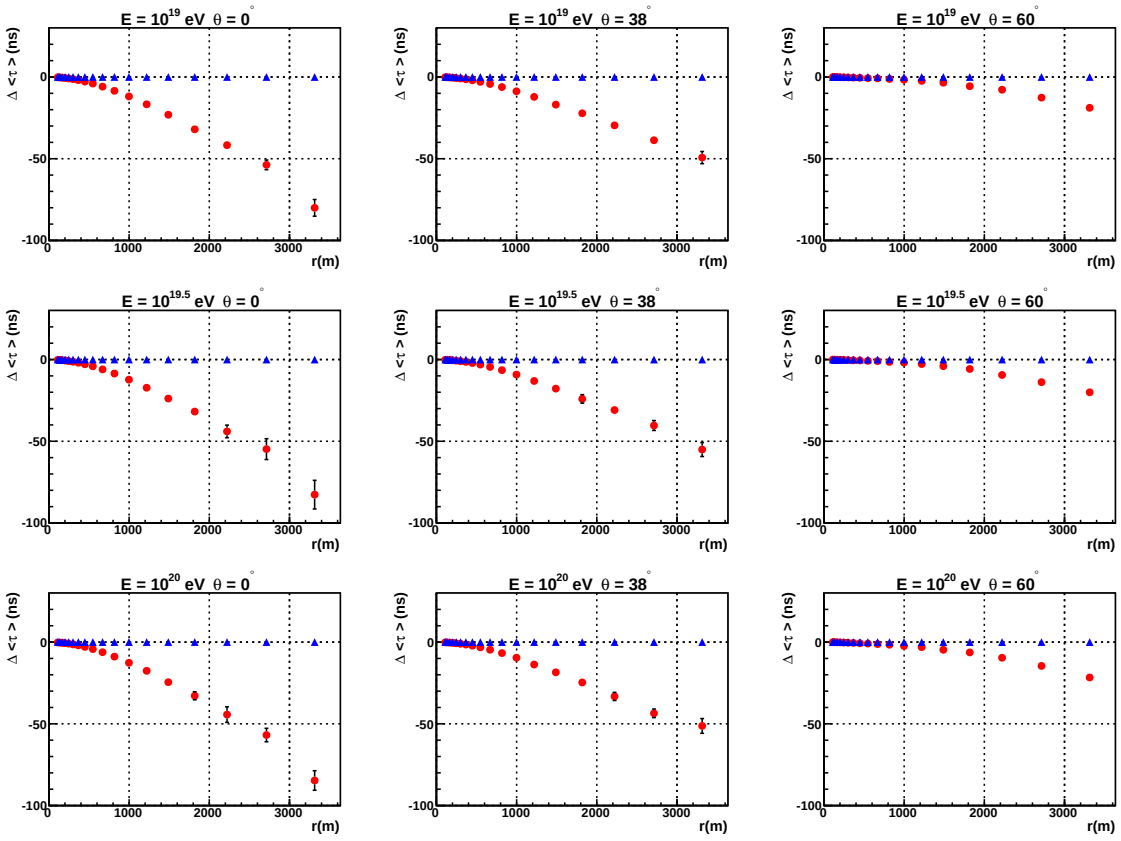

Fig. 5.8. Biases in the **EM mean arrival time**. The red circular points are for the $\overline{\text{Off}}\underline{\text{line}}$ method and the blue triangular points are for the new method. The energies from top to bottom are 10^{19}, $10^{19.5}$, and 10^{20} eV. The zenith angles from left to right are 0, 38 and 60 degrees.

Chapter 6

Muon shower front shape and correlation with first interaction depth, $X_{\mathbf{max}}$ and $X^{\mu}_{\mathbf{max}}$

Abstract

The arrival time distribution of particles at the ground holds information about shower development and mass composition. This chapter focuses on the muon component of the shower. To study the muon front in high detail, showers were generated with CORSIKA using very low (10^{-8}) thinning. This study does not include the effects of a detector. The purpose of this study is to gain a better understanding of the physics of showers and look for hints of possible observables that could be correlated with X_{max}, X^{μ}_{max}, or the 1st interaction depth. The possible effects of a detector will be briefly discussed towards the end of the chapter. One hundred 10^{19} eV showers were each generated at zenith angles of 0°and 60°. Each zenith angle consisted of 60 proton and 40 iron showers. Showers were generated with CORSIKA version 6990 using QGSJET-II-03.

6.1 Introduction

The majority of hadrons produced in an air shower typically have a very small angular deflection from the direction of their parent particle. This means that the hadronic component of an air shower has a very narrow lateral distribution (<10m). For most purposes, including in this study, it can be assumed that the hadronic component of a shower lies exactly on the core. Muons are mostly produced as a result of decay of π^{+} & π^{-}. Muons have a much larger

angular distribution than the hadronic component, due to the momentum of the recoiling neutrino from the pion decay. Muons produced predominantly by pions with an energy near the critical energy (when a charged pion's interaction length is equal to its decay length) have an angular distribution large enough to be easily detected with an array of surface detectors.

Since muons are produced close to the axis and travel in a straight line at close to the speed of light, muons produced at a certain position on the axis will at a later time be along a spherical surface with the centre of curvature at the production point. From this it is possible to determine the production depth of a muon from its timing if the geometry of the shower is known. The area of the ground covered by muons produced at a certain depth does depend on the shower's zenith angle. Nearly vertical showers have muons being produced relatively close to the ground. Because of this, the production profile of muons landing at a certain point on the ground will be largely determined by geometric effects. These effects include the distance from the production point (favouring lower production distances), and the angular distribution of muons produced (favouring higher production distances). These effects make it much more difficult to study the muon production profile. Larger zenith angle showers, such as at 60°, have the majority of muons produced far above the ground so they can cover a core distance of a few km with a sufficient density to be detected. It is possible to study the production profile of muons at high zenith angles and this is the basis of the current MPD reconstructions [44].

6.2 Muon timing study

Figure 6.1 shows the muon production height vs the arrival time at the ground for a vertical shower. There is a reasonable correlation between arrival time and production height suggesting that the SD time profile may approximate the muon production profile.

Figure 6.2 shows the muon production height vs core distance for a vertical proton shower. For small core distances (<200m) the muon component is dominated by muons produced near the ground, as muons produced close to the ground will land with a high concentration in a small area. This is because the ground close to the axis is within the muon production cone along nearly all of the axis. For core distances larger than this, the muon production height peaks at a height increasing with core distance.

If the muon production rate were uniform along the axis, the muon front would be in a conical shape. This is due to a combination of two effects. Due to the inverse square law, the muon component is expected to be dominated by muons produced closest to the ground. Muons are produced with a limited angular distribution, so at a given point on the ground, muons are only seen in large numbers from sufficiently large enough production heights for

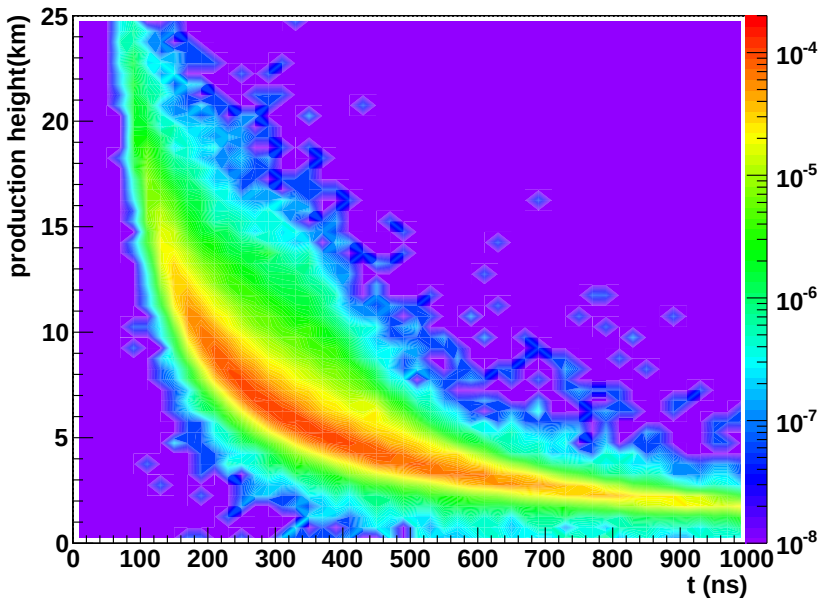

Fig. 6.1. Contour plot of muon production height vs arrival time at the ground behind the plane front for muons with a core distance between 1000 and 1100 m. The shower is a vertical 2×10^{18} eV proton. The contour variable has units of $N_\mu m^{-2} ns^{-1} km^{-1}$.

the point to be within the muon production cone. A combination of these two effects means that muons observed at a given core distance would be dominated by muons produced at a height proportional to core distance, leading to a conical front. Because the muon production is not uniform, the maximum in the muon production height profile at a specific core distance tends to be pushed towards the maximum in muon production. This effect is not large at small core distances, as the muon production rate does not vary greatly over a small range of production heights near the ground, but is more relevant at large core distances.

Figures 6.3 and 6.4 show a contour plot of the muon arrival time at the ground vs core distance. The two black lines correspond to propagation at the speed of light from the 1st interaction height and the maximum in total energy deposit, $X_{\max}$. The first muon arrivals correspond to the 1st interaction. However their density is extremely low and would be difficult to measure even with a detector that covered 100% of the surface. For larger core distances, most of the muons arrive between the corresponding times for 1st interaction and $X_{\max}$. The muons at these core distances mostly come from above the maximum in muon production due to the angular distribution of muons produced. At smaller core distances, there is a greater number of muons arriving later than the time corresponding to $X_{\max}$. The muons produced deeper than $X_{\max}$ dominate at small core distances because they are concentrated over a smaller area around the core due to their limited angular distribution.

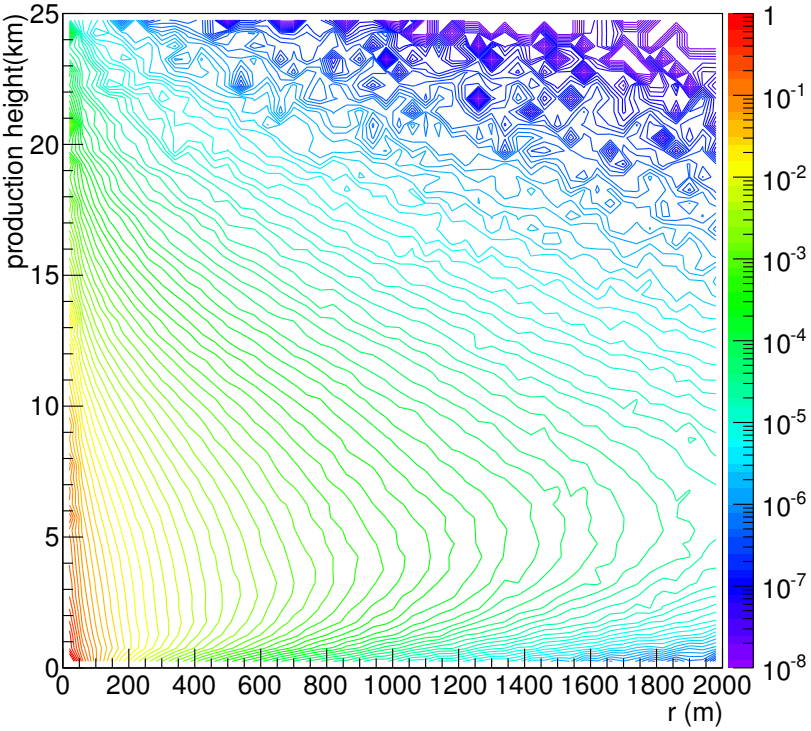

Fig. 6.2. Contour plot of muon production height vs core distance for a vertical 2×10^{18} eV proton. The contour lines indicate the density of muons as $N_{\mu} m^{-2} km^{-1}$.

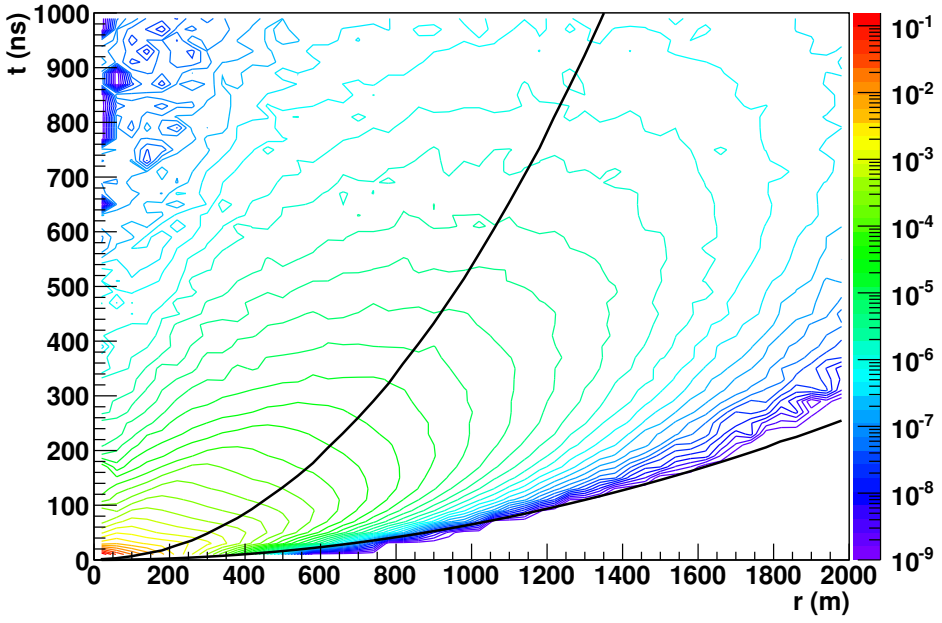

Fig. 6.3. Muon arrival time delay from plane front vs core distance contour plot for a vertical 2×10^{18} eV proton. The contours are in units of N_{μ} $m^{-2} ns^{-1}$. The two black lines correspond to propagation at the speed of light from the 1st interaction height and $X_{\max}$.

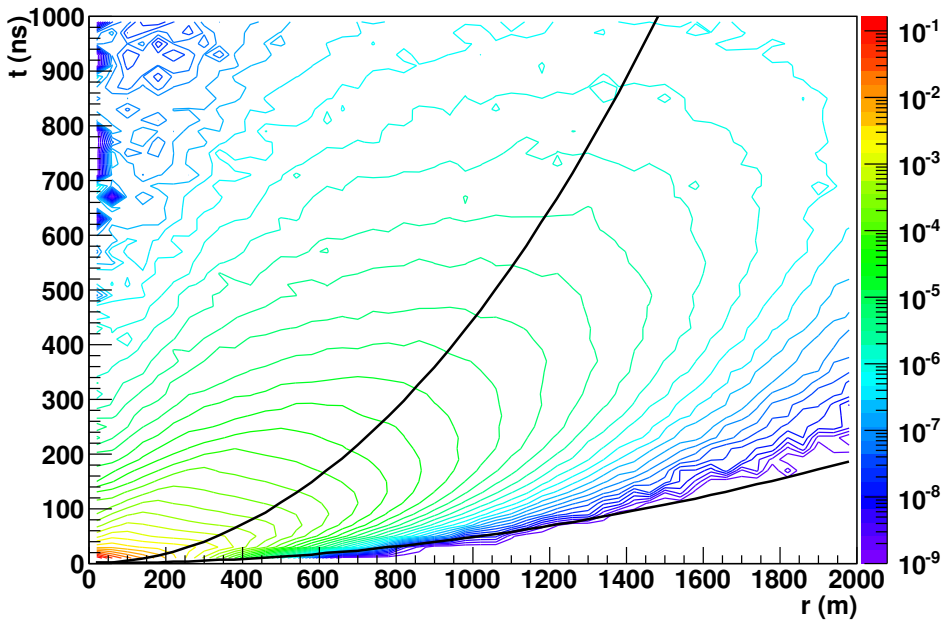

Fig. 6.4. Muon arrival time delay from plane front vs core distance contour plot for a vertical 2×10^{18} eV iron nucleus. The contours are in units of N_μ $m^{-2}ns^{-1}$. The two black lines correspond to propagation at the speed of light from the 1st interaction height and X_{max}.

Different quantiles in the arrival time distribution of muons will most likely correspond to different stages of shower development. To study which quantiles are most useful, several quantiles have been tested in this study. The shape of the shower front at different quantiles were fitted with numerous fitting functions to determine which function is the best fit. Only two functions are shown in this chapter. Figure 6.5 shows the spherical and spherical + cone fits to the shower front. Equation 6.1 is the fitting equation used for the spherical fit. R is the radius of curvature parameter and r is the core distance. Equation 6.2 is the fitting equation used for the spherical + cone fit. b is the cone slope parameter, R is the radius parameter and r is the core distance.

$$t(r) = \frac{R - \sqrt{R^2 - r^2}}{c} \tag{6.1}$$

$$t(r) = \frac{br - \sqrt{R^2 - r^2} + R}{c} \tag{6.2}$$

For the vertical shower it is clear that the spherical fit is not a very good fit to the shower front, especially for larger quantiles. The spherical + cone function fits reasonably well. For 60°, the spherical fits are fairly good and the spherical + cone fits are very similar, with only a small conical component.

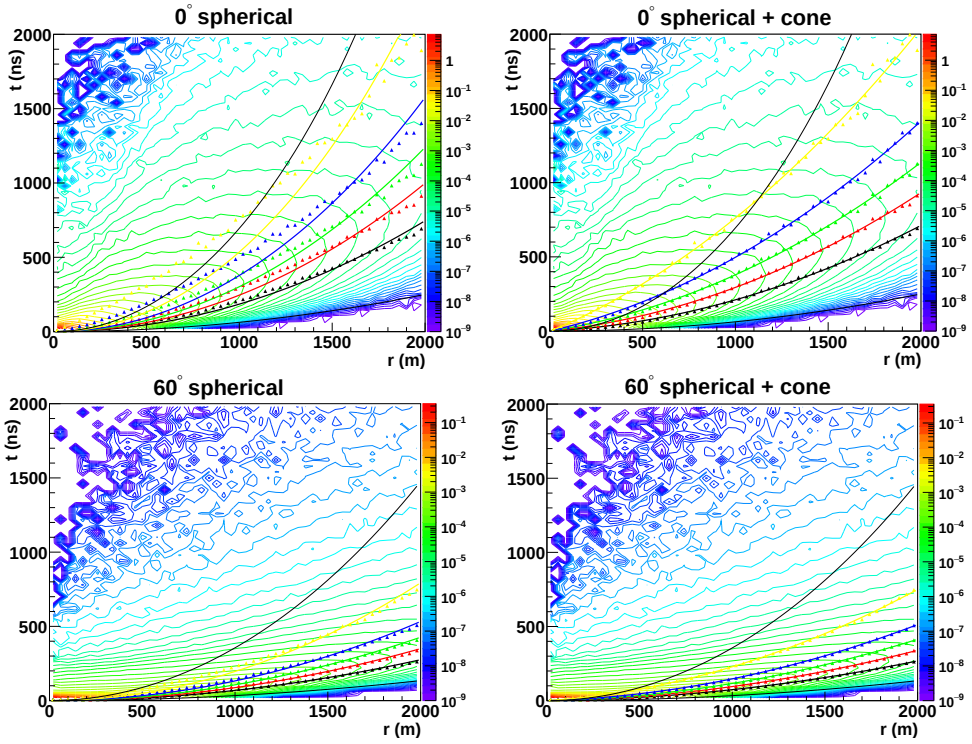

Fig. 6.5. Contour plot of the muon arrival time delay vs core distance for 10^{19} eV proton showers. The contour units are $N_{\mu} m^{-2} ns^{-1}$. The points are the arrival time quantiles for each distance bin. The lines are the fits with a spherical function & a spherical + cone function

The shape of muon arrival time distribution is a lot flatter in the 60° case, and is nearly spherical in shape. This is because most of the muons are produced at higher altitudes, farther away from the ground.

6.3 Muon time fitting study

To see variations between showers and different compositions 100 showers were generated. The showers were 10^{19}eV with 10^{-8} thinning. 60 proton and 40 iron showers were generated. The spherical + cone fitting function (equation 6.2) was applied from quantiles 0.1 to 0.9 in intervals of 0.1. A graph could then be made of the fit parameters vs quantile where each shower is represented by a line to observe how a fit parameter correlates with itself between different quantiles. Figures 6.6 shows the graphs of parameters vs quantile with proton showers colored red and iron showers colored blue.

Both of the parameters show some separation between proton and iron showers. The proton showers are more widely spread and overlap with the iron showers. For vertical showers both the radius and the slope parameters separate compositions well but for 60° the slope does not. This is likely because the cone component is caused by muons produced

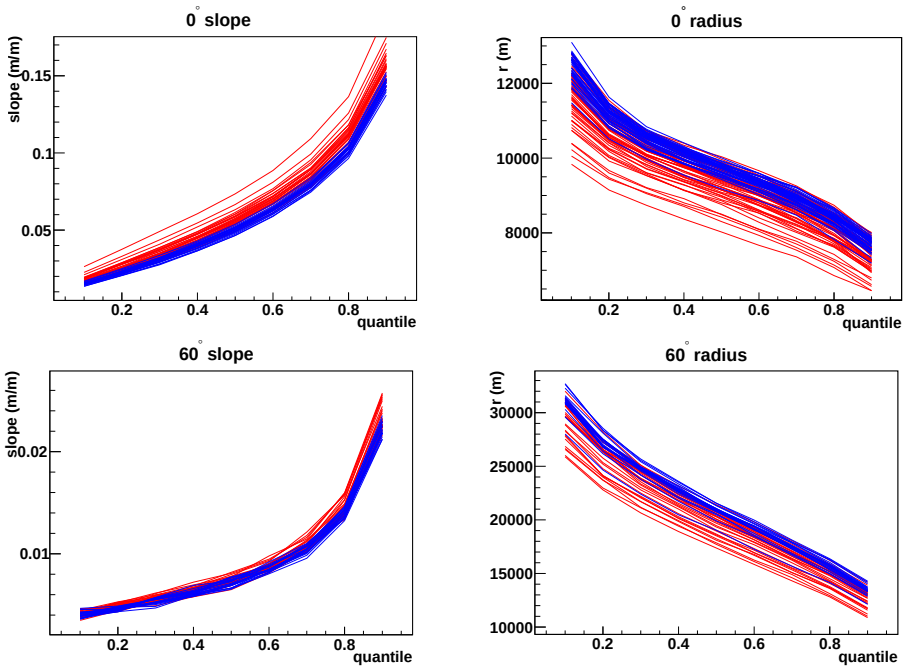

Fig. 6.6. The slope (parameter b, eqn. 6.2) and radius (R) as a function of quantile (details in text), to vertical and 60° 10^{19} eV showers. Proton showers are red and iron showers blue.

near the ground. Only a very small number of muons are produced near the ground for a 60° shower and those muons are produced in a very late stage of shower development which is less likely to correlate with primary particle composition.

It is also useful to see how the fit parameters depend on first interaction height measured vertically above ground level. Figures 6.7 shows the same plots but coloured by first interaction height. The colour gradient begins with red at 15 km above ground level, transitioning to yellow at 25 km, to green at 35 km, and blue at 45 km. Events with very deep 1st interactions seem to be separated from shallower 1st interactions but all other 1st interaction heights are mixed. This is clearer in figures 6.8-6.10.

It is more useful to visualise the parameters as a scatter plot against first interaction distance (measured along the shower axis from ground level), $X_{\rm max}$ and $X^{\mu}_{\rm max}$. Figures 6.8 - 6.11 show scatter plots of the fit parameters. The slope parameter is not shown for 60° showers because the slope is only very small and does not show very good correlation with other shower parameters.

The spherical + cone radius R shows the best correlation with first interaction distance (figures 6.9 a & c). The correlation is also slightly better at the 0.1 quantile. The better correlation for smaller quantiles is expected, as the muons at smaller quantiles correspond to muons produced at earlier stages of development. Larger core distances are dominated by muons produced earlier due to their angular distribution whereas smaller core distances

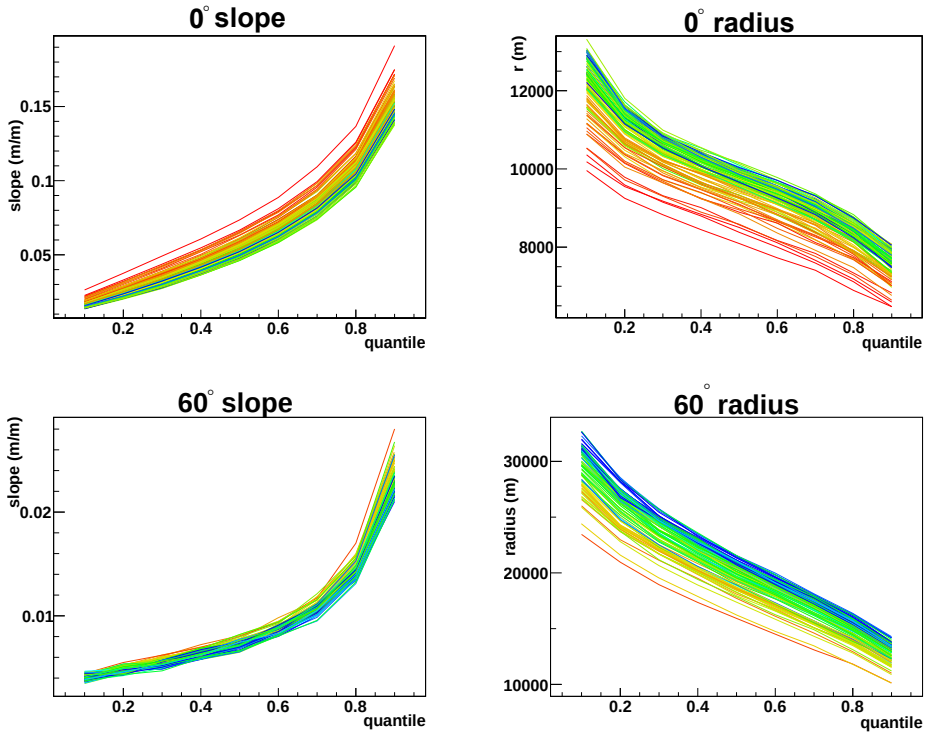

Fig. 6.7. The slope (parameter b in equation 6.2) and radius (R) as a function of quantile (see text for details), for vertical (top) and 60° (bottom) 10^{19} eV showers. The colour gradient begins with red at 15 km above ground level, transitioning to yellow at 25 km, to green at 35 km, and blue at 45 km.

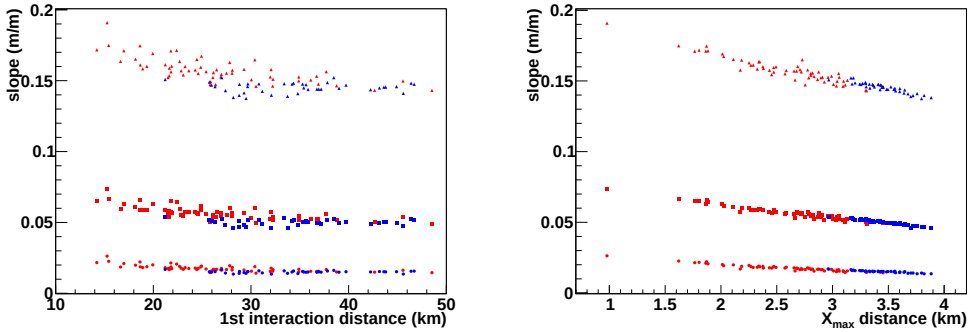

Fig. 6.8. The spherical + cone fit slope (parameter b in equation 6.2) as a function of the 1st interaction distance from the core (left) and of the $X_{\max}$ distance (right) for vertical 10^{19} eV showers. The quantiles are 0.1 (lower clusters), 0.5 (middle clusters) and 0.9 (upper clusters). The red points are for proton showers and the blue points are for iron showers.

are dominated by muons produced later in the shower's development. Thus we expect that the radius R from the spherical + cone fit to be more sensitive to first interaction since the radius parameter has the largest contribution to the shape of the shower front at large core

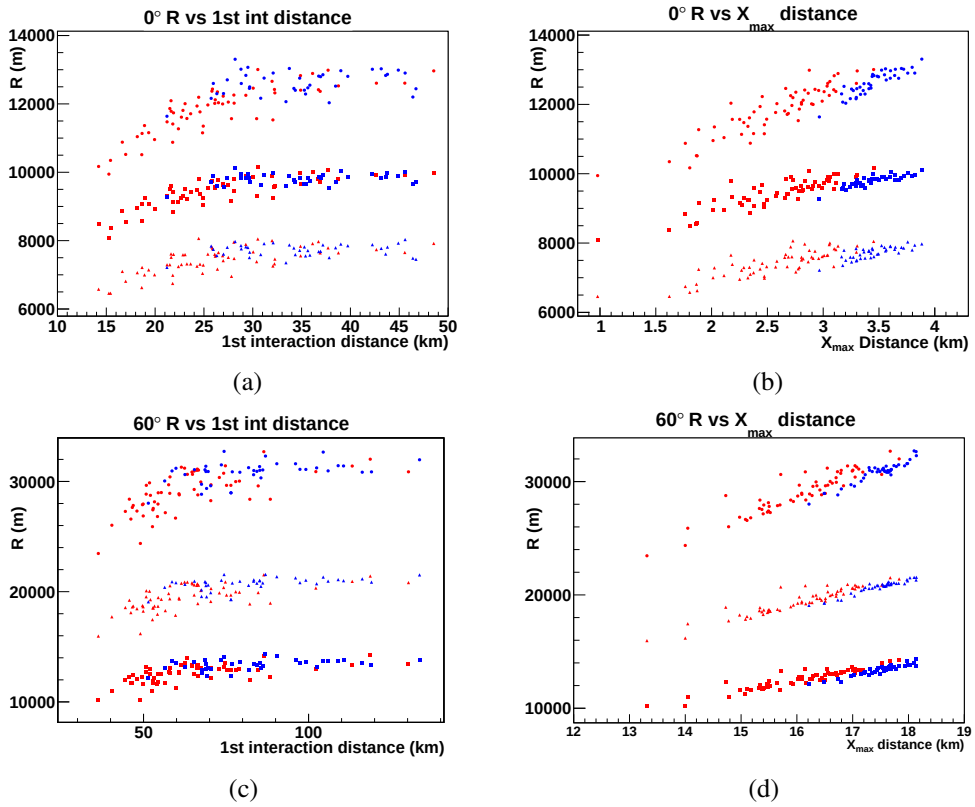

Fig. 6.9. The spherical + cone fit radius (parameter R in equation 6.2) as a function of the 1st interaction distance (left) and of the $X_{\max}$ distance (right) for vertical (top) and 60° (bottom) 10^{19} eV showers. The quantiles are 0.1 (upper clusters), 0.5 (middle clusters) and 0.9 (lower clusters). The red points are for proton showers and the blue points are for iron showers.

distances. The slope parameter b from the spherical + cone fit shows some correlation for vertical showers and almost no correlation for 60° showers. This is expected as the slope is mostly dependent on muons produced near the ground. For 60° showers the muon production has stopped long before reaching the ground, so the slope component is negligible.

The correlations of first interaction distance with the fit parameters are only present for smaller first interaction distances (deeper first interaction depths). There is little correlation at larger first interaction distances. The likely reason for this is that for very shallow first interactions, second and subsequent interactions which are measurable at the surface occur much deeper than the first interaction so the detectable properties of the shower are independent of first interaction height. Measuring even earlier quantiles will probe earlier interactions. Figure 6.10 shows the spherical + cone fit radius R for quantiles 0.1, 0.01, and 0.001. Each of these quantiles represents a different hadronic generation though quantiles 0.01 an 0.001 are impossible to measure with a detector that only covers a small fraction of

the surface. The 0.001 quantile shows a better correlation for deeper first interactions but still do not show good correlation for shallower first interactions.

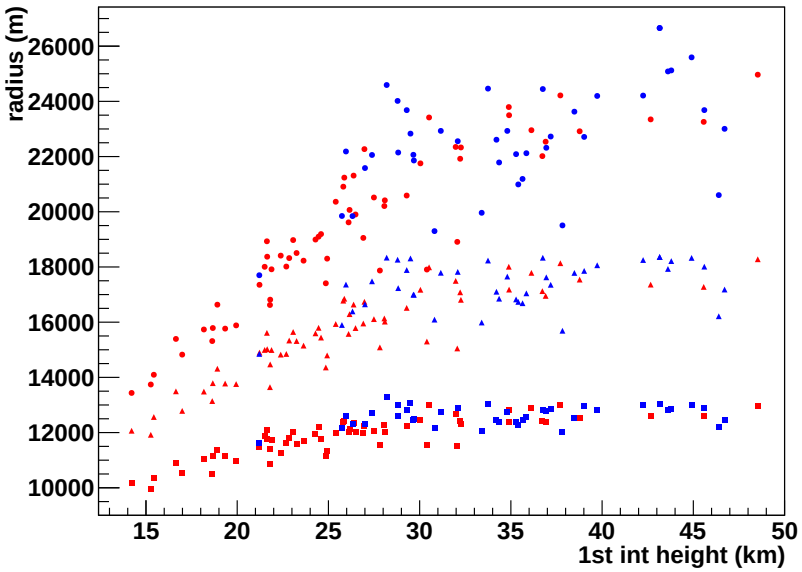

Fig. 6.10. Radius of the spherical + cone fit vs 1st interaction height for vertical showers. The squares are for the 0.1 quantile, the triangles for the 0.01 quantile and the circles for the 0.001 quantile. The red points are for proton showers and the blue points are for iron showers.

A correlation of R with X_{max} is apparent for both 0° and 60° showers. This correlation exists for all 3 quantiles, over the whole range of X_{max} values. As expected, R increases with increasing distance to X_{max}. There is also a small apparent separation between proton and iron showers in this plot, meaning that the radius R not only depends on X_{max}, but also composition. This could allow for a better composition determination if R could be accurately determined from the SD in a hybrid shower. It is also not clear from these plots which quantile shows the best correlation with X_{max}, so further analysis on this matter is required. The slope parameter b decreases with increasing X_{max} distance. It is not entirely clear why this happens. For showers with a smaller X_{max} distance, most of the muons except those very close to the core come from above X_{max} where the shower is still developing. This could mean that muons on average come from a smaller distance since that is where most of the muons are produced, increasing the cone component.

The fit parameters can also be compared with the muon production profile. In this study, X^{μ}_{max} was obtained from the muon profile in the CORSIKA longitudinal file by calculating the rate of change in the number of muons with depth, and finding the maximum. Figure 6.11 shows the radius R against the distance to X^{μ}_{max} along the shower axis. The FD can measure X_{max} with good resolution, and if the SD could measure the X^{μ}_{max} , figure 6.12

shows the proton/iron discrimination power that one could get if using $X_{\max}$ and $X^{\mu}_{\max}$. The distributions of $X_{\max}$ and $X^{\mu}_{\max}$ for proton and iron show an overlap if the distributions are taken separately. However, for showers with a given $X_{\max}$ value have an $X^{\mu}_{\max}$ value that is different depending on primary composition, so if both are known a much better composition separation is achievable.

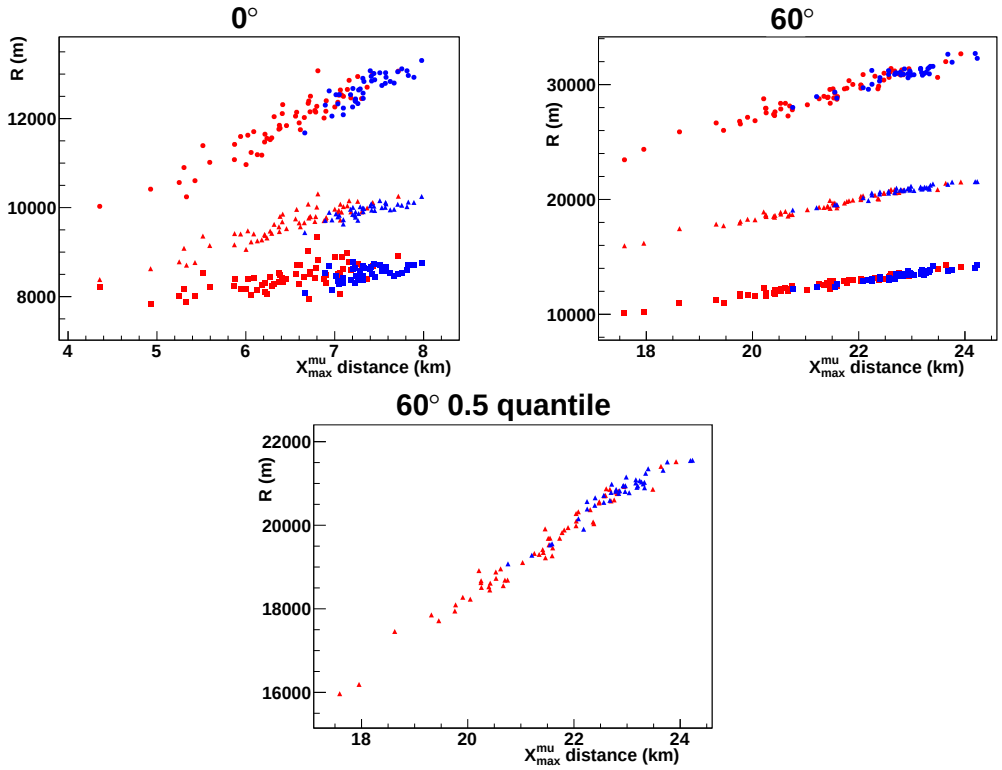

Fig. 6.11. Radius of the spherical + cone fit R vs $X^{\mu}_{\max}$ distance for vertical (left) and 60° (right) showers. The quantiles are 0.1 (lower cluster), 0.5 (middle clusters) and 0.9 (upper clusters). The bottom plot is a zoomed version of the 0.5 quantile for 60 degree showers

The fit parameters show a correlation with the distances to $X^{\mu}_{\max}$ over the whole range of simulated $X^{\mu}_{\max}$. The radius of the spherical + cone fit increases with increasing $X^{\mu}_{\max}$ distance as expected.

When the radius R is plotted against distance to $X^{\mu}_{\max}$, vertical showers show a correlation similarly good to the correlation with radius against $X_{\max}$. For 60° showers, the correlation between radius and distance to $X^{\mu}_{\max}$ is much higher than between radius and distance to $X_{\max}$. For both zenith angles, there is not as much of a separation between protons and iron as there was with distance to $X_{\max}$. This means that the radius is measuring muon development information independently to primary composition. Additionally, the plots of $X_{\max}$ vs $X^{\mu}_{\max}$ show a separation between proton and iron similar to the plots of radius vs distance to $X_{\max}$.

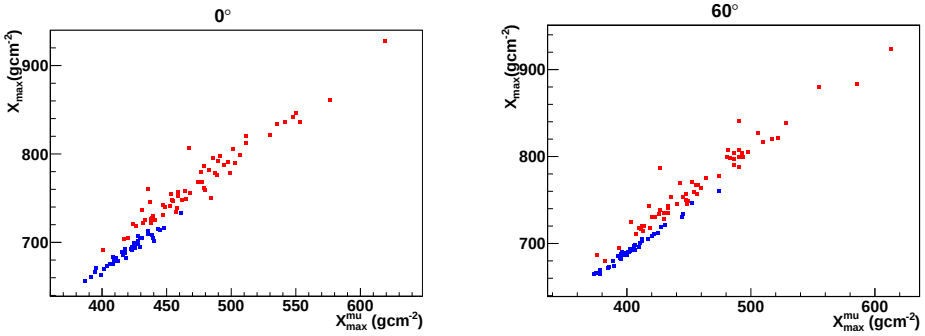

(a) (b)

Fig. 6.12. $X_{\max}$ vs $X^{\mu}_{\max}$ for vertical (left) and 60° (right) showers.

6.3.1 Resolution of shower parameters using shower front shape

In this section, the ability to resolve shower parameters (specifically $X_{\max}$, $X^{\mu}_{\max}$, and 1st interaction depth) using shower front shape is examined. A fit is performed of the shower parameters against spherical + cone fit R, and the RMS difference between the predicted value of the parameter from the true value is found. As the best quantile is not yet known, this is performed over a range of quantiles, to determine which quantile is best. For this method, the depth of 1st interaction, $X_{\max}$, and $X^{\mu}_{\max}$ are used instead of height as they vary more linearly with R, and they are easier to compare to each other. Although the plots shown previously for shower parameters against R show approximately linear trends, a quadratic fit is used to account for any slight non-linearity. Figures 6.13 and 6.14 show the RMS difference vs quantile for the three parameters for vertical and 60° showers.

As expected, for both vertical and 60° showers, the smallest quantiles are best for determining 1st interaction depth, though the dependence on quantile is not very strong, particularly in the 60° case. 1st interaction resolution is better for vertical showers, most likely for two reasons. First, due to the shorter distance from muon production to the ground, radii of curvature are smaller for a given quantile, with more curvature in the shower front for vertical showers, and any change in production depth will translate to a larger change in arrival time at the ground. Secondly, due to geometric effects, muons produced at shallower depths are preferred at larger core distances, so muons from earlier in the shower's development contribute more to the shower front shape.

$X^{\mu}_{\max}$ is best reconstructed for 60° showers. As geometric effects do not lead to a strong preference for muons produced at shallower or deeper depths along the production profile, this is expected. This also explains why $X^{\mu}_{\max}$ resolution is highest using the middle quantiles as these correspond to muons produced around $X^{\mu}_{\max}$. For vertical showers, there is a better

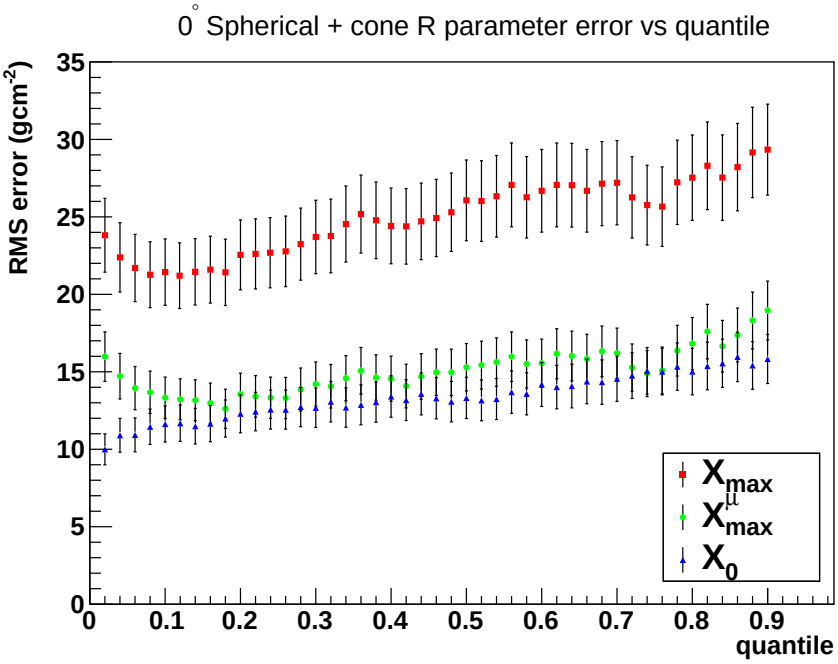

Fig. 6.13. RMS deviation of predicted parameters (1st interaction depth, $X_{\max}$, and $X^{\mu}_{\max}$) vs quantile for vertical showers.

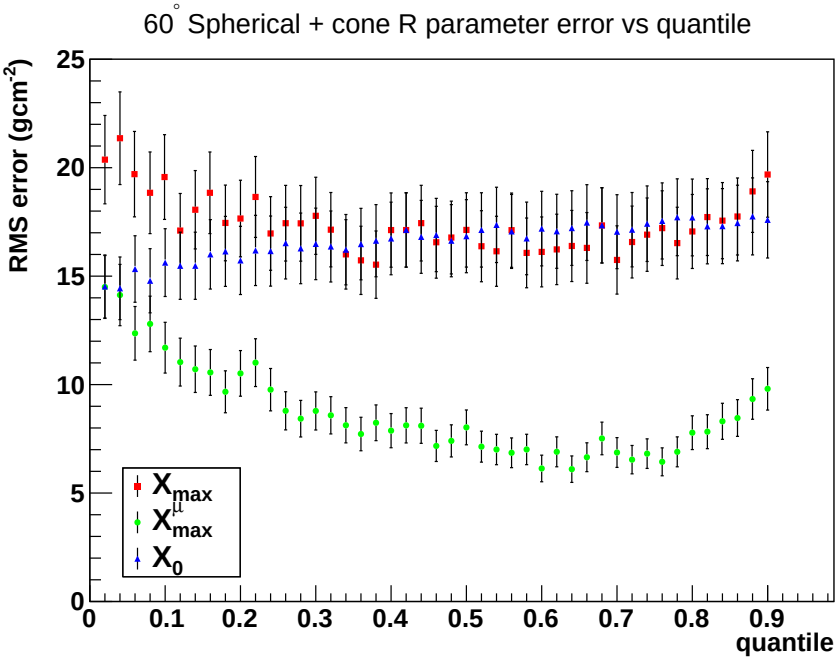

Fig. 6.14. RMS deviation of predicted parameters (1st interaction depth, $X_{\max}$, and $X^{\mu}_{\max}$) vs quantile for 60° showers.

resolution at earlier quantiles. It is not entirely clear why, but geometric effects likely play a role, as they are more relevant at greater depths, which would correspond to later quantiles.

The $X_{\max}$ resolution for both vertical and 60° showers follows a similar trend to the $X^{\mu}_{\max}$ resolution though resolution is poorer in the case of $X_{\max}$. This is expected, as $X_{\max}$ is primarily defined by the electromagnetic component of the shower. As $X_{\max}$ and $X^{\mu}_{\max}$ are correlated, the best indicator of $X_{\max}$ from the muon profile is likely to be $X^{\mu}_{\max}$, so it is expected that the $X_{\max}$ resolution is related to the $X^{\mu}_{\max}$ resolution.

Figures 6.15 - 6.18 show the distributions of $X_{\max}$ and $X^{\mu}_{\max}$ for these 100 showers.

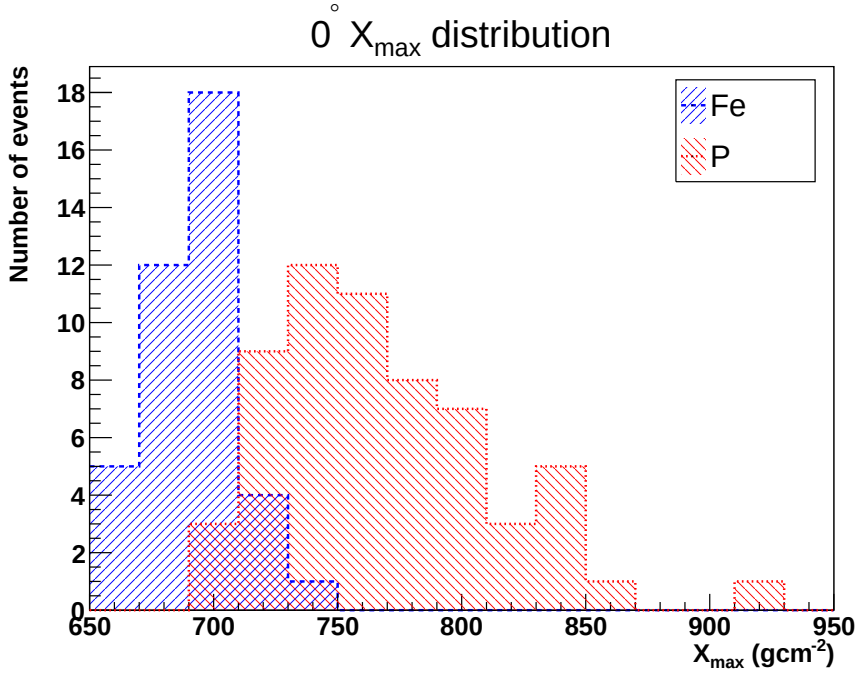

Fig. 6.15. $X_{\max}$ distribution for vertical showers

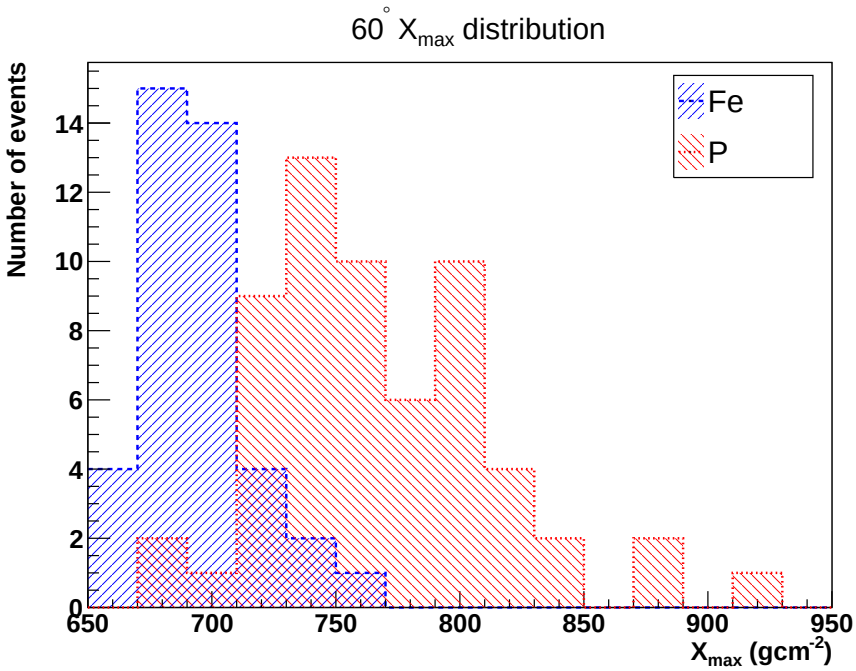

Fig. 6.16. $X_{\max}$ distribution for 60° showers

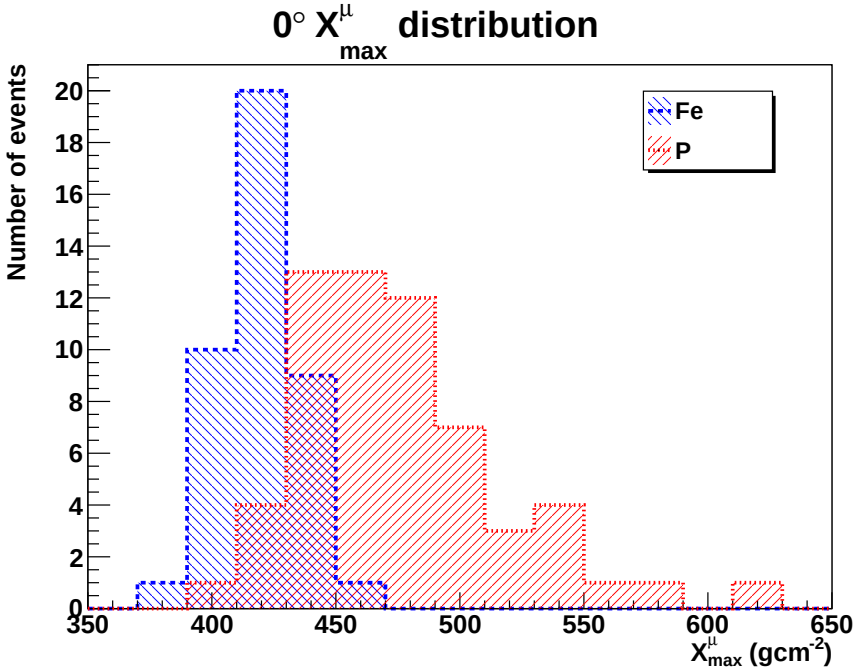

Fig. 6.17. $X^{\mu}_{\max}$ distribution for vertical showers

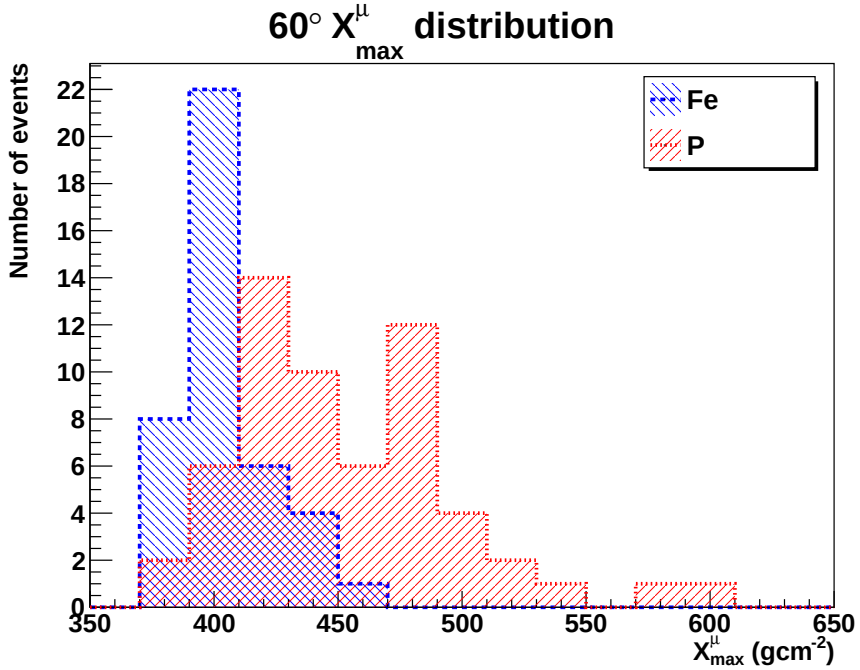

Fig. 6.18. $X^{\mu}_{\max}$ distribution for 60° showers

6.3.2 Detector resolution

This study has so far not considered the effect of a detector in the ability to resolve shower parameters with the shape of the muon front. Here detectability of the shower front shape will be briefly considered.

Detector density

The limited sampling area of a detector array may have difficulties resolving the shower front shape for a number of reasons including a limited sampling due to the sparse array, statistical uncertainty due to the limited area of each detector, and the time resolution of detectors.

A limited sampling due to a sparse array will have the effect of giving timing at a few different core distances. The number of stations will always be at least 3, as this many are required for an event to be reconstructed, with a larger number available at higher energies. This alone would not prevent a reconstruction of shower front shape, as this fit has two parameters, if geometry is already known. If geometry is not known, a larger number of detectors may be needed, as geometry fitting will introduce 3 additional parameters using timing.

Detector area

The statistical uncertainty arising from the limited detector area is likely the greatest concern for reconstructing shower front shape. It may be difficult to determine the uncertainties without a full simulation study, but some conclusions may be drawn from results from the MPD analysis from the Auger collaboration, where a maximum in muon production is found for muons that land on the ground [70]. The method discussed in this chapter is likely to give similar results to the MPD analysis, which is done for showers with a high zenith angle. The MPD analysis could resolve the maximum in muon production depth to within 50 g cm^{-2} at 1.5×10^{19} eV, and 30 g cm^{-2} at 9×10^{19} eV. A similar resolution would be expected with this study for 60° showers. Vertical showers have densities of muons at the ground comparable to that of 60° showers, for core distances used in this study, so $X^{\mu}_{\max}$ resolution is not expected to be worse for vertical events. Additionally, for the MPD study, there was a minimum core distance of 1200 m due to the narrow time distribution of muons at small core distances, where errors due to kinematic delay (from muons having velocities slightly below c), and detector time resolution become dominant. Due to the wider time distribution of muon arrivals at the ground for vertical showers, smaller core distances may be used, where muon densities are greater, potentially allowing better $X^{\mu}_{\max}$ resolution than the MPD analysis.

It is reasonable given these factors, that the upgraded Pierre Auger Observatory surface array may have the ability to resolve a maximum in muon production profile sufficiently to provide useful composition information from shower front shape over a wide range of zenith angles, for energies above $\sim 10^{19}$ eV.

6.4 Conclusions

It can be concluded that for both vertical and 60° showers, muon arrival times correlate well with production height (as seen in figure 6.1). In the case of 60° showers, due to the long distances from muon production to the ground, muons can spread out to a spherical front shape at the ground, with a radius of curvature tracing back to near the maximum in muon production, $X^{\mu}_{\max}$. For vertical showers, the limited angular distribution of muons leads to muons produced at lower altitudes covering a smaller area, leading to shower fronts that are between a conical and spherical shape. Despite the complexities in the shape of shower fronts for vertical showers, the shape of the shower front still closely correlates with $X^{\mu}_{\max}$. With detectors capable of distinguishing the muon component from the electromagnetic component, the determination of $X^{\mu}_{\max}$ is still feasible for vertical showers. This may allow a dataset similar to the MPD dataset over all zenith angles.

Shower front shape for both vertical and 60° showers correlate with $X_{\max}$, but not as well as for $X^{\mu}_{\max}$. Additionally, shower front shape did not depend significantly on composition for a given $X^{\mu}_{\max}$, but it did show a small dependence for a given $X_{\max}$. It may be possible for hybrid events to improve composition resolution using muon shower front shape information.

Though it is theoretically possible to measure the distance to the first interaction using the leading edge of the shower front, it would require an extremely dense array of detectors, given the very low densities of muons in this leading edge.

Chapter 7

Conclusions

Over the course of this work a number of different aspects of UHECR detection have been studied. Firstly, misalignments in the Fluorescence Detector telescopes were discovered, and quantified by detecting inconsistencies in the reconstructed geometry of observed showers. Due to biases observed in simulated events due to resampling of thinned extensive air shower simulations, a new resampling method was developed, where the area used for resampling was allowed to vary to minimise the distance from which particles were sampled into a detector, reducing biases associated with sampling over a large area. Finally, with the Surface Detector array being upgraded with the ability to separate the muon component, simulations were produced to study the shape of the muon shower front, to determine if the shape of the shower front could be used to reconstruct information on the longitudinal profile. It was found that X^{μ}_{max} correlates well with the shape of the shower front, and that it should be feasible at higher energies to determine shower front shape with the surface detector array of the Pierre Auger Observatory.

Telescope Alignment

- A discontinuity was observed in timing fits when crossing between Coihueco telescopes 5 and 6. The most logical explanation for this is a pointing offset of one of the two telescopes relative to the other.
- A relationship between this time discontinuity and the shower geometry was derived for a given relative pointing offset. This relation then allowed for the relative pointing offsets for every pair of adjacent telescopes to be determined. A similar relation was also determined for SDP fits, and provided additional data to fit relative pointing offsets.

- Both timing and SDP data were consistent with relative pointing offsets, and could not be explained by other factors, such as a fixed timing offset.
- It was then necessary to find any offsets in the absolute pointing offsets of telescopes. Surface detector data from hybrid events, with core position and timing, could be used to find any absolute pointing offsets.
- complications arose in determining absolute pointing offsets due to biases in core positions, and uncertainties in timing offset between the Fluorescence Detector and the Surface Detector. A method was developed to correct for these biases, allowing for independent determination of pointing directions using both timing and SDP data from observed showers.
- Though the different methods mostly agreed well, there were some discrepancies between the timing and SDP results, as well as disagreements with other telescope pointing studies. Timing residuals from CLF shots, and geometry differences between FD and SD reconstructions showed that some telescope optics were misaligned in a way that altered the telescopes field of view.
- Physical inspection of the telescope optics showed that this misalignment was present in telescope 4 of Loma Amarilla, which was then corrected.

Resampling

- Cosmic ray shower simulations at the highest energy are enormously computationally intensive, containing hundreds of billions of particles. Because of this, a procedure known as thinning is employed, where only a subset of particles are tracked, and receive a weight based on the probability of being tracked.
- Though thinning preserves the overall statistics of shower properties such as particle densities and time distributions when weighting is applied, the response of a particle detector would contain artificial fluctuations due to there being weighted particles at the ground.
- To prevent these artificial fluctuations, a method called resampling (also known as dethinning) is employed where weighted particles are sampled from a much larger area surrounding the detector, and injected into the detector with unity weight.
- In previously used resampling methods, biases were present in both the density and timing of particles due to the large areas used for resampling, as the density of particles can vary strongly with position.

- A new resampling method was developed, that drew particles from a much smaller area where possible to do so while avoiding artificial fluctuations. This new resampling method was shown to have significantly reduced biases in both particle density and arrival time.
- This new resampling method is now the default method used in the $\overline{\text{Off}}\underline{\text{line}}$ software package, for surface detector simulations.

Shower front shape

- The Pierre Auger Surface Detector is being upgraded with the ability to separate the muon and electromagnetic signals, to be able to resolve mass composition. In addition to densities of these components, timing may also be useful for this, especially the muon component.
- To search for possible composition sensitive information in the shape of the muon front, showers were simulated with a low thinning level, to obtain high statistics on individual events.
- Examining the shape of the shower front over a wide range of quantiles in the arrival time distribution, it was found that the shape is described very well by a sum of a spherical and conical function.
- The radius of the spherical component of the shower front was found to show correlations with X_{max}, X^{μ}_{max}, and first interaction distance. This correlation was quantified over a range of quantiles, to determine what quantiles may be the most useful for resolving these shower parameters using shower front shape.
- It was found that X^{μ}_{max} correlates well with the shape of the shower front over a broad range of quantiles, for both vertical and 60° showers. First interaction depth could be resolved with extremely small quantiles, but these would be very difficult to detect with a sparse detector array.
- It is likely that the Pierre Auger surface detector will be able to resolve the shape of the shower front, and hence X^{μ}_{max}, well enough to gain useful composition information from individual showers.

References

[1] Abbasi, R. U., Abu-Zayyad, T., Allen, M., et al. (2008). First Observation of the Greisen-Zatsepin-Kuzmin Suppression. *Physical Review Letters*, 100(10):101101.

[2] Abu-Zayyad, T., Aida, R., Allen, M., et al. (2012). The surface detector array of the Telescope Array experiment. *Nuclear Instruments and Methods in Physics Research A*, 689:87–97.

[3] Adams, J. H., Ahmad, S., Albert, J. N., et al. (2013). An evaluation of the exposure in nadir observation of the JEM-EUSO mission. *Astroparticle Physics*, 44:76–90.

[4] Allard, D. (2012). Extragalactic propagation of ultrahigh energy cosmic-rays. *Astroparticle Physics*, 39:33–43.

[5] Aloisio, R., Berezinsky, V., Blasi, P., Gazizov, A., Grigorieva, S., and Hnatyk, B. (2007). A dip in the UHECR spectrum and the transition from galactic to extragalactic cosmic rays. *Astroparticle Physics*, 27(1):76–91.

[6] Antoni, T., Apel, W. D., Badea, A. F., et al. (2005). KASCADE measurements of energy spectra for elemental groups of cosmic rays: Results and open problems. *Astroparticle Physics*, 24(1-2):1–25.

[7] Apel, W. D., Arteaga-Velázquez, J. C., Bekk, K., et al. (2011). Kneelike Structure in the Spectrum of the Heavy Component of Cosmic Rays Observed with KASCADE-Grande. *Physical Review Letters*, 107(17):171104.

[8] Argirò, S., Barroso, S. L. C., Gonzalez, J., Nellen, L., Paul, T., Porter, T. A., Prado, L., J., Roth, M., Ulrich, R., and Veberič, D. (2007). The offline software framework of the Pierre Auger Observatory. *Nuclear Instruments and Methods in Physics Research A*, 580:1485–1496.

[9] Arqueros, F., Bellido, J., Covault, C., D'Urso, D., Di Giulio, C., Facal, P., Fick, B., Guarino, F., Malek, M., Matthews, J. A. J., Matthews, J., Meyhand an, R., Monasor, M., Mostafa, M., Petrinca, P., Roberts, M., Sommers, P., Travnicek, P., Valore, L., Verzi, V., and Wiencke, L. (2005). The Central Laser Facility at the Pierre Auger Observatory. In *29th International Cosmic Ray Conference (ICRC29), Volume 8*, volume 8 of *International Cosmic Ray Conference*, page 335.

[10] Arqueros, F., Hörandel, J. R., and Keilhauer, B. (2008). Air fluorescence relevant for cosmic-ray detection—Summary of the 5th fluorescence workshop, El Escorial 2007. *Nuclear Instruments and Methods in Physics Research A*, 597(1):1–22.

[11] Askaryan, G. A. (1962). Excess Negative Charge of the Electron-Photon Shower and Coherent Radiation Originating from It. Radio Recording of Showers under the Ground and on the Moon. *Journal of the Physical Society of Japan Supplement*, 17:257.

[12] Auger, P., Ehrenfest, P., Maze, R., Daudin, J., and Fréon, R. A. (1939). Extensive Cosmic-Ray Showers. *Reviews of Modern Physics*, 11:288–291.

[13] Baltrusaitis, R. M., Cady, R., Cassiday, G. L., et al. (1985). The Utah Fly's Eye detector. *Nuclear Instruments and Methods in Physics Research A*, 240(2):410–428.

[14] Beatty, J. J. and Westerhoff, S. (2009). The Highest-Energy Cosmic Rays. *Annual Review of Nuclear and Particle Science*, 59(1):319–345.

[15] Bellido, J. (2005). Measurement of the time synchronization between the SD and the FD. Technical report, Pierre Auger Observatory. GAP-2005-085.

[16] Bellido, J., Dawson, B., and Saffi, S. (2013). Fixing the Systematics in the Hybrid Reconstruction of the Shower Axis in Loma Amarilla. Technical report, Pierre Auger Observatory. GAP-2013-010.

[17] Benzvi, S. Y., Cester, R., Chiosso, M., Connolly, B. M., Filipčič, A., García, B., Grillo, A., Guarino, F., Horvat, M., Iarlori, M., Macolino, C., Matthews, J. A. J., Melo, D., Mussa, R., Mostafá, M., Pallota, J., Petrera, S., Prouza, M., Rizi, V., Roberts, M., Rodriguez Rojo, J. R., Salamida, F., Santander, M., Sequeiros, G., Tonachini, A., Valore, L., Veberič, D., Westerhoff, S., Zavrtanik, D., and Zavrtanik, M. (2007). The Lidar system of the Pierre Auger Observatory. *Nuclear Instruments and Methods in Physics Research A*, 574(1):171–184.

[18] Bertou, X., Allison, P. S., Bonifazi, C., Bauleo, P., Grunfeld, C. M., Aglietta, M., Arneodo, F., Barnhill, D., Beatty, J. J., Busca, N. G., Creusot, A., Dornic, D., Etchegoyen, A., Filevitch, A., Ghia, P. L., Lhenry-Yvon, I., Medina, M. C., Moreno, E., Nitz, D., Ohnuki, T., Ranchon, S., Salazar, H., Suomijärvi, T., Supanitsky, D., Tripathi, A., Urban, M., and Villasenor, L. (2006). Calibration of the surface array of the Pierre Auger Observatory. *Nuclear Instruments and Methods in Physics Research A*, 568(2):839–846.

[19] Billoir, P. (2008). A sampling procedure to regenerate particles in a ground detector from a "thinned" air shower simulation output. *Astroparticle Physics*, 30:270–285.

[20] Bird, D. J., Corbato, S. C., Dai, H. Y., et al. (1995a). Detection of a Cosmic Ray with Measured Energy Well beyond the Expected Spectral Cutoff due to Cosmic Microwave Radiation. *Astrophysical Journal*, 441:144.

[21] Bird, D. J., Corbató, S. C., Dai, H. Y., et al. (1995b). Results from the Fly's Eye experiment. In *Intersections between Particle and Nuclear Physics*, volume 338 of *American Institute of Physics Conference Series*, pages 839–854.

[22] Bonifazi, C. and Pierre Auger Collaboration (2009). The angular resolution of the Pierre Auger Observatory. *Nuclear Physics B Proceedings Supplements*, 190:20–25.

[23] Botti, A. M. (2019). The AMIGA underground muon detector of the Pierre Auger Observatory - performance and event reconstruction. *International Cosmic Ray Conference*, 36:202.

[24] Boyer, J. H., Knapp, B. C., Mannel, E. J., and Seman, M. (2002). FADC-based DAQ for HiRes Fly's Eye. *Nuclear Instruments and Methods in Physics Research A*, 482(1-2):457–474.

[25] Brack, J. T., Meyhandan, R., Hofman, G. J., and Matthews, J. (2004). Absolute photometric calibration of large aperture optical systems. *Astroparticle Physics*, 20(6):653–659.

[26] Bueno, A., Garcia-Gàmez, D., and Molina, L. (2015). Towards a full understanding of the different contributions to $X^{\mu}_{\rm max}$ bias. Technical report, Pierre Auger Observatory. GAP-2015-034.

[27] Bunner, A. N. (1967). *Cosmic Ray Detection by Atmospheric Fluorescence.* PhD thesis, Cornell University.

[28] Caccianiga, L. (2019). Anisotropies of the Highest Energy Cosmic-ray Events Recorded by the Pierre Auger Observatory in 15 years of Operation. *International Cosmic Ray Conference*, 36:206.

[29] Cazon, L. (2020). Working Group Report on the Combined Analysis of Muon Density Measurements from Eight Air Shower Experiments. *arXiv e-prints*. arXiv:2001.07508.

[30] Chiba, N., Hashimoto, K., Hayashida, N., et al. (1992). Akeno Giant Air Shower Array (AGASA) covering 100 km ^{2} area. *Nuclear Instruments and Methods in Physics Research A*, 311(1-2):338–349.

[31] Collica, L. (2016). Measurement of the muon production depths at the Pierre Auger Observatory. *European Physical Journal Plus*, 131(9):301.

[32] Cronin, J. W. (2005). The highest-energy cosmic rays. *Nuclear Physics B Proceedings Supplements*, 138:465–491.

[33] Dawson, B. (2019). The Energy Scale of the Pierre Auger Observatory. In *36th International Cosmic Ray Conference (ICRC2019)*, volume 36 of *International Cosmic Ray Conference*, page 231.

[34] Dawson, B. R. (2008). Hybrid Performance of the Pierre Auger Observatory. In *International Cosmic Ray Conference*, volume 4 of *International Cosmic Ray Conference*, pages 425–428.

[35] Deligny, O. (2019). The energy spectrum of ultra-high energy cosmic rays measured at the Pierre Auger Observatory and at the Telescope Array. In *36th International Cosmic Ray Conference (ICRC2019)*, volume 36 of *International Cosmic Ray Conference*, page 234.

[36] Dembinski, H., Engel, R., Fedynitch, A., Gaisser, T. K., Riehn, F., and Stanev, T. (2017). Data-driven model of the cosmic-ray flux and mass composition from 10 GeV to 10^{11} GeV. In *35th International Cosmic Ray Conference (ICRC2017)*, volume 301 of *International Cosmic Ray Conference*, page 533.

[37] di Matteo, A., Bister, T., Biteau, J., Caccianiga, L., Deligny, O., Fujii, T., Harari, D., Ivanov, D., Kawata, K., Lundquist, J. P., Menezes, R., Mockler, D., Nonaka, T., Sagawa, H., Tinyakov, P., Tkachev, I., and Troitsky, S. (2020). Full-sky searches for anisotropies in UHECR arrival directions with the Pierre Auger Observatory and the Telescope Array. *arXiv e-prints*. arXiv:2001.01864.

[38] Donato, C. D. et al. (2005). Using star tracks to determine the absolute pointing of the Fluorescence Detector telescopes. Technical report, Pierre Auger Observatory. GAP-2005-008.

[39] Falk, S., Engel, R., Ulrich, R., and Unger, M. (2011). Telescope Alignment Studies. Technical report, Pierre Auger Observatory. GAP-2011-123.

[40] Fuglesang, C. and JEM-EUSO Collaboration (2017). The EUSO program: Imaging of ultra-high energy cosmic rays by high-speed UV-video from space. *Nuclear Instruments and Methods in Physics Research A*, 873:1–4.

[41] Fujii, T., Malacari, M., Albury, J., et al. (2019). A next-generation ground array for the detection of ultrahigh-energy cosmic rays: the Fluorescence detector Array of Single-pixel Telescopes (FAST). In *European Physical Journal Web of Conferences*, volume 210 of *European Physical Journal Web of Conferences*.

[42] Fujii, T., Malacari, M., Bertaina, M., et al. (2016). Detection of ultra-high energy cosmic ray showers with a single-pixel fluorescence telescope. *Astroparticle Physics*, 74:64–72.

[43] Gaisser, T. K. and Stanev, T. (2006). High-energy cosmic rays. *Nuclear Physics A*, 777:98–110.

[44] Garcia-Gamez, D., Bueno, A., Cazon, L., Navas, S., and Pimenta, M. (2010). Composition analysis with MPD distributions: A case study at 60 degree zenith angle. Technical report, Pierre Auger Observatory. GAP-2010-100.

[45] Garcia-Gàmez, D. and Molina, L. (2015). The resampling algorithm in Offline: bias in the time of the particles injected in the surface detectors. Technical report, Pierre Auger Observatory. GAP-2015-006.

[46] Gottowik, M. (2019). Measurements of Inclined Air Showers with the Auger Engineering Radio Array at the Pierre Auger Observatory. *International Cosmic Ray Conference*, 36:274.

[47] Greisen, K. (1966). End to the Cosmic-Ray Spectrum? *Physical Review Letters*, 16(17):748–750.

[48] Hanlon, W. (2019). Telescope Array Hybrid Composition and Auger-TA Composition Comparison. In *European Physical Journal Web of Conferences*, volume 208 of *European Physical Journal Web of Conferences*, page 02001.

[49] Harrison, T., Bellido, J., and Dawson, B. (2010). Alignment of Camera 6 of Coihueco. Technical report, Pierre Auger Observatory. GAP-2010-104.

[50] Haungs, A., Rebel, H., and Roth, M. (2003). Energy spectrum and mass composition of high-energy cosmic rays. *Reports on Progress in Physics*, 66:1145–1206.

[51] Heck, D., Knapp, J., Capdevielle, J. N., Schatz, G., and Thouw, T. (1998). CORSIKA: A Monte Carlo code to simulate extensive air showers. Report FZKA 6019, Karlsruhe.

[52] Heck, D. and Pierog, T. (2019). *Extensive Air Shower Simulations with CORSIKA: A User's Guide*. https://web.ikp.kit.edu/corsika/usersguide/usersguide.pdf.

[53] Heitler, W. (1944). *Quantum Theory of Radiation*. Oxford University Press.

[54] Hersil, J., Escobar, I., Scott, D., Clark, G., and Olbert, S. (1961). Observations of Extensive Air Showers near the Maximum of Their Longitudinal Development. *Physical Review Letters*, 6(1):22–23.

[55] Hess, V. (2018). On the Observations of the Penetrating Radiation during Seven Balloon Flights. *arXiv e-prints*. arXiv:1808.02927.

[56] High Resolution Fly's Eye Collaboration (2005). A Study of the Composition of Ultra-High-Energy Cosmic Rays Using the High-Resolution Fly's Eye. *Astrophysical Journal*, 622(2):910–926.

[57] Hillas, A. M. (1984). The Origin of Ultra-High-Energy Cosmic Rays. *The Annual Review of Astronomy and Astrophysics*, 22:425–444.

[58] Ivanov, A. A. (2015). The Minimum Width of the Arrival Direction Distribution of Ultra-high-energy Cosmic Rays Detected with the Yakutsk Array. *Astrophysical Journal*, 804(2):122.

[59] Ivanov, A. A., Knurenko, S. P., and Sleptsov, I. Y. (2009). Measuring extensive air showers with Cherenkov light detectors of the Yakutsk array: the energy spectrum of cosmic rays. *New Journal of Physics*, 11(6):065008.

[60] Kawata, K., di Matteo, A., Fujii, T., et al. (2019). Updated Results on the UHECR Hotspot Observed by the Telescope Array Experiment. In *36th International Cosmic Ray Conference (ICRC2019)*, volume 36 of *International Cosmic Ray Conference*, page 310.

[61] Keilhauer, B. and Will, M. (2012). Description of atmospheric conditions at the Pierre Auger Observatory using meteorological measurements and models. *European Physical Journal Plus*, 127:96.

[62] Kido, E. and Telescope Array Collaboration (2017). The TAx4 experiment. In *35th International Cosmic Ray Conference (ICRC2017)*, volume 301 of *International Cosmic Ray Conference*, page 386.

[63] Klages, H. and Pierre Auger Collaboration (2012). Enhancements to the Southern Pierre Auger Observatory. In *Journal of Physics Conference Series*, volume 375 of *Journal of Physics Conference Series*, page 052006.

[64] Kobal, M. and Pierre Auger Collaboration (2001). A thinning method using weight limitation for air-shower simulations. *Astroparticle Physics*, 15(3):259–273.

[65] Kümpel, D. (August 2007). *Geometry Reconstruction of Fluorescence Detectors Revisited*. PhD thesis, Bergische Universitaät Wuppertal.

[66] Lawrence, M. A., Reid, R. J. O., and Watson, A. A. (1991). The cosmic ray energy spectrum above $4{\times}10^{17}$ eV as measured by the Haverah Park array. *Journal of Physics G Nuclear Physics*, 17(5):733–757.

[67] Linsley, J. (1963a). Evidence for a Primary Cosmic-Ray Particle with Energy 10^{20} eV. *Physical Review Letters*, 10(4):146–148.

[68] Linsley, J. (1963b). Primary cosmic rays of energy 10^{17} to 10^{20} eV, the energy spectrum and arrival directions. *International Cosmic Ray Conference*, 4:77.

[69] Linsley, J., Scarsi, L., and Rossi, B. (1961). Extremely Energetic Cosmic-Ray Event. *Physical Review Letters*, 6:485–487.

[70] Mallamaci, M. and Pierre Auger Collaboration (2017). Measurements of the depth of maximum muon production and of its fluctuations in extensive air showers above $1.5{\times}10^{19}$ eV at the Pierre Auger Observatory. *International Cosmic Ray Conference*, 301:509.

[71] Matthews, J. (2005). A Heitler model of extensive air showers. *Astroparticle Physics*, 22(5-6):387–397.

[72] Nagano, M. and Watson, A. A. (2000). Observations and implications of the ultrahigh-energy cosmic rays. *Reviews of Modern Physics*, 72(3):689–732.

[73] Newton, D., Knapp, J., and Watson, A. A. (2007). The optimum distance at which to determine the size of a giant air shower. *Astroparticle Physics*, 26(6):414–419.

[74] Nitz, D. F. (2019). New Electronics for the Surface Detectors of the Pierre Auger Observatory. *International Cosmic Ray Conference*, 36:370.

[75] Novotny, V. (2019). Measurement of the spectrum of cosmic rays above $10^{16.5}$ eV with Cherenkov-dominated events at the Pierre Auger Observatory. *International Cosmic Ray Conference*, 36:374.

[76] Ohoka, H., Takeda, M., Hayashida, N., et al. (1997). Further development of data acquisition system of the Akeno Giant Air Shower Array. *Nuclear Instruments and Methods in Physics Research A*, 385:268–276.

[77] Pierre Auger Collaboration (2008). The surface detector system of the Pierre Auger Observatory. *Nuclear Instruments and Methods in Physics Research A*, 586(3):409–420.

[78] Pierre Auger Collaboration (2010). Trigger and aperture of the surface detector array of the Pierre Auger Observatory. *Nuclear Instruments and Methods in Physics Research A*, 613(1):29–39.

[79] Pierre Auger Collaboration (2014a). Probing the radio emission from air showers with polarization measurements. *Physical Review D*, 89(5):052002.

[80] Pierre Auger Collaboration (2014b). Reconstruction of inclined air showers detected with the Pierre Auger Observatory. *Journal of Cosmology and Astroparticle Physics*, 2014(8):019.

[81] Pierre Auger Collaboration (2016). Evidence for a mixed mass composition at the 'ankle' in the cosmic-ray spectrum. *Physics Letters B*, 762:288–295.

[82] Pękala, J. (2019). Production and Quality Control of the Scintillator Surface Detector for the AugerPrime Upgrade of the Pierre Auger Observatory. *International Cosmic Ray Conference*, 36:380.

[83] Pont, B. (2019). A Large Radio Detector at the Pierre Auger Observatory - Measuring the Properties of Cosmic Rays up to the Highest Energies. *International Cosmic Ray Conference*, 36:395.

[84] Protheroe, R. J. (1999). Acceleration and interaction of ultra high energy cosmic rays. In *Topics in Cosmic-Ray Astrophysics*, volume 230, page 247.

[85] Prouza, M. et al. (2005). Star tracking using background data of FD Telescopes-whole star track optimization method. Technical report, Pierre Auger Observatory. GAP-2005-041.

[86] Roulet, E. and Pierre Auger Collaboration (2019). Large-scale anisotropies above 0.03 EeV measured by the Pierre Auger Observatory. *International Cosmic Ray Conference*, 36:408.

[87] Sánchez, F. A. (2019). The muon component of extensive air showers above $10^{17.5}$ eV measured with the Pierre Auger Observatory. *International Cosmic Ray Conference*, 36:411.

[88] Schröder, F. G. (2019). News from Cosmic Ray Air Showers (ICRC 2019 – Cosmic Ray Indirect Rapport). *arXiv e-prints*. arXiv:1910.03721.

[89] Sokolsky, P. and HiRes Collaboration (2011). Final Results from the High Resolution Fly's Eye (HiRes) Experiment. *Nuclear Physics B Proceedings Supplements*, 212:74–78.

[90] Stokes, B. T., Cady, R., Ivanov, D., Matthews, J. N., and Thomson, G. B. (2012). Dethinning extensive air shower simulations. *Astroparticle Physics*, 35(11):759–766.

[91] Takeda, M., Sakaki, N., Honda, K., et al. (2003). Energy determination in the Akeno Giant Air Shower Array experiment. *Astroparticle Physics*, 19(4):447–462.

[92] Tameda, Y. and Telescope Array Experiment (2009). Telescope Array Experiment. *Nuclear Physics B Proceedings Supplements*, 196:74–79.

[93] Telescope Array Collaboration, Shibata, T., Enomoto, A., Fukuda, S., Fukushima, M., Furukawa, K., Ikeda, D., Ikeda, M., Kakihara, K., Ohsawa, S., Sagawa, H., Satoh, M., Shidara, T., Sugimura, T., Yoshida, M., and Telescope Array Collaboration (2008). End-to-end absolute energy calibration of atmospheric fluorescence telescopes by an electron linear accelerator. *Nuclear Instruments and Methods in Physics Research A*, 597(1):61–66.

[94] Tennent, R. M. (1967). The Haverah Park extensive air shower array. *Proceedings of the Physical Society*, 92(3):622–631.

[95] The Pierre Auger Collaboration (1997). The Pierre Auger Observatory design report. (http://www.auger.org/technicalinfo/designreport.html).

[96] The Pierre Auger Collaboration (2010a). A study of the effect of molecular and aerosol conditions in the atmosphere on air fluorescence measurements at the Pierre Auger Observatory. *Astroparticle Physics*, 33(2):108–129.

[97] The Pierre Auger Collaboration (2010b). The fluorescence detector of the Pierre Auger Observatory. *Nuclear Instruments and Methods in Physics Research A*, 620(2-3):227–251.

[98] The Pierre Auger Collaboration (2012). The rapid atmospheric monitoring system of the Pierre Auger Observatory. *Journal of Instrumentation*, 7(9):9001.

[99] The Pierre Auger Collaboration (2013). The Pierre Auger Observatory: Contributions to the 33rd International Cosmic Ray Conference (ICRC 2013).

[100] The Pierre Auger Collaboration (2014). Depth of maximum of air-shower profiles at the Pierre Auger Observatory. I. Measurements at energies above $10^{17.8}$ eV. *Physical Review D*, 90(12):122005.

[101] The Pierre Auger Collaboration (2015). The pierre auger cosmic ray observatory. *Nuclear Instruments and Methods in Physics Research Section A: Accelerators, Spectrometers, Detectors and Associated Equipment*, 798:172 – 213.

[102] The Pierre Auger Collaboration (2016). The Pierre Auger Observatory Upgrade - Preliminary Design Report. *arXiv e-prints*. arXiv:1604.03637.

[103] The Pierre Auger Collaboration (2017). Inferences on Mass Composition and Tests of Hadronic Interactions from 0.3 to 100 EeV using the water-Cherenkov Detectors of the Pierre Auger Observatory. *arXiv e-prints*. arXiv:1710.07249.

[104] The Pierre Auger Collaboration (2019). Data-driven estimation of the invisible energy of cosmic ray showers with the Pierre Auger Observatory. *Phys. Rev. D*, 100(8):082003.

[105] Todero Peixoto, C. J. (2019). Estimating the Depth of Shower Maximum using the Surface Detectors of the Pierre Auger Observatory. *International Cosmic Ray Conference*, 36:440.

[106] Tokuno, H., Tameda, Y., Takeda, M., et al. (2012). New air fluorescence detectors employed in the Telescope Array experiment. *Nuclear Instruments and Methods in Physics Research A*, 676:54–65.

[107] Udo, S., Ogio, S., Takeda, M., et al. (2017). The Telescope Array Low-energy Extension. In *35th International Cosmic Ray Conference (ICRC2017)*, volume 301 of *International Cosmic Ray Conference*, page 544.

[108] Unger, M., Dawson, B. R., Engel, R., Schüssler, F., and Ulrich, R. (2008). Reconstruction of longitudinal profiles of ultra-high energy cosmic ray showers from fluorescence and Cherenkov light measurements. *Nuclear Instruments and Methods in Physics Research A*, 588(3):433–441.

[109] Unger, M., Farrar, G. R., and Anchordoqui, L. A. (2015). Origin of the ankle in the ultrahigh energy cosmic ray spectrum, and of the extragalactic protons below it. *Physical Review D*, 92(12):123001.

[110] Verzi, V. (2019). Measurement of the energy spectrum of ultra-high energy cosmic rays using the Pierre Auger Observatory. *International Cosmic Ray Conference*, 36:450.

[111] Wahrlich, P. S. (2013). *Systematic and statistical uncertainties in cosmic ray arrival direction reconstruction.* PhD thesis, University of Adelaide.

[112] Winn, M. M., Ulrichs, J., Peak, L. S., McCusker, C. B. A., and Horton, L. (1986). The cosmic-ray energy spectrum above 10^{17} eV. *Journal of Physics G Nuclear Physics*, 12(7):653–674.

[113] Younk, P. (2008). FD Telescope Alignment with Golden Hybrids. Technical report, Pierre Auger Observatory. GAP-2008-018.

[114] Younk, P., Diaz, J., Fick, B., and Wiencke, L. (2006). Measurement of the SD-FD time offset using inclined laser shots. Technical report, Pierre Auger Observatory. GAP-2006-005.

[115] Younk, P. and Fick, B. (2006a). FD Telescope Alignment Using CLF Laser Shots. Technical report, Pierre Auger Observatory. GAP-2006-087.

[116] Younk, P. and Fick, B. (2006b). On SDP Reconstruction Accuracy. Technical report, Pierre Auger Observatory. GAP-2006-086.

[117] Yushkov, A. (2019). Mass Composition of Cosmic Rays with Energies above $10^{17.2}$ eV from the Hybrid Data of the Pierre Auger Observatory. *International Cosmic Ray Conference*, 36:482.

[118] Zatsepin, G. T. and Kuz'min, V. A. (1966). Upper Limit of the Spectrum of Cosmic Rays. *Soviet Journal of Experimental and Theoretical Physics Letters*, 4:78.